INVESTIGATION OF MONOTONIC AND CYCLIC LOADING OF PILES IN SAND USING A DIC CALIBRATION CHAMBER

by

Ayda Catalina Galvis Castro

A Dissertation

Submitted to the Faculty of Purdue University

In Partial Fulfillment of the Requirements for the degree of

Doctor of Philosophy

Lyles School of Civil Engineering

West Lafayette, Indiana

December 2020

THE PURDUE UNIVERSITY GRADUATE SCHOOL
STATEMENT OF COMMITTEE APPROVAL

Dr. Rodrigo Salgado, Co-Chair
Lyles School of Civil Engineering

Dr. Monica Prezzi, Co-Chair
Lyles School of Civil Engineering

Dr. Steven T. Wereley
School of Mechanical Engineering

Dr. Weinong Wayne Chen
School of Aeronautics and Astronautics

Approved by:
Dr. Dulcy M. Abraham

Dedicated to my husband Jaime and children, Juan Jose and Gabriel, whose love, sacrifices, support, and encouragement gave me the strength to complete this work.

To my dear Mother and sisters, who have always inspired me.

ACKNOWLEDGMENTS

I would like to express my greatest gratitude to my advisors, Professor Rodrigo Salgado and Professor Monica Prezzi for their endless support and patient guidance throughout my Ph.D. study. I appreciate not only their encouragement to finish this work but also to overcome all difficulties encountered during my time at Purdue.

I would also like to thank the committee members, Professor Steve Wereley and Professor Weinong Wayne Chen. It is a great honor to have you both on my academic committee. I am grateful to Professor Gioacchino Viggiani and Dr. Jeanne Doreau–Malioche for the collaboration that resulted in a paper.

Special thanks are given to my friend and laboratory partner, Dr. Ruben Dario Tovar Valencia. We shared many joys and challenges working in the Bowen laboratory at Purdue University. Without his technical and emotional help, I would not have been able to complete my research.

My sincere thanks to Dr. Fei Han for their valuable discussions during my candidature. Also appreciated was the contribution and help during my experiments from my friend and colleague Eshan Ganju. I would like to acknowledge Mr. Harry Tidrick and Mr. Kevin Brower for their assistance at the Bowen Laboratory.

Finally, I would like to acknowledge the financial support received from the Instituto para el Desarrollo de la Ciencia y Tecnologia en Colombia (Colciencias) and from the award of a Bilsland Dissertation Fellowships.

TABLE OF CONTENTS

LIST OF TABLES 8
LIST OF FIGURES 10
ABSTRACT 17
1. INTRODUCTION 19
2. EFFECT OF LOADING DIRECTION ON THE SHAFT RESISTANCE OF JACKED PILES IN DENSE SAND 23
2.1 Abstract 23
2.2 Introduction 23
2.3 Materials and methods 27
2.3.1 Experimental set-up 27
2.3.2 Test sand 27
2.3.3 Normalised shaft roughness 28
2.3.4 Boundary and scale effects 28
2.3.5 Image analysis 29
2.3.6 Test procedure and test program 29
2.4 Results and discussion 30
2.4.1 Sensor-based results 30
2.4.2 Image-based results 35
2.5 Summary and conclusions 50
2.6 Acknowledgements 52
3. COMPRESSIVE AND TENSILE SHAFT RESISTANCE OF NONDISPLACEMENT PILES IN SAND 53
3.1 Abstract 53
3.2 Introduction 53
3.3 Materials and methods 56
3.3.1 Half-cylindrical calibration chamber 56
3.3.2 Model piles 57
3.3.3 Test sand 58
3.3.4 Image acquisition system and image analysis 59

3.3.5 Test protocol and program 59
3.4 Results and discussion 60
3.4.1 Sensor-based results 60
3.4.2 Degradation of shaft resistance due to CT and TC loading sequences 65
3.4.3 Tensile-to-compressive shaft resistance ratio from first-time loading (FTL) 65
3.4.4 Image-based results 66
3.5 Summary and conclusions 95
3.6 Acknowledgments 97
4. EFFECT OF CYCLIC LOADING ON THE MOBILIZATION OF SHAFT RESISTANCE OF MODEL PILES JACKED IN SAND 98
4.1 Abstract 98
4.2 Introduction 99
4.3 Materials and methods 101
4.3.1 Testing equipment 101
4.3.2 Test sand 103
4.3.3 Image analysis 104
4.3.4 Experimental program 104
4.4 Experimental results 107
4.4.1 Monotonic loading: sensor-based results 107
4.4.2 Cyclic loading: sensor-based and image-based results 120
4.5 Summary and conclusions 140
5. EFFECT OF CYCLIC LOADING ON THE MOBILIZATION OF UNIT BASE RESISTANCE OF MODEL PILES JACKED IN SAND 143
5.1 Abstract 143
5.2 Introduction 144
5.3 Materials and methods 145
5.3.1 Test equipment 145
5.3.2 Test sand 147
5.3.3 Image analysis 148
5.3.4 Test procedure and test program 148
5.4 Experimental results 150

5.4.1 Effect of cyclic displacement half amplitude 150
5.4.2 Effect of number of cycles 166
5.5 Summary and conclusions 177
5.6 Notation 178
6. SUMMARY AND CONCLUSIONS 180
REFERENCES 183
VITA 195
PUBLICATIONS 196

LIST OF TABLES

Table 2.1. Reported values of the tensile-to-compressive shaft resistance ratio SRR................. 25

Table 2.2. Index and mechanical properties of Ohio Gold Frac sand... 27

Table 2.3. Interface friction angles from direct shear tests.. 28

Table 2.4. Roughness parameters of surfaces used before testing (modified after Tovar-Valencia et al. (2018)).. 29

Table 2.5. Test program. 30

Table 2.6. Ratios SRR and SRR_{FTL} from tests performed on jacked model piles. 35

Table 2.7. Thickness of the crushed zone developed during pile installation and thickness of the shear band developed after 15 mm of pile head displacement for the first-time loading stages of monotonically jacked model piles. 36

Table 3.1. Index and mechanical properties of Ohio Gold Frac sand (Adapted from Tovar-Valencia et al. (2018), © ASCE) 58

Table 3.2. Test program. 61

Table 3.3. Peak and limit unit shaft resistances from FTL and STL, and pile head displacement required to mobilize the peak shaft resistance on FTL. 64

Table 3.4. Tensile-to-compressive shaft resistance ratios $SRR_{P,FTL}$ and $SRR_{L,FTL}$ for pre-installed model piles 66

Table 3.5. Average inclination θ_{avg} of the displacement vectors for FTLs on dense and medium-dense sand using model piles with flat and conical bases after $|w|$ = 3.0 mm 71

Table 3.6. Cumulative vertical displacement v (mm) after $|w|$ = 15 mm at h/r_p = 14 and at different normalized radial position r/r_p 77

Table 3.7. Cumulative radial displacement u (mm) after $|w|$ = 15 mm at h/r_p = 14 at different normalized radial position r/r_p 78

Table 3.8. Thickness of the shear band developed after $|\Delta w|$ = 15 mm for the first-time and second-time loading of non-displacement model piles 93

Table 4.1. Equipment components (Adapted from Tovar-Valencia 2019) 103

Table 4.2. Settings for the DIC analysis using VIC 2D (Adapted from Tovar-Valencia et al. 2020) 104

Table 4.3 Test program 107

Table 4.4. Unit shaft resistances mobilized in cyclic load tests.. 124

Table 5.1. Equipment components (Adapted from Tovar-Valencia 2019) 146

Table 5.2. Index properties of Ohio Gold Frac sand ... 147

Table 5.3. Settings in the DIC analysis using VIC-2D (Adapted from Tovar-Valencia et al. 2020) ... 148

Table 5.4. Test program ... 150

Table 5.5. Limit unit base resistance $q_{bL,BC}$ before cycling, maximum unit base resistance $q_{b,max0}$ and minimum unit base resistance $q_{b,min0}$ mobilized in the first cycle, and maximum unit base resistance $q_{b,max}$ and minimum unit base resistance $q_{b,min}$ mobilized in the last cycle for cyclic tests ended at 100 displacement cycles. ... 156

Table 5.6. Values of $q_{b,AC}/q_{bL,BC}$ obtained at four different relative pile base settlements w_b/B for tests with cyclic loading stage performed using a cyclic displacement half amplitude Δw_{cyclic} of 0.25 mm, 0.5 mm, and 1.0 mm. ... 168

Table 5.7. Initial position of soil elements A, B, C, D located around the conical base of the pile for the cycling stage of test CY1.0-N1000 ... 172

LIST OF FIGURES

Figure 2.1. Resistances measured during installation of the model piles in dense sand for tests D-R-TC, D-MR-TC and D-S-TC: (a) unit base resistance, q_b; (b) average limit unit shaft resistance, $q_{sL,avg}$. 31

Figure 2.2. Average unit shaft resistance $q_{s,avg}$ plotted against depth for tension–compression and compression–tension loading tests performed in dense sand using a model pile with a rough shaft (R_n= 0·131): (a) test D-R-TC; (b) test D-R-CT. 32

Figure 2.3. Average unit shaft resistance $q_{s,avg}$ plotted against pile head displacement w for FTL of rough (R_n= 0·131), medium-rough (R_n= 0·064) and smooth (R_n= 0·002) model piles. 34

Figure 2.4. Soil displacement vectors for an absolute value of pile head displacement $|w|$ of 15 mm (pile tip at $h* = 26·5r_p$): (a) tensile loading stage of test D-R-TC; (b) compressive loading stage of test D-R-CT. 38

Figure 2.5. Average direction of displacement vectors along the shaft when the model pile tip is at $h* = 26·5r_p$ and $|w|$= 15 mm: (a) tensile loading stage of test D-R-TC; (b) compressive loading stage of test D-R-CT. 39

Figure 2.6. Vertical and radial displacement profiles at z/r_p = 11 and $|w|$= 15 mm for the tensile loading stage of test D-R-TC and the compressive loading stage of test D-R-CT. 40

Figure 2.7. Radial and shear strain profiles at z/r_p = 11 and $|w|$ = 15 mm for the tensile loading stage of test D-R-TC and the compressive loading stage of test D-R-CT. 41

Figure 2.8. Shear strain increment ΔE_{rz} plotted against the absolute value of pile head displacement $|w|$ of soil elements located at z/r_p = 11 and radial distances of r - r_p= 4·5, 9·6 and 16·6 mm for tensile (test D-R-TC) and compressive (test D-R-CT) loading of rough model pile (ΔE_{rz} is calculated at every $|\Delta w|$ = 1·6 mm ≈ 0·1r_p). 42

Figure 2.9. Radial strain increment ΔE_{rr} plotted against the absolute value of pile head displacement $|w|$ of soil elements located at z/r_p= 11 and radial distances of $r – r_p$ = 4·5 and 16·6 mm for tensile (test D-R-TC) and compressive (test D-R-CT) loading of rough model pile (ΔE_{rr} is calculated every $|\Delta w|$ = 1·6 mm ≈ 0·1r_p). 43

Figure 2.10. Volumetric strain E_{vol} profiles at z/r_p = 11 and magnitude $|w|$ of pile head displacement equal to 15 mm for the tensile loading stage of test D-R-TC and the compressive loading stage of test D-R-CT. 45

Figure 2.11. Direction of the minor principal strain E_2 (largest compressive strain) developed at $|w|$ = 15 mm ($h*$ = 26·5rp) for the: (a) tensile loading stage of test D-R-TC; (b) compressive loading stage of test D-R-CT. 47

Figure 2.12. Magnitude of E_1 and E_2 of soil elements located at z/r_p = 11 plotted against radial position r - r_p relative to the pile shaft at $|w|$= 15 mm for the tensile loading of test D-R-TC and the compressive loading of test D-R-CT (the direction of E_2 is indicated for some data points)....... 48

Figure 2.13. Magnitude and direction of E_1 and E_2 at the end of installation of monotonically jacked model pile (test D-R-TC). 50

Figure 3.1. Schematic of the DIC calibration chamber at Purdue University. 57

Figure 3.2. Model piles. (Adapted from Tovar-Valencia et al. (2018), © ASCE) 58

Figure 3.3. Average unit shaft resistance $q_{s,avg}$ versus penetration depth for the nondisplacement model piles with a flat base in dense and medium-dense sand for (a) compressive-tensile; and (b) tensile-compressive loading sequences. 62

Figure 3.4. Average unit shaft resistance $q_{s,avg}$ versus pile head displacement w from FTL in dense and medium-dense sand samples performed with (a) flat-base; and (b) conical-base model piles. 63

Figure 3.5. Soil displacement vectors after 3 mm of pile head displacement w (negative for tensile loading and positive for compressive loading) for FTL of tests: (a) MD-T(co)#1; (b) MD-CT(co)#2; (c) D-TC(co)#2; (d) D-CT(co)#1; (e) MD-TC(f)#1; (f) MD-CT(f)#2; (g) D-TC(f)#1; and (h) D-CT(f)#1. 67

Figure 3.6. Inclination θ of the displacement vectors versus normalized radial position r/r_p relative to the pile centerline for FTLs after $|w|$=3 mm. 70

Figure 3.7. Cumulative vertical displacement v field after 15 mm of pile head displacement w (negative for tensile loading and positive for compressive loading) for (a) tensile loading in test D-TC(f)#1; (b) compressive loading in test D-CT(f)#2; (c) tensile loading in test MD-TC(f)#1; and (d) compressive loading in test MD-CT(f)#1 72

Figure 3.8. Vertical displacement v profiles at h/r_p = 6 and 14 and after $|w|$=15 mm for FTL tests performed on: (a) dense; and (b) medium-dense sand samples. 73

Figure 3.9. Cumulative radial displacement u after 15 mm pile head displacement w (negative for tensile loading and positive for compressive loading) for (a) tensile loading stage of test D-TC(f)#1; (b) compressive loading stage of test D-CT(f)#2; (c) tensile loading stage of test MD-TC(f)#1; and (d) compressive loading stage of test MD-CT(f)#1. 75

Figure 3.10. Radial displacement u profiles at h/r_p = 6 and 14 and after $|w|$ =15 mm for FTLs performed in (a) dense; and (b) medium-dense sand samples. 76

Figure 3.11. Radial strain E_{rr} field after 15mm of pile head displacement w (negative for tensile loading and positive for compressive loading) for (a) tensile loading in test D-TC(f)#1; (b) compressive loading in test D-CT(f)#1; (c) tensile loading in test MD-TC(f)#1; and (d) compressive loading in test MD-CT(f). 80

Figure 3.12. Radial strain E_{rr} profile after 15 mm of pile head displacement w (negative for tensile loading and positive for compressive loading) for (a) tensile loading in test D-TC(f)#1; (b) compressive loading in test D-CT(f)#1; (c) tensile loading in test MD-TC(f)#1; and (d) compressive loading in test MD-CT(f)#1. 81

Figure 3.13. Radial strain E_{rr} versus absolute value of pile head displacement $|w|$ of soil elements at z =11.5r_p and (a) r/r_p = 1.25, (b) r/r_p = 2.5. 82

Figure 3.14. Shear strain E_{rz} after 3 mm of pile head displacement w (negative for tensile loading and positive for compressive loading) for (a) tensile loading in test D-TC(f)#1; (b) compressive loading in test D-CT(f)#1; (c) tensile loading in test MD-TC(f)#1; and (d) compressive loading in test MD-CT(f)#1 84

Figure 3.15. The $|E_{rz}|$ profiles of soil elements at h/r_p=14 after 3 mm of pile head displacement for FTL tests in (a) dense sand; and (b) medium-dense sand. 85

Figure 3.16. Shear strain E_{rz} versus absolute value $|w|$ of the pile head displacement for soil elements at z =11.5r_p and (a) r/r_p=1.25; and (b) r/r_p=2.5. 86

Figure 3.17. Volumetric strain E_{vol} versus. absolute value $|w|$ of the pile head displacement of soil elements at z = 11.5r_p and (a) r/r_p=1.25; and (b) r/r_p=2.5. 87

Figure 3.18. Inclination α of minor principal strain E_2 (most compressive strain in r,z- plan) versus normalized radial position r/r_p relative to the pile centerline of soil elements located at z/r_p = 11.5 and after $|w|$ = 3.0 mm for FTLs. 89

Figure 3.19. Shear strain E_{rz} evolution during CT and TC loading sequences of soil elements located at z =11r_p and: (a) r/r_p=1.25; (b) r/r_p=3.0. 90

Figure 3.20. Strain paths for CT and TC loading sequences of soil elements located at r/r_p=1.25 and at z =11r_p: (a) E_{rr} versus E_{rz} for test MD-CT(f)#2; (b) E_{rr} versus E_{rz} for test MD-TC(f)#2; (c) α versus E_{rz} for test MD-CT(f)#2; (d) α versus shear strain E_{rz} for test MD-TC(f)#2 91

Figure 4.1. Experimental facility for model pile testing at the Bowen Laboratory, Purdue University 102

Figure 4.2 Pile head displacement w (positive when the pile head moves downward) vs. time of a typical displacement-controlled cyclic load test (from point A to B: pre-loading of the model pile in compression with a pile head displacement $w = w_{\text{mean}}$ and from point B to C: first load cycle). 106

Figure 4.3. Unit shaft resistance mobilized in compressive load tests performed before cyclic loading in dense and medium-dense sand. 108

Figure 4.4. Influence of mean displacement w_{mean} on the post-cycling unit shaft resistance: unit shaft resistance ratio $q_{\text{s,AC}}/q_{\text{sL,BC}}$ vs. pile head displacement w for tests with cyclic loading stage performed using cyclic displacement half amplitudes Δw_{cyclic} of (a) 0.5 mm and (b) 1.0 mm... 109

Figure 4.5. Influence of frequency f on the post-cycling unit shaft resistance: unit shaft resistance ratio $q_{\text{s,AC}}/q_{\text{sL,BC}}$ vs. pile head displacement w for tests M0.5-CY0.7-F1.0-N100 (f = 1.0 Hz) and M0.5-CY0.7-F0.1-N100 (f = 0.1 Hz) 110

Figure 4.6. Influence of cyclic displacement half amplitude Δw_{cyclic} on the post-cycling unit shaft resistance: unit shaft resistance ratio $q_{\text{s,AC}}/q_{\text{sL,BC}}$ vs. pile head displacement w for tests with cyclic loading stage performed using mean displacement w_{mean} of 0.5 mm and ended at 100 displacement cycles 111

Figure 4.7. Unit shaft resistance ratio $q_{\text{s,AC}}/q_{\text{sL,BC}}$ corresponding to w = 4 mm, 6 mm, 10 mm, and 38 mm vs. cyclic displacement half amplitude Δw_{cyclic} for tests with cyclic loading stage performed using mean displacement w_{mean} of 0.5 mm. 112

Figure 4.8. Influence of number N_c of cycles on the post-cycling unit shaft resistance: unit shaft resistance ratio $q_{s,AC}/q_{sL,BC}$ vs. pile head displacement for tests with cyclic loading stage performed using cyclic displacement half amplitudes Δw_{cyclic} of (a) 0.25 mm and (b) 1.0 mm. 113

Figure 4.9. Unit shaft resistance ratio $q_{s,AC}/q_{sL,BC}$ corresponding to w = 4 mm vs. cyclic displacement half amplitude Δw_{cyclic} for tests with cyclic loading stage ended at 100 and 1,000 displacement cycles. 114

Figure 4.10. Unit shaft resistance ratio $q_{s,AC}/q_{sL,BC}$ corresponding to w = 4 mm vs. number N_c of cycles for tests with cyclic loading stage performed using cyclic displacement half amplitudes Δw_{cyclic} equal to 0.25 mm, 0.5 mm and 1.0 mm. 115

Figure 4.11. Unit shaft resistance q_s mobilized in the compressive load tests performed before and after cycling loading vs. pile head displacement w for tests in (a) medium-dense sand [test M0.5-CY1.0-F0.1-N100(*)] and (b) dense sand [test M0.5-CY1.0-F0.1-N100]. 116

Figure 4.12. Influence of relative density on the post-cycling unit shaft resistance: unit shaft resistance ratio $q_{s,AC}/q_{sL,BC}$ vs. pile head displacement w for tests in dense [test M0.5-CY1.0-F0.1-N100] and medium-dense sand samples [test M0.5-CY1.0-F0.1-N100(*)]. 117

Figure 4.13. Unit shaft resistance q_s, normalized by the surcharge σ_{v0}, mobilized in the compressive load tests performed before and after cycling loading vs. pile head displacement w for tests performed with surcharges of (a) 50 kPa [M0.5-CY0.7-F1.0-N1000] and (b) 90 kPa [M0.5-CY0.7-F0.1-N100$^{(+)}$]. 119

Figure 4.14. Influence of surcharge σ_{v0} on the post-cycling unit shaft resistance: unit shaft resistance ratio $q_{s,AC}/q_{sL,BC}$ vs. pile head displacement w for tests M0.5-CY0.7-F1.0-N1000 and M0.5-CY0.7-F1.0-N1000$^{(+)}$. 120

Figure 4.15. Unit shaft resistance q_s mobilized during cyclic loading for tests: (a) M0.5-CY0.5-F0.1-N100 (Δw_{cyclic} = 0.5 mm) and (b) M0.5-CY1.5-F0.1-N100 (Δw_{cyclic} = 1.5 mm). 121

Figure 4.16. Effect of number N_c of cycles and cyclic displacement half amplitude Δw_{cyclic} on the unit shaft resistance mobilization in cyclic loading: (a) maximum unit shaft resistance $q_{s,max}$ normalized by $q_{sL,BC}$ (in compression) vs. N_c and (b) minimum unit shaft resistance $q_{s,min}$ normalized by $q_{sL,BC}$ (in tension) vs. N_c. 123

Figure 4.17. Maximum unit shaft resistance $q_{s,max}$ normalized by $q_{s,max0}$ vs. number N_c of cycles mobilized during cyclic load tests... 125

Figure 4.18. Soil displacement vectors after cyclic loading (100 cycles) for tests: (a) M0.5-CY0.25-F0.1-N100, (b) M0.5-CY0.5-F0.1-N100, (c) M0.5-CY0.7-F0.1N100, (d) M0.5-CY1.0-F0.1-N100, and (e) M0.5-CY1.5-F0.1-N100. 127

Figure 4.19. Average cumulative displacements along the pile shaft ($6 < z/r_p < 11$) at given radial positions r from the pile centerline vs. cyclic displacement half amplitude Δw_{cyclic}: (a) average cumulative radial displacement u_{avg} (positive values of radial displacement indicate that soil elements move away from the pile shaft, and negative values indicate that they move towards it) and (b) average cumulative vertical displacement v_{avg} (positive values of vertical displacement indicate that soil elements move up, and negative values indicate that they move down)......... 128

Figure 4.20. Cumulative radial displacement u (positive when soil elements move away from the pile shaft and negative when they move towards it) vs. N_c of soil elements located initially at $r = 1.5r_p$ and $z = 9.5r_p$ during cyclic loading for tests M0.5-CY0.25-F0.1-N100, M0.5-CY0.5-F0.1-N100, M0.5-CY0.7-F0.1-N100, M0.5-CY1.0-F0.1-N100, and M0.5-CY1.5-F0.1-N100. 130

Figure 4.21. Cumulative vertical displacement v (positive when soil elements move up and negative when they move down) vs. N_c of soil elements located initially at $r = 1.5r_p$ and $z = 9.5r_p$ during cyclic loading for tests: (a) M0.5-CY0.25- F0.1- N100, (b) M0.5-CY0.5-F0.1-N100, (c) M0.5-CY0.7 -F0.1-N100, (d) M0.5-CY1.0-F0.1-N100, and (e) M0.5-CY1.5-F0.1-N100. 131

Figure 4.22. Contours of cumulative radial strain E_{rr} (positive for radial stretching and negative for radial compression) at the end of cyclic loading for tests: (a) M0.5-CY0.25-N100-F0.1, (b) M0.5-CY0.5-N100-F0.1, (c) M0.5-CY0.7-N100-F0.1, (d) M1.0-CY0.25-N100-F0.1, and (e) M0.5-CY1.5-N100-F0.1 133

Figure 4.23. Cumulative radial strain E_{rr} vs. N_c of soil elements located initially at $r = 1.5r_p$ and $z = 9.5r_p$ during cyclic loading for tests: M0.5-CY0.25-F0.1-N100, M0.5-CY0.5-F0.1-N100, M0.5-CY0.7-F0.1-N100, M0.5-CY1.0-F0.1-N100, and M0.5-CY1.5-F0.1-N100 134

Figure 4.24 Contours of cumulative shear strain E_{rz} at the end of cyclic loading for tests: (a) M0.5-CY0.25-F0.1-N100, (b) M0.5-CY0.5-F0.1-N100, (c) M0.5-CY0.7-F0.1-N100, (d) M0.5-CY1.0-F0.1-N100, and (e) M0.5-CY1.5-F0.1-N100. 136

Figure 4.25. Cumulative shear strain E_{rz} vs. N_c of soil elements located initially at $r = 1.5r_p$ and $z = 9.5r_p$ during cyclic loading for tests: M0.5-CY0.25-F0.1-N100, M0.5-CY0.5-F0.1-N100, M0.5-CY0.7-F0.1-N100, M0.5-CY1.0-F0.1-N100, and M0.5-CY1.5-F0.1-N100. 137

Figure 4.26. Effect of relative density D_R on the evolution of unit shaft resistance mobilized during cyclic loading: (a) normalized maximum unit shaft resistance $q_{s,max}/q_{sL,BC}$ vs. N_c, and (b) normalized minimum unit shaft resistance $q_{s,min}/q_{sL,BC}$ vs. N_c. 139

Figure 4.27. Strain paths of soil elements located at $r=1.5r_p$ and $z=9.5r_p$ during cyclic loading of tests: (a) M0.5-CY1.0-F0.1-N100, and (b) M0.5-CY1.0-F0.1-N100$^{(+)}$. 140

Figure 5.1. Experimental setup at the Bowen Laboratory – Purdue University, USA. 147

Figure 5.2. Effect of cyclic displacement half amplitude Δw_{cyclic} on the unit base resistance q_b: Unit base resistance q_b mobilized in the compressive load tests before and after cycling versus relative settlement w_b/B at the pile base for tests (a) CY0.25-N100, (b) CY1.0-N100, and (c) CY3.0-N100. 151

Figure 5.3. Ratio $q_{b,AC}/q_{b,BC}$ of the unit base resistance after cycling to the unit base resistance before cycling versus Δw_{cyclic} and $\Delta w_{cyclic}/D_{50}$ at different values of relative settlement w_b/B at the pile base. 153

Figure 5.4. Unit base resistance q_b and pile head displacement w (positive downward and positive upward) versus time for the cyclic loading stage of tests: (a) CY0.25-N100, (b) CY0.5-N100, (c) CY1.0-N100, and (d) CY3.0-N100. 154

Figure 5.5. Effect of cyclic displacement half amplitude Δw_{cyclic} on the cyclic unit base resistance $q_{b,max}$ mobilized during the cyclic loading stage of tests ended at 100 displacement cycles:

maximum unit base resistance $q_{b,max}$ normalized by the maximum unit base resistance $q_{b,max0}$ mobilized in the first cycle of cyclic loading versus number N_c of cycles. 155

Figure 5.6. Digital images at the end of the cycling stage of tests: (a) CY0.5-N100, (b) CY1.0-N100, (c) CY1.5-N100, and (d) CY3.0-N100. 157

Figure 5.7. Contours of normalized radial displacement $u/\Delta w_{cyclic}$ (positive when soil moves away from the model pile centerline) near the conical base after 100 cycles with cyclic displacement half amplitude Δw_{cyclic} of (a) 0.25 mm, (b) 0.5 mm, (c) 1.0 mm, (d) 1.5 mm, and (e) 3.0 mm. 160

Figure 5.8. Contours of normalized vertical displacement $v/\Delta w_{cyclic}$ (positive when soil elements move upward) near the conical base after 100 cycles with cyclic displacement half amplitude Δw_{cyclic} of (a) 0.25 mm, (b) 0.5 mm, (c) 1.0 mm, (d) 1.5 mm, and (e) 3.0 mm. 161

Figure 5.9. Contours of volumetric strain E_{vol} (positive values indicating dilation) near the conical base after 100 cycles with cyclic displacement half amplitude Δw_{cyclic} of (a) 0.25 mm, (b) 0.5 mm, (c) 1.0 mm, (d) 1.5 mm, and (c) 3.0 mm.. 163

Figure 5.10. Heat map of volumetric strain E_{vol} (positive values indicating dilation) near the conical base at the maximum downward movement of the pile (push-in) in cycles (a) 10, (c) 20, (e) 50, and (g) 100, and at the maximum upward movement of the pile (pull-out) in cycles (b) 10, (d) 20, (f) 50, and (h) 100 for test CY3.0-N100. 165

Figure 5.11. Effect of number N_c of cycles on the unit base resistance $q_{b,AC}$ mobilized in the static load test performed after cycling normalized by the limit unit base resistance $q_{bL,BC}$ measured before cycling for tests with cyclic loading stage performed with cyclic displacement half amplitudes Δw_{cyclic} of (a) 0.25 mm, (b) 0.5 mm, and (c) 1.0 mm. 167

Figure 5.12. Maximum unit base resistance $q_{b,max}$ normalized by the maximum unit base resistance $q_{b,max0}$ measured in the first cycle of cyclic loading stage versus number of cycles for tests CY3.0-N100, CY0.25-N2000, CY0.5-N1000, and CY1.0-N1000... 169

Figure 5.13. Digital images at the end of cycle number (a) 100, (b) 200, (c) 400, and (d) 1,000; (e) maximum unit base resistance $q_{b,max}$ normalized by the maximum unit base resistance $q_{b,max0}$ in the first cycle of cyclic loading (on the left vertical axis) and normalized area of crushed particles A_c/A_b (on the right vertical axis) versus number N_c of cycles for test CY1.0-N1000. 171

Figure 5.14. Trajectory of soil elements (A, B, C, D) near the conical base of the pile during the cycling stage of test CY1.0-N1000: normalized radial position versus normalized vertical position of (a) soil element A [$r/r_p = 2.5$, $h/r_p = 1.7$], (b) soil element B [$r/r_p = 2.5$, $h/r_p = 0$], (c) soil element C [$r/r_p = 0$, $h/r_p = -1.6$], and (d) soil element D [$r/r_p = 1.0$, $h/r_p = 0.8$]. The selected N_c values are indicated in the red boxes. 173

Figure 5.15. Displacements of soil elements (A, B, C and D) near the conical base during the cycling stage of test CY1.0-N1000 (f = 1.0 Hz): (a) radial displacement u (positive when soil elements move away from the centerline of the model pile and negative when they move towards it) and (b) vertical displacement v (positive when soil elements move upward and negative when they move downward).. 175

Figure 5.16. Cumulative strains of soil elements (A, B, C, and D) around the conical base during the cycling stage of test CY1.0-N1000 (f = 1.0 Hz): (a) radial strain E_{rr} (positive when soil elements

stretch radially); (b) vertical strain E_{zz} (positive when soil elements stretch vertically); (c) shear strain E_{rz}; (d) volumetric strain E_{vol}. 176

ABSTRACT

Understanding the response of piles subjected to cyclic loads is critical for piles subjected to extreme loading conditions, particularly in the offshore environment in which platforms and wind farms operate. Not only there is no specific understanding of quantitative aspects of the impact of cyclic loading on pile resistance, but also the mechanisms governing the cyclic and post-cyclic response of piles in silica sands are not well understood. The mechanisms governing pile resistance mobilization under monotonic (tensile and compressive) or cyclic axial loading were investigated by performing instrumented model piles tests in a novel half-cylindrical calibration chamber with three viewing windows that allow the capturing of digital images of the sand domain and the instrumented model pile during installation and testing.

A set of tensile-compressive and compressive-tensile load tests were performed to study the effect of loading direction on the shaft resistance of model displacement and non-displacement piles. Measurements of displacements and deformations in the sand domain were obtained through the digital image correlation (DIC) technique. The tensile-to-compressive shaft resistance ratios were found to be a function of the loading history (installation method), loading sequence, and pile surface roughness. The results show that the tensile-to-compressive shaft resistance ratios are always less than one for jacked piles and nearly one for fresh preinstalled piles. The results from DIC analyses revealed that, when the loading direction is reversed, the soil elements near the pile shaft contract, and the direction of the principal strains rotate by about 90 degrees.

A series of model pile experiments that included installation, monotonic and cyclic load tests were performed to study the effect of cyclic loading on the limit unit shaft resistance and limit and ultimate unit base resistance of displacement piles. The impact of (1) cyclic displacement half amplitude, (2) number of displacement cycles, (3) relative density, and (4) initial stress state on the pile resistance was assessed based on the pile load measurements obtained before and after cycling and on the displacement and strain fields from the DIC analysis. A minimal effect on the limit unit shaft resistance was observed after cycling in tests performed with small cyclic displacement half amplitudes (= 0.25 mm), regardless of the number of cycles (up to 2,000 cycles). For 100 cycles or more applied with cyclic displacement half amplitudes greater 0.7 mm, the limit unit shaft resistance after cyclic loading was found to be always smaller than the limit unit shaft resistance before cyclic loading. It was observed that the degradation of the limit unit shaft

resistance after cycling increases with increasing initial vertical stress and with decreasing relative density. From the DIC analysis, it was found that the decrease in the limit unit shaft resistance after cyclic loading is linked to the radial contraction and the development of cyclic and permanent shear strains in soil elements near the pile shaft during cyclic loading. Finally, the results show that the ultimate unit base resistance can drop significantly after cycling. The magnitude of the drop in the ultimate unit base resistance depends on both the magnitude of the cyclic displacement and the number of cycles. This experimental program's results provide a framework to improve the prediction of the capacity of piles subjected to cyclic loading.

1. INTRODUCTION

Over the last decade, the offshore wind sector has played an important role in the future of renewable energy systems. The global offshore wind market grew nearly 30% per year between 2010 and 2018, and it is projected to expand significantly over the next decades (IEA 2019). This accelerated growth has benefited the offshore foundation engineering industry as pile foundations are frequently used to support these offshore structures. One of the major requirements for the offshore foundation engineering practice is designing cost-efficient pile foundations that can safely handle the cyclic loads imposed by wave and wind action. Nevertheless, estimation of the axial capacity of piles subjected to cyclic loads remains a challenge in geotechnical engineering.

It is generally accepted in research and practice that the mechanical response of a pile to axial loading depends to a great extent on the pile installation method. Pile foundations can be categorized based on their installation method into three main groups: displacement piles (e.g., closed-ended driven piles or precast reinforced concrete driven piles), non-displacement piles (e.g., bored piles or drilled shafts) and partial-displacement piles (e.g., auger cast-in-place or open-ended pipe piles, in some soils). Displacement piles are prefabricated pile foundations installed by driving or jacking them into the ground. The installation process of a displacement pile causes significant changes in the void ratio and stress state of the *in situ* soil surrounding the pile (Basu et al. 2010). Non-displacement piles are constructed by backfilling with concrete a cylindrical void in the ground created by drilling. For an ideal non-displacement pile, the volume of the soil extracted matches the pile's volume and shape; therefore, the density and stress state of the *in situ* soil surrounding a non-displacement pile are minimally affected by the installation process (Fleming et al. 2008; Salgado 2008; Viggiani et al. 2014). For partial-displacement piles, the installation causes smaller changes in density or *in situ* stress state than that produced by the installation of displacement piles (Basu et al. 2010).

A pile's total axial resistance is calculated as the summation of its base (Q_b) and shaft (Q_s) resistances when it is loaded in compression and, only as its shaft resistance (Q_s), when loaded in tension. The shaft resistance is mobilized by friction between the pile shaft and the surrounding soil. The base resistance results from the compressive resistance mobilized in the soil underneath the base of the pile (Salgado 2008). During a compressive loading test, the pile shaft resistance is fully mobilized to its limit value (limit shaft resistance Q_{sL}) before the base resistance is mobilized.

After full mobilization of shaft resistance, then any additional compressive axial load that is applied at the pile head is carried by the soil at the pile base; at the limit load Q_L the pile plunges into the ground. At plunging, the base and shaft resistances have reached their limiting values (Q_{bL} and Q_{sL}). During a tensile loading test, pullout of the pile occurs once the limit shaft resistance in tension is fully mobilized.

In the offshore environment, the forces imposed by wind or wave action are frequently transferred to a pile as tensile and/or compressive axial loads. Many studies have indicated that the shaft capacity of displacement piles in sand is lower for tensile loading than for compressive loading (Beringen et al. 1979; Chow 1997; Lehane 1992; De Nicola and Randolph 1993; Randolph 2003). In contrast, for fresh non-displacement piles in sand, the shaft capacity for tensile and compressive loading is similar (Chen and Kulhawy 2002; Le Kouby et al. 2013; Kulhawy 2004). Some of the available design methods used to estimate the axial static capacity of piles in sand consider the effect of loading direction on the shaft capacity (tension versus compression shaft capacity). For example, the ICP-05 (Jardine et al. 2005), NGI-05 (Clausen et al. 2005), FUGRO-05 (Kolk et al. 2005) and UWA-05 method (Lehane et al. 2005b) incorporate factors to account for the effect of loading direction on the shaft capacity of displacement piles in sand. Despite the experimental evidence of comparable non-displacement pile response under tensile and compressive loading, the Load and Resistance Factor Design (LRFD) approach recommends applying lower resistance factors to the computed nominal shaft resistances for tensile loading than for compressive loading (Brown et al. 2010). Different hypotheses have been proposed to explain the differences in tensile and compressive shaft resistance of piles in sand (Fioravante et al. 2010a; Lehane et al. 1993; De Nicola and Randolph 1993); however, no direct observations have revealed the differences in the mechanisms of resistance mobilization in tensile and compressive loading. Other aspects, such as the effect of the loading history (De Nicola and Randolph 1999) and pile shaft surface roughness (Tehrani et al. 2016; Tovar-Valencia et al. 2018), known to affect the pile response to loading are not yet considered in the current available designed methods.

To date, there have been few field studies to investigate cyclic loading effects on the capacity of full-scale piles in sand. Among these studies are the set of axial cyclic and static tensile load tests performed on six driven piles at Dunkirk, France, by Jardine and Standing (2012, 2000) and the set of cyclic and static compressive load tests conducted on five bored piles at Loon-Plage, France, by Puech et al. (2013). Jardine and Standing (2012, 2000) showed that the tensile shaft pile capacity of driven piles in sand could either increase after low-level cyclic loading or decrease significantly after high-level cyclic loading. Puech et al. (2013) showed that the total compressive pile capacity of bored piles could also increase after cyclic loading and suggested that the increase of the total pile capacity is a consequence of a substantial increase in pile base capacity. However, limited experimental data are available on the effects of axial cyclic loading on the base resistance of piles in sand; fully instrumented test piles are required to obtain both the pile base resistance and the shaft resistance. Despite the lack of data on cyclic testing on full-scale piles in sand, various laboratory experiments have been undertaken using model piles. These include model piles experiments in pressurized calibration chambers (Foray et al. 2010; Le Kouby et al. 2004; Poulos 1989a; Rimoy et al. 2012; Tsuha et al. 2015) and centrifuges (Bekki et al. 2013, 2020; Blanc et al. 2015; Li et al. 2012). Results from model pile experiments in calibration chambers have shown that the pile shaft capacity degradation is primarily controlled by the cyclic displacement amplitude and number of cycles (Le Kouby et al. 2004; Poulos 1989a). Of note is the Imperial College mini-pile which has been used to measure the local stresses developed during cyclic loading at the pile shaft (Foray et al. 2010; Tsuha et al. 2015). The results from these studies have highlighted the complexity of the soil stress history at the pile-soil interface.

Recently, various geotechnical laboratories have been able to implement in experiments image capturing and analysis, such as the digital image correlation (DIC) technique (Arshad et al. 2014; DeJong et al. 2003; Doreau-Malioche et al. 2018; Paniagua et al. 2013; Tehrani et al. 2016; Tovar-Valencia et al. 2018; White et al. 2003), to visualize and quantify the deformation and strain fields within a soil domain. The main goal of this thesis is to show how the use of the DIC technique in combination with model pile experiments in a novel calibration chamber enables the identification and visualization of key mechanisms governing the mobilization of unit shaft and unit base resistance under monotonic or cyclic loading. The results from this work are a valuable data set against which theoretical or numerical approaches can be tested.

This article-based thesis is organized into six chapters. The first chapter gives an introduction to the dissertation topics and a description of the main objectives of this research. Chapter 2 analyzes the effect of loading direction on the shaft resistance of jacked piles in dense sand. Values of the tensile-to-compressive shaft resistance ratios of jacked piles are provided to estimate the tensile limit unit shaft resistance. A mechanism explaining the lower shaft resistance measured in tensile loading is proposed based on the DIC analysis results and the microscopic observation of the soil near the pile shaft-sand interface. Chapter 3 evaluates the effect of loading direction, loading sequence, pile base geometry, and relative density on the mobilization of shaft resistance in compressive and tensile loading of non-displacement piles in sand. The main mechanisms contributing to the pile response are discussed. Chapter 4 studies the effect of cyclic loading conditions on the shaft resistance of jacked piles in sand and discusses the main mechanisms controlling the cyclic and post-cyclic static loading response of jacked piles. An expression that allows estimation of shaft resistance degradation due to cyclic loading is proposed for jacked piles in dense sand. Chapter 5 evaluates the influence of number of displacement cycles and cyclic displacement amplitude on the ultimate and limit unit base resistance. The chapter also presents the displacements and strains in the sand domain near the conical base of the model pile. Finally, Chapter 6 summarizes the results, key observations and the major contribution from this research.

2. EFFECT OF LOADING DIRECTION ON THE SHAFT RESISTANCE OF JACKED PILES IN DENSE SAND

This chapter is reproduced from the paper by Ayda Catalina Galvis-Castro, Ruben Dario Tovar-Valencia, Rodrigo Salgado, Monica Prezzi (2019): "Effect of loading direction on the shaft resistance of jacked piles in dense sand" published in Géotechnique 69 (1).

2.1 Abstract

The design of piles subjected to tensile loading is usually done by applying a correction factor on the shaft resistance calculated for compressive loading, but experimental data on what this correction factor should be are limited. This chapter presents the results of a series of tensile-compressive (TC) and compressive-tensile (CT) static loading tests performed on instrumented model piles (with three different values of surface roughness) jacked into dense sand samples prepared in a half-cylindrical calibration chamber with digital image correlation (DIC) capability. Digital images of the model pile and sand were taken during loading of the pile in each test and processed using the DIC technique to obtain the soil displacement and strain fields. Results from local sensors showed that the ratio of the tensile-to-compressive shaft resistance of jacked piles is always less than one and depends on both the sequence of loading (CT or TC) and the pile surface roughness. The lower shaft resistance measured in tensile loading is due to the rotation of principal strains that occurs upon reversal of loading direction. Localization of shear strains occurred within a thin band of sand around the pile shaft.

2.2 Introduction

Many studies have indicated that the shaft capacity of piles in sand is lower under tensile loading than under compressive loading (Beringen et al. 1979; Chow 1997; Hussein and Sheahan 1993; Le Kouby et al. 2013; Lehane 1992; El Naggar and Wei 2000; De Nicola and Randolph 1999; O'Neill 2001; Randolph 2003; Rao and Venkatesh 1985). Table 2.1 contains values for the ratio of tensile-to-compressive shaft resistance (SRR) found in the literature. The values vary within a relatively wide range. Some current design methods for driven piles in sand have adopted empirical approaches to account for the effect of loading direction on shaft capacity (Jardine et al. 2005; Kolk et al. 2005; Lehane et al. 2005b). In general, most of the design guidelines recommend the use of a reduction of 10-30% of the shaft capacity in compression to obtain the tensile capacity of driven piles in sand.

Different mechanisms have been proposed to explain the drop in shaft resistance in tension (De Nicola & Randolph, 1993; Lehane et al., 1993; De Nicola & Randolph, 1999; Fioravante et al, 2010). These can be reduced to essentially four hypotheses:

a) differences in the radial stress field around the pile due to the Poisson effect (expansion/contraction) in the pile (De Nicola and Randolph 1993);
b) reduction of the radial stresses in the lower part of the pile due to the development of a “relaxed bulb” (Fioravante et al., 2010);
c) increase in the mean stress level in the soil around the pile when it is loaded in compression and the opposite when the pile is loaded in tension (De Nicola & Randolph, 1993; Lehane et al., 1993);
d) changes in the mean effective stress along the pile shaft due to rotation of the principal stress directions depending on the pile loading direction (De Nicola & Randolph, 1993; Lehane et al., 1993).

Loukidis & Salgado (2008) did not observe the Poisson effect in finite-element analyses of a wished-in-place pile in sand modelled using a realistic bounding-surface constitutive model (Loukidis and Salgado 2009), suggesting that the difference in stiffness between the pile material and soil was too large for a build-up in normal stress at the interface to result from any radial pile expansion due to the Poisson effect.

Fioravante et al. (2010) performed tensile and compressive loading tests on non-displacement model piles embedded in sand in a centrifuge and observed that the shaft resistance values near the base of the model piles were different depending on the loading direction, whereas, at other locations along the model piles, the shaft resistance values were approximately the same. These results led Fioravante et al. (2010) to suggest that the formation of a “relaxed bulb” of soil around the pile base during pullout is one of the reasons why the tensile-to-compressive shaft capacity ratio is less than one.

Table 2.1. Reported values of the tensile-to-compressive shaft resistance ratio SRR.

References	Method	Pile type	Installation procedure	Soil	SRR
Beringen *et al*. (1979)	Static load tests in the field	Open-ended and closed-ended piles	Driven	Over-consolidated deposit of sand	Open-ended pile: 0.63 (§) Closed-ended pile: 0.80 (§)
Lehane (1992)	Static load tests in the field	Closed-ended piles	Jacked	Fine-medium uniform sand at Lebenne	0.83 (i)
Hussein & Sheahan (1993)	Static load tests in the field	Pre-stressed square concrete piles	Driven	Deposit of clayey sand and sandy clay at Myers	0.76 (§), (‡)
(Chow 1997)	Static load tests in the field	Closed-ended and open-ended tubular piles	Jacked and driven	Dense Marine sand at Durkirk	Closed-ended jacked piles: 0.75(*), 0.82 -0.86 (§), and 0.86 (i) Open-ended driven piles: 0.76 (i)
Rao & Venkatesh (1985)	Static load tests in calibration chamber	Closed-ended piles	Jacked	Uniform coarse and uniform medium sand	Smooth piles: 0.5 - 0.9 Rough piles:0.8
Amira *et al.* (1995)	Static load tests in calibration chamber	Closed-ended piles	Preinstalled	Dry and dense Inagi sand	0.48(§)
El Naggar & Wei, (2000) and Wei *et al.* (1998)	Static load tests in calibration chamber	Tapered and straight-side wall tubular piles	Preinstalled	Loose and medium-dense sand	Tapered piles: 0.33 - 0.68 (i) Straight-side wall tubular pile: 0.59 – 0.70 (i)
O'Neill (2001) and O'Neill & Raines (1991)	Static load tests in calibration chamber	Open-ended and closed-ended tubular piles	Driven	San Jacinto River sand	0.74
De Nicola & Randolph (1999)	Static load tests in centrifuge	Open, sleeved and closed-ended piles	Driven	Medium-dense to dense silica sand	Sleeved piles: 0.6(i), 0.53-0.70(§), and 0.69(*) Open-ended piles: 0.48-0.82(i), 0.47-0.61(§), and 0.63-0.83(*) Closed-ended piles: 0.53(§)

(*) *SRR* from tensile-to-compressive loading sequence; (§) *SRR* from compressive-to-tensile loading sequence; (i) *SRR* from first-time tensile and first-time compressive loadings; (‡) compressive shaft capacity based on field dynamic tests.

Lehane et al. (1993) used results of K_0-consolidated triaxial (compression and extension) tests performed in Labenne sand, which is a sub-rounded to sub-angular sand (Belheine et al., 2009; Diaz & Rodríguez-Roa, 2010), to help explain the effect of loading direction on the shaft capacity of displacement piles. Lehane et al. (1993) found that a 90° rotation of the principal stresses (with respect to the principal stress direction after K_0 consolidation), as in triaxial extension (TXE) tests, leads to a reduction in the deviatoric stress and a contractive soil response accompanied by strain softening. In contrast, samples loaded in the same direction as the consolidation stress, as in triaxial compression (TXC) tests, exhibit a dilative response, with strain hardening. Lehane et al. (1993) suggested that the shaft capacity of displacement piles in sand is greater in compressive loading because, during pile loading, the soil is loaded in the same direction as it was loaded during pile installation. Contrastingly, in tension, the loading direction is opposite to that during pile installation, leading to a reduction in radial effective stresses.

Fabric anisotropy can be expected even if particles are well rounded and approximately equidimensional. Wong & Arthur (1985) used an extensive series of drained tests performed in a directional shear cell (Arthur et al,. 1977, 1981) to study induced anisotropy on samples of Leighton Buzzard sand, whose particles are rounded (Arthur & Menzies, 1972; Konagai et al., 1992; Altuhafi, et al, 2013; Senetakis et al, 2013;). Wong & Arthur (1985) concluded that any plastic deformation in sandy soils induces anisotropy, even in soils with rounded particles and an initially isotropic fabric. Similar observations were made by Oda & Konishi (1974) and Subhash et al. (1991).

In this chapter, the tensile and compressive resistances of jacked piles in sands are studied through calibration chamber testing. These piles may be installed monotonically or through multiple jacking strokes (Basu et al. 2011; Gavin and O'Kelly 2007; Jardine et al. 2013; White and Lehane 2004; Yang et al. 2014). The chapter reports the results of a series of experiments carried out on model piles monotonically jacked into dense sand samples. The digital image correlation (DIC) technique was used to obtain the displacement and strain fields generated during loading of model piles tested in tension and compression, which provide insights into the mobilization of shaft resistance in tensile and compressive loading and help elucidate the underlying mechanisms causing the differences in pile response to loading. The experiments and their results are discussed next.

2.3 Materials and methods

2.3.1 Experimental set-up

Model pile experiments were performed in a half-cylindrical steel chamber (diameter = 1.68 m and height = 1.25 m), a jacking system with 50 kN capacity and an imaging system. The front wall of the chamber contains a 76-mm-thick polymethyl methacrylate (PMMA) window supported by a steel frame. To prevent scratching of the PMMA, a clear, annealed glass sheet is attached to the PMMA wall on the sample side before each test. A vertical stress can be applied using an air-pressurised rubber bladder and a reaction steel lid bolted to the chamber. Arshad *et al*. (2014) provides a more detailed description of the test set-up.

The closed-ended model pile consists of a 31.75 mm-diameter half-circular rod made of brass and a 60° half-conical tip that houses a miniature compression load cell with capacity of 10 kN. The pile is assembled with a 20 kN (tension/compression) load cell at the head. The model pile has a smooth surface, but its surface roughness can be changed by attaching sandpaper to its shaft.

2.3.2 Test sand

The test sand is a silica sand (SiO_2 = 99.7%) known as Ohio Gold Frac sand, which has sub-angular to sub-rounded particles with high sphericity and is classified as a poorly graded sand. The sand properties are summarized in Table 2.2. Table 2.3 provides the values of the interface critical-state friction angle δ of the sand when sheared against brass, sand, and sandpaper, as well as for the pile shaft-glass interface obtained from interface direct shear tests.

Table 2.2. Index and mechanical properties of Ohio Gold Frac sand.

D_{50} (mm)	C_u	C_c	e_{max}	e_{min}	G_s	ϕ_{cs}^{DS} (degrees)	ϕ_{cs}^{RS} (degrees)	ϕ_{cs}^{TXC} (degrees)
0.62	1.44	0.94	0.81	0.59	2.65	32.0	31.3	32.6

Note: D_{50} = mean particle size, C_u = coefficient of uniformity, C_c = coefficient of curvature, e_{max} = maximum void ratio, e_{min} = minimum void ratio, G_s =specific gravity, ϕ_{cs}^{DS} = critical-state friction angle obtained from direct shear tests; ϕ_{cs}^{TXC} = critical-state friction angle obtained from triaxial compression (TXC) tests; ϕ_{cs}^{RS} = critical-state friction angle obtained from ring shear tests.

Based on the particle size distribution curves obtained from specimens of crushed sand particles carefully recovered from a 5 mm-thick annular zone around the shaft of the jacked model pile after a test performed under a surcharge of 70kPa (Tovar-Valencia et al. 2018), the authors calculated the values of the breakage parameter B_r, as defined by Einav (2007), to be 41.6 % near the pile base (h/r_p = 3.5) and 26.4 % at 0.29 m (corresponding to h/r_p = 18.5) above the pile base.

Table 2.3. Interface friction angles from direct shear tests.

Interface	Interface friction angle δ (degrees)
Sand-glass	9.0
Brass-glass (greased brass surface)	9.3
Brass-sand	19.7
Sandpaper grit#320 -sand	25.0
Sandpaper grit#120 -sand	28.4

Note: all interface friction angles involving sand are at critical state.

2.3.3 Normalised shaft roughness

Three different values of pile surface roughness were considered based on roughness measurements performed on three industrial steel piles (Tovar-Valencia et al. 2018) and the grit of available sandpaper. Table 2.4 summarizes the values of the surface roughness parameters R_a, R_t, R_{max} and R_n and indicates that the surface roughness values used in the model pile tests is comparable to those of industrial steel piles. A detailed discussion on scale effects related to surface roughness and model pile diameter can be found in Tovar-Valencia et al. (2018). The essential scale effects refer to the thickness of the shear band, which is a function of the particle size and pile surface roughness, and the pile diameter. Pile unit shaft resistance is a function of the ratio of pile diameter to shear band thickness (Loukidis and Salgado 2008) because a shear band of the same size produces more significant dilatancy-related changes in soil state next to the pile for smaller values of that ratio.

2.3.4 Boundary and scale effects

The configuration of the half-cylindrical calibration chamber imposes a BC3 (passive radial rigid wall) condition on the soil samples (Ghionna & Jamiolkowski, 1991; Salgado et al., 1998). The chamber-to-pile diameter ratio D_c/B is 52 and, thus, small to negligible chamber boundary effects on the test results are expected (Salgado 2013). Base boundary effects were minimized in the tests by maintaining the distance between the base of the chamber and the pile tip greater than 18*B*. The ratio of the model pile diameter *B* to the D_{50} of the test sand was 51.2, which is sufficient to avoid scale effects at the pile base (Gui & Bolton, 1998; Salgado, 2013).

Table 2.4. Roughness parameters of surfaces used before testing (modified after Tovar-Valencia et al. (2018)).

Surface	R_a [(1)] (μm)	R_t [(2)] (μm)	R_{max} [(3)] (μm)	R_n [(4)]
Most rusted pipe pile	19.63	159.2	65.99	0.106
Least rusted pipe pile	3.43	49.08	18.57	0.030
Internal pipe pile surface	19.46	172.18	66.46	0.107
Sandpaper grit # 120	24.31	173.85	81.14	0.131
Sandpaper grit # 320	7.63	55.77	39.70	0.064
Brass	0.22	2.25	1.27	0.002

(1) R_a = centreline average roughness over a travel length L = 25 mm.

(2) R_t = distance normal to the surface from the highest peak to the deepest valley measured over a traveling length L = 25 mm.

(3) $R_{max} = r_t$ /n, where n = int (L/L_m), r_t is the distance normal to the surface between the highest peak and the deepest valley within a single sampling length $L_m = D_{50}$ and measured sequentially along a traveling length L = 25 mm.

(4) $R_n = R_{max} / D_{50}$ (Uesugi and Kishida 1986a; b).

2.3.5 Image analysis

The analysis of the images obtained from the three complementary metal-oxide semiconductor (CMOS) cameras was performed using the DIC technique. The software VIC-2D (Correlated Solutions 2009) was used to process the images. A subset size of 25 by 25 pixels, which gives a resolution higher than 27 microns owing to a subpixel interpolation scheme implemented in VIC-2D (Sutton et al., 2009), was used to process the images. Further details on camera calibration, speckle pattern, precision and accuracy can be found in Arshad et al. (2014), Tehrani et al. (2016) and Tovar-Valencia et al. (2018).

2.3.6 Test procedure and test program

Sand samples with height equal to 1050 mm were prepared in the calibration chamber using the air pluviation technique (Arshad et al. 2014). The sand samples had an average relative density, DR, of 89%. After preparation of each sample, the jacking system was set in place and a surcharge of 70 kPa was applied at the top of the sample. The model pile was positioned in nearly perfect alignment with the flat chamber wall so as to prevent sand intrusion between the pile and the glass during installation. For all tests, the samples were aged for 1 day. The model pile was then monotonically jacked into the sand sample at a constant rate of 0.8 mm/sec until the desired pile base depth was reached. The pile head load was then reduced to zero, simulating the end of pile installation. A sequence of tension-compression (TC) or compression-tension (CT) static load tests immediately followed. The quasi-static tests were displacement-controlled with a rate of 0.12 mm/s. The minimum displacement achieved during static loading of the model pile was approximately 1.0B (30 mm). The model pile base load Q_b and the head load Q_t were recorded throughout the tests at a frequency of 2 readings per second. Each of the three digital CMOS cameras were set to take images at a rate of two frames per second (fps) from one observation window.

Six model pile tests were performed in the half-cylindrical calibration chamber in dense sand samples. The test designation is given in Table 2.5.

Table 2.5. Test program.

Test [(1)]	Relative density D_R (%)	Shaft surface	Installation depth (mm)
D-R-TC	90	SP grit #120	400
D-R-CT	89	SP grit #120	370
D-MR-TC	88	SP grit #320	400
D-MR-CT	90	SP grit #320	370
D-S-TC	90	Brass	400
D-S-CT	88	Brass	370

Note: D = dense sand sample, R = rough shaft, MR = medium rough shaft, S = smooth shaft, TC = tensile followed by compressive loading, and CT = compressive followed by tensile loading, SP, sandpaper.
[(1)] All tests performed on monotonically installed jacked model piles with 70 kPa surcharge on the calibration chamber sand samples.

2.4 Results and discussion

2.4.1 Sensor-based results

Figure 2.1 shows the unit base resistance q_b and unit shaft resistance $q_{s,avg}$ developed during installation of rough, medium-rough and smooth model piles (Test D-R-TC, D-MR-TC and D-S-TC). The flat side of the half-circular model pile was always in contact with the glass, so measured shaft resistance is slightly greater than the actual shaft resistance that would develop by pile-sand friction only. The values reported are corrected for this.

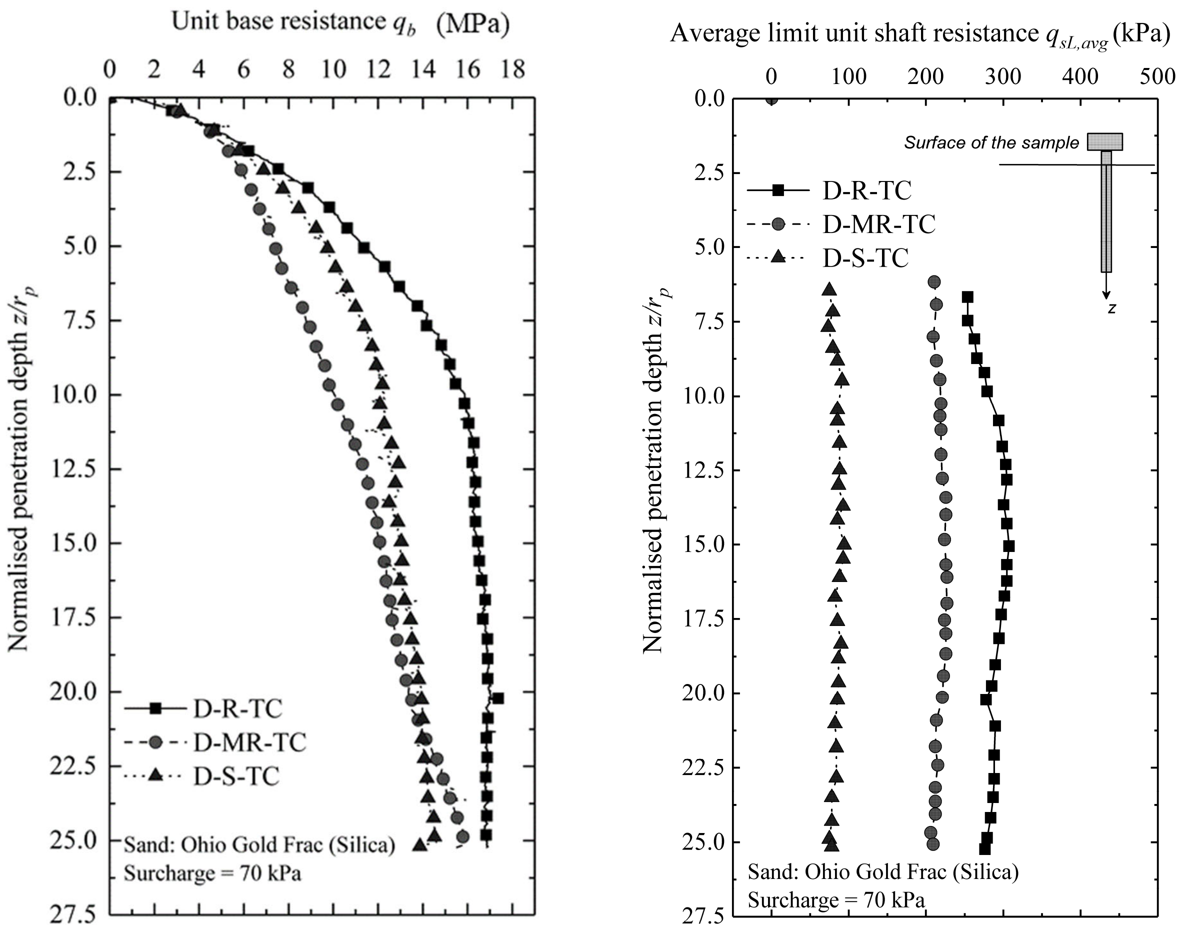

(a) (b)

Figure 2.1. Resistances measured during installation of the model piles in dense sand for tests D-R-TC, D-MR-TC and D-S-TC: (a) unit base resistance, q_b; (b) average limit unit shaft resistance, $q_{sL,avg}$.

Figure 2.1 shows that, at $z/r_p = 25$, the unit shaft resistance is fully mobilized and increases significantly with increasing surface roughness (i.e., $q_{sL,avg}$ for the rough pile is 220% greater than for the smooth pile). The unit base resistance q_b varies between 14.5 and 16 MPa at the end of pile installation (at $z/r_p = 25$). Particle crushing below the pile base can be easily detected from the images (crushed particles are lightly coloured); particle crushing occurs when q_b exceeds approximately 5 MPa.

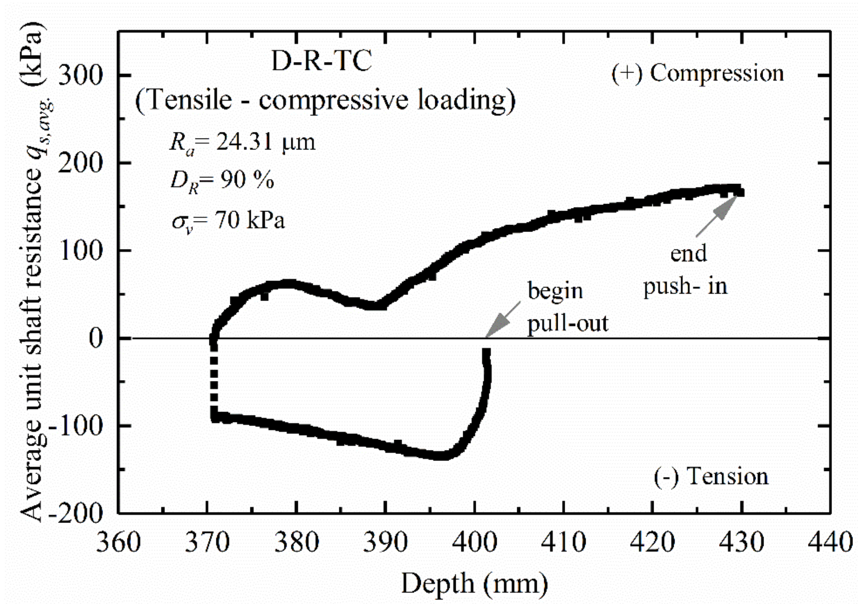

(a)

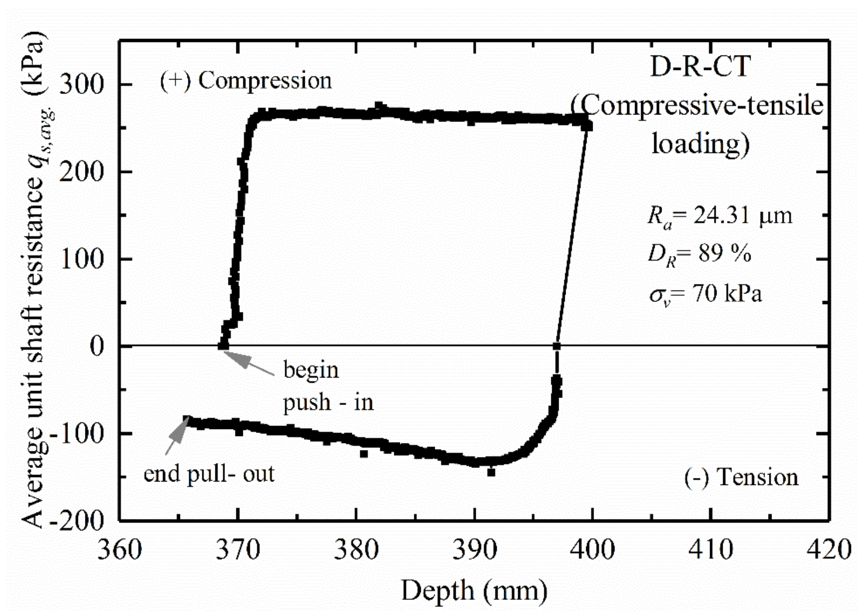

(b)

Figure 2.2. Average unit shaft resistance $q_{s,avg}$ plotted against depth for tension–compression and compression–tension loading tests performed in dense sand using a model pile with a rough shaft (R_n= 0·131): (a) test D-R-TC; (b) test D-R-CT.

Figure 2.2(a) shows the average unit shaft resistance $q_{s,avg}$ plotted against depth recorded during the loading sequence of test D-R-TC. The model pile was first pulled out from an initial base depth of ≈ 400 mm to a base depth of ≈ 370 mm (corresponding to a pile head displacement

$w \approx -30$ mm $\approx -1B$). During this tensile loading stage, the absolute maximum value of $q_{s,avg}$ was 136.0 kPa at $w \approx -3.7$ mm. The model pile was then pushed down from ≈ 370 mm to ≈ 430 mm (corresponding to $w \approx 60$ mm $\approx 2B$). During this compressive loading stage, $q_{s,avg}$ started to increase significantly only after the base crossed a depth of 390mm (at which $w \approx 0.7B$). This can be attributed to the collapse of the cavity formed below the base of the pile during the previous tensile loading stage, which created a very loose sand zone near the base, as also pointed out by Fioravante *et al*. (2010). After a depth of ≈ 390 mm, $q_{s,avg}$ increases continuously reaching a maximum value of 170 kPa after 60 mm of pile head displacement (at a depth of 430 mm). Similar trends were observed in tests D-MR-TC and D-S-TC tests.

Figure 2.2(b) shows the average unit shaft resistance $q_{s,avg}$ plotted against depth recorded during the loading sequence of test D-R-CT. In this test, the model pile is first pushed down to a depth of 400 mm (corresponding to $w \approx 30$ mm $\approx 1B$). Then, it is pulled out for $w \approx -30$ mm $\approx -1B$ to a pile base depth equal to 370 mm. The absolute maximum value of $q_{s,avg}$ during compressive and tensile loading was 250 kPa at $w \approx 3.1$ mm and 131.5 kPa at $w \approx -5.1$ mm, respectively. Lower magnitudes of $q_{s,avg}$ in tensile, rather than compressive, loading were also observed in tests D-MR-TC and D-S-TC.

By comparing the tensile loading of test D-R-TC (Figure 2.2 (a)) and test D-R-CT (Figure 2.2(b)), it can be seen that the loading direction sequence (TC or CT) has little influence on the absolute maximum value of $q_{s,avg}$ (131.5 kPa for D-R-CT and 136.0 kPa for D-R-TC) measured in tension; this is because the compressive loading has an effect on the unit shaft resistance in the subsequent tensile loading that is similar to that of installation. In contrast, the maximum value of $q_{s,avg}$ in compression is significantly affected by the loading direction sequence. The maximum value of $q_{s,avg}$ during compressive loading for test D-R-TC ($q_{s,avg} = 170$ kPa at $w \approx 60$ mm) was 32% less than that in test D-R-CT ($q_{s,avg} = 250$ kPa at $w \approx 3.1$ mm). It should be noted, after tensile loading, the maximum $q_{s,avg}$ in compression does not reach the value measured in the test in which the pile is first tested in compression, even after a pile head displacement w of $2B$. These results suggest that the tensile loading induces substantial changes in the stress states of the sand elements next to model pile. This may be related, in part, to what happens below the base of the pile; however, because the compressive loading was extended until the pile base was a full diameter beyond its position before the tensile loading was applied, this alone would not explain the difference. Peaks in shaft resistance were not observed in the load-settlement curves during compressive loading, which suggests that most of the dilatancy was already mobilised during the installation process. For both compressive and tensile loading, $q_{sL,avg}$ is defined as the maximum absolute value of $q_{s,avg}$.

The average unit shaft resistance $q_{s,avg}$ for the first-time loading (FTL) performed subsequently to pile installation is plotted against the pile head displacement w in Figure 2.3 for all the tests. Positive values of pile head displacement indicate compressive loading, while negative values indicate tensile loading. Figure 2.3 shows that, in the FTL, the magnitude of $q_{sL,avg}$ is greater when the pile is first loaded in compression than when it is loaded first in tension. It is also observed that there is an increase in $q_{sL,avg}$ when the surface roughness increases.

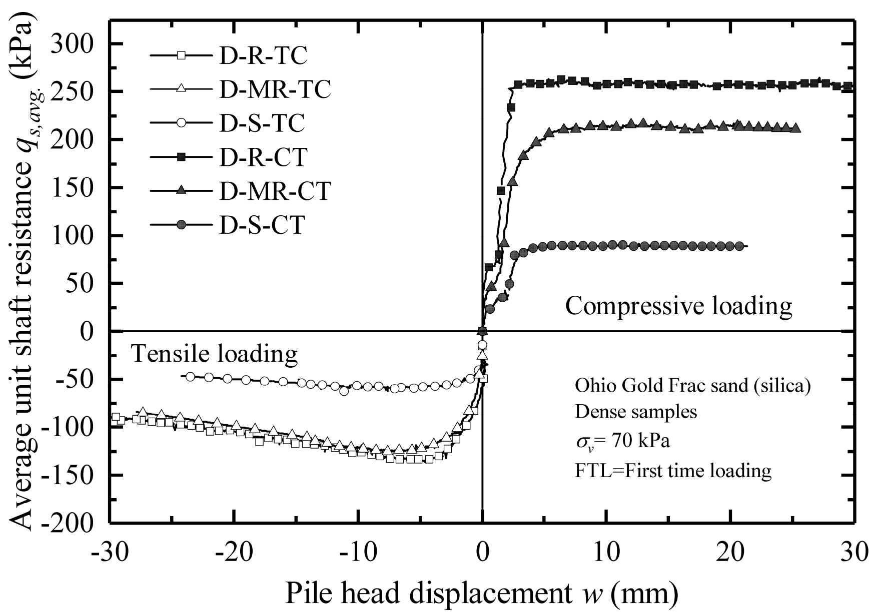

Figure 2.3. Average unit shaft resistance $q_{s,avg}$ plotted against pile head displacement w for FTL of rough (R_n= 0·131), medium-rough (R_n= 0·064) and smooth (R_n= 0·002) model piles.

Two different tension-to-compression shaft resistance ratios were calculated: (*a*) the ratio SRR for $q_{sL,avg}$ measured in tension and compression for the same sample (same test) and (*b*) the ratio SRR_{FTL} for $q_{sL,avg}$ measured from the FTLs. The results provided in Table 2.6 – in terms of $q_{sL,avg}$ measured during each loading stage, SRR and SRR_{FTL} – show that: (*a*) SRR and SRR_{FTL} are less than one; (*b*) SRR is always greater when the model pile is first loaded in tension (owing to the lower shaft capacity that results in the subsequent compressive loading); and (*c*) SRR_{FTL} tends to decrease as the pile surface roughness increases.

Table 2.6. Ratios SRR and SRR_{FTL} from tests performed on jacked model piles.

Test	$q_{sL,\,avg}$ (kPa).		SRR[(1)]	SRR_{FTL}[(2)]
	Tensile loading stage	Compressive loading stage		
D-S-CT	−58.0	89.0	0.65	0.67
D-S-TC	−60.0	68.0	0.88	
D-MR-CT	−117.0	210.0	0.56	0.59
D-MR-TC	−123.0	147.0	0.84	
D-R-CT	−131.5	250.0	0.53	0.54
D-R-TC	−136.0	170.0	0.80	

(1) SRR is the ratio of the $|q_{sL,\,avg}|$ in tension divided by $q_{sL,\,avg}$ in compression for the same test.
(2) SRR_{FTL} is the ratio of $|q_{sL,\,avg}|$ in tension divided by $q_{sL,\,avg}$ in compression, both measured from FTL, for the same shaft surface roughness and relative density.

2.4.2 Image-based results

The DIC results reported here follow the same coordinate reference system used by Arshad *et al*. (2014). The horizontal distance from the centreline of the model pile to any soil element is denoted by r. The vertical distance from the sample surface to a soil element at any given depth is z. The penetration depth h^* is measured from the surface of the sample to the pile base. The vertical distance of a soil element with respect to the pile base is represented by h (h = 0 at the pile base, positive above it, and negative below it). These variables can be normalised with respect to the model pile radius, r_p.

Figure 2.4 through Figure 2.13 correspond to tensile and compressive loading from FTLs performed on a jacked model pile with rough shaft for a magnitude $|w|$ of pile head displacement equal to 15 mm, unless otherwise mentioned. A value of $|w|$ = 15 mm was sufficient for full shaft resistance mobilization.

2.4.2.1 Crushed particle zone and shear band

The average thickness t_{cb} of the crushed particle band, before and after pile loading, was estimated for all the tests by measuring the radial distances from the pile shaft to the boundary where the changes in colour of the sand particles were visually noticeable. The values of t_{cb} before pile loading (i.e., after pile installation) are summarized in Table 2.7, indicating that t_{cb} values do not depend significantly on the pile surface roughness ($t_{cb,avg}$ = 2.3 mm ± 0.2 mm). The crushed particle band was measured again after the last static load tests; no change in particle band thickness was observed after the loading tests. This demonstrates that most, if not all, of the particle crushing occurred at the base of the pile during jacking. The particle size distribution curves obtained from specimens of crushed sand particles recovered along the pile shaft indicate that the roughness of the shaft has a negligible effect on the final gradation of the crushed sand. Both Yang et al. (2010) and Tovar-Valencia et al. (2018) concluded that crushing occurs below the base of the pile and that, for silica sand, crushing depends on the sand relative density and the vertical stress magnitude.

Table 2.7. Thickness of the crushed zone developed during pile installation and thickness of the shear band developed after 15 mm of pile head displacement for the first-time loading stages of monotonically jacked model piles.

Test	R_n	t_{cb} (mm)	t_s (mm)	t_s / D_{50}
D-R-TC	0.131	2.4	2.00	3.23
D-MR-TC	0.064	2.4	1.70	2.74
D-S-TC	0.002	2.2	-	-
D-R-CT	0.131	2.4	1.80	2.9
D-MR- CT	0.064	2.3	1.30	2.1
D-S- CT	0.002	2.2	-	-

Note: D_{50} (= 0.62 mm) is the mean particle size of the sand before installation and testing (before any crushing), R_n is the normalized roughness, t_{cb} is the thickness of the crushed particles band, t_s is the thickness of the shear band.

Videos recorded with a microscope during the static load tests show the formation of a shear band along the pile shaft of rough and medium-rough model piles, but not for smooth model piles. Visual tracking of particles was used to estimate the t_s values (Tovar-Valencia et al. 2018). The values of t_s for all the first static load tests are reported in Table 2.7. It is observed that for piles with medium-rough or rough surfaces, the shear band develops within the zone of crushed particles ($t_s < 2.0$ mm $\approx 3.2D_{50}$). During compressive loading, shearing happens in a more localised zone next to the pile shaft, as the estimated t_s values are smaller in compressive than in tensile loading. Additionally, the values of t_s increase with increasing surface roughness.

2.4.2.2 Displacement vectors during loading

Figure 2.4 shows the magnitude and direction of the displacement vectors in the tensile loading stage of test D-R-TC and the compressive loading stage of test D-R-CT. Maximum displacements measured with DIC are concentrated in a narrow band next to the crushed particle zone. The magnitude of the displacement decreases (at a higher rate in compression than in tension) with increasing normalised radial position, r/r_p. This observation also indicates that the shearing is more localised and affects a smaller volume of soil outside the shear band for compressive than for tensile loading. For both tensile and compressive loading, the piles with a smooth shaft mobilise displacements to smaller distances from the pile surface than the piles with a rough shaft.

The pattern of the displacement vectors around the pile tip in compressive loading shown in Figure 2.4(b) is consistent with that proposed by Salgado & Prezzi (2007) and observed by Arshad et al. (2014). Vectors immediately below the model pile tip are sub-vertical, pointing down, while the radial component of the displacement dominates further away from the tip and to the side. Between these two zones, there is a transition region where the displacement vectors rotate from a vertical to a radial direction. The same is observed for tensile loading in Figure 2.4(a), but with the vector directions approximately reversed. The directions of the displacement vectors suggest that, near the pile base, the stress level decreases during tensile loading because of cavity collapse, whereas it increases in compressive loading due to cavity expansion. The change in stress level below the pile base is considered to have little influence in reducing the shaft resistance in tension; however, this reduction in stress level at the base affects the development of the shaft resistance of the subsequent compressive loading, as shown in Figure 2.2(a).

The authors calculated the average orientation of the displacement vectors within a zone limited by $1.15 < r/r_p < 2$ (18.25 mm $< r <$ 31.75 mm) and $8.5 < z/r_p < 20.5$ (103.19 mm $< z <$ 325.43 mm) using their magnitude as a weighing factor (Arshad et al., 2014). Figure 2.5 shows the displacement vectors of the zone defined above for tensile and compressive FTLs for the rough pile. Results indicate that, next to the model pile: (*a*) the average orientation of the displacement vectors in tensile loading (105°, measured counter-clockwise from the r/r_p axis on the right side and clockwise on the left side of the pile) is nearly opposite to that in compressive loading (= −82º); (*b*) soil elements move further during tensile than compressive loading; and (*c*) the main displacement component is the vertical displacement for both loading directions.

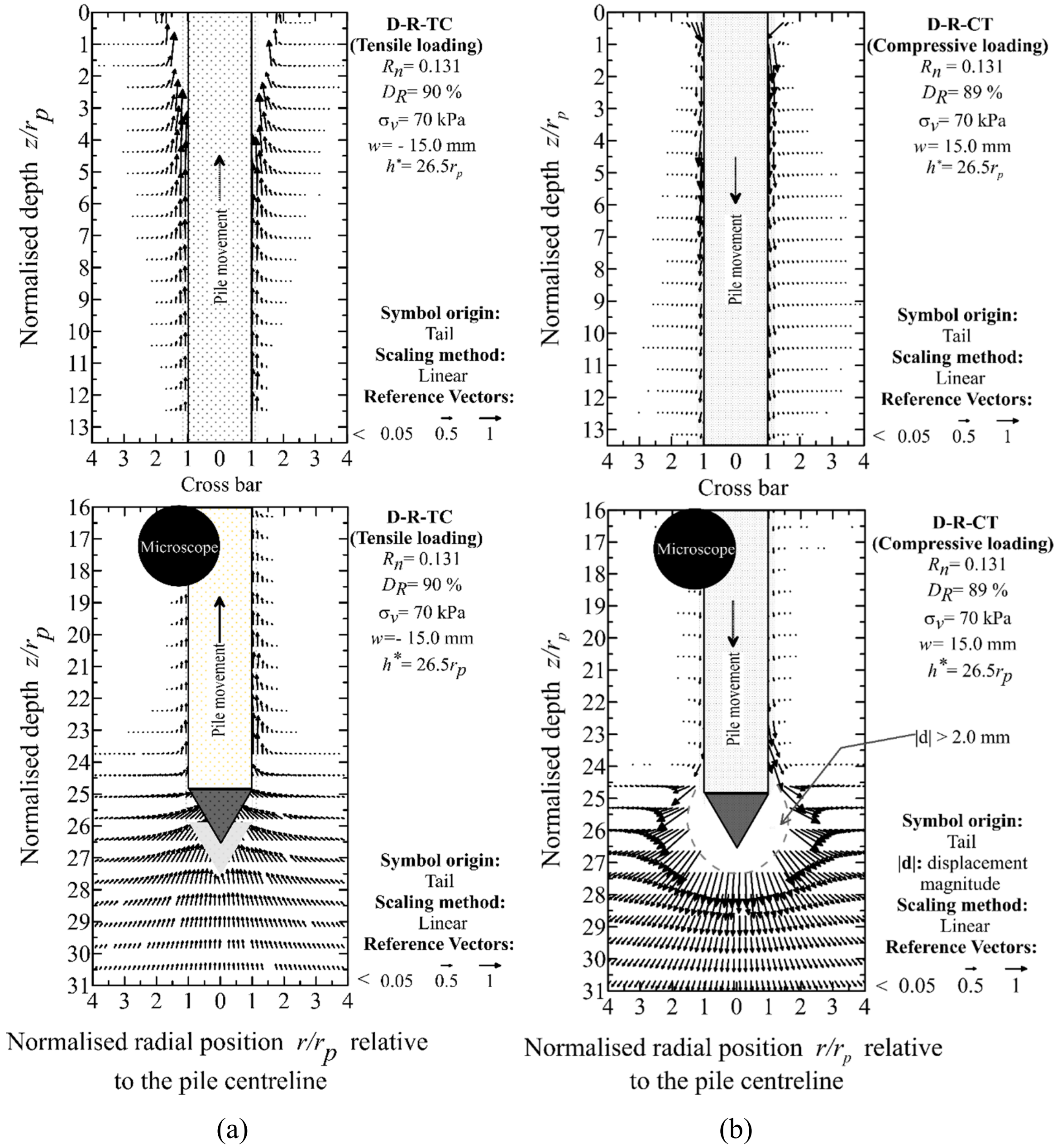

Figure 2.4. Soil displacement vectors for an absolute value of pile head displacement $|w|$ of 15 mm (pile tip at $h^* = 26{\cdot}5r_p$): (a) tensile loading stage of test D-R-TC; (b) compressive loading stage of test D-R-CT.

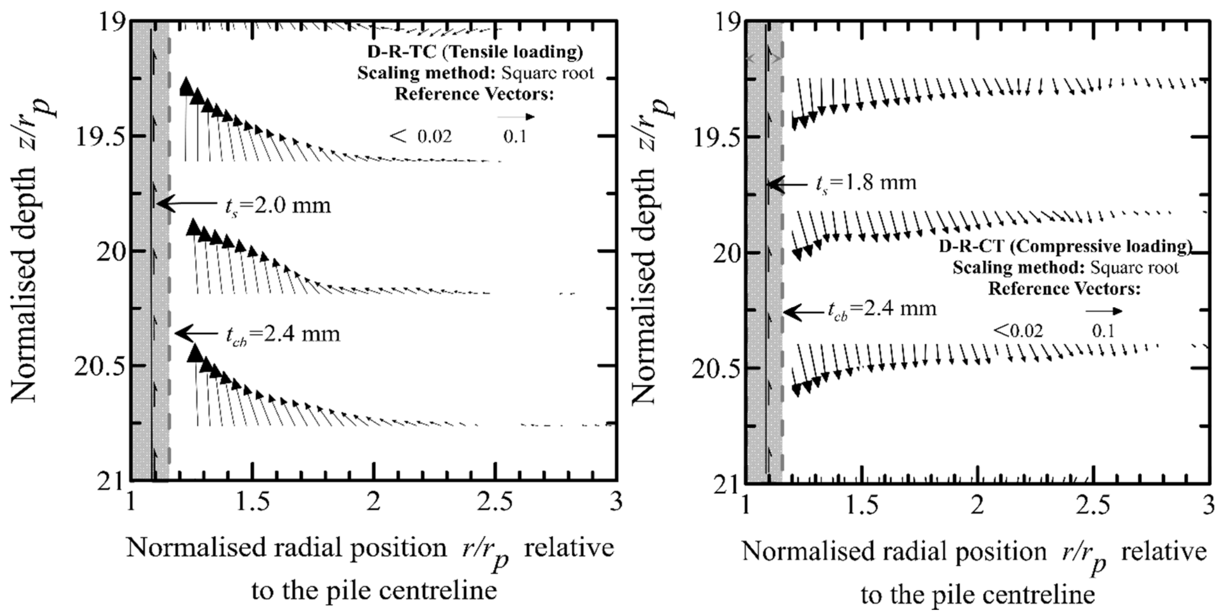

(a) (b)

Figure 2.5. Average direction of displacement vectors along the shaft when the model pile tip is at $h^* = 26{\cdot}5r_p$ and $|w|$= 15 mm: (a) tensile loading stage of test D-R-TC; (b) compressive loading stage of test D-R-CT.

2.4.2.3 Vertical and radial displacements along the shaft during loading

Figure 2.6 shows the cumulative vertical displacement *v* (positive when soil elements move upward and negative when they move downward) and cumulative radial displacement *u* (positive when soil elements move away from the pile shaft and negative when they move towards it) plotted against the radial position r - r_p relative to the pile shaft for soil elements located at z/r_p = 11 for the FTL of tests D-R-TC and D-R-CT. For a given r - r_p position, the vertical displacement magnitude $|v|$ is greater for tensile than for compressive loading. For compressive loading, the profiles of *v* along the pile shaft were very comparable, suggesting that the shear band forms along the entire shaft with approximately the same thickness. However, for tensile loading, the top boundary influenced the *v* profiles down to $z = 6.5r_p$. During loading, the magnitude of *v* of sand next to the pile shaft decreases as the roughness of the shaft decreases. Soil elements near the pile shaft tend to move radially towards the pile shaft in tensile loading and radially away from the pile shaft in compressive loading. However, the magnitudes are significantly smaller than those observed during installation of jacked piles and during loading of non-displacement piles (Tehrani et al. 2016). The maximum cumulative radial displacement *u* at z/r_p = 9.5 is equal to 0.05 mm for both tensile and compressive loading (but with opposite directions) and occurs close to the shaft, at r - r_p = 7.8 mm for tensile loading and at r - r_p = 3.0 mm for compressive loading. This observation suggests that the mode of installation has a major influence on the magnitudes of u of the soil elements close to the pile shaft and that, in the case of jacked piles, the bulk of the radial displacements happen during pile installation.

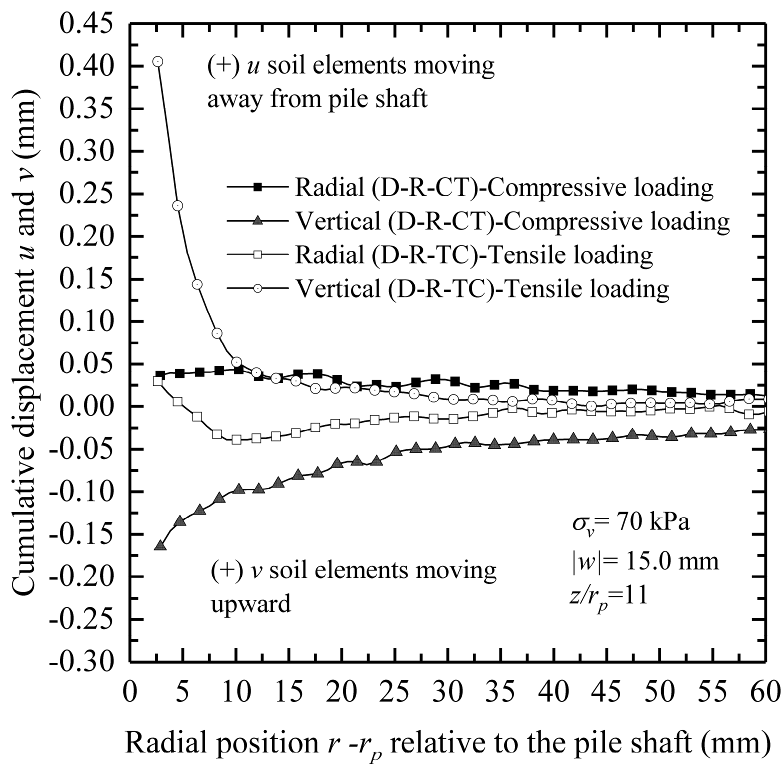

Figure 2.6. Vertical and radial displacement profiles at z/r_p = 11 and $|w|$= 15 mm for the tensile loading stage of test D-R-TC and the compressive loading stage of test D-R-CT.

2.4.2.4 Cumulative and incremental radial and shear strains during loading

The Green-St. Venant strain tensor is obtained using the continuum mechanics formulation implemented in the post-processing tool of VIC-2D software (Sutton et al., 2009). The solid mechanics sign convention is followed, so that positive radial strains E_{rr} represent stretching of the soil element radial dimension, whereas negative radial strains E_{rr} indicate the opposite, compression.

Figure 2.7 shows the cumulative radial strain E_{rr} and shear strain E_{rz} of soil elements located at a depth $z/r_p = 11$ plotted against the radial position $r - r_p$ relative to the pile shaft for the FTL of tests D-R-TC and D-R-CT. In both cases of loading, the radial strains E_{rr} of the leftmost soil elements captured by the DIC analysis, which are immediately next to the crushed band (at $r - r_p = 2.4$ mm), are negative, indicating radial contraction. In tensile loading, elements located in the 12.9 mm < $r - r_p$ < 45.0 mm interval stretch (radial strains E_{rr} take positive values). The values of E_{rr} become negligible ($|E_{rr}| < 0.05\%$) for $r - r_p > 45.0$ mm in tensile loading and $r - r_p > 25.0$ mm in compressive loading. The magnitude of E_{rz} at a given $r - r_p$ position is greater in tensile than in compressive loading and increases as the roughness of the shaft increases.

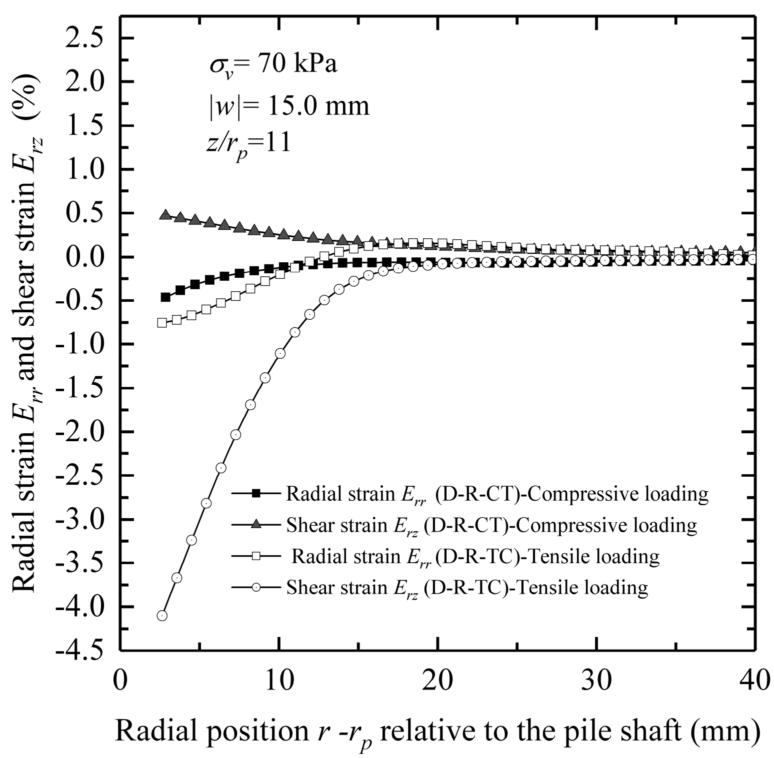

Figure 2.7. Radial and shear strain profiles at $z/r_p = 11$ and $|w| = 15$ mm for the tensile loading stage of test D-R-TC and the compressive loading stage of test D-R-CT.

Figure 2.8 shows the shear strain increment ΔE_{rz} of elements located at a radial distance $r - r_p = 4.5$, 9.2 and 16.6 mm calculated as the difference between consecutive cumulative shear strains E_{rz} corresponding to pile head displacements differing by 1.6 mm ($\approx 0.1 r_p$) plotted against the current pile head displacement for tensile (test D-R-TC) and compressive (test D-R-CT) loading. The results indicate that the shear strain increment ΔE_{rz} decreases with increasing $|w|$. For soil elements located at $r - r_p < 9.2$ mm, the magnitude of ΔE_{rz} is always greater for tensile than for compressive loading.

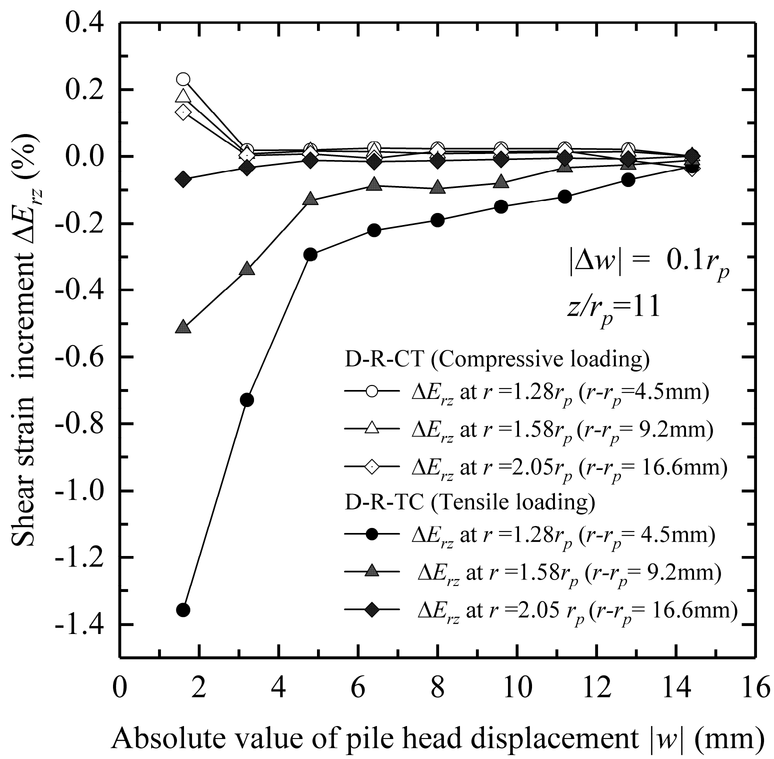

Figure 2.8. Shear strain increment ΔE_{rz} plotted against the absolute value of pile head displacement $|w|$ of soil elements located at $z/r_p = 11$ and radial distances of $r - r_p = 4{\cdot}5$, $9{\cdot}6$ and $16{\cdot}6$ mm for tensile (test D-R-TC) and compressive (test D-R-CT) loading of rough model pile (ΔE_{rz} is calculated at every $|\Delta w| = 1{\cdot}6$ mm $\approx 0{\cdot}1 r_p$).

Figure 2.9 shows the radial strain increment ΔE_{rr} of elements located at a radial distance $r - r_p = 4.5$ and 16.6 mm, calculated as the difference between consecutive cumulative radial strains E_{rr} corresponding to pile head displacements differing by 1.6 mm ($\approx 0.1 r_p$) plotted against the current pile head displacement for tensile (test D-R-TC) and compressive (test D-R-CT) loading. For tensile loading, the soil element near the pile shaft ($r - r_p = 4.5$ mm) contracts radially ($\Delta E_{rr} < 0$) during most of the loading process, but at a rate that decreases with increasing magnitude $|w|$ of the pile head displacement. The radial contraction observed near the pile shaft during tensile loading is consistent with the observed decrease in the normal radial stress and unit shaft resistance upon tensile loading. In contrast, for compressive loading, the soil element near the pile shaft (at $r - r_p = 4.5$) experiences first radial extension for $|w| < 3.2$ mm, then, for higher values of $|w|$, the soil contracts slightly. At a radial distance $r - r_p = 16.6$ mm, the soil elements experience small radial deformation for $|w| < 3.2$, then stop deforming.

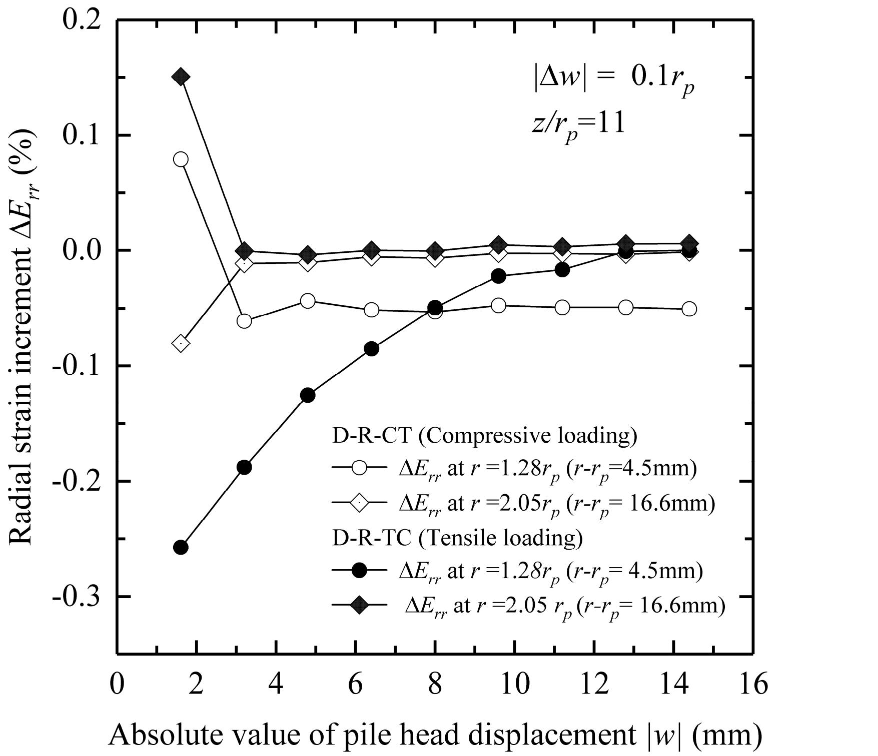

Figure 2.9. Radial strain increment ΔE_{rr} plotted against the absolute value of pile head displacement $|w|$ of soil elements located at z/r_p= 11 and radial distances of $r - r_p = 4{\cdot}5$ and $16{\cdot}6$ mm for tensile (test D-R-TC) and compressive (test D-R-CT) loading of rough model pile (ΔE_{rr} is calculated every $|\Delta w| = 1{\cdot}6$ mm $\approx 0{\cdot}1 r_p$).

2.4.2.5 Volumetric strains during loading

The Lagrangian volumetric strain E_{vol} can be calculated from the deformation gradient **F** using E_{vol} = det**F** - 1, where **F** is the deformation

$$\mathbf{F} = \mathbf{I} + \nabla\mathbf{u} = \begin{bmatrix} 1+\dfrac{\partial u}{\partial r} & 0 & \dfrac{\partial u}{\partial z} \\ 0 & 1+\dfrac{u}{r} & 0 \\ \dfrac{\partial v}{\partial r} & 0 & 1+\dfrac{\partial v}{\partial z} \end{bmatrix} \tag{2.1}$$

where **I** is the identity matrix, $\nabla\boldsymbol{u}$ is the displacement gradient tensor, u and v are the radial and vertical displacement at the centre of a soil element; r is the radial distance from the centre of the soil element to the centreline of the model pile; and z is the vertical distance from the sample surface to a soil element. Figure 2.10 shows the cumulative Lagrangian volumetric strain E_{vol} (positive when soil element dilates and negative when soil element contracts) at different radial distances r - r_{p} from the pile shaft in tensile (test D-R-TC) and compressive (test D-R-CT) loading.

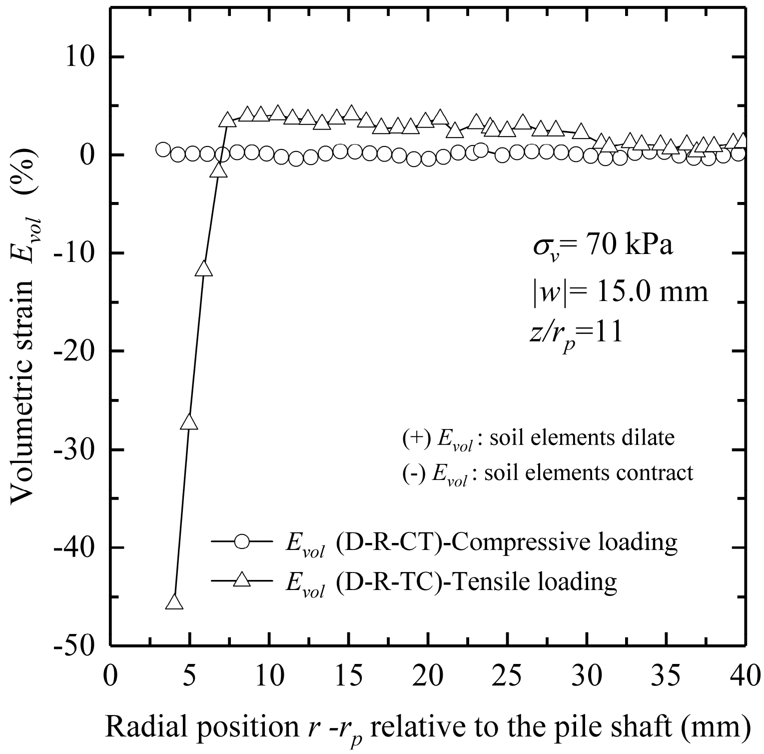

Figure 2.10. Volumetric strain E_{vol} profiles at z/r_p = 11 and magnitude $|w|$ of pile head displacement equal to 15 mm for the tensile loading stage of test D-R-TC and the compressive loading stage of test D-R-CT.

In tensile loading, the soil elements contract near the pile shaft ($E_{vol} \approx -45\%$) but dilate slightly ($E_{vol} \approx 4\%$) between 6.8 mm < r - r_p < 40.0 mm. This process is consistent with a reduction in lateral stress against the pile and with a unit shaft resistance lower than that observed for compressive loading, for which the soil elements outside the crushed particle band exhibit negligible volumetric strains. DIC information is not available inside the shear band (r - r_p < 3.0 mm).

2.4.2.6 Principal strains during loading

Figure 2.11 shows the direction of the minor principal component E_2 (i.e., the largest compressive principal strain) of the Green-St. Venant strain tensor in the r-z plane for FTLs of the rough model pile. During compressive loading (Figure 2.11(b)), the load is transferred obliquely with an inclination of − 45° immediately outside the crushed band and tends to bend towards the vertical direction further away from the pile shaft (nearly −60° at $z/r_p = 3$). This mechanism is consistent with the arching effect on soils in compressive pile loading (i.e., oblique conical transfer of stress) as observed by Loukidis & Salgado (2008) and Touma & Reese (1974). Contrastingly, in tensile loading (Figure 2.11(a)), the direction of E_2 is approximately reversed (with inclination approximately equal to +45° close to the pile, increasing to nearly +60° further away from it).

Figure 2.12 shows how the principal strain magnitudes change with increasing $r - r_p$ for soil elements located at a normalized depth $z/r_p = 11$ along $r - r_p$ in the FTL of tests D-R-TC and D-R-CT. The orientation of E_2 of the soil elements at $r - r_p = 2.7$, 6.5, 15.8 and 28.8 mm are also shown in Figure 2.12. For both loading cases, principal strains E_1 and E_2 greater than 0.1% are limited to a band of about 15 mm thick (measured from the pile shaft). The magnitudes of the principal strains are greater in tensile than in compressive loading. For a given $r - r_p$ location, the absolute magnitudes of E_1 and E_2 in tensile loading are approximately the same. The approximate equality of principal strain magnitudes characterises a process of shearing in the vertical direction, along the pile shaft.

The average orientation of E_2 within the zone limited by $1.15 < r/r_p < 2$ (18.25 mm $< r <$ 31.75 mm) and $8.5 < z/r_p < 20.5$ (103.19 mm $< z <$ 325.43 mm) was calculated, using its magnitude as a weighing factor. The results indicate that the average direction of E_2 for compressive loading is equal to −39.2° and, for tensile loading, it is equal to + 41.8°, approximately perpendicular to each other.

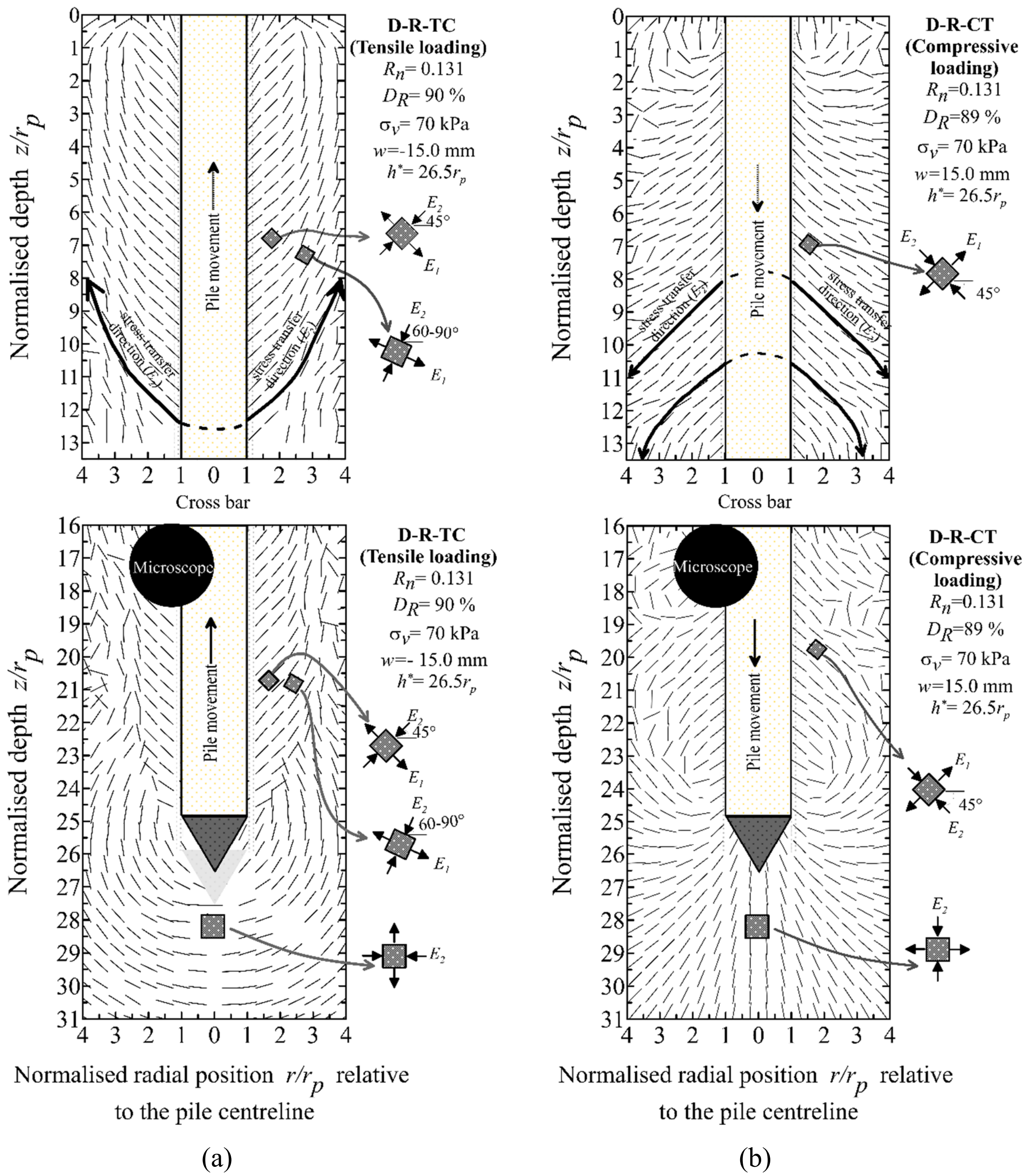

Figure 2.11. Direction of the minor principal strain E_2 (largest compressive strain) developed at $|w|$ = 15 mm (h^* = 26·5rp) for the: (a) tensile loading stage of test D-R-TC; (b) compressive loading stage of test D-R-CT.

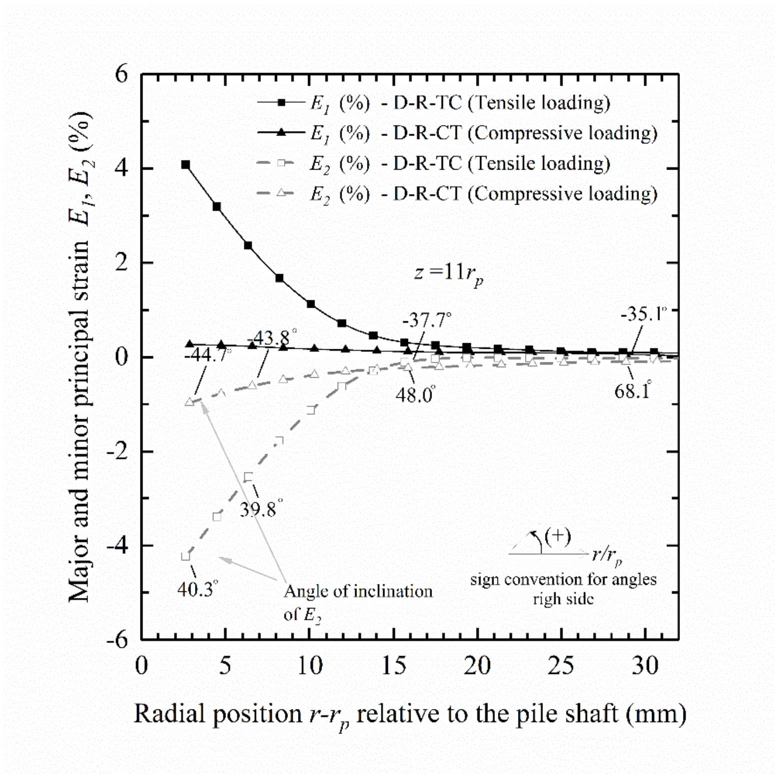

Figure 2.12. Magnitude of E_1 and E_2 of soil elements located at $z/r_p = 11$ plotted against radial position $r - r_p$ relative to the pile shaft at $|w|= 15$ mm for the tensile loading of test D-R-TC and the compressive loading of test D-R-CT (the direction of E_2 is indicated for some data points).

2.4.2.7 Effect of installation on principal strain direction

Figure 2.13 shows the direction and magnitude of the principal strains at the end of model pile installation of test D-R-CT. The average inclination of the maximum compressive strain E_2 is −40.0° measured from the horizontal axis. Keeping in mind that sample deposition and subsequent one-dimensional consolidation yields a vertical (−90°) compressive strain, there is a principal strain rotation of 50° caused by pile installation.

2.4.2.8 Fabric and its effect on the mechanical response of sand

Oda (1972b) and Subhash *et al*. (1991) observed that, in shearing of photo-elastic granular materials, the contact normals align with the maximum principal compressive stress direction. In more recent studies, Fonseca (2011) and Fonseca et al. (2012) investigated, using microcomputed tomography, the three-dimensional fabric evolution of Reigate sand after shearing in triaxial tests.

Confirming previous work by Subhash et al. (1991) and Oda (1972a). Fonseca (2011) observed that, in the post-peak regime, outside the shear band, the contact normals tend to align with the most compressive principal stress direction (vertical direction in TXC).

During monotonic jacking of the model pile, the sand near the shaft is pre-sheared. This process induces a rotation of the principal strains, as shown in Figure 2.13, and thus a change in the directions of the contact normals. For compressive loading, the load transfer mechanism is like that during pile installation (i.e. similar directions of the most compressive strain E_2 were observed for pile installation and compressive loading), which means that the shearing during compressive loading does not induce meaningful changes in the soil fabric. In contrast, at the end of tensile loading, the direction of E_2 rotates from −40° before to +42° after tensile loading. During this process, the fabric rotates so that contact normals realign with the direction of the principal strains to accommodate the new loading direction. Consequently, in tensile loading, the soil elements outside the shear band would be expected to become less stiff. The fact that the initial fabric is stiffer in compression than in tension is seen by observing strains in soil elements near the pile shaft during loading; they all undergo less deformation in compressive loading; they do not exhibit the significant contraction observed in tensile loading.

In the case of driven or cyclically jacked piles, the difference between the shaft resistance in tension and compression is expected to be less than for monotonically jacked piles because of the partial load reversal during installation. Tension-to-compression shaft resistance ratios are still anticipated to be less than one because of the net downward movement of the pile during installation, which still produces an anisotropic fabric, notwithstanding the rebounds at the end of individual blows or cycles.

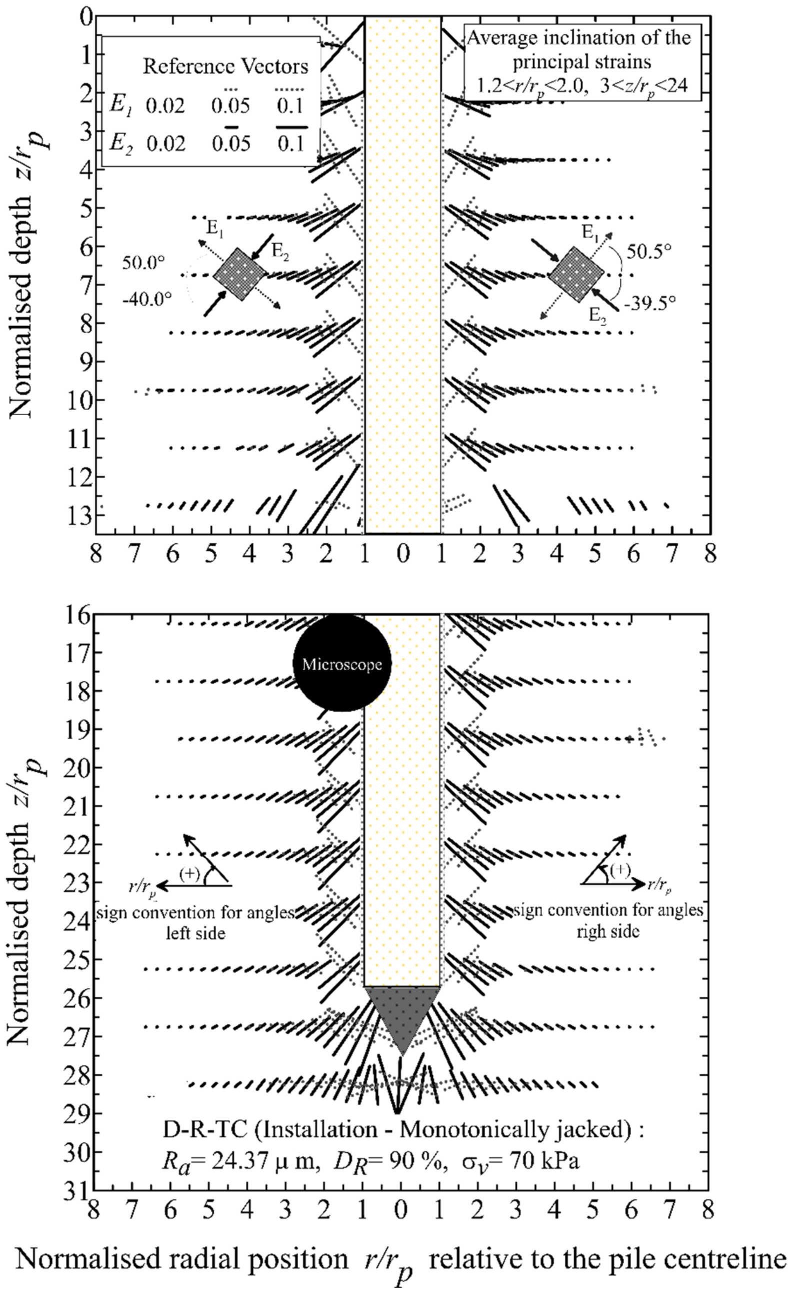

Figure 2.13. Magnitude and direction of E_1 and E_2 at the end of installation of monotonically jacked model pile (test D-R-TC).

2.5 Summary and conclusions

This chapter has presented the results of a series of loads tests performed on instrumented jacked model piles starting with tensile, then followed by compressive loads (TC sequence) or with the reverse sequence, compression-tension (CT). Three different model pile surface roughness values, corresponding to relative roughness R_n = 0.002, 0.064, 0.131, were studies in the experiments. The tests were performed in dense sand samples prepared in a half-cylindrical chamber. Digital images of the pile and the surrounding sand were captured during pile testing and then analysed using the DIC technique.

The loading sequence, tension followed by compression (TC) or compression followed by tension (CT), affects the ratio SRR of tensile-to-compressive shaft resistance. The SRR ratios are always greater when the model pile is loaded first in tension (TC sequence) owing to the lower shaft capacity that results in the subsequent compression loading. In general, the SRR values calculated from CT tests are comparable to the SRR values calculated from FTL tensile and compressive resistances, referred to as SRR_{FTL}. The values of SRR_{FTL} range from 0.67 for the smooth pile to 0.54 for the roughest pile. Both SRR and SRR_{FTL} are always less than one and decrease with increasing pile surface roughness.

The average direction of the displacement vectors for compressive loading is nearly the opposite of that observed for tensile loading. Outside the crushed particle band, the vertical displacements are more localised and have smaller magnitudes for compressive than for tensile loading. The magnitude of shear strains at a given radial location is greater in tensile than in compressive loading. The soil elements near the pile shaft contract more during tensile than compressive loading.

In compressive loading, the induced principal strains have approximately the same direction as just after monotonic jacking installation. In contrast, the reversal of loading direction that occurs in tensile loading leads to a strain state with principal strains rotated by 90° with respect to their directions at the end of pile installation. The fabric in that case has to evolve during tensile loading until it realigns in a way consistent with the new direction of the most compressive strain E_2, resulting in lower shaft resistance.

Digital images taken at the end of pile installation using a microscope show the presence of a zone of crushed particles along the pile shaft. The value of the thickness t_{cs} of this zone is unaffected by the pile surface roughness and does not vary during static loading. The shear band thickness t_s, estimated visually by tracking of particles across images, is smaller in compressive than in tensile loading, increases with increasing surface roughness and has a thickness that is less than t_{cs}. No shear band is observed for smooth piles.

2.6 Acknowledgements

The authors would like to acknowledge the support from the 'Instituto para el Desarrollo de la Ciencia y Tecnología en Colombia, Colciencias' and the National Science Foundation. This material is based in part upon work supported by the National Science Foundation under grant award number 1562538. The authors are very grateful for the support received from the programme director, Rick Fragaszy. Any opinions, findings and conclusions or recommendations expressed in this material are those of the author(s) and do not necessarily reflect the views of the National Science Foundation.

3. COMPRESSIVE AND TENSILE SHAFT RESISTANCE OF NONDISPLACEMENT PILES IN SAND

This chapter is reproduced from the paper by Ayda Catalina Galvis-Castro, Ruben Dario Tovar-Valencia, Rodrigo Salgado, Monica Prezzi (2019): "Compressive and tensile shaft resistance of non-displacement piles in sand" published in Journal of Geotechnical and Geoenvironmental Engineering, 2019, Vol.145(9).

3.1 Abstract

This chapter presents the results of a series of tensile-compressive (TC) and compressive-tensile (CT) static load tests performed on instrumented model piles preinstalled in silica sand samples prepared in a half-cylindrical calibration chamber with viewing windows along its symmetry plane. Images of the model pile and the surrounding soil were captured during axial loading through the observation windows using digital cameras and were subsequently analyzed using the digital image correlation (DIC) technique to generate the displacement and strain fields in the sand domain. The shaft resistances mobilized during the experiments were obtained using load cells placed at the head and the base of the model piles. The results obtained from the load tests revealed that reversal of loading direction substantially reduces the unit shaft resistance. This response was attributed to a drop in the radial strain exhibited by the soil elements surrounding the model pile shaft, which could be explained by a misalignment of the principal axes of the stress and fabric tensors resulting from load reversal. The results also indicated that the tensile-to-compressive shaft resistance ratio of fresh preinstalled piles is always nearly one.

3.2 Introduction

Certain structures supported by nondisplacement piles — also known as bored piles or drilled shafts (Fleming et al. 2008; Salgado 2008; Viggiani et al. 2014) — are sufficiently light, in comparison with moments applied by wind forces or other lateral forces, that individual piles in a group may be loaded in tension (uplift). In design, it has been proposed that the shaft capacity of bored piles in sand under tensile loading be reduced from the value calculated for compressive loading by a factor ranging from 0.74 to 0.88 (O'Neill and Reese 1999) or that a lower resistance factor (10% lower) be used when computing the nominal shaft resistances in a load and resistance factor design (LRFD) approach (Brown et al. 2010).

Results from physical modeling (De Nicola and Randolph 1999; O'Neill 2001; Vipulanandan *et al*. 1989) and field tests on driven and jacked piles in sand (Beringen et al. 1979; Chow 1997; Hussein and Sheahan 1993; Jardine et al. 2006; Lehane et al. 1993) indicate that the shaft capacity of piles in sand is lower under tensile loading than under compressive loading. De Nicola and Randolph (1993) suggested that the primary cause for this lower tensile capacity is the expansion and contraction of the pile due to Poisson's ratio and proposed a theoretical expression to quantify the tensile-to-compressive shaft capacity ratio of displacement piles. Results from finite-element analysis on nondisplacement piles (Loukidis and Salgado 2008) indicate that, in a compressive loading of a concrete pile, the increase in pile diameter due to Poisson's effect is small, and that the radial stresses developed on the pile shaft are comparable to those on a perfectly rigid pile. This suggests that Poisson's ratio has a negligible effect on the shaft resistance of piles. Changes in mean effective stress along the pile shaft due to rotation of principal stress and strain directions (Galvis-Castro et al. 2019b; Jardine et al. 2005, 1993; De Nicola and Randolph 1993) and reduction in the stress below the pile base due to development of a relaxed bulb (Fioravante et al. 2010b; De Nicola and Randolph 1999) have been shown to have greater influence on the reduction in shaft resistance observed in driven and jacked piles tested under tension.

Based on a substantially large load test database of 100 field load tests (54 tests in tension and 46 test in compression) performed on drilled shafts installed mainly in medium-dense soils varying from gravelly sand to silty sand, Chen and Kulhawy (2002) evaluated the shaft resistance of piles and indicated that the shaft resistance in compressive and tensile loading differed by less than 4%. This result was confirmed by Kulhawy (2004), Ismael (2001), Kulhawy and Hirany (1989), and Stas and Kulhawy (1984).

Bored piles or drilled shafts are constructed by backfilling a cylindrical void, created by drilling, with concrete (Salgado et al. 2017); thus, the density and stress state of the soil surrounding a nondisplacement pile are minimally affected by installation. In laboratory conditions, nondisplacement piles have been studied using preinstalled or wished-in-place model piles in calibration chamber (Le Kouby et al. 2013; Tehrani et al. 2016). Experiments performed in calibration chambers using instrumented model piles allow the separation of the shaft and base resistances (Arshad et al. 2014; Jardine et al. 2009; Lee and Poulos 1991) in a controlled environment, which is not feasible in the field unless fully instrumented piles are used.

Le Kouby *et al.* (2013) studied the influence of loading direction on the shaft resistance of rough model piles ($R_n = R_{max}/D_{50} = 1.0$) embedded in medium-dense Fontainebleau sand samples ($D_{50} = 0.2$ mm). The model pile tests were performed in a calibration chamber that had a diameter of 254 mm and a height of 700 mm using a pile with a diameter of 20 mm and a length of 735 mm. The instrumented model pile was positioned inside the calibration chamber before the pluviation of the sand. The results showed similar magnitudes of the peak shaft resistance measured from first-time tensile and first-time compressive load tests and nearly symmetrical shaft resistance versus pile head displacement curves resulting from compressive and tensile loading of non-displacement model piles. This response was attributed to the pile preinstallation, which did not preload the soil in any way (Le Kouby et al. 2013).

De Nicola and Randolph (1999) performed centrifuge tests with an acceleration equal to 100 *g* to study the response of open-ended and closed-ended driven piles in dense silica sand under tensile and compressive loading. The prototype embedment length varied from 5 to 19 m; its diameter was 1.6 m, and its wall thickness was 0.055 m. The piles were subjected to a minimum of two static loadings, which included sequences of static compressive followed by static tensile loading (CT) using the open-ended and closed-ended piles, and static tensile loading followed by a static compressive load (TC) using the open-ended piles. The piles were loaded statically to at least a pile head displacement of 10% of the pile diameter, but the average shaft resistance was calculated at a pile head displacement of 5% of the pile diameter for each loading stage. The tensile-to-compressive shaft resistance ratio (shaft resistance was estimated as the difference in load between the top and bottom strain gauges) for the CT sequence was reported to vary from 0.46 to 0.59 for closed-ended piles and from 0.47 to 0.61 for open-ended piles. The ratio for the TC sequence ranged from 0.63 to 0.83 for open-ended piles. Similar ratios (0.53 in the CT loading sequence and 0.80 in the TC loading sequence for a model pile with a rough shaft surface) were found by (Galvis-Castro et al. 2019b) based on loading tests performed on model jacked piles. These results highlight the importance of loading history and loading sequence on the response of displacement piles.

The digital image correlation (DIC) technique (Sutton et al. 2009; Take 2015; White et al. 2003) can be used to study soil undergoing deformation, because it allows determination of displacement and strain fields from analyses of images. The DIC technique has been used in connection with calibration chamber testing to study fundamental geomechanics boundary value problems, such as cone penetration and pile loading (Arshad et al. 2014; Tehrani et al. 2016; Tovar-Valencia et al. 2018; White and Bolton 2004)

This chapter presents the results of a series of tension-compression (TC) and compression-tension (CT) loading tests performed on nondisplacement model piles pre-installed (wished in place) in silica sand. The effect of loading direction on the shaft capacity of virgin piles and pre-tested piles for two relative densities is discussed. The DIC technique was used to obtain the displacements, strain fields, and direction of principal strains during loading of the model piles. The experimental results enable greater understanding of the effect of loading direction on mobilized shaft resistance during static loading; this understanding can be used to refine pile design methods.

3.3 Materials and methods

3.3.1 Half-cylindrical calibration chamber

The tests were performed in a half-cylindrical calibration chamber with DIC capabilities (Figure 3.1). This chamber has been used in the past to study the cone penetration process and the effect of pile surface roughness on the shaft resistance of displacement and nondisplacement piles in sand (Arshad et al. 2014; Tehrani et al. 2016; Tovar-Valencia et al. 2018). The chamber, which imposes a BC3 (passive radial rigid wall) boundary condition on the soil samples (Ghionna and Jamiolkowski 1991; Salgado *et al.* 1998), has a height H of 1.25 m and a diameter D_c of 1.68 m. The flat side of the chamber has a poly(methyl methacrylate) (PMMA) panel reinforced by a steel frame that provides three transparent observation windows, enabling the capture of digital images of the soil and the model pile during testing. Vertical stress (surcharge) was applied at the top of the sample using an air-pressurized rubber bladder and a reaction steel lid bolted to the chamber. To minimize the effect of slight surcharge differences detected by Jardine *et al.* (2013), the membrane was placed above a rigid plate that had a rectangular space of 4.3 cm by 2.2 cm in which the pile was located. A removable loading system of 50-kN capacity was used to perform tensile and compressive loading under displacement-controlled conditions.

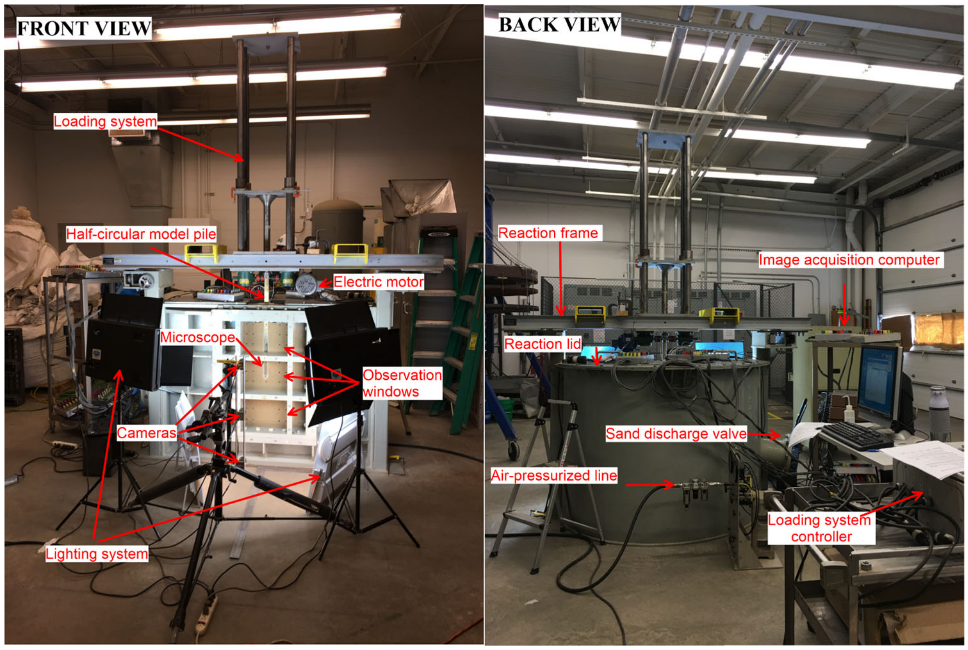

Figure 3.1. Schematic of the DIC calibration chamber at Purdue University.

3.3.2 Model piles

Two half-circular model piles were used in the testing. Both were rods made of brass; they had the same diameter B = 31.75 mm and length L= 915 mm but had two different base geometries: one had a flat base and one had a half-conical base with a 60° apex angle (Figure 3.2). Each model pile was instrumented with a miniature load cell and a top load cell to measure the resistances at the base and head, respectively. The surface roughness of the half-circular model piles was modified by attaching sandpaper (grit #120) to the pile shaft, increasing the original pile diameter B = 31.75 mm by less than 0.05 mm. To ensure perfect attachment of the sandpaper to the piles shaft, we used an ethyl cyanoacrylate base glue [Super Glue Professional from Loctite (Rocky Hill, Connecticut)], which had a high strength (tensile strength of 17 MPa), a low viscosity, and a short curing time. The shaft surface roughness of the pile was defined in terms of the maximum roughness R_{max} (Tovar-Valencia *et al.* 2018; Uesugi and Kishida 1986) and the normalized roughness R_n=R_{max}/D_{50}. For both model piles, R_{max} was equal to 81.14 μm and R_n was equal to 0.131.

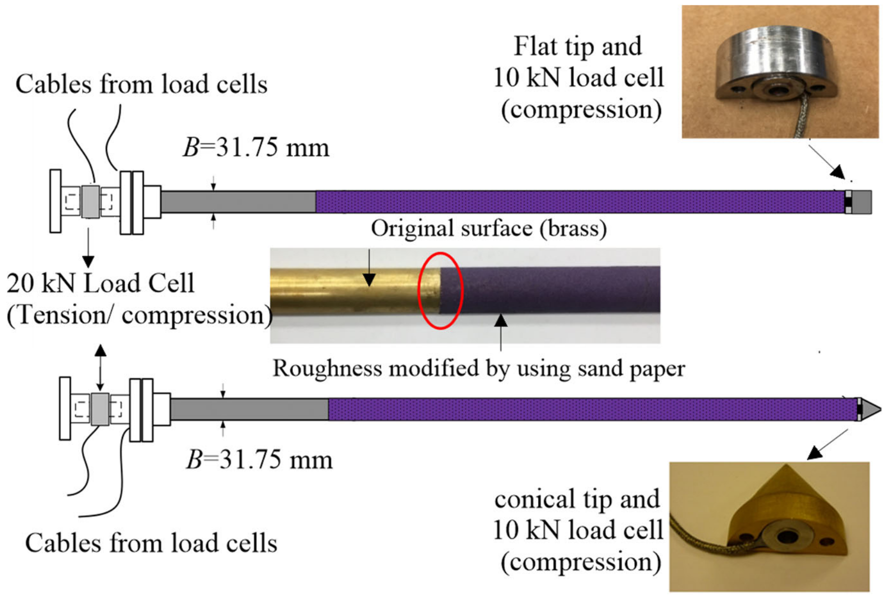

Figure 3.2. Model piles. (Adapted from Tovar-Valencia et al. (2018), © ASCE)

3.3.3 Test sand

The test sand was a silica sand (SiO_2 = 99.7%) known as Ohio Gold Frac sand that has subangular to subrounded particles with high sphericity and is classified as poorly-graded (SP). Table 3.1 shows the sand properties and the interface friction angle of the sand when sheared against sandpaper.

Table 3.1. Index and mechanical properties of Ohio Gold Frac sand (Adapted from Tovar-Valencia et al. (2018), © ASCE)

D_{50} (mm)	C_u	C_c	e_{max}	e_{min}	G_s	ϕ_{cs}^{DS} (°)	ϕ_{cs}^{RS} (°)	ϕ_{cs}^{TXC} (°)	$\delta_c^{s\text{-}p}$ (°)	$\delta^{b\text{-}g}$ (°)
0.62	1.44	0.94	0.81	0.59	2.65	32.0	31.3	32.6	28.4	9.3

Note: e_{max} and e_{min}, are the maximum and minimum densities of the sand, respectively, determined based on ASTM D4253-16 (ASTM D4253-16, 2016) and ASTM D4254-16 (ASTM D4254-16, 2016); ϕ_{cs}^{DS} = critical-state friction angle obtained from direct shear tests; ϕ_{cs}^{TXC} = critical-state friction angle obtained from triaxial compression (TXC) tests; ϕ_{cs}^{RS} = critical-state friction angle obtained from ring shear tests; $\delta_c^{s\text{-}p}$ = interface critical-state friction angles of the sand -sandpaper grit#120 from direct shear tests; $\delta^{b\text{-}p}$ = interface friction angle of the brass-glass from direct shear tests.

The chamber-to-pile diameter ratio D_c/B was 52; consequently, minimal chamber boundary effects on the test results were expected (Salgado 2013). Base boundary effects were minimized in the tests by maintaining a distance higher than $18B$ between the base of the chamber and the pile tip. In addition, during load testing, the stresses at the base of the chamber were monitored by a load cell located at the bottom of the chamber.

3.3.4 Image acquisition system and image analysis

The image acquisition system used to record the images consisted of three complementary metal-oxide semiconductor (CMOS) cameras with five-megapixel resolution equipped with low distortion lenses with fixed focal length of 12.5 mm and a computer equipped with camera control and acquisition software (XCAP version 2.3). The three CMOS cameras were positioned in front of the three observation windows of the chamber (one per window) to take synchronized digital images of |the soil domain at a rate of two frames per second. The field of view of each camera covered the area of one of the three observation windows. The three observation windows were illuminated by a set of fluorescent and LED lamps. Displacement and strain fields in the soil domain were obtained using the digital image correlation technique. This technique uses a correlation algorithm to locate the same pattern of grey level intensity from the undeformed image to a distorted image (Sutton et al. 2009). The image analysis was performed using the commercial DIC software VIC-2D version 2009. A 25 × 25-pixel ($7.4D_{50} \times 7.4D_{50}$) subset size (defined as the size of the set of pixels to be tracked across the images) and a subpixel interpolation scheme implemented in VIC-2D led to a resolution in displacement measurements higher than 27 μm. Further details on camera calibration, speckle pattern, precision, and accuracy can be found in Arshad (2014).

3.3.5 Test protocol and program

Nineteen model pile tests were performed in the DIC calibration chamber in dense and medium-dense sand samples (Table 3.2). The model piles were preinstalled in the calibration chamber before sample preparation following the procedure described by Tehrani et al. (2016). Sample preparation was done by air pluviation using a large pluviator positioned at the top of the calibration chamber (Arshad et al. 2014; Lee et al. 2011). The target sample densities were achieved by changing the flow rate through addition or removal of diffuser sieves. The relative density was on average equal to 89.6% with a standard deviation of 1.8% for the dense sand samples and equal to 65.9% with a standard deviation of 2.8% for the medium-dense samples. Prior to testing, all the samples were aged for one day with a surcharge of 70 kPa applied on the top of the sample. A sequence of tension-compression or compression-tension static load tests immediately followed. All static load tests were carried out at a rate of 0.1 mm/s. The total and base resistances were recorded throughout the tests; at the same time, digital images were captured from each observation window of the DIC calibration chamber. Table 3.2 provides the details of the pile load tests. The tests are identified by a code that specifies the sand density (D = dense sand; MD = medium-dense sand), the type of pile base (co = conical base; f = flat base), the loading sequence (TC = tensile loading followed by compressive loading; CT = compressive loading followed by tensile loading), and a number for each test of each type (preceded by "#"). The absolute value of the pile head displacement $|w_t|$ at the end of each loading stage is also included in Table 3.2.

3.4 Results and discussion

3.4.1 Sensor-based results

Figure 3.3(a) shows the average unit shaft resistance $q_{s,avg}$ versus penetration depth for the CT loading tests performed on dense sand [D-CT(f)#1] and medium-dense sand [MD-CT(f)#2]. During first-time loading (FTL), the model pile was pushed down from an initial base depth of 370 mm to a base depth of 400 mm, corresponding to a pile head displacement w = 30 mm (approximately 1B). The magnitude of $q_{s,avg}$ in compression increases with increasing penetration depth until it reached a peak value [peak unit shaft resistance q_{sP} = 89.3 and 37.8 kPa for FTL in tests D-CT(f)#1 and MD-CT(f)#2, respectively]. After the peak, the magnitude of $q_{s,avg}$ decreased and tended to stabilize at the limit unit shaft resistance q_{sL} [q_{sL} = 67.0 and 32.2 kPa for FTL in tests D-CT(f)#1 and MD-CT(f)#2, respectively]. In the subsequent loading, the second-time loading (STL), the model pile was then pulled up from a base depth of 400 mm for at least $|\Delta w|$ = 30 mm (approximately 1B) to 370 mm in test D-CT(f)#1. During this tensile loading, $q_{s,avg}$ decreased and reached a minimum value after a pile head displacement Δw of approximately -5 mm ($q_{s,avg}$ = -27.0 kPa and -12.7 kPa at a base depth of 395 mm in tests D-CT(f)#1 and MD-CT(f)#2, respectively). As the base depth continued to decrease during STL, the magnitude of $q_{s,avg}$ tended to drop at a low rate [=0.6 kPa/mm in test D-CT(f)#1 and 0.09 kPa/mm in test MD-CT(f)#2].

Figure 3.3(a) also shows that, during CT loading sequences, $|q_{s,avg}|$ was always greater in first-time loading (FTL).

Table 3.2. Test program.

Test code	Relative density D_R (%)	Base geometry	Initial embedment depth L_e (mm)	$\lvert w_t \rvert$ for FTL (mm)	$\lvert w_t \rvert$ for STL (mm)
D-CT(f)#1	93	flat	370	30.0	33.0
D-CT(f)#2	89			30.0	31.0
D-TC(f)#1	88		400	16.0	35.4
D-TC(f)#2	90			17.0	37.0
MD-CT(f)#1	64		370	30.0	60.0
MD-CT(f)#2	68			30.0	50.0
MD-C(f)#3	65			30.0	0
MD-TC(f)#1	66		400	31.0	51.0
MD-TC(f)#2	72			22.6	42.6
MD-T(f)#3	69			30.0	0
D-CT(co)#1	88	conical	370	30.0	34.0
D-CT(co)#2	88			60.0	60.0
D-TC(co)#1	90		400	16.0	35.0
D-TC(co)#2	91			32.0	54.0
MD-CT(co)#1	62		370	30.0	32.0
MD-CT(co)#2	64			30.0	51.0
MD-CT(co)#3	65			60.0	60.0
MD-TC(co)#1	66		400	60.0	90.0
MD-T(co)#2	65			30.0	0

Note: TC = tensile followed by compressive loading; CT = compressive followed by tensile loading; D = dense sand; MD = medium-dense sand; co = conical base; f = flat base; #n = number of tests with similar loading sequence, base geometry, and relative density; $|w_t|$ = absolute value of the pile head displacement at the end of loading; FTL= first-time loading; STL = second-time loading.
All tests were performed with a surcharge of 70 kPa at the top of the sample, all model piles were "wished in place," and all had the same surface roughness (R_n= 0.131).

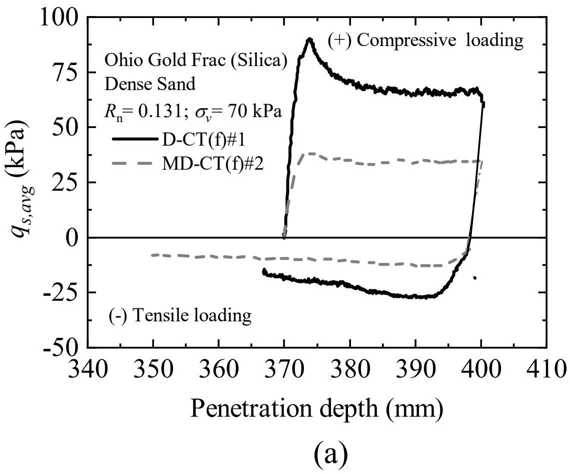

Figure 3.3. Average unit shaft resistance $q_{s,avg}$ versus penetration depth for the nondisplacement model piles with a flat base in dense and medium-dense sand for (a) compressive-tensile; and (b) tensile-compressive loading sequences.

Figure 3.3(b) shows the average unit shaft resistance $q_{s,avg}$ versus penetration depth during the TC loading sequence in dense sand [D-TC(f)#2] and medium-dense sand [MD-TC(f)#1]. In FTL, the model pile was first pulled up from an initial base depth of 400 mm to a base depth of 370 mm (corresponding to w=-30 mm). The peak in shaft resistance was observed in FTLs at a base depth of about 397.3 mm for dense [q_{sP} = -90.4 kPa for the FTL in test D-TC(f)#2] and 398.2 mm for medium-dense sand [q_{sP} =-42.0 kPa for the FTL in test MD-TC(f)#1]. After the peak, $|q_{s,avg}|$ decreased continuously as the penetration depth decreased. The reduction of $|q_{s,avg}|$ occurred at a lower rate in medium-dense [=1.4 kPa/mm in the FTL in test MD-TC(f)#1] than in dense sand [=2.3 kPa/mm for the FTL in test D-TC(f)#2]. During STL, the model pile was pushed down to a base depth of 420 mm. This meant that the pile penetrated almost a pile diameter beyond its position at the beginning of FTL (= 400 mm). Despite the large pile displacement involved in the compressive loading, the mobilized $|q_{s,avg}|$ in the STL was always lower than the $|q_{sP}|$ in the FTL, for tests D-TC(f)#2 and MD-TC(f)#1. For example, in the STL of the dense sand sample, $|q_{s,avg}|$ at a depth of 420 mm was 3.6 times smaller than $|q_{sP}|$ in the FTL. This indicates that, with a TC loading sequence, the reversal of loading direction induces a substantial degradation in the available shaft resistance for the STL.

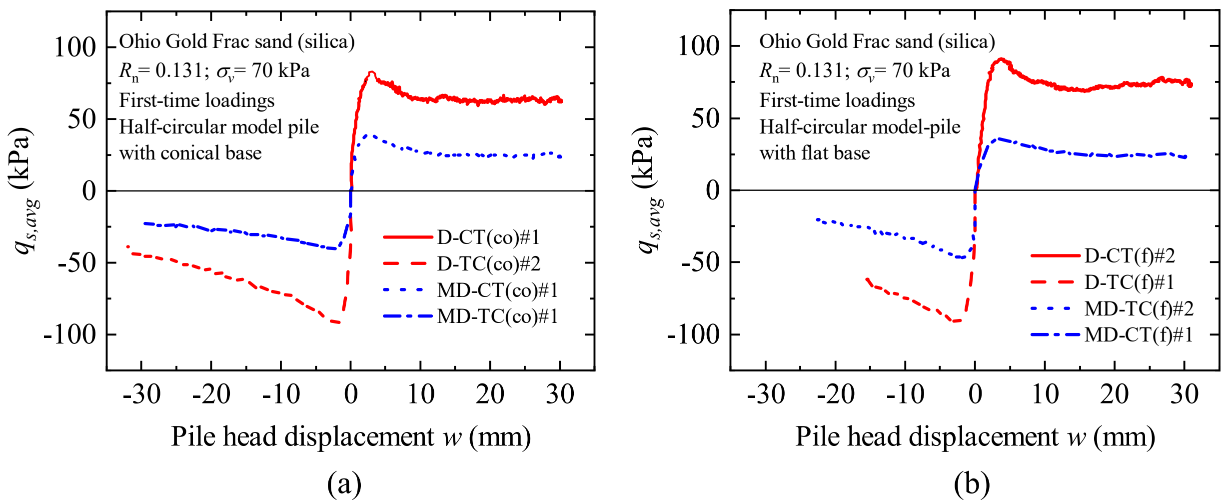

Figure 3.4. Average unit shaft resistance $q_{s,avg}$ versus pile head displacement w from FTL in dense and medium-dense sand samples performed with (a) flat-base; and (b) conical-base model piles.

Figure 3.4(a and b) show the average unit shaft resistance $q_{s,avg}$ versus pile head displacement w of four representative first-time loading tests using model piles with flat and conical bases, respectively. Positive values of pile head displacement w indicate compressive loading, while negative values indicate tensile loading. In dense sand samples, $|q_{sP}|$ measured for the compressive loading stage in test D-CT(f)#2 (q_{sP} = 89.3kPa) was comparable to the $|q_{sP}|$ for the tensile loading in test D-TC(f)#1 (q_{sP} =-90.5 kPa), indicating a negligible effect of the loading direction on the peak shaft resistance measured in FTL. Similar values of $|q_{sP}|$ were measured in the compressive and tensile FTL in tests performed in medium-dense sand [tensile loading in tests MD-TC(f)#2 and MD-TC(co)#1 and compressive loading in tests MD-CT(f)#1 and MD-CT(co)#1].

In general, the value of $|q_{sP}|$ tended to develop at a magnitude $|w|$ of the pile head displacement that was slightly smaller in tensile loading than in compressive loading [e.g., in the compressive loading in test D-CT(f)#2, w_P = 3.8 mm = 0.12B, and in the tensile loading in test D-TC(f)#1, w_P = -2.6 mm = - 0.08B]. Figure 3.4 also indicates that the effect of the pile base geometry on the peak and limit unit shaft resistance was negligible. We also observed that the value of $|q_{sP}|$ mobilized in dense sand [e.g., q_{sP} = 89.3 kPa for FTL in test D-CT(f)#2] was 2.5 times greater than the value developed in medium-dense sand [e.g., q_{sP} = 35.8kPa for the FTL in test MD-CT(f)#2].

Table 3.3 shows the peak values of the unit shaft resistance measured in first-time loading ($q_{sP,FTL}$), the limit unit shaft resistances from first-time loading ($q_{sL,FTL}$) and from the subsequent reverse loading ($q_{sL,STL}$), and the pile head displacement (w_P) at which the peak in shaft resistance was observed for FTL. For both compressive and tensile loading, $q_{sL,FTL}$ was defined as the value of $q_{s,avg}$ measured at an absolute value of the pile head displacement $|w|$ of 15 mm (approximately 0.5B), corresponding to a base depth of 385 mm. For the tensile phase of a CT loading test, $q_{sL,STL}$ was defined as the minimum value of $q_{s,avg}$ recorded during tensile loading. For the compressive phase of TC loading sequence, $q_{sL,STL}$ was the value of $q_{s,avg}$ measured at a pile base depth that was 15 mm (approximately 0.5B) beyond the pile base position before the start of the tensile loading phase.

Table 3.3. Peak and limit unit shaft resistances from FTL and STL, and pile head displacement required to mobilize the peak shaft resistance on FTL.

Test code	$q_{sP,FTL}$ (kPa)	$q_{sL,FTL}$ (kPa)	w_P (mm)	$q_{sL,STL}$ (kPa)	$D=\|q_{sL,STL}\|/\|q_{sL,FTL}\|$
D-CT(f)#1	89.3	67.0	3.8	-26.7	0.40
D-CT(f)#2	89.3	68.4	3.8	-26.8	0.39
D-TC(f)#1	-90.5	-65.9	-2.6	28.0	0.42
D-TC(f)#2	-90.4	-65.1	-2.6	28.0	0.43
MD-CT(f)#1	35.8	25.7	3.5	-9.8	0.38
MD-CT(f)#2	37.8	32.2	3.5	-12.4	0.39
MD-TC(f)#1	-42.0	-27.0	-1.8	15.4	0.57
MD-TC(f)#2	-45.3	-25.9	-1.8	13.6	0.53
D-CT(co)#1	82.0	65.0	3.4	-28.4	0.44
D-CT(co)#2	83.0	66.0	3.4	-30.0	0.45
D-TC(co)#1	-92.0	-63.0	-2.4	32.4	0.52
D-TC(co)#2	-91.0	-63.0	-2.4	33.0	0.52
MD-CT(co)#1	38.0	25.2	3.2	-12.0	0.48
MD-CT(co)#2	36.6	28.0	2.8	-11.5	0.41
MD-CT(co)#3	39.0	23.9	3.3	-10.5	0.44
MD-TC(co)#1	-40.6	-28.6	-2.3	11.2	0.39

Note: $q_{sP,FTL}$ =peak unit shaft resistance from a first-time loading (FTL); $q_{sL,FTL}$ is the limit unit shaft resistance from a first-time loading (FTL); $q_{sL,STL}$ is the limit unit shaft resistance from a second-time loading (STL); $q_{sL,FTL}$ is obtained as the value of $q_{s,avg.}$ measured at $|w|$ = 15 mm (≈ 0.5B) (at a penetration depth = 385 mm); $q_{sL,STL}$ from a TC loading sequence is obtained as the value of $q_{s,avg.}$ measured at a base depth 0.5B beyond the initial position of the FTL; $q_{sL,STL}$ from a CT loading sequence is obtained as the minimum value of $q_{s,avg.}$ during the tensile loading;
w_P is the pile head displacement required to mobilize the peak unit shaft resistance; and D is the shaft resistance degradation factor calculated as $|q_{sL,STL}|$ / $|q_{sL,FTL}|$ Unit shaft resistances have been corrected to account for the friction developed during loading between the flat surface of the model pile and the glass attached to the poly(methyl methacrylate) (PMMA) window.

3.4.2 Degradation of shaft resistance due to CT and TC loading sequences

A degradation factor D, defined as the ratio of $|q_{sL,STL}|$ to $|q_{sL,FTL}|$ measured in the same test, was used to quantify the reduction in shaft resistance due to the reversal of the loading direction during CT and TC loading sequences. The values of D calculated for each test are reported in Table 3.3. The results show that (1) the degradation factor D was always less than 0.6; (2) the pile base geometry had a negligible effect on the values of D (e.g., in TC loading in dense sand, D = 0.39 for the model piles with both flat and conical bases); (3) the differences between the average degradation factors D for dense and medium-dense sand were negligible; and (4) the value of D tended to be slightly less in CT than in TC loading, except when the magnitude of the pile head displacement during first-time tensile loading exceeds 1B [as in test MD-TC(co)#1, for which D = 0.39] because of the cavity of soil that was left behind by the retracting pile, which was filled with soil moving in from the regions around the pile. What is clear from these results is that, once the pile settlement is large enough to fully mobilize shaft resistance in one direction, the limit shaft resistance upon load reversal will be substantially less.

3.4.3 Tensile-to-compressive shaft resistance ratio from first-time loading (FTL)

Table 3.4 shows the arithmetic mean values of the limit and peak unit shaft resistances for dense and medium-dense sand measured from first-time tensile and first-time compressive loadings. Based on the magnitudes reported in Table 3.4, two tension-to-compression shaft resistance ratios were calculated: (1) the ratio $SRR_{P,FTL}$ of the average peak unit shaft resistance $\overline{q}_{sP,FTL}$ from the tensile loading to the average peak unit shaft resistance $\overline{q}_{sP,FTL}$ from the compressive loading for tests with similar relative densities; and (2) the ratio $SRR_{L,FTL}$ of the average limit unit shaft resistance $\overline{q}_{sL,FTL}$ from the tensile loading to the average limit unit shaft resistance $\overline{q}_{sL,FTL}$ from the compressive loading for tests with similar relative densities. The results, summarized in Table 3.4, show that $SRR_{P,FTL}$ varies from 1.06 to 1.09, and $SRR_{L,FTL}$ varies from 0.96 to 1.02. These results demonstrate that, for virgin non-displacement piles, the effect of loading direction on the shaft resistance, at least for $|w|$ < 15 mm (approximately 0.5B), is negligible. These results confirm the observations of Le Kouby et al. (2013).

Table 3.4. Tensile-to-compressive shaft resistance ratios $SRR_{P,FTL}$ and $SRR_{L,FTL}$ for pre-installed model piles

Relative density	$\overline{q}_{sP,FTL}$ (kPa) Compressive loading	$\overline{q}_{sP,FTL}$ (kPa) Tensile loading	$SRR_{P,FTL}$	$\overline{q}_{sL,FTL}$ (kPa) Compressive loading	$\overline{q}_{sL,FTL}$ (kPa) Tensile loading	$SRR_{L,FTL}$
MD	37.9	-41.2	1.09	26.8	-27.4	0.96
D	85.9	-91.0	1.06	66.6	-64.3	1.02

Note: $\overline{q}_{sP,FTL}$ = arithmetic average of peak unit shaft resistances measured for first-time loading tests with similar relative densities and loading directions; $\overline{q}_{sL,FTL}$ = arithmetic average of limit unit shaft resistances measured for first-time loading of tests with similar relative densities and loading directions; $SRR_{P,FTL}$ = tension-to-compression peak shaft resistance ratio calculated as $\overline{q}_{sP,FTL}$ for tensile loading divided by $\overline{q}_{sP,FTL}$ for compressive loading; $SRR_{L,FTL}$ = tension-to-compression limit shaft resistance ratio calculated as $\overline{q}_{sL,FTL}$ for tensile loading divided by $\overline{q}_{sL,FTL}$ for compressive loading.

3.4.4 Image-based results

3.4.4.1 Soil displacements from first-time loading tests

Figure 3.5 shows the displacement vector fields, linearly scaled by the magnitude of the displacement, after an absolute value of the pile head displacement $|w|$ of 3 mm was reached for first-time tensile and compressive loading tests on medium-dense and dense sand samples for piles with flat and conical bases. A value of $|w|$ = 3 mm was selected because it approaches the displacement required to reach the peak of the average shaft resistance. The displacement vectors shown in Figure 3.5 are plotted in the z/r_p versus r/r_p space, where z is the vertical distance from the sample surface to a soil element, r is the radial distance of a soil element relative to the pile axis, and r_p is the radius of the model pile. Only displacement vectors with magnitudes greater than 0.1 mm and less than 3.0 mm are displayed in Figure 3.5. The pattern of the displacement vectors around the pile shaft shows that the magnitude of the displacement decreases with increasing r/r_p. Near the pile shaft, the orientation of the displacement vectors was subvertical, pointing in the same direction as that of loading. In general, the piles mobilize displacements to smaller distances from the pile shaft in medium-dense than in dense sand samples. There was also minimal effect of the base geometry on the pattern of the displacement vectors around the pile shaft.

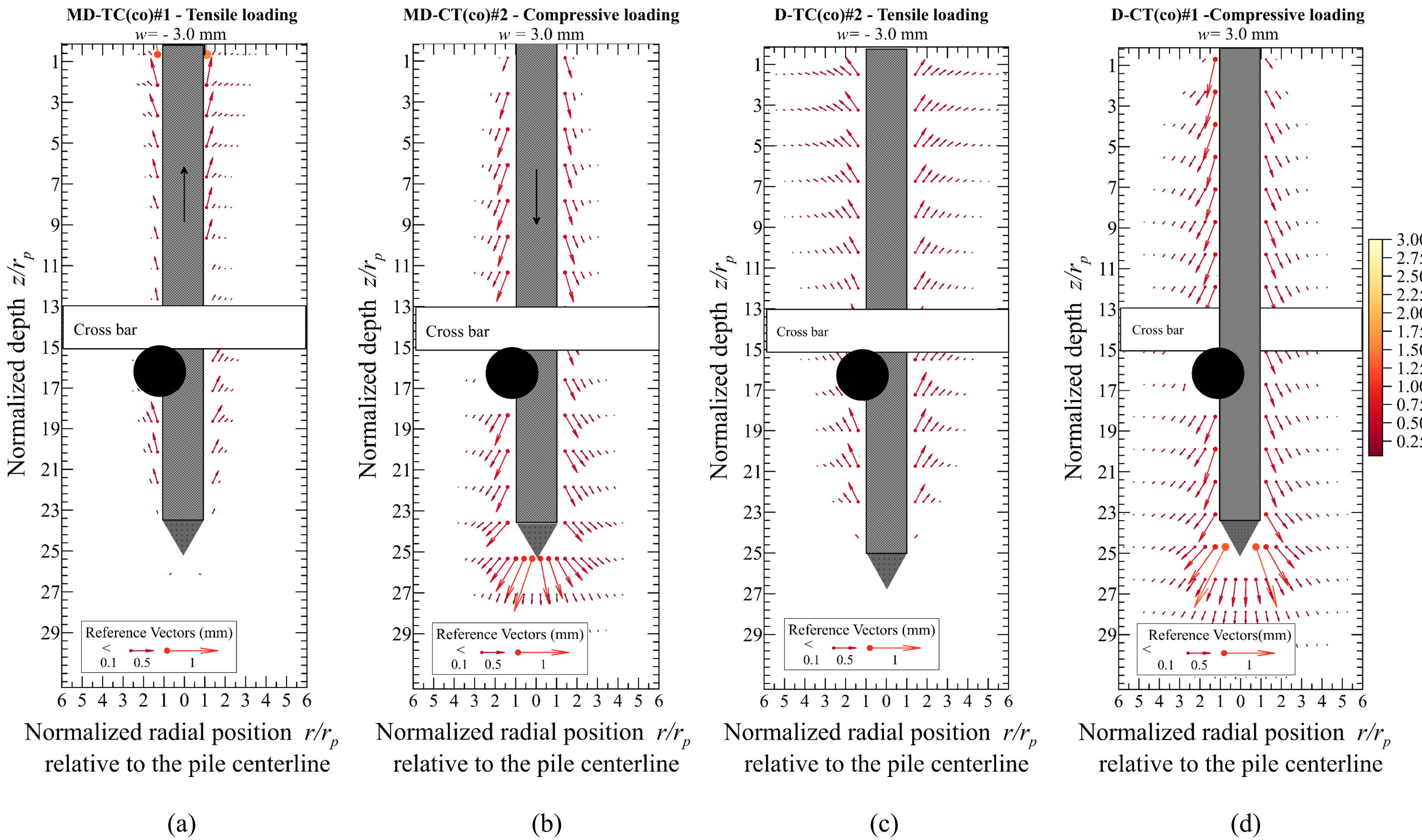

Figure 3.5. Soil displacement vectors after 3 mm of pile head displacement *w* (negative for tensile loading and positive for compressive loading) for FTL of tests: (a) MD-T(co)#1; (b) MD-CT(co)#2; (c) D-TC(co)#2; (d) D-CT(co)#1; (e) MD-TC(f)#1; (f) MD-CT(f)#2; (g) D-TC(f)#1; and (h) D-CT(f)#1.

Figure 3.5 continued

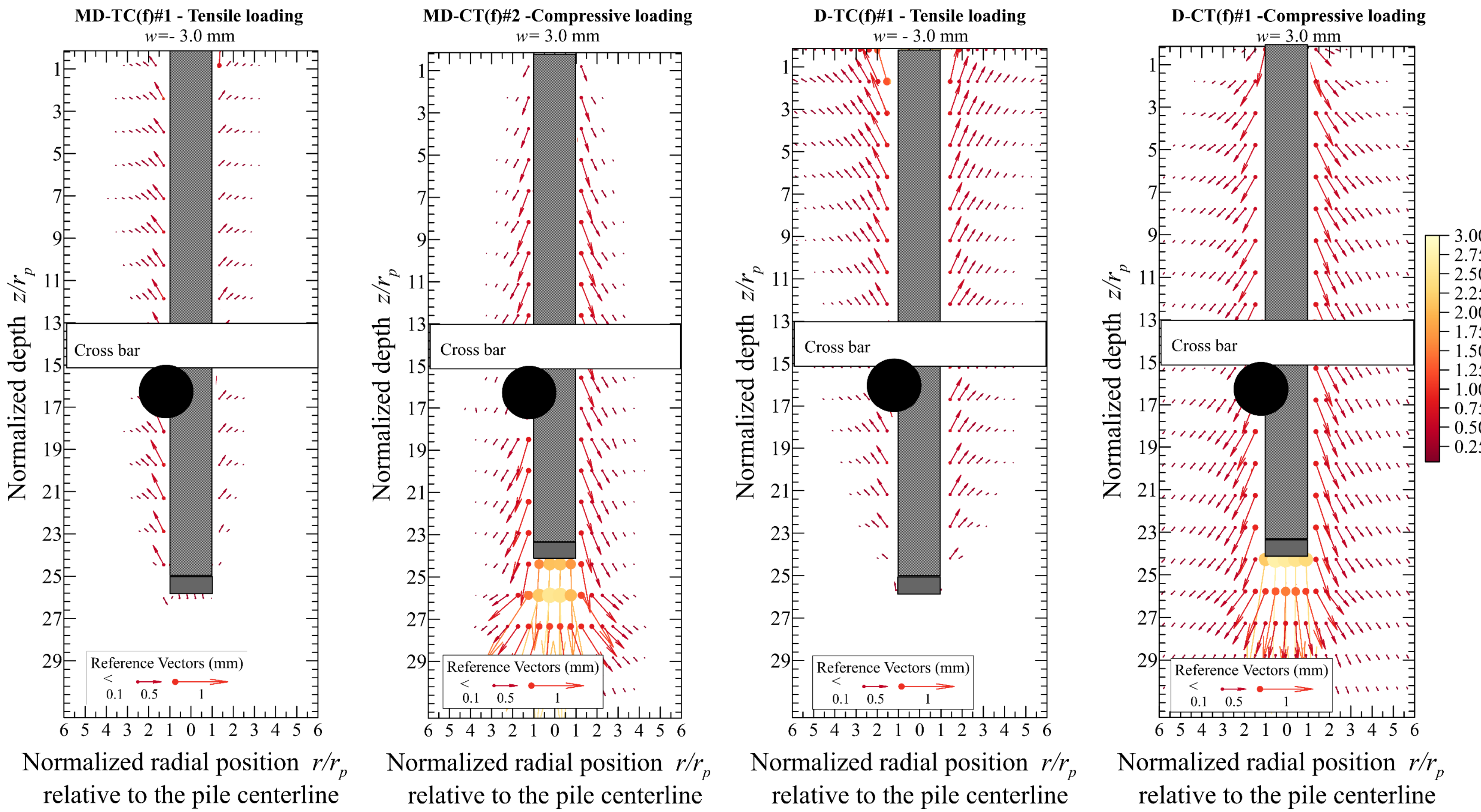

(e) (f) (g) (h)

Figure 3.6 shows the inclination θ of the displacement vectors versus the normalized radial position r/r_p relative to the pile centerline at $|w|$ = 3 mm for first-time compressive and tensile loading tests. The profiles are shown for elements located initially at a normalized depth z/r_p = 11.5, sufficiently far from the influence of the top and base boundaries of the chamber. The inclination θ is shown only for displacement vectors with magnitude greater than 0.1 mm. The angle that the displacement vectors made with the horizontal (measured counterclockwise on the right side of the pile and clockwise on the left side of the pile) was highest close to the pile shaft. At r/r_p = 1.19 (r-r_p = 3.0 mm), the average value of θ is 69.3º for tensile loading and −72.1º for compressive loading, indicating that, after $|w|$ = 3 mm, the displacement vectors for both loading directions (tension and compression) made angles with the horizontal of approximately the same magnitude. Between $2 < r/r_p < 3$, the magnitudes of θ exhibit the largest drop, with a higher rate of reduction in tensile loading than in compressive loading. For tensile loading, the magnitude of θ at r/r_p = 3 was 50% of that measured at r/r_p = 1.19; for compressive loading, the value of $|\theta|$ at r/r_p = 3 was almost 80% of that measured at r/r_p = 1.19. Away from the pile shaft, the vertical component of the soil displacement tended to dominate for compressive loading but was more or less in balance with the horizontal component for tensile loading [e.g., in dense sand at r/r_p = 3.2 [r-r_p = 34.9 mm], θ = 47.1° for tensile loading and -60.9° for compressive loading]. The profiles of θ in medium-dense sand followed trends similar to those observed for dense sand, except when the model pile was loaded in tension, when lower values of θ were measured in medium-dense sand. For example, in medium-dense sand at r/r_p = 3.2, θ was 10° less than the value measured in dense sand, but the difference in θ was only 4° close to the pile shaft.

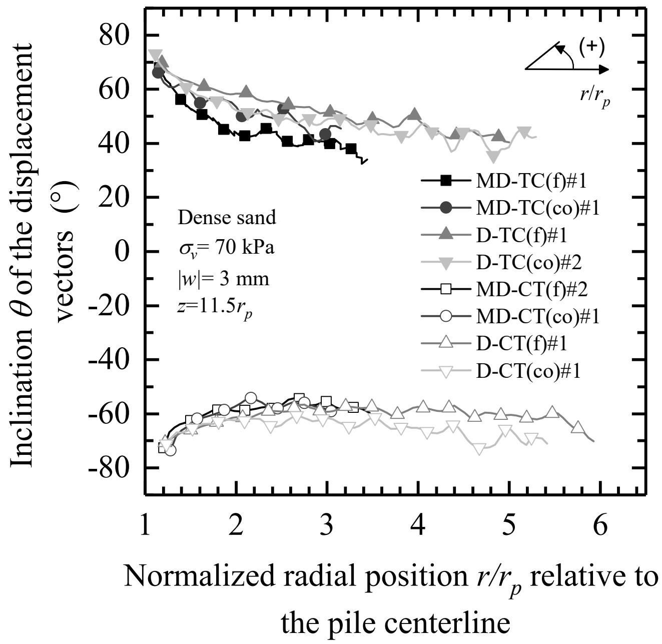

Figure 3.6. Inclination θ of the displacement vectors versus normalized radial position r/r_p relative to the pile centerline for FTLs after $|w|$=3 mm.

The average inclination θ_{avg} of the displacement vectors was calculated for compressive and tensile loading tests at $|w|$ = 3 mm in a zone limited by $1.15 < r/r_p < 2.0$ and $8.5 < z/r_p < 20.5$, using its magnitude as weighting factor. The results are summarized in Table 3.4. The magnitudes of θ_{avg} for tensile and compressive loading tests were comparable in dense sand, confirming the previous observation from Figure 6; near and along the pile shaft, where the displacements were maximum, the displacement vectors were oriented at an average angle of 65° in tensile loading and -66° in compressive loading. For medium-dense sand, the value of $|\theta_{avg}|$ tended to differ by about 10°. No effect of the base geometry on the direction of the displacement vectors of the soil elements was observed.

Table 3.5. Average inclination θ_{avg} of the displacement vectors for FTLs on dense and medium-dense sand using model piles with flat and conical bases after $|w|$ = 3.0 mm

Test	θ_{avg} (º) from FTL	Test	θ_{avg} (º) from FTL
D-TC(f)#1	61.1	D-CT(f)#2	-65.2
MD-TC(f)#1	56.0	MD-CT(f)#1	-63.6
D-TC(co)#1	63.5	D-CT(co)#1	-65.0
MD-TC(co)#1	54.0	MD-CT(co)#1	-64.7

Note: θ_{avg} = average inclination of the displacement vectors within a zone limited by 1.15 < r/r_p < 2.0 and 8.5 < z/r_p < 20.5. Positive angles are measured counterclockwise and clockwise from the r/r_p -axis on the right and left side of the pile, respectively.

Figure 3.7 shows the contours of the cumulative vertical displacements v (positive when soil elements move up and negative when they move down) developed after an absolute value of pile head displacement $|w|$ of 15 mm for FTL in tests with the flat-base model pile. The contours shown in Figure 3.7, Figure 3.9, Figure 3.11, and Figure 3.14 are plotted in the h/r_p versus r/r_p space, where h is the vertical distance of a soil element from the pile base (h = 0 at the pile base, positive above the pile base, and negative below the pile base). Figure 3.7 shows that the magnitude of the vertical displacement decreased with increasing distance from the pile shaft. Vertical displacements tended to be larger in compressive loading than in tensile loading, with the difference increasing with increasing relative density

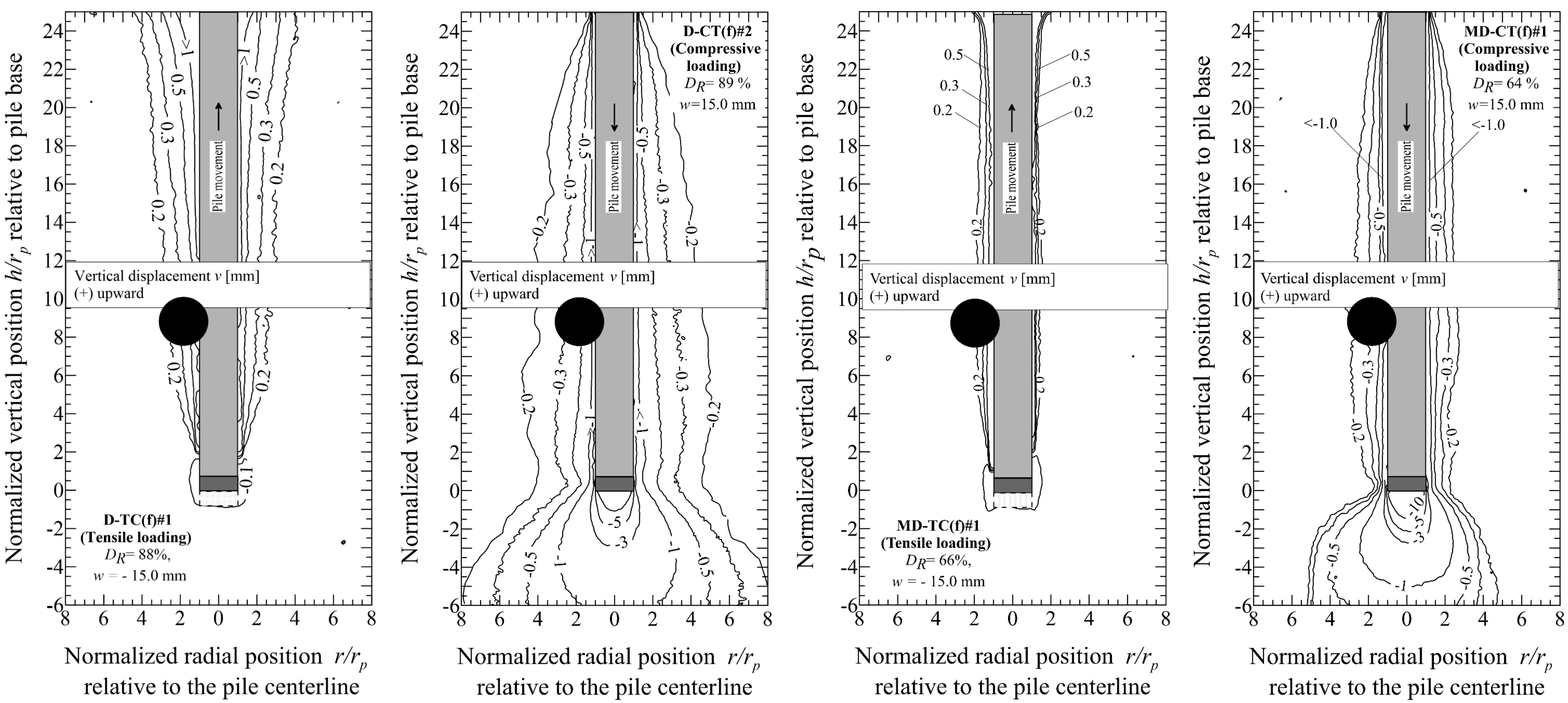

(a) (b) (c) (d)

Figure 3.7. Cumulative vertical displacement v field after 15 mm of pile head displacement w (negative for tensile loading and positive for compressive loading) for (a) tensile loading in test D-TC(f)#1; (b) compressive loading in test D-CT(f)#2; (c) tensile loading in test MD-TC(f)#1; and (d) compressive loading in test MD-CT(f)#1.

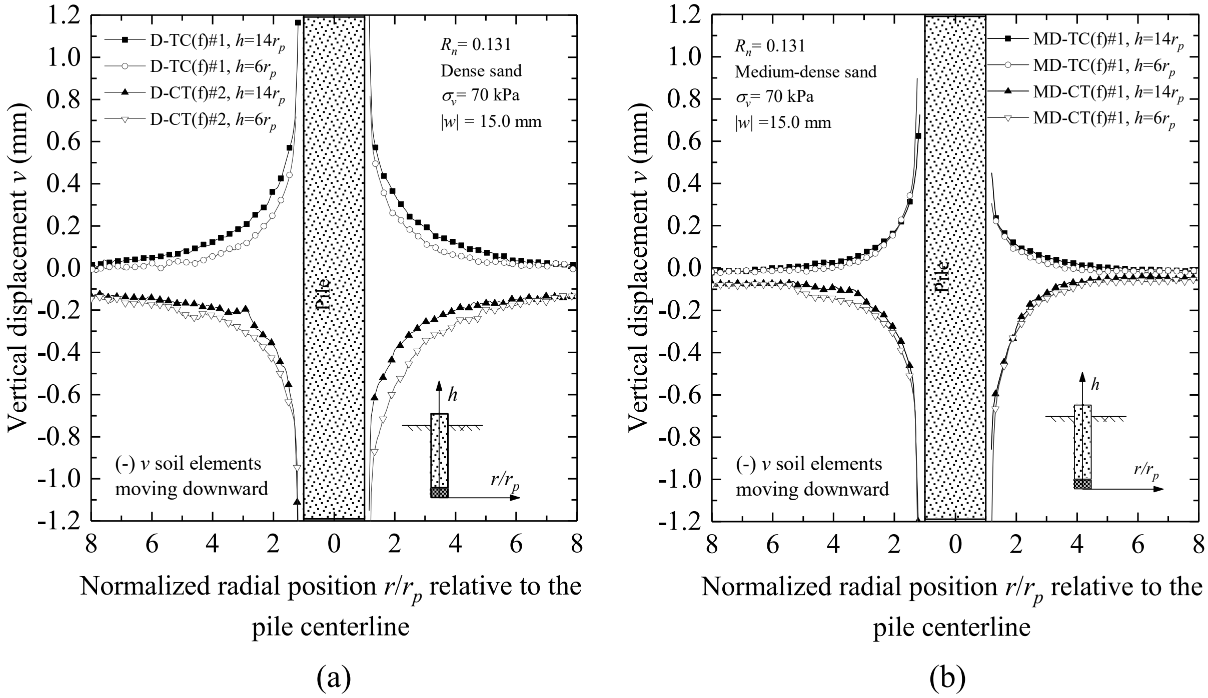

Figure 3.8. Vertical displacement v profiles at h/r_p = 6 and 14 and after $|w|$=15 mm for FTL tests performed on: (a) dense; and (b) medium-dense sand samples.

Figure 3.8 shows the vertical displacement v of elements located at h/r_p = 6 and 14 versus normalized distance r/r_p from the pile centerline. Vertical displacements with magnitude greater than 0.2 mm did not extend beyond $r = 3.0r_p$ and $2.0r_p$ for dense and medium-dense sand, respectively. Figure 3.8(a) shows that, for dense sand, the magnitude of the vertical displacement at a given r/r_p tended to increase with increasing h/r_p for tensile loading, while the opposite happened for compressive loading. In medium-dense sand, the differences between the magnitude of v at h/r_p = 6 and 14 for a given r/r_p distance was smaller ($|\Delta v|$ less than 0.02 mm on average) than the differences measured in dense sand ($|\Delta v|$ up to 0.1 mm).

Figure 3.9 shows the contours of cumulative radial displacement u (positive when soil elements move away from the pile shaft and negative when they move towards it) after an absolute value of the pile head displacement $|w|$ equal to 15 mm for the FTL in tests with the flat-base model pile. The soil elements surrounding the pile shaft move radially away from it in both tensile and compressive loading and for both dense and medium-dense sand.

Figure 3.10 shows the profiles of radial displacement u of soil elements located at a normalized distance h/r_p = 6 and 14 versus the normalized radial distance r/r_p from the pile centerline. The magnitudes of u were maximum near the pile shaft (approximately 0.32 mm for both tensile and compressive loading in dense sand) and decreased with increasing r/r_p, at a higher rate in medium-dense sand than in dense sand. Along the pile shaft (in a zone delimited by $6 < h/r_p < 14$), the differences between the radial displacements developed during compressive and tensile loading are minimal.

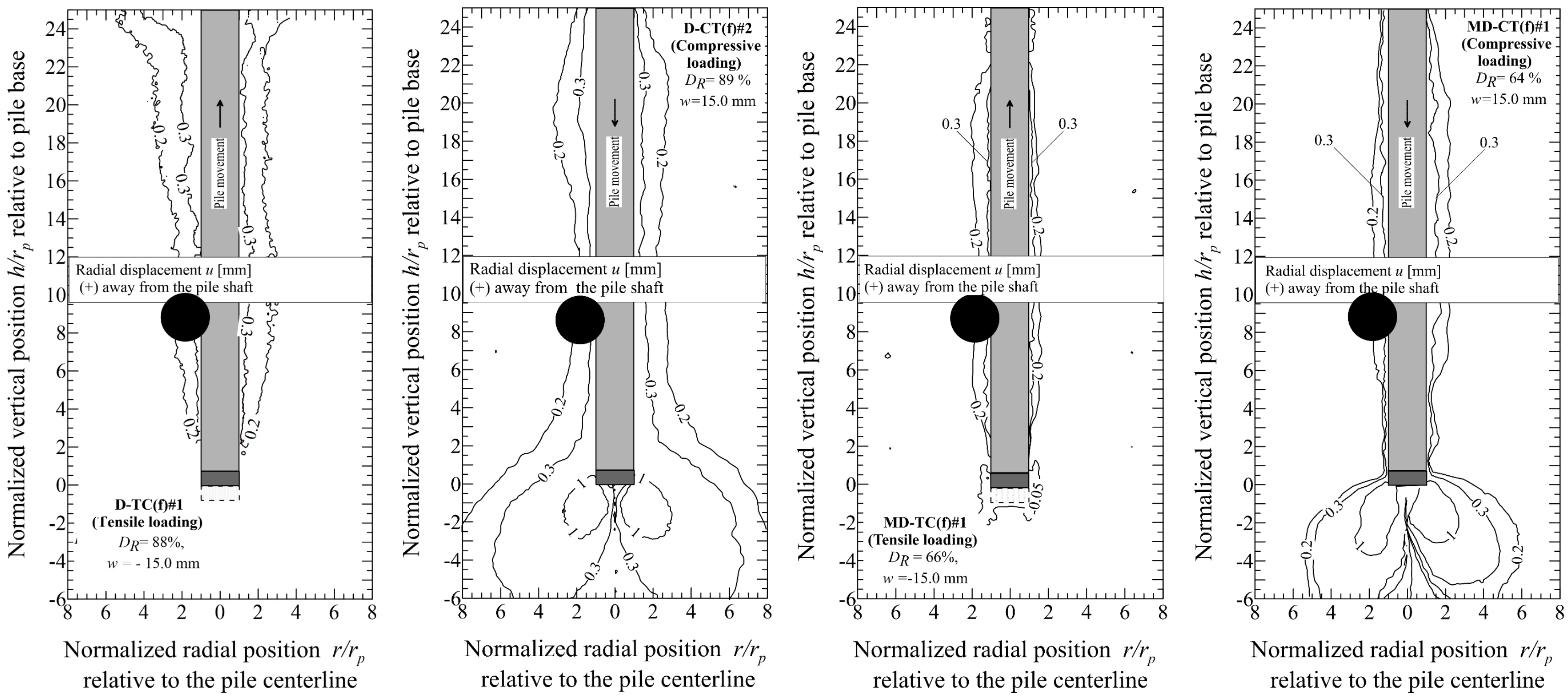

(a) (b) (c) (d)

Figure 3.9. Cumulative radial displacement u after 15 mm pile head displacement w (negative for tensile loading and positive for compressive loading) for (a) tensile loading stage of test D-TC(f)#1; (b) compressive loading stage of test D-CT(f)#2; (c) tensile loading stage of test MD-TC(f)#1; and (d) compressive loading stage of test MD-CT(f)#1.

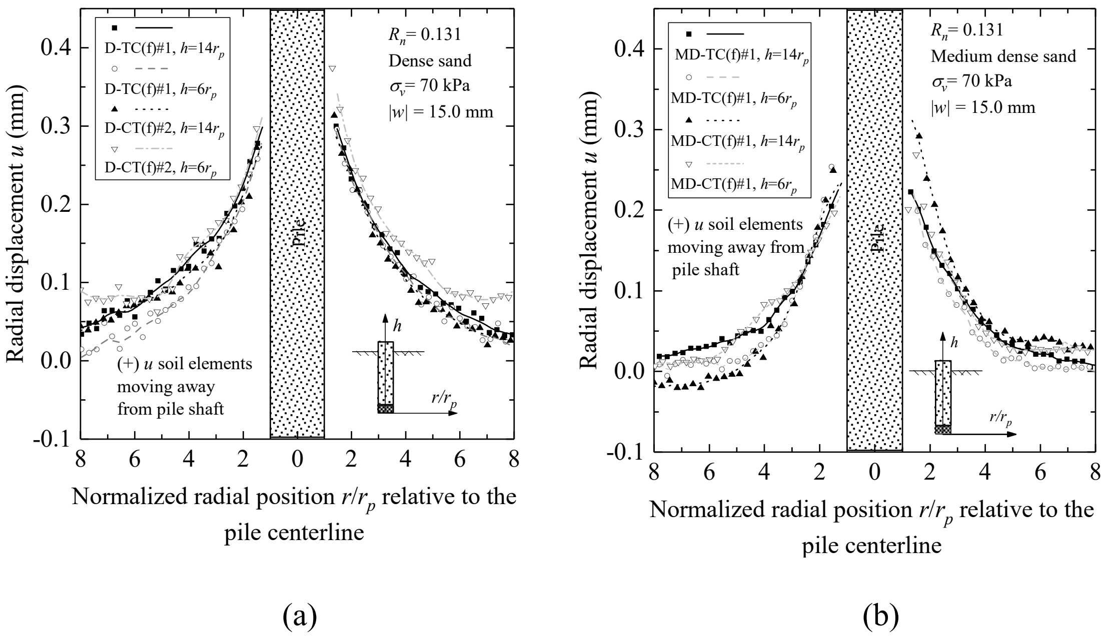

Figure 3.10. Radial displacement u profiles at h/r_p = 6 and 14 and after $|w|$ =15 mm for FTLs performed in (a) dense; and (b) medium-dense sand samples.

Table 3.6 and Table 3.7 contain the values of radial and vertical displacements accumulated after $|w|$ =15 mm for FTL tests at different radial distances r/r_p from the pile centerline. The values of u reported in Table 3.6 were obtained as the average of u on the right and the left side of the pile shaft, both at the same radial distance r/r_p. A similar approach was followed to obtain the values of v reported in Table 3.7. For a given r/r_p position, the value of radial displacement u is always higher in dense [u = 0.32 mm at r/r_p =1.2 for the FTL in test D-CT(f)#2] than in medium-dense sand [u = 0.24 mm at r/r_p =1.2 for the FTL in test MD-CT(f)#1]. At similar r/r_p positions and relative densities, the values of u from tensile loading were approximately the same as those from compressive loading [i.e., for tests D-TC(f)#1 and D-CT(f)#2, u = 0.32 mm at r/r_p =1.2].

Table 3.6. Cumulative vertical displacement v (mm) after $|w|$ = 15 mm at h/r_p = 14 and at different normalized radial position r/r_p

r/r_p	v (mm)			
	Test D-TC(f)#1	Test D-CT(f)#2	Test MD-TC(f)#1	Test MD-CT(f)#1
1.2	1.000	-0.945	0.547	-0.996
1.25	0.825	-0.891	0.464	-0.859
1.3	0.638	-0.651	0.394	-0.744
1.35	0.625	-0.652	0.337	-0.646
1.4	0.549	-0.583	0.292	-0.567
1.45	0.551	-0.573	0.260	-0.509
1.5	0.535	-0.550	0.243	-0.472
1.55	0.487	-0.524	0.230	-0.449
1.6	0.491	-0.485	0.218	-0.428
1.65	0.439	-0.505	0.206	-0.407
1.7	0.437	-0.476	0.194	-0.387
1.75	0.418	-0.468	0.184	-0.368
1.8	0.401	-0.452	0.173	-0.351
1.85	0.386	-0.411	0.164	-0.335
1.9	0.376	-0.428	0.156	-0.320
1.95	0.371	-0.387	0.148	-0.304
2	0.347	-0.385	0.141	-0.289
2.2	0.303	-0.340	0.117	-0.239
2.4	0.270	-0.321	0.101	-0.202
2.6	0.235	-0.299	0.087	-0.175
2.8	0.218	-0.228	0.073	-0.159
3	0.196	-0.237	0.059	-0.133
3.2	0.175	-0.237	0.050	-0.111
3.4	0.162	-0.218	0.040	-0.093
3.6	0.143	-0.217	0.034	-0.095
3.8	0.131	-0.204	0.026	-0.086
4	0.122	-0.194	0.021	-0.080
4.2	0.107	-0.184	0.020	-0.084
4.4	0.094	-0.185	0.018	-0.079
4.6	0.091	-0.169	0.012	-0.073
5	0.079	-0.166	0.006	-0.065
5.5	0.053	-0.161	0.001	-0.060
6	0.037	-0.149	-0.004	-0.059
6.5	0.032	-0.141	-0.008	-0.058
7	0.027	-0.134	-0.014	-0.065
8	0.013	-0.133	-0.020	-0.069

Table 3.7. Cumulative radial displacement u (mm) after $|w|$ = 15 mm at h/r_p = 14 at different normalized radial position r/r_p

r/r_p	u (mm)			
	Test D-TC(f)#1	Test D-CT(f)#2	Test MD-TC(f)#1	Test MD-CT(f)#1
1.2	0.316	0.321	0.238	0.243
1.25	0.310	0.313	0.230	0.244
1.3	0.304	0.306	0.223	0.244
1.35	0.298	0.298	0.225	0.242
1.4	0.293	0.290	0.225	0.240
1.45	0.287	0.283	0.223	0.236
1.5	0.282	0.276	0.212	0.232
1.55	0.276	0.270	0.208	0.227
1.6	0.271	0.263	0.202	0.220
1.65	0.266	0.257	0.194	0.212
1.7	0.261	0.251	0.191	0.204
1.75	0.256	0.245	0.189	0.197
1.8	0.251	0.239	0.182	0.190
1.85	0.247	0.233	0.182	0.184
1.9	0.242	0.228	0.176	0.178
1.95	0.237	0.223	0.171	0.173
2	0.233	0.218	0.166	0.168
2.2	0.216	0.201	0.149	0.153
2.4	0.201	0.186	0.133	0.141
2.6	0.187	0.168	0.125	0.130
2.8	0.174	0.153	0.109	0.118
3	0.164	0.142	0.102	0.105
3.2	0.155	0.135	0.093	0.094
3.4	0.147	0.132	0.081	0.085
3.6	0.138	0.127	0.075	0.077
3.8	0.131	0.117	0.065	0.069
4	0.123	0.107	0.057	0.064
4.2	0.116	0.098	0.052	0.057
4.4	0.109	0.090	0.051	0.048
4.6	0.103	0.084	0.040	0.044
5	0.092	0.078	0.042	0.036
5.5	0.077	0.069	0.040	0.025
6	0.065	0.058	0.027	0.022
6.5	0.057	0.049	0.021	0.020
7	0.050	0.042	0.017	0.019
8	0.038	0.035	0.009	0.015

A rough estimation of the soil stiffness can be carried out by using an expression deduced from cavity expansion analysis, which relates the increase in radial stress $\Delta\sigma'_h$ to the radial expansion u of the soil (Boulon and Foray 1986; Lehane et al. 2005a). Based on the radial displacement u exhibited by the closest soil element to the pile shaft (see Table 3.7), we obtained that the equivalent normal stiffness k_n ($=\Delta\sigma'_h/u$) (Lehane et al. 2005) is 2 times higher in dense sand than in medium-dense sand.

3.4.4.2 Radial strains from first-time loadings (FTLs)

Figure 3.11 shows the values of the cumulative radial strain E_{rr} in the soil around the model pile with the flat base after a pile head displacement equal to 15 mm (pointing up for tensile and down for compressive loading) for dense and medium-dense sand. Radial and shear strains were obtained from the Green-St. Venant strain tensor using the continuum mechanics functions implemented in the postprocessing tool of VIC2D. Positive values of E_{rr} indicate radial stretching, whereas negative values of E_{rr} indicate radial contraction. As shown in Figure 3.11, at $|w|$ = 15 mm, soil elements located along a thin band adjacent to the pile shaft, bounded by $r/r_p < 1.4$ and $4 < h/r_p < 20$, stretched radially ($E_{rr} > 0$) for both the tensile and compressive loading directions. In compressive loading, the stretching of the soil elements developed evenly along almost the entire length of the pile shaft, whereas in tensile loading, the thickness of the band was more irregular along the shaft. Outside this zone ($r/r_p > 1.4$ and $4 < h/r_p < 20$), the soil elements contracted radially for both loading directions. Although greater radial stretching of the soil elements within the shear band were expected (Han et al. 2017; Salgado 2008), the DIC results are not available for $r/r_p <$ 1.15 next to the pile shaft.

Figure 3.12 shows the cumulative radial strain E_{rr} of soil elements (for which $6 < h/r_p < 16$) versus the normalized radial distance r/r_p from the pile centerline at $|w|$= 15 mm for first-time tensile and compressive loading tests performed in dense and medium-dense sand samples. For each test shown in Figure 3.12 – D-TC(f)#1, D-CT(f)#1, MD-CT(f)#1 and MD-CT(f)#1 – the average E_{rr} profile (estimated by averaging, for a given r/r_p distance, the values of E_{rr} between $6 < h/r_p < 16$) is also included in Figure 3.12. The results show that the radial strain profiles for compressive and tensile loading tests were very similar. Soil elements stretched radially near the shaft at $r/r_p < 1.51$ ($r-r_p = 8.10$ mm) in dense sand and at $r/r_p < 1.38$ ($r-r_p = 6.03$ mm) in medium-dense sand, while soil elements contracted radially within $1.51 < r/r_p < 6.0$ (8.10 mm $< r-r_p <$ 79.38 mm) in dense sand and within $1.38 < r/r_p < 5.08$ (6.03 mm $< r-r_p <$ 64.77 mm) in medium-dense sand samples.

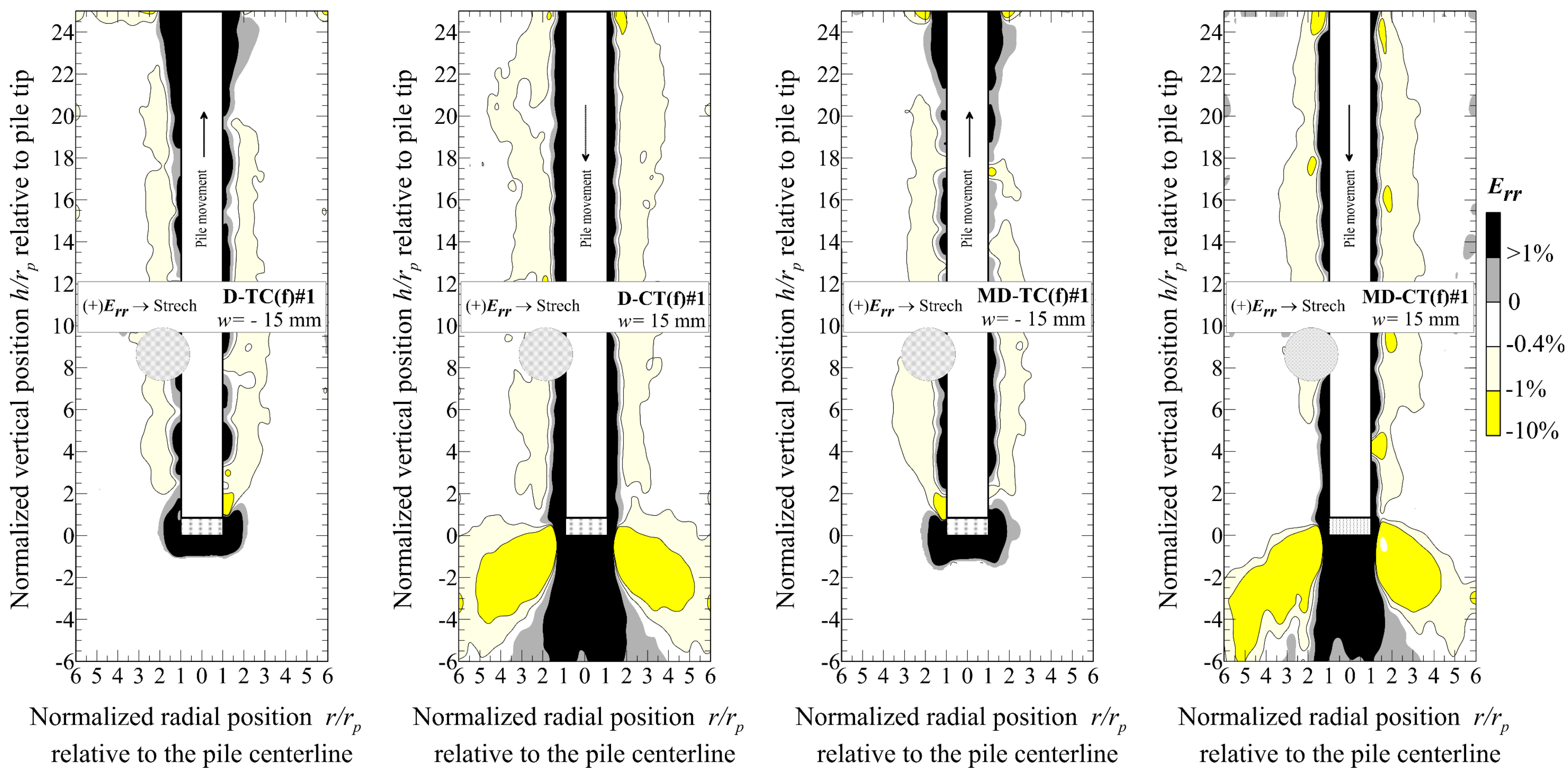

(a) (b) (c) (d)

Figure 3.11. Radial strain E_{rr} field after 15mm of pile head displacement w (negative for tensile loading and positive for compressive loading) for (a) tensile loading in test D-TC(f)#1; (b) compressive loading in test D-CT(f)#1; (c) tensile loading in test MD-TC(f)#1; and (d) compressive loading in test MD-CT(f).

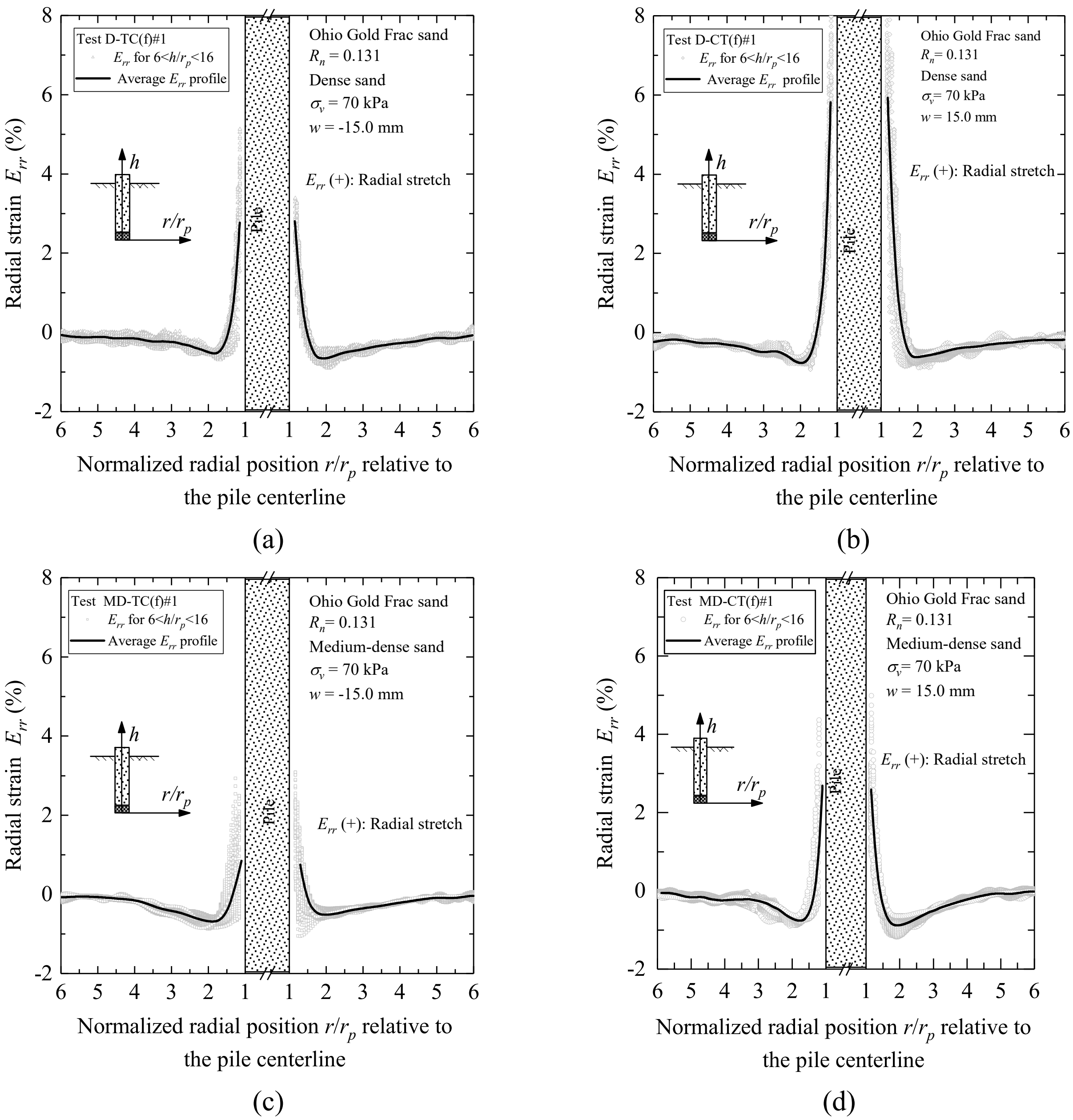

Figure 3.12. Radial strain E_{rr} profile after 15 mm of pile head displacement w (negative for tensile loading and positive for compressive loading) for (a) tensile loading in test D-TC(f)#1; (b) compressive loading in test D-CT(f)#1; (c) tensile loading in test MD-TC(f)#1; and (d) compressive loading in test MD-CT(f)#1.

Figure 3.13 shows the evolution of radial strain E_{rr} for two soil elements, located at r/r_p =1.25 (r-r_p = 3.97 mm) and r/r_p =2.5 (r-r_p = 23.81 mm) and z/r_p = 11.5, with increasing $|w|$ for the tensile loading phases of tests D-TC(f)#1 and MD-TC(f)#1 and the compressive loading phases of tests D-CT(f)#1 and MD-CT(f)#1. In samples of similar relative densities, the E_{rr} versus $|w|$ curves for the two soil elements for first-time tensile loading were comparable to those for first-time compressive loading. Figure 3.13(a) shows that, close to the pile shaft, at r/r_p =1.25, the soil elements stretched radially as the value of $|w|$ increased during first-time tensile and compressive loading tests. Farther away radially from the pile shaft, at r/r_p = 2.5 [Figure 3.13(b)], the soil elements contracted radially for $|w|$ < 3.5 mm; for $|w|$ > 3.5 mm, the rate of radial deformation decreased for both tensile and compressive loading and tended to stabilize with increasing $|w|$.

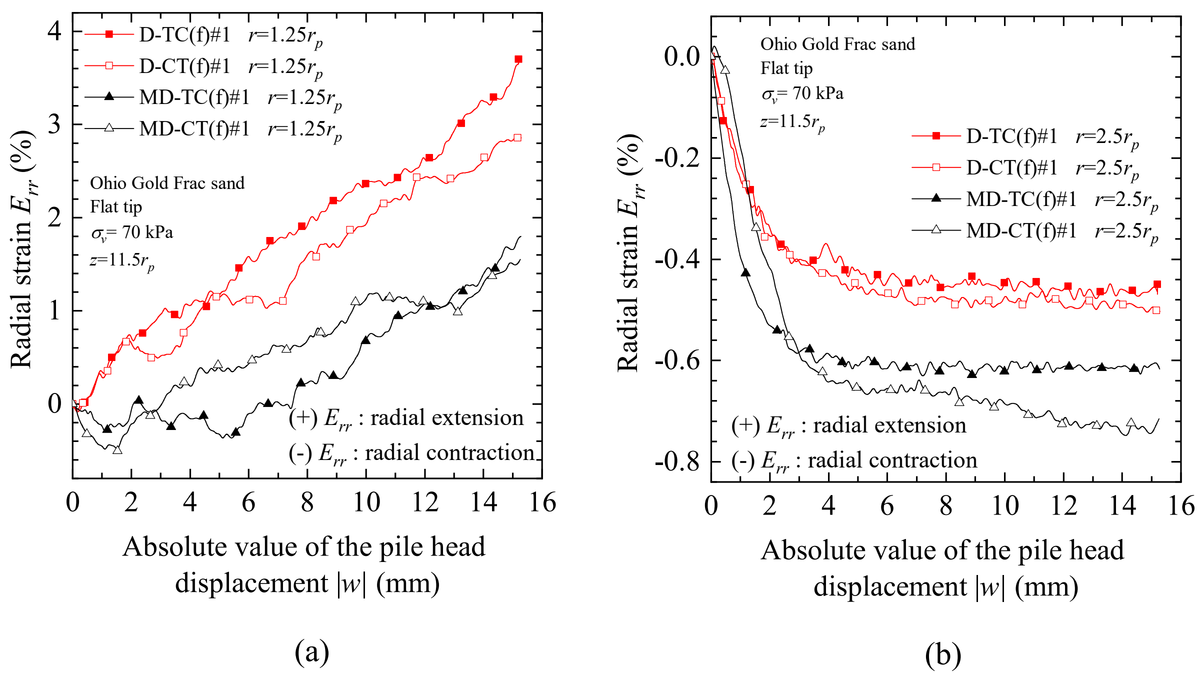

Figure 3.13. Radial strain E_{rr} versus absolute value of pile head displacement $|w|$ of soil elements at z =11.5r_p and (a) r/r_p = 1.25, (b) r/r_p = 2.5.

Figure 3.14 shows the spatial distribution of the shear strain E_{rz} accumulated after an absolute value of pile head displacement $|w|$ equal to 3 mm for first-time tensile and compressive loading for dense and medium-dense sand. The sign of the shear strain E_{rz}, adopted to describe the direction in which the soil distorts in compressive or tensile loading, is based on the concept of increase or reduction of an initially right angle. As shown in (Salgado 2008), a simple way to identify the right angle that must be used to set the shear strain sign is to first visualize a soil element in the r, z- plane on the right side of the model pile. Then, we locate an uppercase Greek letter Γ at one of the corners of the soil element so that the vertical leg of Γ is parallel to the z-axis, and the horizontal leg of Γ is parallel to the r-axis. The shear strain is positive when the right angle of the uppercase Greek letter Γ increases and is negative when the right angle decreases. On the left side of the model pile, the sign of the shear strain is the same as the sign defined for the *r*, *z*- plane on the right side of the model pile. For dense sand samples, the maximum magnitude of the shear strain ($|E_{rz}| > 1.0\%$) developed within a band around the pile shaft extending to practically the same radial distance in tensile and compressive loading (r/r_p values of approximately 1.92 and 1.88 mm, respectively).

Figure 3.15 shows the profiles of $|E_{rz}|$ for soil elements located at $h/r_p = 14$ versus the normalized radial distance r/r_p from the pile centerline accumulated after $|w| = 3.0$ mm. Profiles of $|E_{rz}|$ were used to facilitate the comparison between $|E_{rz}|$ behavior in tensile and compressive loading tests. The results show that, for similar relative densities, the $|E_{rz}|$ profiles for compressive and tensile loadings were almost identical. The magnitudes of E_{rz} were highest close to the pile shaft; for $r/r_p = 1.25$, $|E_{rz}| = 3.0\%$ on average for dense sand and $|E_{rz}| = 2.7\%$ on average for medium-dense sand. As r/r_p increased, $|E_{rz}|$ decreased at similar rates for tensile and compressive loading tests, but at a lower rate in medium-dense than in dense sand samples.

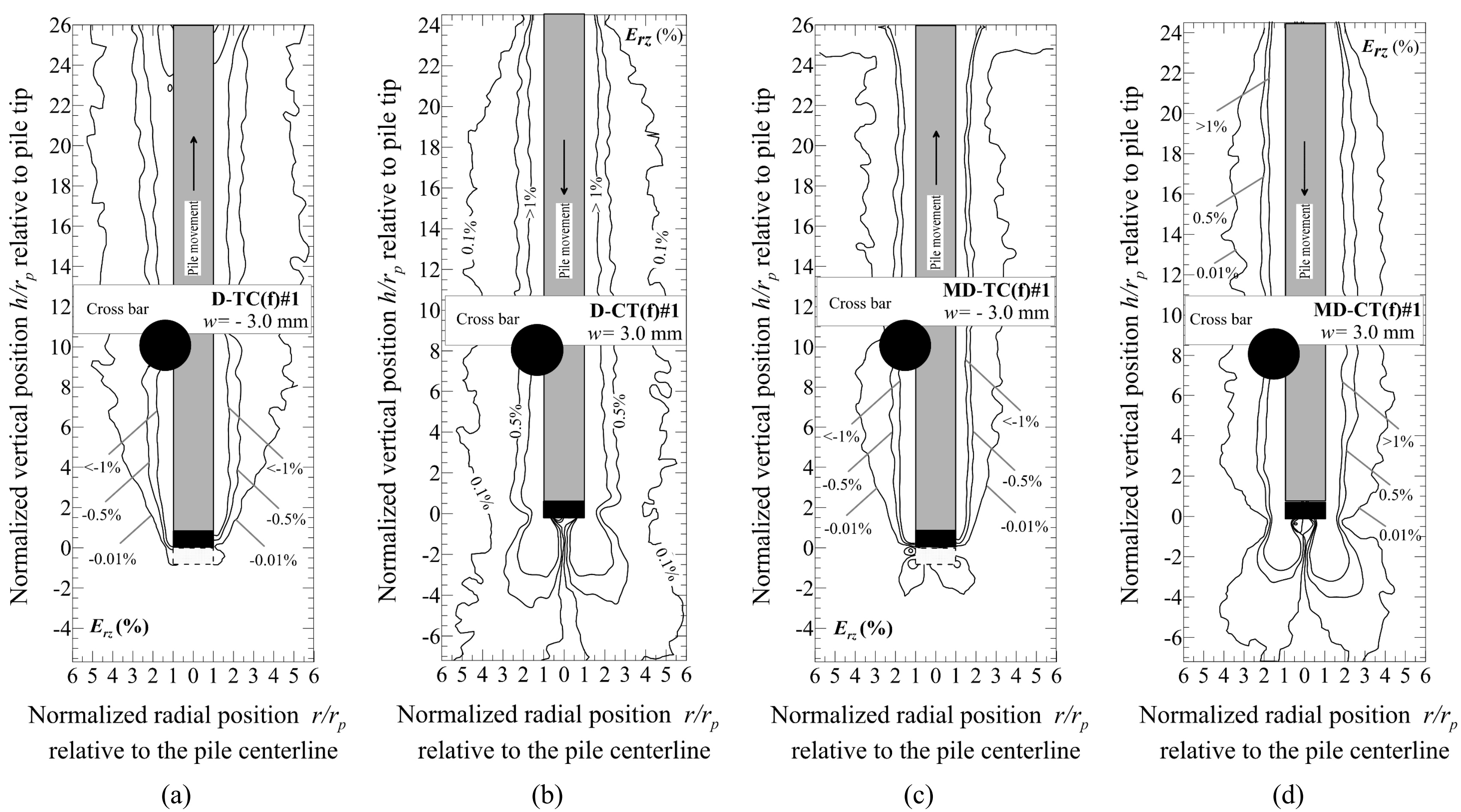

Figure 3.14. Shear strain E_{rz} after 3 mm of pile head displacement w (negative for tensile loading and positive for compressive loading) for (a) tensile loading in test D-TC(f)#1; (b) compressive loading in test D-CT(f)#1; (c) tensile loading in test MD-TC(f)#1; and (d) compressive loading in test MD-CT(f)#1

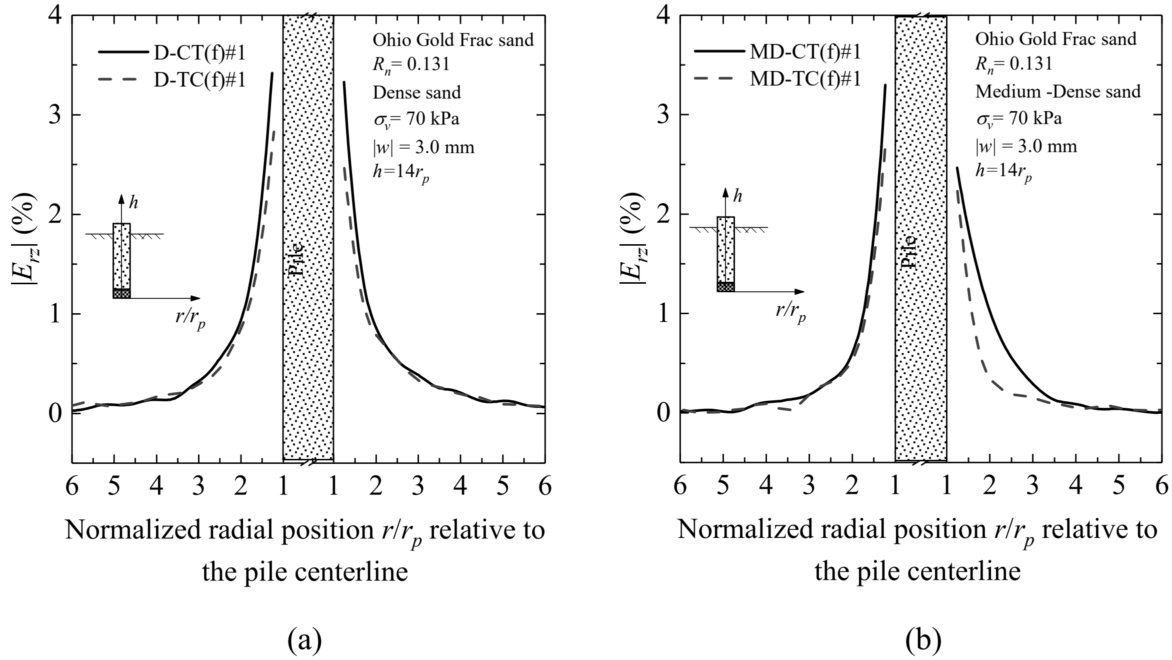

Figure 3.15. The $|E_{rz}|$ profiles of soil elements at h/r_p=14 after 3 mm of pile head displacement for FTL tests in (a) dense sand; and (b) medium-dense sand.

Figure 3.16 shows the evolution of the shear strain E_{rz} of soil elements located at a depth z/r_p of 11.5 and at two different radial distances from the pile shaft with increasing $|w|$. The soil elements examined come from the tensile loading in tests D-TC(f)#1 and MD-TC(f)#1, and the compressive loading in tests D-CT(f)#1 and MD-CT(f)#1. As shown in Figure 3.16a), for tensile and compressive loading, the shear strain magnitude $|E_{rz}|$ of the soil elements at r/r_p =1.25 increased with increasing $|w|$. At a radial distance r/r_p = 2.5, as shown in Figure 3.16(b), $|E_{rz}|$ increased with $|w|$ in tensile and compressive loading tests, but at a lower rate than the rate exhibited by the elements located closer to the pile shaft. The magnitude of E_{rz} stayed relatively constant for $|w|$>3.5 mm, occurring at more or less the same value of $|w|$ at which the peak in shaft resistance was observed. The radial and shear strain magnitudes and their behavior with increasing $|\Delta w|$ were comparable for tensile and compressive loading tests performed in samples with the same relative densities, and thus support the near-to-one values found in the $SRR_{P,FTL}$ and $SRR_{L,FTL}$ ratios.

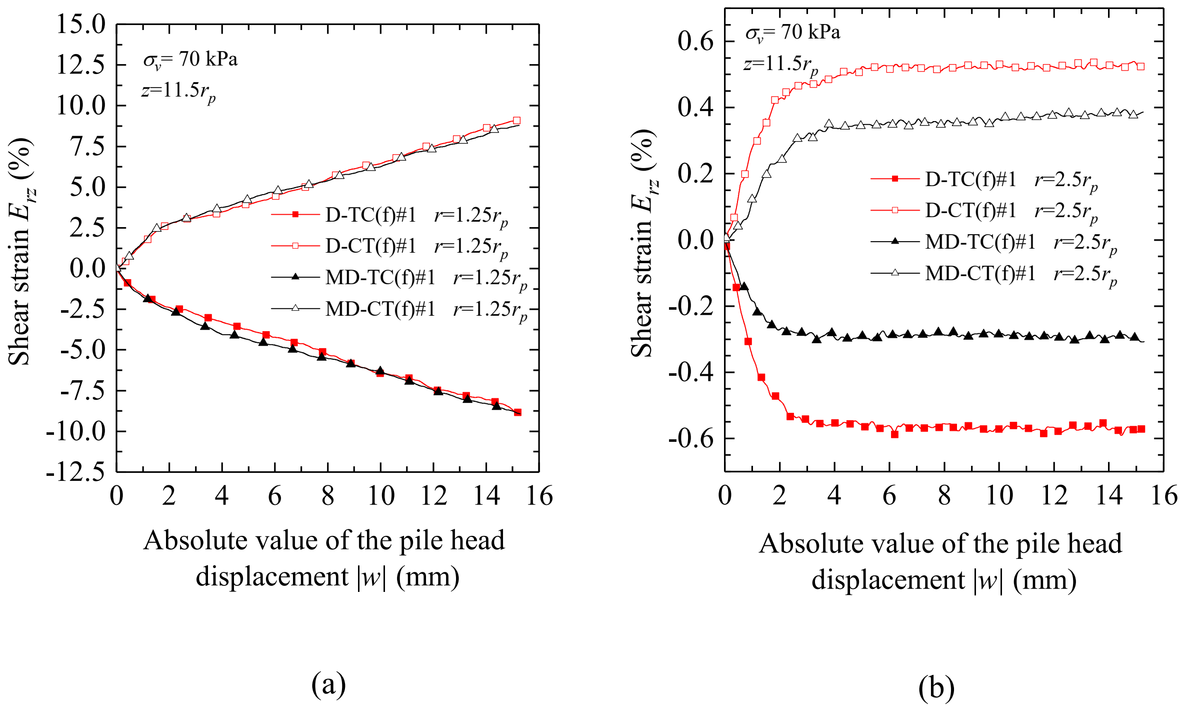

Figure 3.16. Shear strain E_{rz} versus absolute value $|w|$ of the pile head displacement for soil elements at z =11.5r_p and (a) r/r_p=1.25; and (b) r/r_p=2.5.

3.4.4.3 Volumetric strain during first-time loadings (FTLs)

Figure 3.17 shows the cumulative volumetric strain E_{vol} of soil elements located at a normalized depth z/r_p = 11.5 and radial position r/r_p =1.25 and 2.5 versus the absolute value of the pile head displacement $|w|$ for tensile and compressive loading tests in dense and medium-dense sand. The volumetric strain E_{vol} is calculated as

$$E_{vol} = \det \mathbf{F} - 1 = \prod_{i=1}^{3} \sqrt{1 - 2E_i} - 1 \tag{3.1}$$

where **F** = deformation gradient; and E_i (i = 1, 2, and 3) corresponds to the principal strains of the Green-Saint Venant strain tensor (Lubliner 2008). The principal strain E_1 and E_2 are obtained from the two-dimensional DIC analyses, and the E_3 component was estimated as $E_3 = 0.5[1-(1+ u/r)^2]$ (Tehrani et al. 2017). The sign of the principal strains E_1, E_2, and E_3 follow the solid mechanics sign convention — tensile strain is assumed positive, and compressive strain is assumed negative.

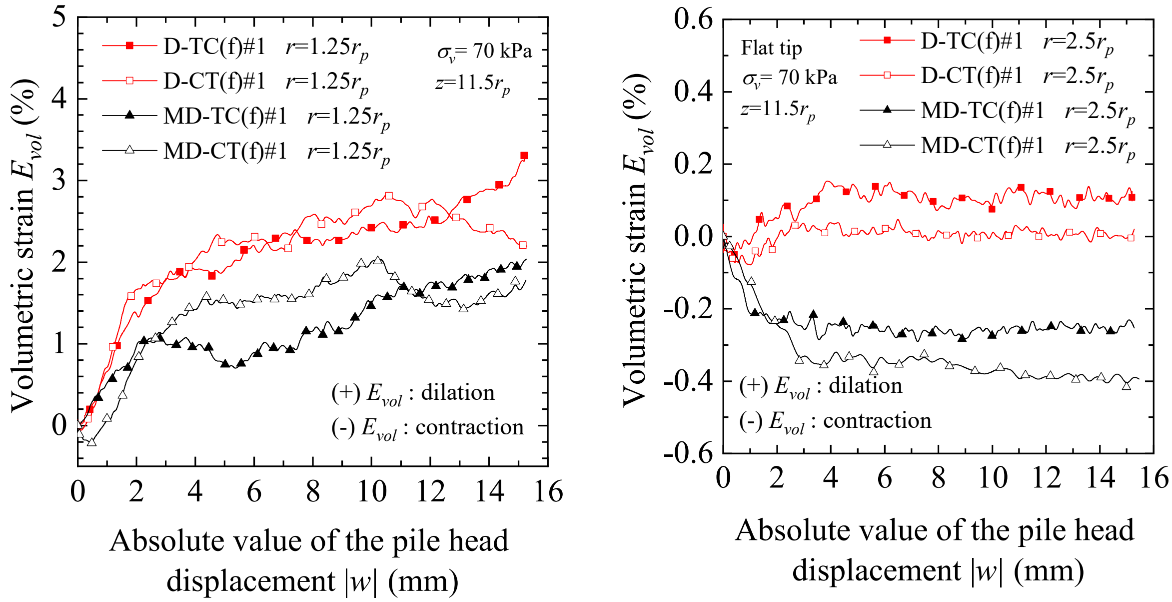

(a) (b)

Figure 3.17. Volumetric strain E_{vol} versus. absolute value |w| of the pile head displacement of soil elements at z = 11.5r_p and (a) r/r_p=1.25; and (b) r/r_p=2.5.

The volumetric strain results shown in Figure 3.17 confirm that dilation (positive values of E_{vol}) of the soil elements was highly localized to a thin band that extended radially to a distance r-r_p of approximately 9.5 mm (r/r_p = 1.6) and r-r_p of approximately 23.8 mm (r/r_p = 2.5) relative to the pile shaft in medium-dense and dense sand, respectively. In either compression or tensile loading, the soil elements at r/r_p = 1.25 dilated with a comparable volumetric strain E_{vol} for a given value of |w|. During the FTL tests, the magnitude of the volumetric observed in dense sand was slightly greater than that observed in medium-dense sand, all else being equal.

Figure 3.17(b) shows that, for dense sand, the soil elements at r/r_p = 2.5 first contracted modestly for |w|< 2.0 mm, and then tended to dilate slightly with the maximum rate of dilation occurring around |w| of approximately 3.5 mm. By contrast, with medium-dense sand, the soil elements exhibited only contractile behavior. For |w| > 4.0 mm, the soil elements reached approximately constant volumetric strain condition. For a given soil-element position next to the pile shaft, the differences between the volumetric strain behavior for first-time tensile and first-time compressive loading tests were negligible.

From the results shown in Figure 3.11 to Figure 3.17, three different regions adjacent to the model pile shaft can be identified: (1) a region between the pile shaft and the shear band (r/r_p < 1.2) in which large vertical displacement occurs; (2) an annulus-shaped region between 1.2 < r/r_p < 1.5 dominated by dilation of the soil elements; and (3) a region further away, radially, in which the soil elements undergo mainly radial contraction.

3.4.4.4 Inclination α of the principal strain E2 from first-time loading tests (FTLs)

Figure 3.18 shows the inclination α of the minor principal strain E_2 (i.e., E_2 is the largest compressive principal strain and E_1 is the largest tensile strain in the r,z-plane) versus the normalized radial position r/r_p relative to the pile centerline at a normalized depth z/r_p = 11.5 for first-time tensile and compressive loading tests in dense and medium-dense sand. Experimental investigation with simple and directional shear apparatus performed using sand and a photoelastic material (Arthur et al. 1977, 1981; Oda and Konishi 1974; Subhash et al. 1991; Wong and Arthur 1985) and discrete element method (DEM) analyses (Guo and Zhao 2013; Yimsiri and Soga 2010, 2011) have suggested that any plastic deformation in sand induces fabric anisotropy, even in soils with rounded particles. It is also accepted that the fabric evolves during any condition of loading and that its evolution depends on the rotation of principal stress direction (Gao and Zhao 2017; Li et al. 2018; Woo and Salgado 2015; Yang et al. 2016).

In these experiments, as the pile was being loaded for the first time, either by tensile or compressive loading, the soil elements surrounding the pile shaft started shearing vertically, resulting in the rotation of the principal strains E_1 and E_2. As shown in Figure 3.18, the minor principal strain E_2 of soil elements located close to the pile shaft, at r/r_p =1.25 (r-r_p = 3.97 mm), tilted −45.5° and +46.6° in compressive and tensile loading, respectively, with respect to the horizontal after $|w|$ = 3 mm, indicating that, independent of the loading direction, the principal strains in tensile and compressive loading rotate by the same amount but in opposite directions. For soil elements located farther away from the pile shaft, the rotation of the principal strains was smaller. At r/r_p = 4.5 (r-r_p = 55.56 mm), E_2 rotates by an angle of −21.5° and +22.6° with respect to the horizontal in compressive and tensile loading, respectively. The behavior of the principal strains along the pile shaft in tension and compression loading were in agreement with the results from the sensors presented previously, which showed negligible differences in peak and limit shaft resistance of model pile tested for the first-time loading in tension and compression(for samples with the same relative densities).

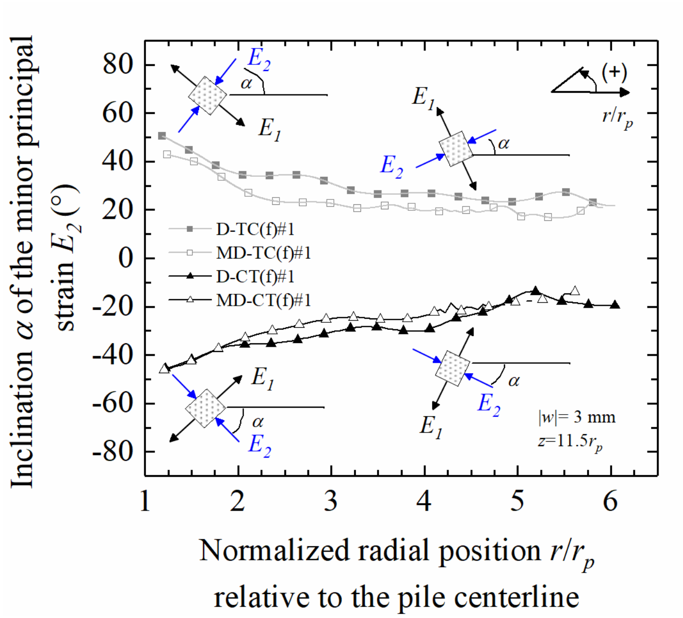

Figure 3.18. Inclination α of minor principal strain E_2 (most compressive strain in r,z- plan) versus normalized radial position r/r_p relative to the pile centerline of soil elements located at z/r_p = 11.5 and after $|w|$ = 3.0 mm for FTLs.

3.4.4.5 Evolution of the radial and shear strains and the inclination of the most compressive strain during CT and TC loading sequences

Figure 3.19 shows the cumulative shear strain E_{rz} of two selected soil elements during tensile-compressive [MD-TC(f)#2] and compressive-tensile [MD-CT(f)#2] loading tests performed in medium-dense sand samples. Two positions of the soil elements were chosen, one at r/r_p = 1.25, z/r_p = 11, and the other at r/r_p= 3.0, z/r_p= 11, on the right side of the pile. Figure 3.19(a) shows that, as the magnitude $|w|$ of the pile head displacement increased during the first-time tensile or compressive loading, the shear strain magnitude $|E_{rz}|$ also increased. As soon as the loading direction was reversed (the load reversal point LR is shown in Figure 3.19), E_{rz} started to decrease in the tensile loading phase of test MD-CT(f)#2 and increase in the compressive loading phase of test MD-TC(f)#2;these trends continued until the end of the STL.

Figure 3.19(b) shows the shear strain E_{rz} exhibited by the soil elements located at r/r_p= 3.0 and z/r_p= 11 during the CT and TC loading sequences. Although the loading direction was reversed for the STL, at this location, the sign of E_{rz} did not change, and the E_{rz} magnitude did not decrease significantly.

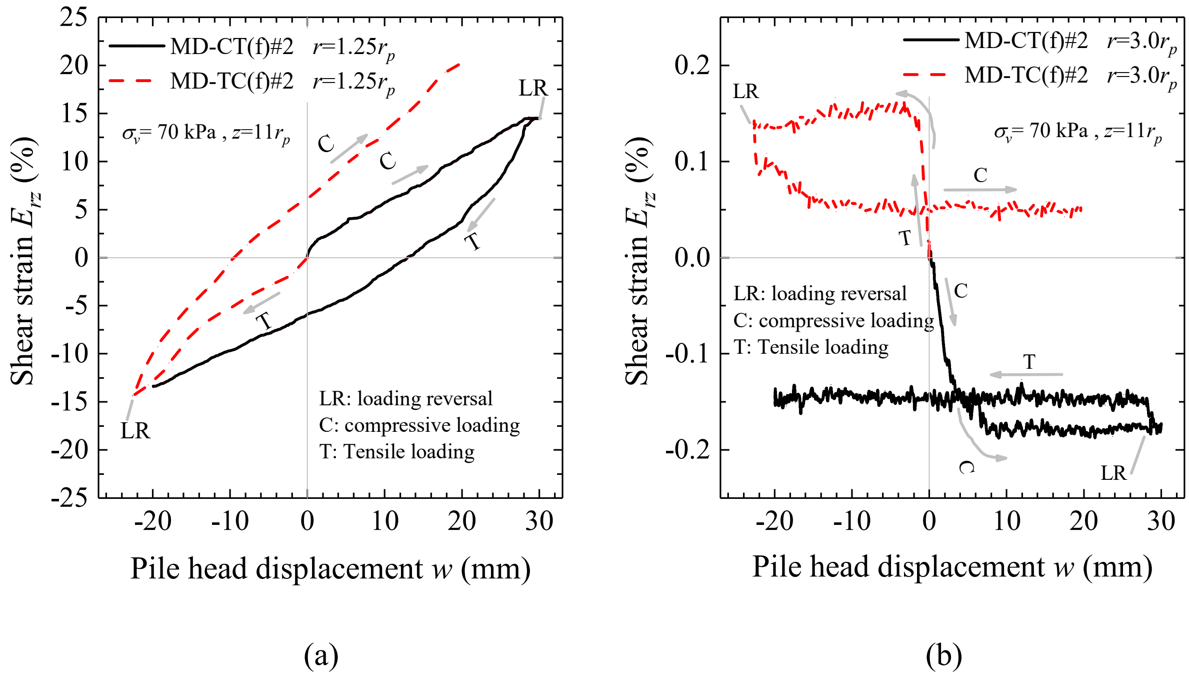

Figure 3.19. Shear strain E_{rz} evolution during CT and TC loading sequences of soil elements located at z =11r_p and: (a) r/r_p=1.25; (b) r/r_p=3.0.

Figure 3.20(a) and (b) show the strain paths in terms of the radial stress E_{rr} versus the shear strain E_{rz} for a soil element positioned at r/r_p = 1.25*,* z/r_p = 11 for CT and TC loading tests MD-CT(f)#2 and MD-TC(f)#2, respectively. During the FTL, in both compressive and tensile loading, the radial strain increment ΔE_{rr} was positive, indicating that soil elements dilate with increasing $|E_{rz}|$. The radial strain E_{rr} was maximum when the shear strain E_{rz} reached its maximum magnitude; this occurred at the end of the first-time loading. As soon as the loading was reversed (LR), the magnitude of the radial strain E_{rr} started to decrease until it reached a minimum value of E_{rr} of approximately 1% at E_{rz} = 0 in both the CT and TC loading sequences. The reduction of the radial strain exhibited by the soil elements in the vicinity of the pile shaft (r/r_p = 1.25*)* during the SLT resulted in a decrease in the radial stress, and, consequently, a reduction in the unit shaft resistance, as indicated by values of the unit shaft resistance degradation factor *D* below one. This mechanism is often referred to as friction degradation (Gavin and O'Kelly 2007; White and Bolton 2002;

White and Lehane 2004). Figure 3.20(a) and (b) also show that, after the shear E_{rz} returned to zero in the STL (E_{rr} reaches its minimum value E_{rr} of approximately 1%), the radial strain E_{rr} increased again until the end of the STL.

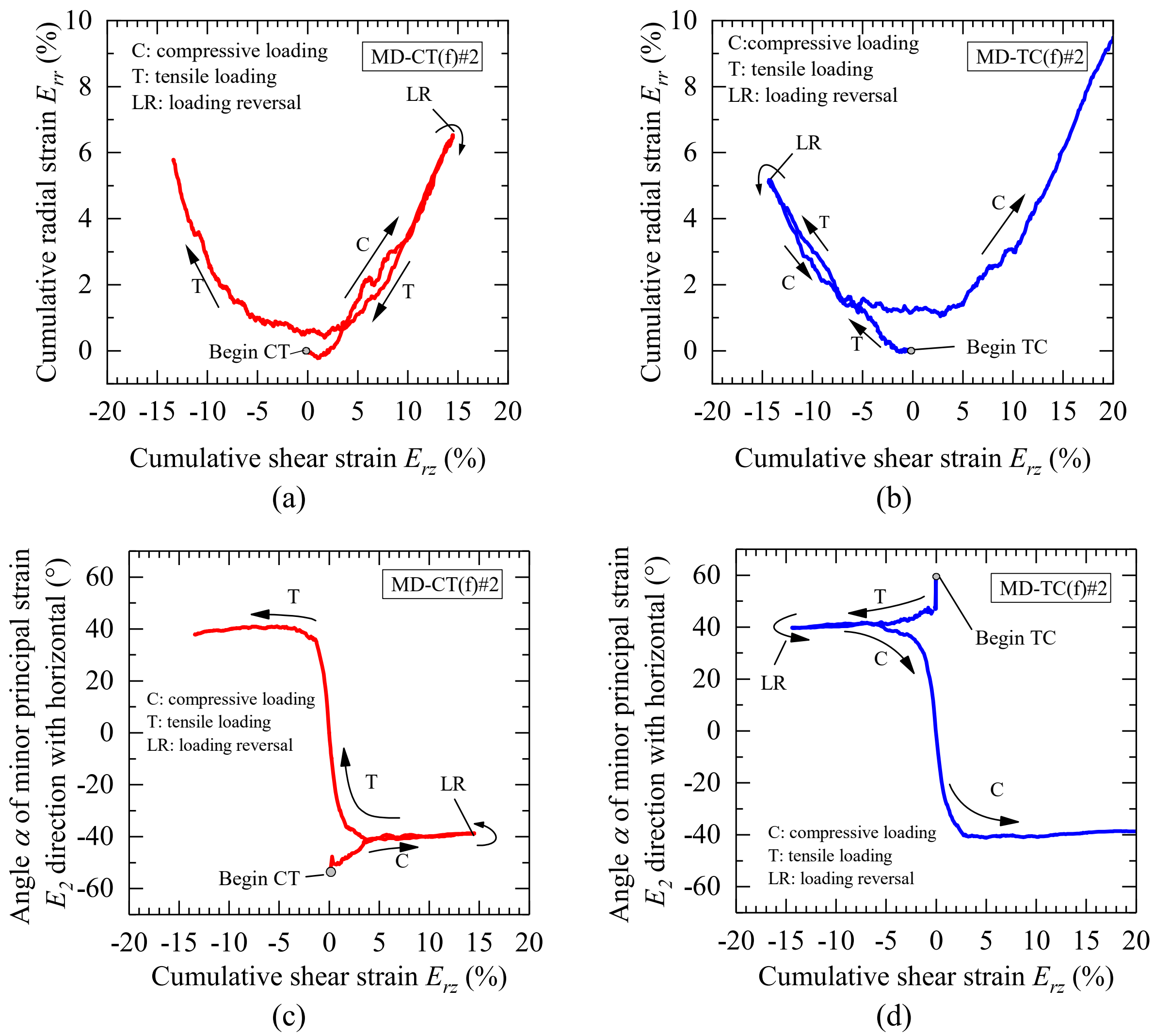

Figure 3.20. Strain paths for CT and TC loading sequences of soil elements located at r/r_p=1.25 and at z =11r_p: (a) E_{rr} versus E_{rz} for test MD-CT(f)#2; (b) E_{rr} versus E_{rz} for test MD-TC(f)#2; (c) α versus E_{rz} for test MD-CT(f)#2; (d) α versus shear strain E_{rz} for test MD-TC(f)#2.

Figure 3.20(c) and (d) show the angle α of the minor principal strain E_2 with the horizontal versus the shear strain E_{rz} of the same soil elements analyzed in Figure 3.20(a) and (b), respectively. During the compressive loading stage in test MD-CT(f)#2, the direction α of the principal strain E_2 had a minimum value of – 50.2° at low shear strain of E_{rz} = 0.6%, then increased slightly to –

41.2° at E_{rz} =4.0%, and remained constant until E_{rz} reached its maximum magnitude (E_{rz} = 14.5%). When the loading was reversed, α remained at a value of – 41.2° until the shear strain returned to E_{rz} = 4.0%. As E_{rz} continued to decrease, α gradually rotated 82.6° towards + 40.9° at E_{rz} = – 4.7. The inclination α = +40.9° remained approximately constant until the end of the tensile loading. A similar rotation of the minor principal strain direction occurred during the TC loading test, with the difference that α started with an inclination of + 46.7° at E_{rz} = - 0.6%, decreased to +41.7% at E_{rz} = - 4.0%, and gradually rotated −82.1° towards + 40.4° at E_{rz} = 3.4%. The inclination of the minor principal strain remained at a constant inclination of – 40.4° until the end of the second loading stage (compressive loading).

The similar values of shaft resistance degradation factor D found for the CT and TC loading sequences are supported by the fact that the E_{rr} versus E_{rz} and α versus E_{rz} paths in the CT loading test are nearly the mirror images of the corresponding paths for the TC loading test. This response can be attributed to the similar initial fabric (i.e., dry pluviation and one-dimensional consolidation) and the same mode of fabric evolution that soil elements experience during the CT and TC loading sequences.

3.4.4.6 Shear band

The formation of a shear band along the pile shaft is a key process in the development of the shaft resistance of axially loaded piles, and thus correct quantification of the thickness of the shear band is important for accurately capturing the mobilization of the unit shaft resistance (Fioravante et al. 2010b; Han et al. 2017; Loukidis and Salgado 2008; Tehrani et al. 2016). The study of the formation and development of shear bands along a structural element-soil interface in a quantitative manner has recently become possible through the development of image processing algorithms (such as DIC and discrete particle tracking algorithms). For the present experiments, the boundary of the shear band was defined using the particle tracking procedure described by Tovar-Valencia et al. (2018). This procedure consists in tracking at least 25 particles close to the shaft across digital images taken with a microscope as the pile is loaded. Once the model pile head has moved an absolute value of 15 mm, which is sufficient for full shaft resistance mobilization, the shear band thickness t_s is defined as the radial distance from the pile shaft to the radius at which particle movement in the direction of shearing drops sharply.

Table 3.8 shows the shear band thicknesses t_s measured during FTL and STL as a multiple of the mean particle size D_{50}. The values of t_s range from $3.5D_{50}$ to $4.2D_{50}$. Tehrani et al. (2016) reported similar values of shear band thickness (t_s =$3.2D_{50}$ in dense sand and t_s =$3.4D_{50}$ in medium-dense sand) developed during compressive loading of a nondisplacement pile with a comparable normalized surface roughness R_n= 0.098 [R_n as defined in Tovar-Valencia et al. (2018)].

The results shown in Table 3.8 also indicate that, for FTL, the shear band thickness developed for tensile loading was only 3.0% greater than for compressive loading in samples with similar relative densities. For STL, the difference between t_s in tensile and compressive loading increased slightly to 5.4%. In general, the shear band thickness t_s seems to be relatively insensitive to the loading direction. During STL, the thickness of the shear band decreases 4.4% on average with respect to the value of t_s measured during FTL in both the CT and TC loading tests performed in samples with similar relative densities.

Table 3.8. Thickness of the shear band developed after $|\Delta w|$ = 15 mm for the first-time and second-time loading of non-displacement model piles

Test code	Relative density D_R (%)	*FTL*		*STL*	
		t_s (mm)	t_s / $D_{50}^{(1)}$	t_s (mm)	t_s / $D_{50}^{(1)}$
D-CT(f)#1	93	2.3	3.7	2.2	3.5
D-TC(f)#1	89	2.3	3.7	2.3	3.7
MD-CT(f)#1	88	2.6	4.2	2.3	3.7
MD-TC(f)#1	90	2.5	4.0	2.4	3.9

Note: t_s =shear band thickness estimated by tracking of particles from an observation point at a depth z/r_p= 17.0 after $|\Delta w|$ = 15 mm in FTL and STL; D_{50} = mean particle size equal to 0.62 mm; FTL= first-time loading; STL= second time loading.

Based on the DIC analysis reported in Table 3.7, we estimate that the radial displacement u developed in the shear band is about $0.02r_p$ (= $3.94R_{max}$) in dense and $0.015r_p$ (= $2.96R_{max}$) in medium-dense sand.

3.4.4.7 Scale effects on shaft resistance

It is well known that, due to scale effects, a model-size pile with diameter less than a limiting value develops greater unit shaft resistance than a prototype pile under similar conditions (Foray et al. 1998; Lehane et al. 2005a; Loukidis and Salgado 2008). This scale effect on the shaft resistance of model piles is associated with the ratio t_s/B of the thickness of the shear band that forms adjacent to the pile shaft during axial loading to the pile diameter and the ratio B/D_{50} of the pile diameter to the mean particle size of the soil. Loukidis and Salgado (2008) and Salgado et al. (2017) performed one-dimensional finite-element analyses to study the effect of t_s/B on the value of the coefficient of lateral earth pressure K of nondisplacement piles. The results showed that, for t_s/B <0.01, the value of K was stable. Such results, if scale effects were a function only of the value of t_s/B, would imply that the magnitude of the limit unit shaft resistance q_{sL} for a model pile would be expected to be comparable to that of a full-scale pile.

The scale effect for model piles becomes important when $t_s/B > 0.01$, because the value of K increases with increasing t_s/B. Based on centrifuge model pile tests, Foray et al. (1998) and Fioravante (2002) suggested that scale effects on shaft resistance can be assumed to be negligible when the ratio B/D_{50} exceeds 200 [according to Foray et al. (1998)] or 50 [according to Fioravante (2002)]. These thresholds can be related to a threshold in terms of t_s/B if the shear band thickness is known.

From Table 3.8, the shear band thickness t_s for FTL in dense sand is 2.3 mm (= $3.7D_{50}$); therefore, the value of t_s/B corresponds to 0.072, which is greater than 0.01. This indicates that the values of q_{sL} reported in Table 3.3 cannot be directly applied to prototype scale. For t_s/B equal to 0.072, a correction factor of 0.62 (Loukidis and Salgado 2008) could be applied to the measured q_{sL} in order to obtain an estimate of q_{sL} for prototype conditions.

Because the shear band thickness t_s seems to be relatively insensitive to the loading direction, it is reasonable to assume that the degradation factor D as well as the tensile-to-compressive unit shaft resistance ratios $S_{RRP,FTL}$ and $S_{RRL,FTL}$ are not affected by the scale effects present in our results.

3.4.4.8 Surface roughness

Another aspect to be considered when using model piles to study prototype piles is the normalized surface roughness R_n (Garnier et al. 2007). Due to the high surface roughness of bored piles (made of cast-in-situ concrete) and the interlocking created between the concrete surface and sand particles during loading, shearing takes place within the soil and not at the soil-pile interface. Consequently, for nondisplacement piles, the interface can be assumed to be perfectly rough. In this case, the limit unit shaft resistance is controlled by the shear strength of the soil, and the interface friction angle takes the value of the mobilized friction angle. From interface direct shear tests, an interface becomes fully rough when the normalized roughness R_n exceeds 0.2 according to (Fioravante et al. 2010b), and this number could be higher (see, e.g., Tehrani et al. (2016)). The surface roughness of the model pile used in these experiments (R_n = 0.131) would not, according to these results, produce the maximum limit unit shaft resistance. However, the images collected during the experiments do show the shear band developing inside the soil mass, which is consistent with the concept of perfect roughness.

3.5 Summary and conclusions

This paper presented the results of a series of static load tests performed on model nondisplacement piles preinstalled in silica sand. Two different pile base geometries, a flat base and a conical base, were studied, both with similar surface roughness (normalized roughness R_n =0.131). Load tests were carried out in dense and medium-dense sand samples prepared in a half-cylindrical calibration chamber. Digital images of the pile and the surrounding sand were captured during static load tests and analyzed using the DIC technique. The piles were loaded in two different sequences: (1) tensile and then compressive loading (TC loading sequence) and (2) compressive and then tensile loading (CT loading sequence).

For both loading sequences, tension followed by compression (TC) or compression followed by tension (CT), reversal of the loading direction substantially reduces the unit shaft resistance. The shaft resistance degradation factor D was always less than 0.6 for both TC and CT loading sequences and tended to be slightly lower in CT than in TC loading, except when the pile head displacement magnitude during the first-time tensile loading exceeds 32 mm (approximately 1B). The relative density of the sand samples and the loading sequence of the pile have minimal influence on the values of D for nondisplacement piles.

When comparing the pile responses from first-time loading (FTL), the magnitudes of peak unit shaft resistance and limit unit shaft resistance $q_{sP,FTL}$ and $q_{sL,FTL}$, respectively, measured in compressive loading were comparable to those measured in tensile loading for the same relative densities. This resulted in values of tensile-to-compressive unit shaft resistance ratio at peak shaft resistance ($SRR_{P,FTL}$) or at its limit ($SRR_{L,FTL}$) close to one. The minimal effect of loading direction on the unit shaft resistance of fresh nondisplacement piles in sand suggests that no reduction factor is needed when computing the unit shaft resistance of bored piles subjected to monotonic loading.

For first-time loading, the displacement vectors for both loading directions (tension and compression) make angles with the horizontal with approximately the same magnitude. Just outside the shear band, soil elements surrounding the pile shaft moved radially away from the pile shaft with, magnitudes of radial displacement almost identical in tensile and compressive loading and with magnitude decreasing with increasing radial distance measured from the pile shaft. Regardless whether the pile was loaded first in tension or compression, the soil elements dilated radially within a thin band adjacent to the pile shaft and contracted radially further out. The magnitudes of the shear and radial strains were comparable in tensile and compressive loading. The principal strains rotated by the same amount but in opposite directions depending on whether tension or compression was applied first. At peak shaft resistance, the directions of the minor principal strain E_2 with respect to the horizontal were − 45.5° and + 46.6° in in compressive and tensile loading, respectively, but this angle decreased for soil elements located further away, radially.

The radial and shear strains E_{rr} and E_{rz} and the minor principal strain orientation α evolved during CT and TC loading sequences. As soon as the loading direction was reversed, the magnitudes of the cumulative shear strain E_{rz} and radial strain E_{rr} dropped. This reduction mayhave been caused by the misalignment of the principal axes of the stress and fabric tensors resulting from load reversal. As the second-time loading (STL) continued, the soil fabric would tended to realign in a way consistent with the new direction of the principal axes of the stresses. At the end of the STL stage, the angle α of the minor principal strain E_2 with the horizontal rotated about 90° or about -90° for a CT and TC loading sequences, respectively. The reduction in the radial strain exhibited by the soil elements during the STL was consistent with the mechanism of friction degradation, as demonstrated by the values below one of the unit shaft resistance degradation factor D. The results also suggest that shaft resistance degradation occurs at a fast rate, with substantial drops already upon the first load reversal.

The shape of the pile base was found to have negligible influence on the shaft resistance and on the displacement and the strain fields around the pile shaft. The shear band thickness t_s, estimated visually by tracking the movement of sand particles across images, varied from t_s = 2.16 mm (=3.5D_{50}) to t_s =2.52 mm (= 4.1D_{50}). In general, t_s was smaller for STL than for FTL and was only 3% larger for tensile loading than for compressive loading.

3.6 Acknowledgments

The authors would like to acknowledge the support from the Instituto para el Desarrollo de la Ciencia y Tecnología en Colombia, Colciencias.

4. EFFECT OF CYCLIC LOADING ON THE MOBILIZATION OF SHAFT RESISTANCE OF MODEL PILES JACKED IN SAND

This chapter will be submitted to a peer-reviewed journal for publication.

4.1 Abstract

Monotonic compressive and cyclic load tests were performed on a closed-ended model pile jacked into sand samples in a half-cylindrical calibration chamber with digital image correlation (DIC) capabilities. The model pile was instrumented, enabling the determination of unit shaft resistance mobilized during the monotonic and cyclic load tests. During the cyclic tests, images of the pile shaft and the surrounding sand were taken using digital cameras and analyzed to obtain the displacement and strain fields in the sand domain using the DIC technique. The study shows that the limit unit shaft resistance after cycling is lower than the initial (before cycling) limit unit shaft resistance when the displacement cycles (100 cycles) are performed with cyclic displacement half amplitude greater than 0.7 mm. However, this threshold of cyclic displacement half amplitude decreases as the number of cycles increases. The loss of limit unit shaft resistance after cyclic loading increases with increasing initial vertical stress, cyclic displacement half amplitude, and number of cycles and with decreasing relative density. Furthermore, the DIC results reveal that the degradation of the limit unit shaft resistance is due to radial contraction and the development of cumulative shear strains in soil elements near the pile shaft during cyclic loading.

Keywords: cyclic loading, sand, model piles, DIC technique

4.2 Introduction

Certain structures supported by deep foundations are always subjected to cyclic loading during their service life. Wind turbines and offshore platforms are examples of structures that rely on the ability of the foundations to sustain cyclic loads induced by environmental loads such as those due to wind and wave action. Cyclic loading can significantly affect the response of a pile to loading by reducing its static capacity. Furthermore, when a pile is subjected to cyclic loading, serviceability limit states may be reached due to excessive pile head displacements (Benzaria et al. 2013; Jardine and Standing 2000; Karlsrud et al. 1986; Puech et al. 2012).

One of the most comprehensive sets of pile load tests were carried out at Dunkirk, France, by Chow (1997) and Jardine and Standing (2000, 2012) to investigate cyclic loading effects on the static shaft capacity of displacement piles in sand. Load-controlled, axial cyclic and static tensile load tests were performed on full-scale open-ended driven piles. From these experiments, Jardine and Standing (2012) observed that, at low-level cyclic loading (load oscillating between zero and a tensile load with magnitude not exceeding 38% of the pre-cycling maximum tensile resistance), piles were able to sustain a large number of cycles (more than 1,000 uniform cycles) without generating significant permanent pile head displacements. Furthermore, the tested piles showed an increase in the tensile shaft capacity after cycling. In contrast, high-level cyclic loading (load oscillating between zero and a tensile load with magnitude not exceeding 92% of the pre-cycling maximum tensile resistance) caused excessive permanent pile head displacements (i.e., pile head displacement greater than 10% of the pile diameter B within less than 12 cycles), leading to a reduction of the tensile pile shaft capacity.

Jardine et al. (2012) and Puech and Garnier (2017) suggested that, for relatively compressible piles installed in sandy soils, the decrease in shaft resistance due to cyclic loading is not uniform along the pile shaft. Thus, understanding the mechanisms controlling the local mobilization of shaft resistance along the soil-pile interface is crucial in the estimation of the global pile shaft response to cyclic loads. Calibration chamber experiments allow a high-quality, detailed examination of the mechanisms involved in the mobilization of unit shaft resistance of a segment of a pile.

The behavior of soil-pile interfaces during and after cyclic loading has been studied by performing monotonic and cyclic constant-normal stiffness (CNS) shear tests on sand-steel interfaces (Airey et al. 1992; Al-Douri and Poulos 1992; DeJong et al. 2003; Fakharian and Evgin

1997; Mortara et al. 2007). By comparing the monotonic response of sand-steel interfaces before and after cycling, Tabucanon et al. (1995) and Mortara et al. (2007) showed that the post-cyclic shear strength drops with increasing cyclic displacement amplitude or number of cycles.

Results from model pile experiments in calibration chambers have shown that the decrease in shaft capacity due to cyclic loading depends on several factors, including the cyclic displacement, number of cycles, type of soil, and type of pile (Al-Douri 1992; Al-Douri and Poulos 1995; Le Kouby et al. 2004; Lee and Poulos 1991; Poules 1984; Poulos 1989a). According to Poulos (1984), the post-cyclic shaft resistance decreases only when the cyclic displacement amplitude exceeds the magnitude of the displacement required to fully mobilize the unit shaft resistance under monotonic loading. Le Kouby et al. (2004) indicated that non-displacement piles are more susceptible to experience a decrease in shaft capacity after cyclic loading than displacement piles. Poulos (1984, 1989a) suggested that a drop in the mobilized unit shaft resistance is less severe in silica sand than in calcareous sand and that the vertical stress has minimal effect on the degradation of shaft resistance due to cycling.

Foray et al. (2010), Rimoy et al. (2012) and Tsuha et al. (2012) studied the response of piles subjected to axial cyclic loading using the Imperial College mini-ICP (diameter = 36 mm) pile in a pressurized calibration chamber. Measurements of the local radial and shear stresses at the shaft of the mini-ICP model pile showed that, under high-level cycling (e.g., cyclic displacement varying from -2 mm to +3 mm per cycle), the stress path formed loops that reached the tension and compression failure envelopes. The radial stress decreased as cycling progressed. According to Jardine et al. (2012), the main factor behind the loss of shaft capacity is the decrease of the local radial stress in the soil next to the pile shaft during cyclic loading.

Image-based measurement techniques have been used to study the deformation of soil elements near sand-structure interfaces by performing cyclic CNS shear tests (DeJong et al. 2003, 2006) and axial cyclic loading tests on a displacement pile in a mini calibration chamber (Doreau-Malioche et al. 2018). From the CNS shear tests, DeJong et al. (2003) and Westgate and DeJong (2006) observed that, under both displacement- and load-controlled cyclic conditions, the shear band at the interface exhibited a net contraction after each cycle. The magnitude of this contraction increased as the number of cycles increased. This cumulative contraction was linked to the decrease in the normal stress typically measured in cyclic CNS tests. Despite possible scale effects, Doreau-Malioche et al. (2018) also found that the sand next to a sand-pile interface contracts radially when a model pile is subjected to displacement-controlled loading cycles.

This paper presents the results of a series of monotonic and cyclic displacement-controlled load tests performed on a model pile jacked in silica sand samples prepared in a half-cylindrical calibration chamber with Digital Image Correlation (DIC) capabilities. We investigate the effects of cyclic displacement, number of cycles, relative density, initial vertical stress and frequency on shaft resistance mobilization during monotonic and cyclic loading. We also present the strain and displacement fields in the sand domain obtained during cyclic loading of the jacked model pile and discuss the primary mechanisms controlling its response to cyclic loading.

4.3 Materials and methods

4.3.1 Testing equipment

Model pile tests were performed in a half-cylindrical calibration chamber at Purdue University, USA (Figure 4.1). Details of the calibration chamber and the testing equipment used in the experiments reported in this paper are provided in Table 4.1. The front wall of the calibration chamber contains three observation windows that allow capturing of digital images of the model pile and the surrounding sand domain during testing.

The model pile consists of an instrumented half-circular rod with a conical base. The model pile dimensions and surface roughness parameters are also included in Table 4.1. The installation and the monotonic and cyclic loading of the model pile were performed using a hydraulic actuator mounted on a removable steel frame, as shown in Figure 4.1. The loads Q_T at the head of the model pile were measured using a 42-kN capacity tension-compression load cell (Model WMC, Interface Inc., Scottsdale, Arizona) connected at the top of the model pile. The loads Q_b at the base of the model pile were measured using a cluster of 4 strain gauges (Kyowa Americas Inc. model KFG-2-350-C1-23) installed oppositely to each other in a brass cylinder located inside the conical tip of the model pile.

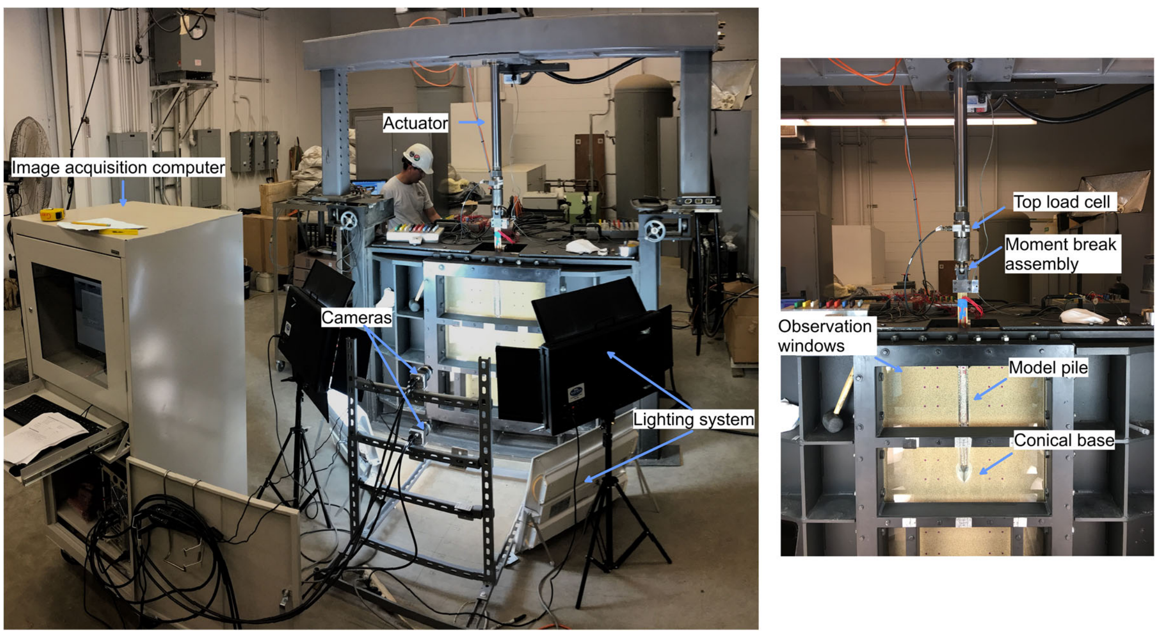

Figure 4.1. Experimental facility for model pile testing at the Bowen Laboratory, Purdue University.

Table 4.1. Equipment components (Adapted from Tovar-Valencia 2019)

Component	Details
Calibration chamber	Half-cylindrical calibration chamber with DIC capabilities
• Diameter *D*	1680 mm
• Height *H*	1200 mm
• Observation windows	300 mm (width) x 250 mm (height)
Model pile	Half-circular bass rod with conical tip (60°-apex angle)
• Pile diameter *B*	38.1 mm
• Pile length *L*	800 mm
• D/B	44.1
• B/D_{50}	61.4
• $R^*_{\max}$ [c]	83.01 μm
• R^*_n [b]	0.134
Surcharge device	Inflatable rubber bladder at the top of the sample
Boundary conditions	Perfectly rigid lateral wall & constant vertical stress (BC3)[c]
Loading system	Servo-controlled hydraulic actuator
Digital cameras & lenses	1 per observation window
• Camera type	CMOS[d] cameras
• Camera resolution	12 Megapixels
• Lenses	60 mm focal length low distortion
• Image capture rate	From 2 to 20 pictures per second
Lighting system	Two fluorescent (55W) and 2 LED (42 W) lights

[a] Absolute roughness as defined in Tovar-Valencia et al. (2018).
[b] Normalized surface roughness parameter (= $R^*_{\max} / D_{50}$).
[c] Boundary conditions as described in Ghionna and Jamiolkowski (1991) and Salgado et al. (1998).
[d] Complementary Metal-Oxide Semiconductor cameras.

4.3.2 Test sand

The test sand is Ohio Gold Frac (OGF), a poorly-graded silica sand (SiO_2=99.7%) with a mean particle size D_{50} of 0.62 mm. The critical-state friction angle of the sand is 32.5° in triaxial compression and 32.0° in direct shear. Sandpaper grit #120 was attached to the pile surface to increase its roughness. The sand-sandpaper (sandpaper grit #120) interface friction angle δ_c obtained from direct shear tests is 31.4°. As shown in Table 4.1, the normalized surface roughness R^*_n (Tovar-Valencia et al. 2018) of the model pile with sandpaper attached to it is 0.134, and thus it is considered a rough surface (Galvis-Castro et al. 2019b; Tovar-Valencia et al. 2018). Han et al. (2018) provided all the properties and morphological parameters of OGF sand.

4.3.3 Image analysis

Two CMOS cameras were positioned in front of the top and middle observation windows of the calibration chamber to take synchronized digital images of the sand domain at a rate ranging from 5 pictures per second, for cyclic tests performed with small cyclic displacement amplitude and low frequency (0.1 Hz), to 20 pictures per second, for cyclic tests performed with large cyclic displacement amplitude and high frequency (1.0 to 2.0 Hz). The two-dimensional Digital Image Correlation DIC technique was used to obtain the displacement and strain fields in the sand domain surrounding the model pile during cycling loading. The fundamentals of the DIC technique are described in Arshad et al. (2014) and Pan et al. (2009). The commercial software VIC-2D (Correlated Solutions 2009) was used to analyze the digital images captured in the experiments. The settings used in VIC-2D are summarized in Table 4.2.

Table 4.2. Settings for the DIC analysis using VIC 2D (Adapted from Tovar-Valencia et al. 2020)

Parameter	Value (description)
Subset size [a]	35 x 35 pixels (≈ $5D_{50}$ by $5D_{50}$)
Step or grid size [b]	8 pixels
Area of interest in the picture	300 mm x 250 mm
Scale of the image	0.095 mm / pixel
Correlation criterion	Normalized squared differences and exhaustive search [c]

[a] Size of the set of pixels to be tracked across images.
[b] Size of the square grid used to extract results.
[c] This correlation criterion seeks the minimum difference in grey-level intensity of an image pattern of the subset in the reference and deformed/displaced images (Pan et al. 2009; Sutton et al. 2009; Take 2015).

4.3.4 Experimental program

Twenty-five sand samples were prepared in the DIC calibration chamber (Table 4.3). The samples were prepared by air pluviation (Lee et al. 2011). The target sample densities were achieved by changing the flow rate through the addition or removal of a diffuser sieve. For each sand sample, testing consisted of the following four stages: (1) pile installation, (2) monotonic compressive loading before cycling, (3) displacement-controlled cyclic loading, and (4) monotonic compressive loading after cycling.

The model pile was installed using jacking strokes 10 mm in length at a rate of 1.0 mm/s to a target base depth of 415 mm (= 10.9B). The pile head load was reduced to zero ($Q_T \approx 0$ kN) between strokes. This procedure was repeated until the desired penetration depth was reached. The loading system was detached from the head of the model pile to unload the pile, simulating the end of the pile installation stage (stage 1) of the test.

Two compressive load tests were performed per sample: one before and one after cyclic loading. In the pre-cycling compressive loading (stage 2), the model pile was pushed down for a distance of approximately 12 mm (i.e., 12 mm ≈ 0.3*B*), while, in the post-cycling compressive loading (stage 4), the pile head was pushed down about 38 mm (i.e., 38 mm ≈ 1*B*). Both compressive load tests were performed at a constant rate of 0.1 mm/s (1/10 of the installation rate).

The cyclic load tests were performed using a servo-controlled hydraulic actuator designed to impose sinusoidal pile head displacements. Only one displacement-controlled cyclic test (stage 3) was performed per sample. Figure 4.2 shows that the displacement w oscillates between a maximum displacement w_{max} and a minimum displacement w_{min}, from which we can calculate (i) the mean displacement w_{mean} as $(w_{\text{max}} + w_{\text{min}})/2$ and (ii) the cyclic displacement half amplitude Δw_{cyclic} as $(w_{\text{max}} - w_{\text{min}})/2$, which is half of the amplitude of the sinusoidal displacement wave. The cyclic tests were performed by first applying a pre-defined value of w_{mean} on the model pile. The value of w_{mean} was set to correspond to a reasonable estimate of the working load on the pile. This will be discussed in detail later in the paper. This pre-loading is illustrated in Figure 4.2 as the trajectory from point A, at which the load at the top of the model pile is zero and $w = 0$, to point B, at which the load at the top of the model pile is greater than zero and $w = w_{\text{mean}}$. A complete displacement cycle is illustrated in Figure 4.2 by the displacement vs. time response from point B to point C. The number N_c of cycles and the frequency f were two of the variables considered in the testing plan.

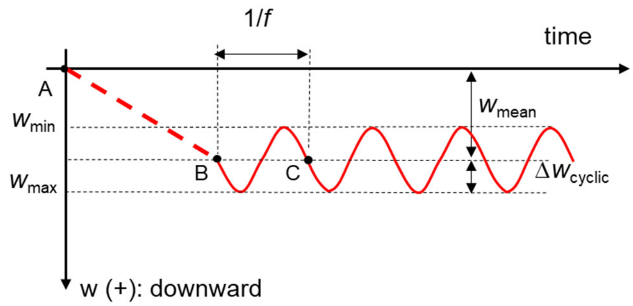

Figure 4.2 Pile head displacement w (positive when the pile head moves downward) vs. time of a typical displacement-controlled cyclic load test (from point A to B: pre-loading of the model pile in compression with a pile head displacement $w = w_{mean}$ and from point B to C: first load cycle).

Table 4.3 presents the test program. Each test is identified by a test code that describes the cyclic test parameters: mean displacement w_{mean}, denoted by M; cyclic displacement half amplitude Δw_{cyclic}, denoted by CY; frequency f, denoted by F; and number N_c of cycles, denoted by N. The number that follows these notation letters in the test code represents the value of the variable (values are in millimeters for w_{mean} and Δw_{cyclic} and in Hz for f). All the tests were performed in dense sand samples, except for test M0.5-CY1.0-F0.1-N100$^{(*)}$, which was performed in medium-dense sand. A surcharge (initial vertical stress σ_{v0}) of 50 kPa was applied at the top of the samples, except for test M0.5-CY0.7-F1.0-N1000$^{(+)}$, which was performed with a surcharge of 90 kPa.

Table 4.3 Test program

#	Test code[a,b,c]	Relative density D_R	Mean displacement w_{mean}	Cyclic displacement half amplitude Δw_{cyclic}	Number of cycles N_c	Frequency f
		%	mm	mm		Hz
1	M0.5-CY0.25-F0.1-N100	91.3	0.50	0.25	100	0.1
2	M0.5-CY0.25-F1.0-N1000	94.3	0.50	0.25	1,000	1.0
3	M0.5-CY0.25-F2.0-N2000	92.0	0.50	0.25	2,000	2.0
4	M1.0-CY0.5-F0.1-N100	88.0	1.00	0.50	100	0.1
5	M1.7-CY0.5-F0.1-N100	87.1	1.70	0.50	100	0.1
6	M0.5-CY0.5-F1.0-N1000	91.4	0.50	0.50	1,000	1.0
7	M0.5-CY0.5-F0.1-N100	92.7	0.50	0.50	100	0.1
8	M0.7-CY0.5-F0.1-N100	92.7	0.70	0.50	100	0.1
9	M2.4-CY0.5-F0.1-N100	92.7	2.40	0.50	100	0.1
10	M0.5-CY0.6-F0.1-N100	93.6	0.50	0.60	100	0.1
11	M0.5-CY0.7-F1.0-N1000	94.3	0.50	0.70	1,000	1.0
12	M0.5-CY0.7-F1.0-N100	92.0	0.50	0.70	100	1.0
13	M0.5-CY0.7-F0.1-N100	92.3	0.50	0.70	100	0.1
14	M0.5-CY0.8-F0.1-N100	93.6	0.50	0.80	100	0.1
15	M1.7-CY0.85-F0.1-N100	88.5	1.70	0.85	100	0.1
16	M0.5-CY1.0-F0.1-N100	88.2	0.50	1.00	100	0.1
17	M1.0-CY1.0-F0.1-N100	92.1	1.00	1.00	100	0.1
18	M0.5-CY1.0-F1.0-N1000	86.9	0.50	1.00	1,000	1.0
19	M0.5-CY1.0-F1.0-N200	88.3	0.50	1.00	200	1.0
20	M0.5-CY1.2-F1.0-N100	92.0	0.50	1.20	100	1.0
21	M0-CY1.5-F0.2-N500	85.6	0.00	1.50	500	0.2
22	M1.0-CY1.5-F0.2-N500	85.6	1.00	1.50	500	0.2
23	M0.5-CY1.5-F0.1-N100	88.3	0.50	1.50	100	0.1
24	M0.5-CY1.0-F0.1-N100(*)	59.4	0.50	1.00	100	0.1
25	M0.5-CY0.7-F1.0-N1000(+)	80.0	0.50	0.70	1,000	1.0

[a] Test code: M"#"= mean displacement w_{mean} followed by its value in mm, CY"#"= cyclic displacement half amplitude Δw_{cyclic} followed by its value in mm, N"#" = number N_c of cycles, F"#" = frequency f followed by its value in Hz.
[b] Except for test M0.5-CY0.7-F0.1-N100(+), all the tests were performed with a surcharge of 50 kPa.
[c] Except for test M0.5-CY1.0-F0.1-N100(*), all the tests were performed in dense sand samples.

4.4 Experimental results

4.4.1 Monotonic loading: sensor-based results

4.4.1.1 Monotonic loading before cycling

Figure 4.3 shows the unit shaft resistance q_s mobilized in a typical compressive load test performed before cycling. The mobilized unit shaft resistance was calculated by subtracting the load at the base from the load at the head of the pile and then by dividing it by the surface area of the pile shaft in contact with the sand. In compressive loading, q_s reached a maximum value of

216.0 kPa in dense sand and 81.4 kPa in medium-dense sand. The unit shaft resistance is fully mobilized after a pile head displacement w equal to 4.0 mm (= 0.11B) in dense sand and 2.3 mm (= 0.06B) in medium-dense sand, and then it stabilizes at its limiting value as the pile head displacement increases.

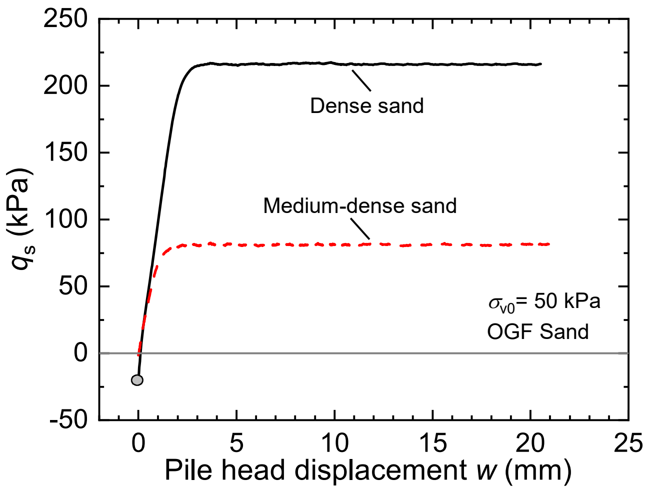

Figure 4.3. Unit shaft resistance mobilized in compressive load tests performed before cyclic loading in dense and medium-dense sand.

4.4.1.2 Effect of the mean displacement w_{mean} on unit shaft resistance

The effect of the mean displacement w_{mean} on the unit shaft resistance mobilized in compressive loading was evaluated through the unit shaft resistance ratio $q_{s,AC}/q_{sL,BC}$, defined as the ratio of the unit shaft resistance $q_{s,AC}$ measured in the compressive load test performed after cycling to the limit unit shaft resistance $q_{sL,BC}$ obtained in the compressive load test performed before cycling. Figure 4.4(a) and (b) show the profiles of $q_{s,AC}/q_{sL,BC}$ vs. pile head displacement w for tests with cyclic loading stage performed using cyclic displacement half amplitude Δw_{cyclic} of 0.5 mm and 1.0 mm, respectively. For the tests shown in Figure 4.4(a), the curves of $q_{s,AC}/q_{sL,BC}$ vs. w are comparable (they differ by less than 16% with reference to the curve with w_{mean} = 0.5 mm). Figure 4.4(b) also shows that, for cyclic tests performed with w_{mean} = 0.5 mm and 1.0 mm, the results in terms of $q_{s,AC}/q_{sL,BC}$ are similar. The results shown in Figure 4.4 suggest that the influence of w_{mean} on the post-cyclic unit shaft resistance response is minimal to negligible as long as the maximum downward movement (i.e., w_{max}) of the pile head is smaller than the pile head displacement required to mobilize $q_{sL,BC}$ in compressive loading.

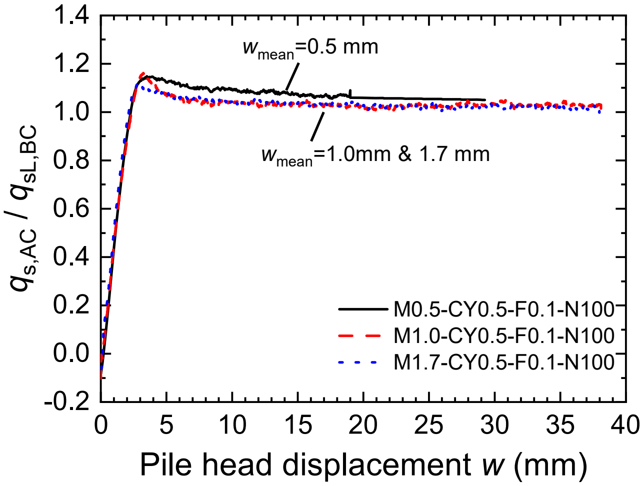

(a)

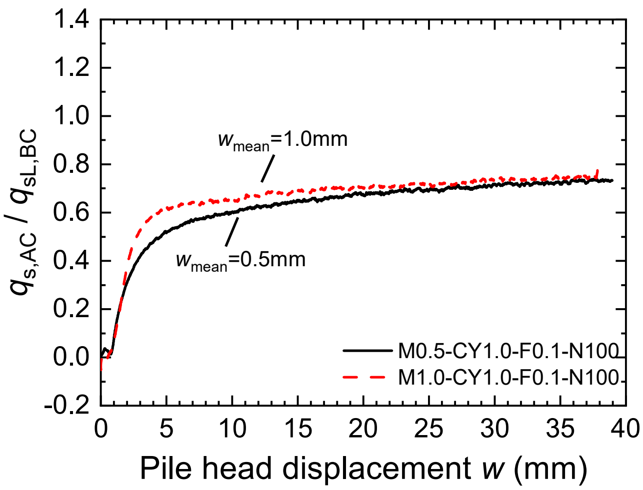

(b)

Figure 4.4. Influence of mean displacement w_{mean} on the post-cycling unit shaft resistance: unit shaft resistance ratio $q_{s,AC}/q_{sL,BC}$ vs. pile head displacement w for tests with cyclic loading stage performed using cyclic displacement half amplitudes Δw_{cyclic} of (a) 0.5 mm and (b) 1.0 mm.

4.4.1.3 Effect of frequency f on unit shaft resistance

Figure 4.5 compares the $q_{s,AC}/q_{sL,BC}$ vs. w curves for tests M0.5-CY0.7-F1.0-N100 and M0.5-CY0.7-F0.1-N100. The difference between these two tests is the frequency applied in the cyclic loading stage of the tests. Figure 4.5 shows that the values of $q_{s,AC}/q_{sL,BC}$ for the tests performed with low frequency (i.e., $f = 0.1$ Hz) and high frequency (i.e., $f = 1.0$ Hz) are comparable. Therefore, the effect of frequency on the post-cycling unit shaft resistance is small for model piles jacked in silica sand within the loading rate range of these tests. As shown in Table 4.3, the frequencies used in the cyclic loading stage of the tests varied from 0.1 Hz to 2.0 Hz. For the range of frequencies and cyclic displacement half amplitudes considered in these experiments, the model pile achieved a maximum loading rate of 6 mm/s and a minimum loading rate of 0.1 mm/s in the cyclic tests. This is consistent with previous observations by Al-Douri and Poulos (1992) who indicated that the loading rate (=1.0 mm/min and 2 mm/min) had only little influence on the results of cyclic direct shear tests on sand. Based on field tests on driven piles in sand, Rimoy et al. (2013) also suggested that loading rate effects on shaft capacity are likely to be insignificant for piles in sand.

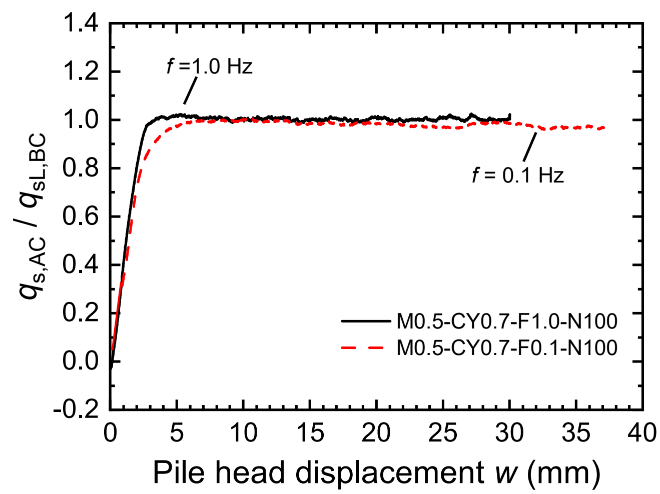

Figure 4.5. Influence of frequency f on the post-cycling unit shaft resistance: unit shaft resistance ratio $q_{s,AC}/q_{sL,BC}$ vs. pile head displacement w for tests M0.5-CY0.7-F1.0-N100 (f = 1.0 Hz) and M0.5-CY0.7-F0.1-N100 (f = 0.1 Hz).

4.4.1.4 Effect of cyclic displacement half amplitude Δw_{cyclic} on unit shaft resistance

Figure 4.6 shows the $q_{s,AC}/q_{sL,BC}$ vs. w curves for tests with the cyclic loading stage performed using cyclic displacement half amplitudes ranging from 0.25 mm to 1.5 mm. Peaks in $q_{s,AC}/q_{sL,BC}$ are observed for tests with Δw_{cyclic} equal to 0.25 mm, 0.5 mm, and 0.6 mm (tests M0.5-CY0.25-F0.1-N100, M0.5-CY0.5-F0.1-N100, and M0.5-CY0.6-F0.1-N100). The peaks occur approximately at a pile head displacement w equal to 4 mm and correspond to $q_{s,AC}/q_{sL,BC}$ values greater than 1.0, indicating a small improvement of the post-cyclic unit shaft resistance. However, as loading progresses, $q_{s,AC}/q_{sL,BC}$ decreases and stabilizes at a value of 1.0. In contrast, for Δw_{cyclic} greater than 0.7 mm (tests M0.5-CY1.0-F0.1-N100 and M0.5-CY1.5-F0.1-N100), the values of $q_{s,AC}/q_{sL,BC}$ within the 4 mm $\leq w <$ 38 mm range are less than 1.0, indicating a drop of the post-cyclic unit shaft resistance. Increases in the shaft resistance of model piles after cyclic loading with small cyclic displacements have also been reported by Foray et al. (2010) and Le Kouby et al. (2004). Foray et al. (2010) measured a 17% increase in the tensile shaft capacity after subjecting a model pile (B = 36 mm) to 7,000 cycles with cyclic displacement half amplitude of 0.04 mm (= $0.001B = 0.19D_{50}$). Le Kouby et al. (2004) reported a gain in shaft resistance of 30% after applying 50 displacement-controlled cycles with a cyclic displacement half amplitude of 0.1 mm ($=0.01B = 0.50D_{50}$).

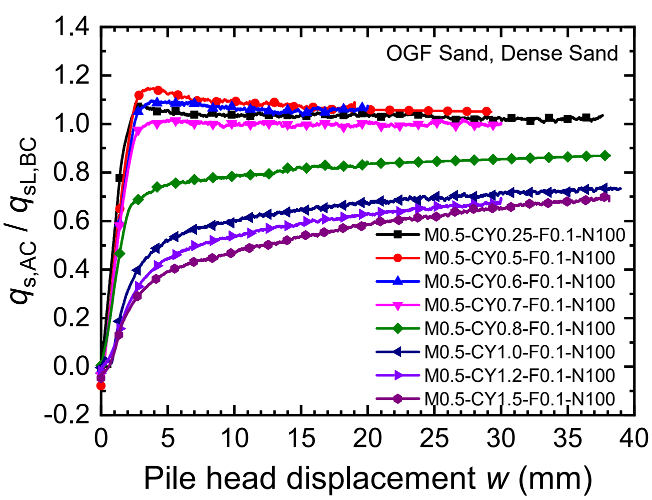

Figure 4.6. Influence of cyclic displacement half amplitude Δw_{cyclic} on the post-cycling unit shaft resistance: unit shaft resistance ratio $q_{s,AC}/q_{sL,BC}$ vs. pile head displacement w for tests with cyclic loading stage performed using mean displacement w_{mean} of 0.5 mm and ended at 100 displacement cycles.

Figure 4.7 shows the curves of the unit shaft resistance ratio $q_{s,AC}/q_{sL,BC}$ vs. the cyclic displacement half amplitude Δw_{cyclic} for the following values of pile head displacement w: (i) 4.0 mm, which is the displacement w_L required to mobilize the limit unit shaft resistance in compressive loading before cyclic loading in dense sand; (ii) 6 mm; (iii) 10 mm; and (iv) 38 mm ($\approx 1B$). Figure 4.7 was drafted using the results from the same tests shown in Figure 4.6 (i.e., tests with w_{mean} = 0.5 mm, σ_{v0} = 50 kPa, and N_c = 100 cycles). For w = w_L= 4.0 mm, the unit shaft resistance ratio $q_{s,AC}/q_{sL,BC}$ reaches a maximum value of 1.14 at Δw_{cyclic} = 0.6 mm (= 0.17w_L), then decreases to a value of 0.5 as Δw_{cyclic} increases from 0.6 to 1.0 mm. Figure 4.7 also shows that, for Δw_{cyclic} greater than 0.7 mm, $q_{s,AC}/q_{sL,BC}$ increases as the pile head displacement w increases. However, $q_{s,AC}/q_{sL,BC}$ is always lower than 1.0 even at a pile head displacement of 38 mm (= 1B). This result indicates that the limit unit shaft resistance is significantly affected by uniform cycles (N_c = 100) of cyclic displacement half amplitude Δw_{cyclic} greater than 0.7 mm.

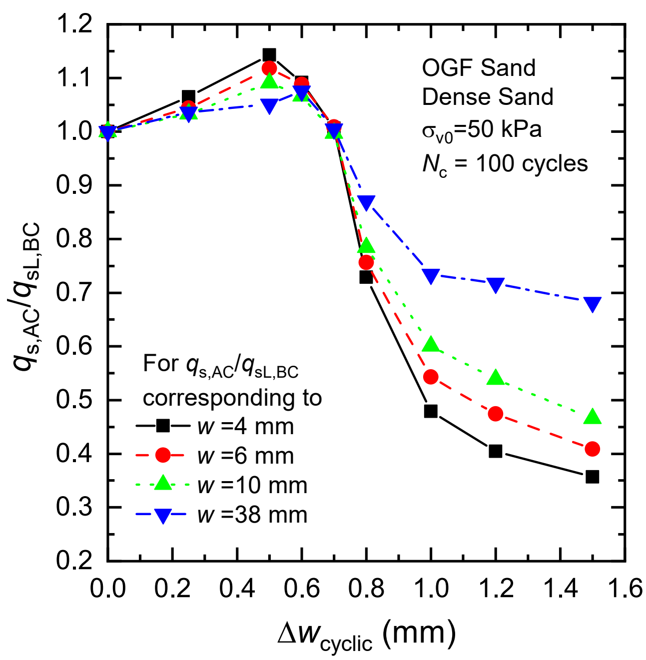

Figure 4.7. Unit shaft resistance ratio $q_{s,AC}/q_{sL,BC}$ corresponding to w = 4 mm, 6 mm, 10 mm, and 38 mm vs. cyclic displacement half amplitude Δw_{cyclic} for tests with cyclic loading stage performed using mean displacement w_{mean} of 0.5 mm.

4.4.1.5 Effect of number N_c of cycles on unit shaft resistance

Figure 4.8 compares the $q_{s,AC}/q_{sL,BC}$ vs. w curves for tests with the same cyclic displacement half amplitude but ended at different number of displacement cycles. Figure 4.8(a) shows the results for Δw_{cyclic} = 0.25 mm (tests M0.5-CY0.25-F0.1-N100, M0.5-CY0.25-F1.0-N1000 and M0.5-CY0.25-F2.0-N2000) and Figure 4.8(b) shows the results for Δw_{cyclic}=1.0 mm (tests M0.5-CY0.7-F0.1-N100 and M0.5-CY0.7-F1.0-N1000). In Figure 4.8(a), the values of $q_{s,AC}/q_{sL,BC}$ for

N_c= 1,000 and 2,000 cycles differ by less than 1% with respect to the values of $q_{s,AC}/q_{sL,BC}$ for N_c=100 cycles. On the other hand, in Figure 4.8(b), the value of $q_{s,AC}/q_{sL,BC}$ at $w = w_L$= 4.0 mm drops significantly when the number of cycles increases from 100 to 1,000 cycles (i.e., at w = 4 mm, $q_{s,AC}/q_{sL,BC}$ = 1.0 for test M0.5-CY0.7-F1.0-N100, while $q_{s,AC}/q_{sL,BC}$ = 0.6 for test M0.5-CY0.7-F1.0-N1000).

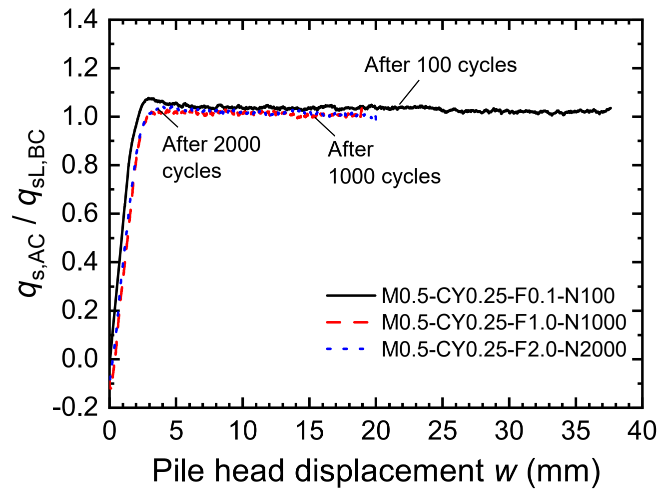

(a)

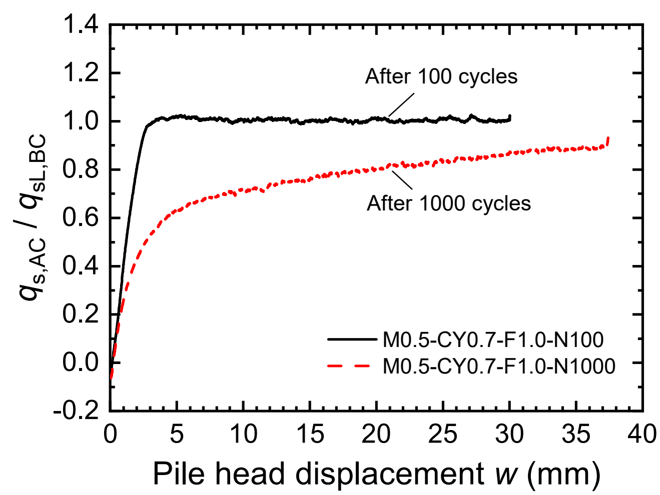

(b)

Figure 4.8. Influence of number N_c of cycles on the post-cycling unit shaft resistance: unit shaft resistance ratio $q_{s,AC}/q_{sL,BC}$ vs. pile head displacement for tests with cyclic loading stage performed using cyclic displacement half amplitudes Δw_{cyclic} of (a) 0.25 mm and (b) 1.0 mm.

Figure 4.9 shows the unit shaft resistance ratio $q_{s,AC}/q_{sL,BC}$ corresponding to w = 4 mm vs. cyclic displacement half amplitude w_{cyclic} for tests with N_c=100 and 1,000 cycles. As mentioned before, the largest drop in $q_{s,AC}/q_{sL,BC}$ occurs for Δw_{cyclic} = 0.7 mm when the number of cycles increases from 100 to 1,000; the $q_{s,AC}/q_{sL,BC}$ ratio for $q_{s,AC}$ measured at w = 4 mm and 1,000 cycles is 42% less than that for 100 cycles.

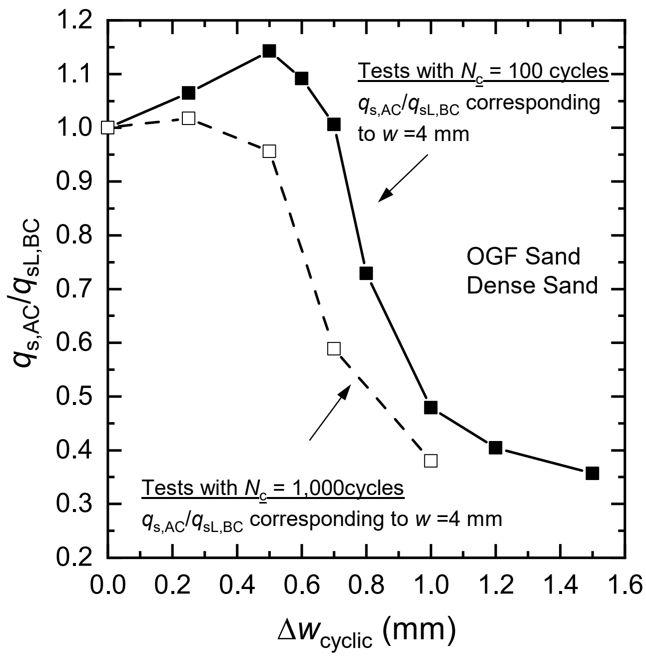

Figure 4.9. Unit shaft resistance ratio $q_{s,AC}/q_{sL,BC}$ corresponding to w = 4 mm vs. cyclic displacement half amplitude Δw_{cyclic} for tests with cyclic loading stage ended at 100 and 1,000 displacement cycles.

Figure 4.10 shows that, for Δw_{cyclic} = 0.25 mm, the $q_{s,AC}/q_{sL,BC}$ ratios decrease by less than 3% as the number of cycles increases from 100 to 1,000 and 2,000 cycles. These results indicate that the unit shaft resistance is not affected by cyclic loading when the cycles are applied with a Δw_{cyclic} smaller than or equal to 0.25 mm, regardless of the number of cycles (100 to 1,000 and 2,000 cycles). For Δw_{cyclic}=1.0 mm, $q_{s,AC}/q_{sL,BC}$ decreases at a slow rate for N_c greater than 100. The value of $q_{s,AC}/q_{sL,BC}$ corresponding to w = 4 mm decreases by 20% when the number of cycles increases from 100 cycles to 200 cycles, but then only by an additional 5% from 200 cycles to 1,000 cycles. This result suggests that, for values of the cyclic displacement half amplitude Δw_{cyclic} exceeding 0.25 mm, there is a threshold number of cycles that produces the maximum degradation of the unit shaft resistance due to cyclic loading. The unit shaft resistance ratio is not affected by an increase in the number of cycles beyond this threshold value, which depends on the magnitude of the cyclic displacement half amplitude. The greater the cyclic displacement, the smaller is the number of cycles required for $q_{s,AC}/q_{sL,BC}$ to reach a stable value.

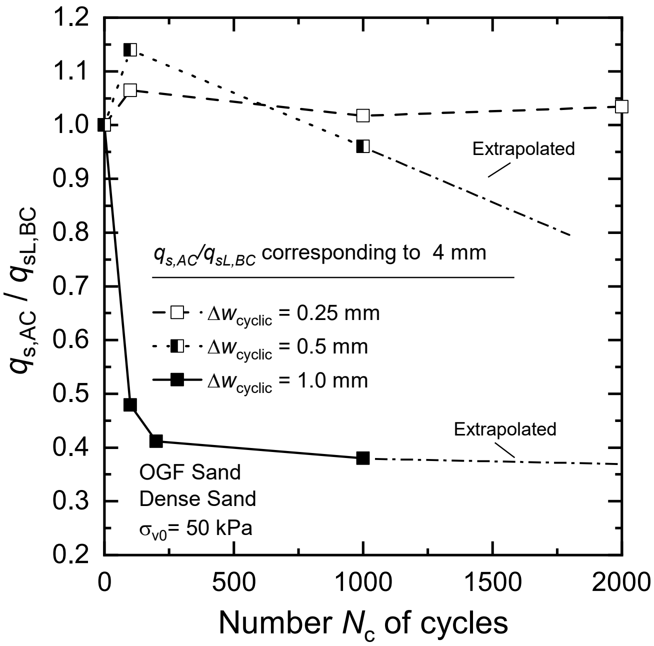

Figure 4.10. Unit shaft resistance ratio $q_{s,AC}/q_{sL,BC}$ corresponding to w = 4 mm vs. number N_c of cycles for tests with cyclic loading stage performed using cyclic displacement half amplitudes Δw_{cyclic} equal to 0.25 mm, 0.5 mm and 1.0 mm.

4.4.1.6 Effect of relative density D_R on shaft shear stress

Figure 4.11 compares the unit shaft resistance mobilized in the compressive load tests performed before and after cyclic loading for tests M0.5-CY1.0-F0.1-N100$^{(*)}$ and M0.5-CY1.0-F0.1-N100. The difference between these two tests is the relative density (D_R = 59.4% for test M0.5-CY1.0-F0.1-N100$^{(*)}$ and D_R = 88.2% for test M0.5-CY1.0-F0.1-N100). Figure 4.11(a) shows that, for medium-dense sand, the mobilized unit shaft resistance in the compressive load test performed after cycling is always smaller than that mobilized in the compressive load test performed before cycling. As shown Figure 4.11 (b), a similar effect is observed for dense sand. The results show that, after 100 displacement cycles of cyclic displacement half amplitude equal to 1.0 mm, the unit shaft resistance mobilized in both dense and medium-dense sand decreases.

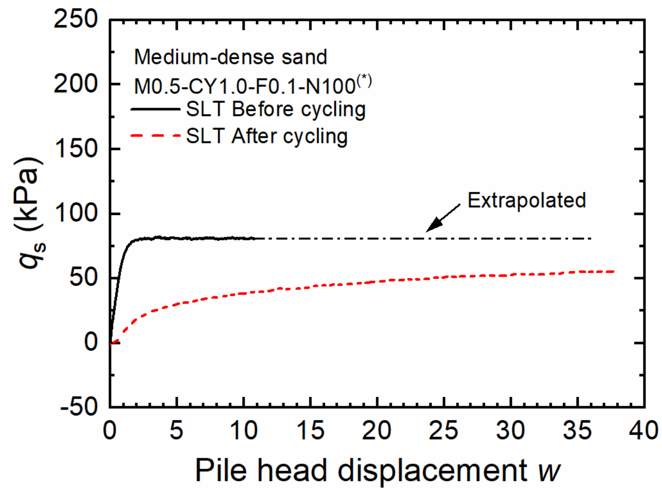

(a)

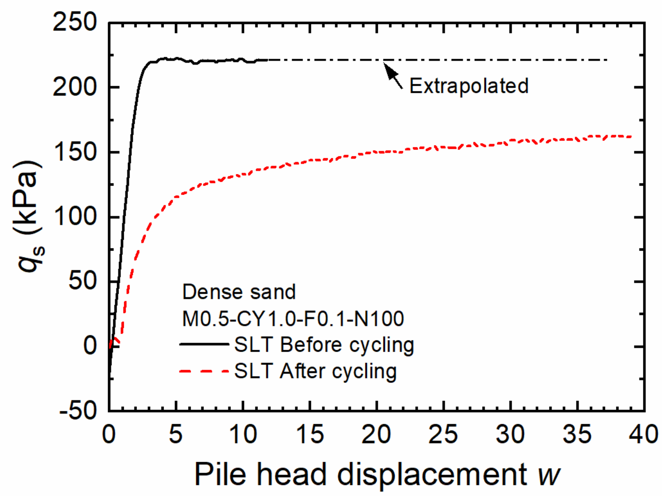

(b)

Figure 4.11. Unit shaft resistance q_s mobilized in the compressive load tests performed before and after cycling loading vs. pile head displacement w for tests in (a) medium-dense sand [test M0.5-CY1.0-F0.1-N100(*)] and (b) dense sand [test M0.5-CY1.0-F0.1-N100].

Figure 4.12 compares the profiles of the unit shaft resistance ratio $q_{s,AC}/q_{sL,BC}$ vs. pile head displacement w of tests in dense [test M0.5-CY1.0-F0.1-N100] and medium-dense sand [test M0.5-CY1.0-F0.1-N100(*)]. The results show that (i) the value of $q_{s,AC}/q_{sL,BC}$ is smaller in medium-dense sand than in dense sand for w > 2mm, but the difference tends to decrease with increasing pile head displacement; and (ii) the value of $q_{s,AC}/q_{sL,BC}$ tends to stabilize to a value approximately equal to 0.65 and 0.70 at the end of loading for dense and medium-dense sand, respectively. Based on CNS cyclic and monotonic direct shear tests on sand-steel interfaces, Tabucanon et al. (1995) reported on the response of dense and loose sand samples sheared monotonically for a horizontal displacement of 7.5mm after 50 cycles with a cyclic displacement half amplitude of 1 mm. Tabucanon et al. (1995) showed that the decrease in limit shear stress at sand-steel interface was more significant in loose sand than in dense sand. These results suggest that, in general, as the relative density decreases, the greater is the decrease in limit unit shaft resistance due to cyclic loading.

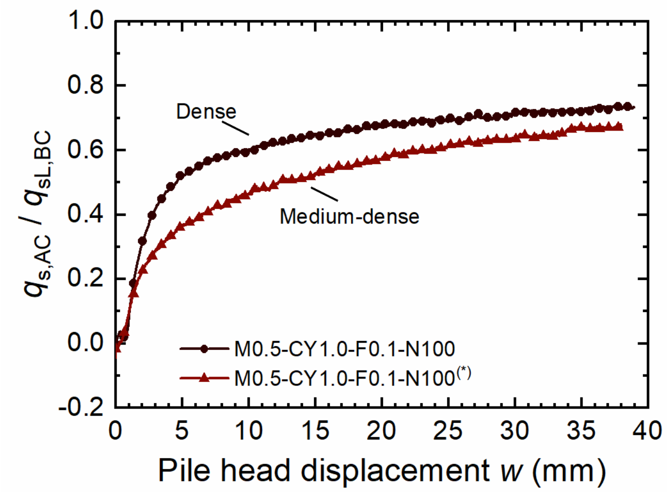

Figure 4.12. Influence of relative density on the post-cycling unit shaft resistance: unit shaft resistance ratio $q_{s,AC}/q_{sL,BC}$ vs. pile head displacement w for tests in dense [test M0.5-CY1.0-F0.1-N100] and medium-dense sand samples [test M0.5-CY1.0-F0.1-N100(*)].

4.4.1.7 Effect of surcharge σ_{v0} on unit shaft resistance

Figure 4.13(a) and Figure 4.13(b) show the unit shaft resistance q_s mobilized in the compressive load tests performed before and after cyclic loading, normalized by the surcharge σ_{v0}, for tests M0.5-CY0.7-F0.1-N1000 and M0.5-CY0.7-F0.1-N1000$^{(+)}$. As indicated in Table 4.3, test M0.5-CY0.7-F0.1-N1000 was performed with σ_{v0} = 50 kPa, while test M0.5-CY0.7-F0.1-N1000$^{(+)}$ was performed with σ_{v0} = 90 kPa. In the calibration chamber, the surcharge (initial vertical stress) simulates the depth at which a pile section is being studied. Figure 4.13(a) and (b) show that, for $w > w_L$ (i.e., w_L = 4.0 mm in dense sand, as shown in Figure 4.3), the greater the surcharge, the smaller is the value of q_s/σ_{v0}. We can estimate the average shaft resistance coefficient β (= q_{sL}/σ_{v0})

for the compressive load tests performed before and after cycling. The value of β_{BC} before cycling is 4.6 for σ_{v0} = 50 kPa; while, for σ_{v0} = 90 kPa, the value of β_{BC} before cyclic is 3.6. These results indicate that β increases with decreasing depth or initial vertical stress, which agrees with the results from one-dimensional finite element analysis of piles jacked in sand reported by Basu et al. (2011) and experimental data from tests on driven and jacked piles (Randolph et al. 1994). After cyclic loading, the value of β_{AC} after cycling decreases 13% for the test performed with σ_{v0} = 50 kPa and 40% for the test performed with σ_{v0} = 90 kPa (i.e., β_{AC} = 4.0 for σ_{v0} = 50 kPa and β_{AC} = 2.5 for σ_{v0} = 90 kPa).

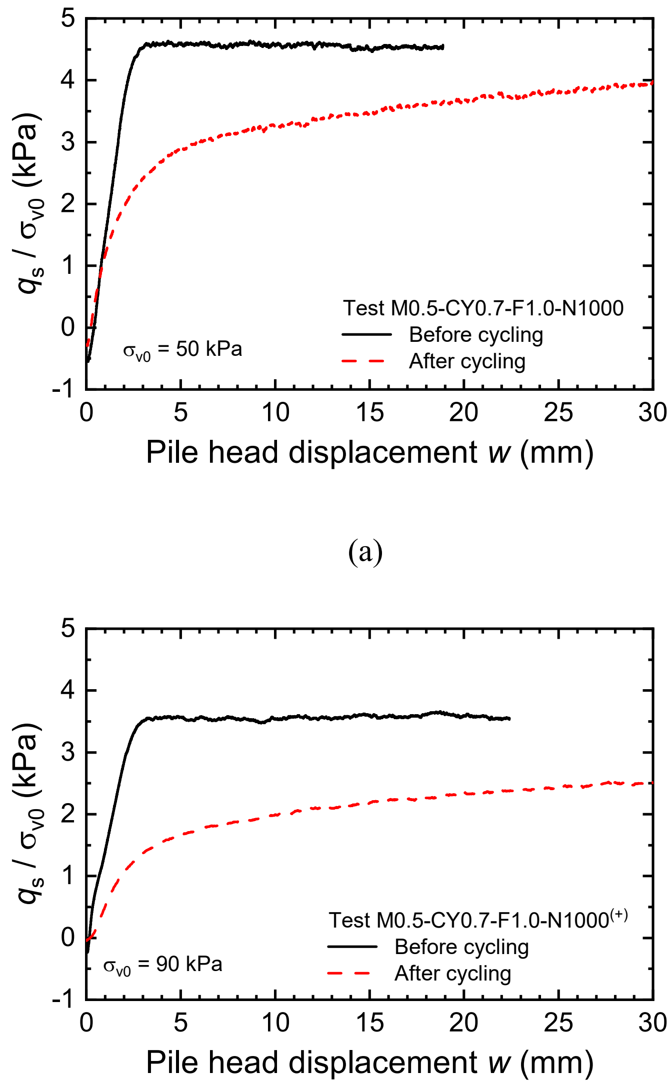

(a)

(b)

Figure 4.13. Unit shaft resistance q_s, normalized by the surcharge σ_{v0}, mobilized in the compressive load tests performed before and after cycling loading vs. pile head displacement w for tests performed with surcharges of (a) 50 kPa [M0.5-CY0.7-F1.0-N1000] and (b) 90 kPa [M0.5-CY0.7-F0.1-N100$^{(+)}$].

Figure 4.13(a) and Figure 4.13(b) also show that, after 1,000 displacement cycles of cyclic displacement half amplitude equal to 1.0 mm, q_s/σ_{v0} mobilized in the compressive load test after cycling is smaller than that mobilized before cycling for tests with surcharges of 50 kPa and 90 kPa. The effect of surcharge or initial vertical stress on the unit shaft resistance after cycling can also be evaluated using the unit shaft resistance ratio $q_{s,AC}/q_{sL,BC}$. Figure 4.14 shows the $q_{s,AC}/q_{sL,BC}$

vs. w curves for the same tests shown in Figure 4.13. The $q_{s,AC}/q_{sL,BC}$ values for the test performed with a surcharge of 90 kPa are smaller than those for the test performed with a surcharge of 50 kPa. For rigid piles, this suggests the unit shaft resistance ratio decreases with increasing depth. This result is consistent with the observations made by Al-Douri (1992) based on model pile tests in a calibration chamber.

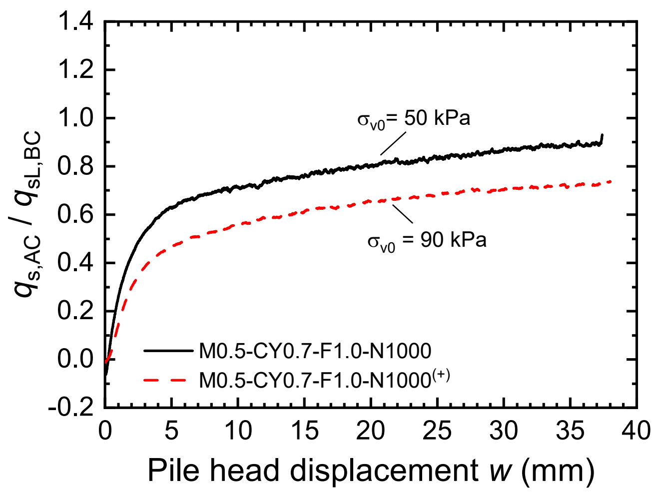

Figure 4.14. Influence of surcharge σ_{v0} on the post-cycling unit shaft resistance: unit shaft resistance ratio $q_{s,AC}/q_{sL,BC}$ vs. pile head displacement w for tests M0.5-CY0.7-F1.0-N1000 and M0.5-CY0.7-F1.0-N1000$^{(+)}$.

4.4.2 Cyclic loading: sensor-based and image-based results

4.4.2.1 Effect of cyclic displacement half amplitude Δw_{cyclic} and number N_c of cycles

Unit shaft resistance mobilization

Figure 4.15 (a) and Figure 4.15 (b) show the unit shaft resistance q_s mobilized in the cyclic loading stage of tests M0.5-CY0.5-F0.1-N100 (Δw_{cyclic} = 0.5 mm) and M0.5-CY1.5-F0.1-N100 (Δw_{cyclic} = 1.5 mm). In Figure 4.15, $q_{s,max}$ is the maximum unit shaft resistance mobilized in each cycle (i.e., the maximum value of q_s measured in each downward stroke), $q_{s,min}$ is the minimum unit shaft resistance mobilized in each cycle (i.e., the minimum value of q_s measured in each upward stroke), and $q_{s,0}$ is the unit shaft resistance mobilized in the pre-loading stage of the cyclic loading test. Table 4.4 provides the values of $q_{s,max}$ and $q_{s,min}$ measured in the first and last cycle of the tests, and the values of $q_{s,0}$ normalized by $q_{sL,BC}$. So long as w_{mean} does not exceed the displacement required to mobilize the limiting unit shaft resistance before cycling (i.e., w_L = 4.0 mm for dense sand, as shown in Figure 4.3), $q_{s,0}$ increases with increasing w_{mean}. For example, as provided in Table 4.4, for tests M0.5-CY0.25-F0.1-N100, M1.0-CY0.5-F0.1-N100 and M1.7-CY0.5-F0.1-N100, the value of $q_{s,0}$ is 0.19$q_{sL,BC}$, 0.4$q_{sL,BC}$, and 0.63$q_{sL,BC}$, respectively.

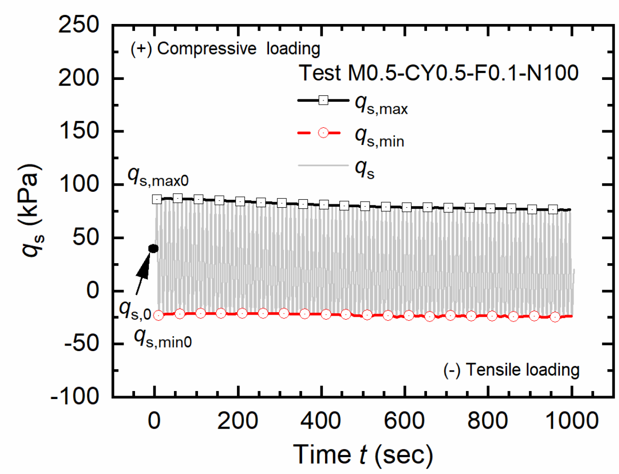

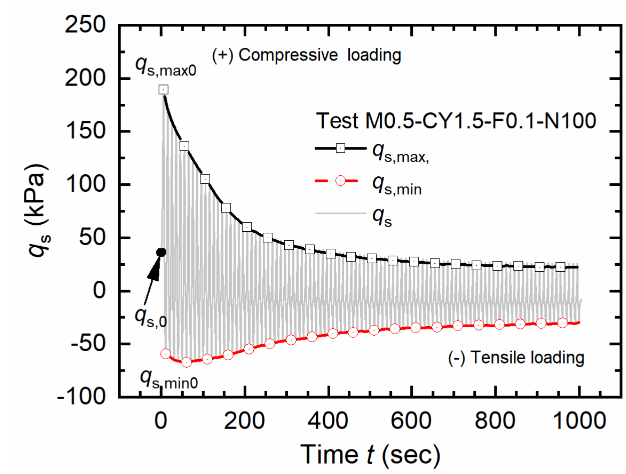

(a) (b)

Figure 4.15. Unit shaft resistance q_s mobilized during cyclic loading for tests: (a) M0.5-CY0.5-F0.1-N100 (Δw_{cyclic} = 0.5 mm) and (b) M0.5-CY1.5-F0.1-N100 (Δw_{cyclic} = 1.5 mm).

Figure 4.15(a) shows that for Δw_{cyclic} = 0.5 mm, $q_{s,max}$ and $q_{s,min}$ remain approximately constant with time (t <1000 sec). The value of $q_{s,max}$ ranges from 85.1 kPa (first peak) to 76.4 kPa (last peak), while the value of $q_{s,min}$ ranges from -23.3 kPa (first valley) to -24.0 kPa (last valley). In contrast, for Δw_{cyclic} = 1.5 mm [see Figure 4.15(b)], the magnitudes of $q_{s,max}$ and $q_{s,min}$ decrease with time. At the end of the cycling stage, $q_{s,max}$ is 11.7% of the maximum unit shaft resistance $q_{s,max0}$ measured in the first cycle, and $q_{s,min}$ is 50.7% of the minimum unit shaft resistance $q_{s,min0}$ measured in the first cycle.

Figure 4.16 shows $q_{s,max}$ normalized by $q_{sL,BC}$ in compression and $q_{s,min}$ normalized by $q_{sL,BC}$ in tension vs. number N_c of cycles for the same tests shown in Figure 4.15. As shown in Figure 4.16, the greater the value of Δw_{cyclic}, the greater the magnitude of $q_{s,max}/q_{sL,BC}$ and $q_{s,min}/q_{sL,BC}$ mobilized in the first cycle. Figure 4.16(a) shows that, for Δw_{cyclic} = 1.5 mm, 90% of $q_{sL,BC}$ is mobilized in the first cycle. In contrast, for Δw_{cyclic} = 0.25 mm, $q_{s,max}$ mobilized in the first cycle is only 25% of $q_{sL,BC}$. Similarly, Figure 4.16(b) shows that, for Δw_{cyclic} equal to 1.5 mm and 0.25 mm, $q_{s,min}$ mobilized in the first cycle is 50% and 5% of $q_{sL,BC}$ in tension, respectively.

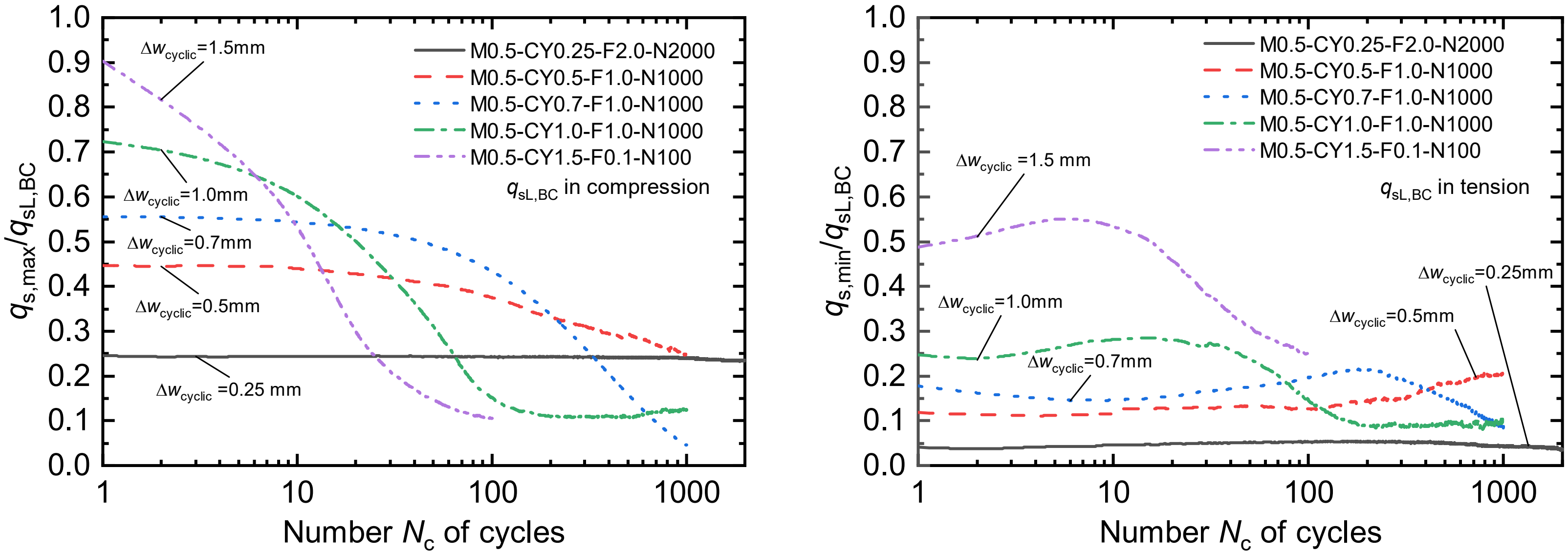

(a) (b)

Figure 4.16. Effect of number N_c of cycles and cyclic displacement half amplitude Δw_{cyclic} on the unit shaft resistance mobilization in cyclic loading: (a) maximum unit shaft resistance $q_{s,max}$ normalized by $q_{sL,BC}$ (in compression) vs. N_c and (b) minimum unit shaft resistance $q_{s,min}$ normalized by $q_{sL,BC}$ (in tension) vs. N_c.

Table 4.4. Unit shaft resistances mobilized in cyclic load tests

Test code	$q_{sL,BC}$ (kPa)	$q_{s,0}/q_{sL,BC}$	$q_{s,max0}$ (kPa)	$q_{s,min0}$ (kPa)	$q_{s,max}$ in last cycle (kPa)	$q_{s,min}$ in last cycle (kPa)
M0.5-CY0.25-F0.1-N100	225.3	0.19	66.8	1.4	63.5	-1.1
M0.5-CY0.25-F1.0-N1000	225.3	0.22	75.3	1.5	74.6	0.3
M0.5-CY0.25-F2.0-N2000	224.5	0.14	55.0	-5.3	52.7	-4.3
M1.0-CY0.5-F0.1-N100	214.9	0.40	152.0	-1.3	79.1	-29.6
M1.7-CY0.5-F0.1-N100	215.1	0.79	197.0	21.2	94.8	-15.9
M0.5-CY0.5-F1.0-N1000	198.0	0.20	84.3	-13.0	46.9	-22.3
M0.5-CY0.5-F0.1-N100	210.9	0.17	86.1	-23.3	76.5	-23.3
M0.7-CY0.5-F0.1-N100	227.5	0.31	147.5	-27.6	83.4	-30.4
M2.4-CY0.5-F0.1-N100	212.0	0.98	208.6	34.8	109.3	-5.8
M0.5-CY0.6-F0.1-N100	226.4	0.17	97.4	-17.5	87.0	-18.5
M0.5-CY0.7-F1.0-N1000	228.5	0.21	127.0	-23.5	20.4	-11.5
M0.5-CY0.7-F1.0-N100	225.5	0.16	111.7	-25.3	79.4	-30.0
M0.5-CY0.8-F0.1-N100	239.5	0.20	135.7	-25.0	64.8	-20.0
M1.7-CY0.85-F0.1-N100	214.0	0.63	202.2	-11.3	62.0	-25.7
M0.5-CY1.0-F0.1-N100	221.6	0.20	155.0	-29.9	45.3	-15.7
M1.0-CY1.0-F0.1-N100	210.2	0.27	147.4	-23.5	67.7	-32.8
M0.5-CY1.0-F1.0-N1000	217.0	0.21	156.9	-31.2	28.1	-12.4
M0.5-CY1.0-F1.0-N200	224.2	0.21	156.9	-29.5	26.7	-9.7
M0.5-CY1.2-F1.0-N100	227.3	0.20	177.8	-37.4	33.0	-25.7
M0-CY1.5-F0.2-N500	215.4	-0.07	78.3	-55.0	32.5	-17.6
M1.0-CY1.5-F0.2-N500	219.4	0.42	214.1	-51.2	41.5	-22.3
M0.5-CY1.5-F0.1-N100	209.6	0.19	189.2	-59.2	24.4	-31.3
M0.5-CY1.0-F0.1-N100(*)	82.5	0.38	75.3	-11.8	14.0	-6.3
M0.5-CY0.7-F0.1-N100(+)	320.8	0.17	140.0	-33.1	28.0	-19.1

Test code: M"#"= mean displacement w_{mean} followed by its value in mm, CY"#"= cyclic displacement half amplitude Δw_{cyclic} followed by its value in mm, N"#" = number N_c of cycles, F"#" = frequency f followed by its value in Hz.
$q_{sL,BC}$ is the limit unit shaft resistance measured from the compressive load test performed before cycling.
$q_{s,0}$ is the unit shaft resistance stress mobilized in the pre-loading stage of the cyclic load test (i.e., q_s for $w = w_{mean}$).
$q_{s,max}$ is the maximum unit shaft resistance mobilized in each cycle and $q_{s,min}$ is the minimum unit shaft resistance mobilized in each cycle of a cyclic load test.
$q_{s,max0}$ is the maximum unit shaft resistance mobilized in the first cycle and $q_{s,min0}$ is the minimum unit shaft resistance mobilized in the first cycle of a cyclic load test.

Figure 4.17 compares the curves of $q_{s,max}/q_{s,max0}$ ($q_{s,max0}$ is the value of $q_{s,max}$ measured in the first cycle) vs. number N_c of cycles for the same tests shown in Figure 4.16. Figure 4.17 shows that, within the first ten cycles, $q_{s,max}/q_{s,max0}$ decreases with increasing the number of cycles. The rate of reduction in $q_{s,max}/q_{s,max0}$ is higher as the cyclic displacement half amplitude Δw_{cyclic} increases. For Δw_{cyclic} = 0.25 mm, the changes in $q_{s,max}/q_{s,max0}$ are negligible, even after 2,000 cycles. For Δw_{cyclic} > 0.7 mm, $q_{s,max}/q_{s,max0}$ reaches a minimum value before 100 cycles and remains approximately constant as the number of cycles increases. For Δw_{cyclic} in the range of 0.5 mm and 0.7 mm, $q_{s,max}/q_{s,max0}$ may continue to decrease even after 1,000 cycles. Similar response during cyclic loading has been reported by Airey et al. (1992), Fakharian and Evgin (1997), DeJong et al. (2006), and Mortara et al. (2007) from interface shear box testing under constant normal stiffness.

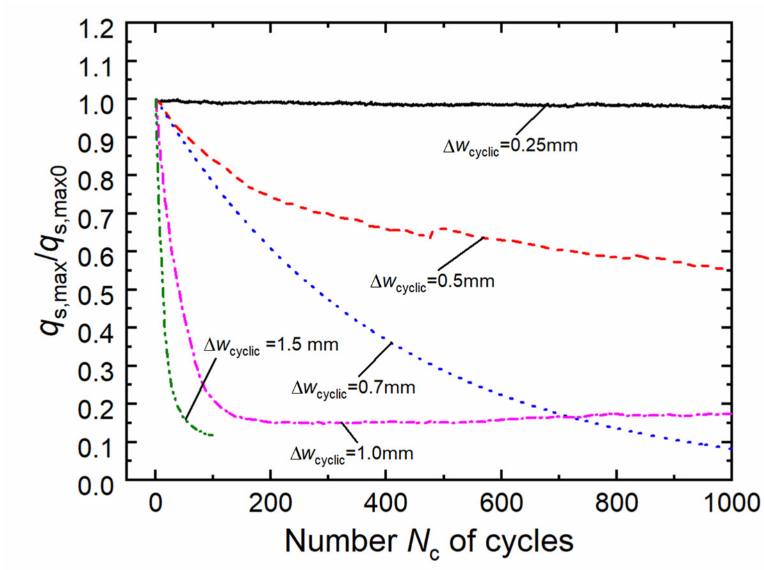

Figure 4.17. Maximum unit shaft resistance $q_{s,max}$ normalized by $q_{s,max0}$ vs. number N_c of cycles mobilized during cyclic load tests.

Displacement fields in the sand domain

Figure 4.18 shows the magnitude and direction of the soil displacement vectors after cyclic loading for tests M0.5-CY0.25-F0.1-N100, M0.5-CY0.5-F0.1-N100, M0.5-CY0.7-F0.1-N100, M0.5-CY1.0-F0.1-N100, and M0.5-CY1.5-F0.1-N100 (Δw_{cyclic} ranging from 0.25 mm to 1.5 mm and N_c = 100). The magnitude of the displacement vectors plotted in Figure 4.18 corresponds to the total displacement that a soil element experiences from the beginning to the end of a cyclic load test. As shown in Figure 4.18, the displacement vectors are plotted in z/r_p vs. r/r_p, space, where z is the vertical distance from the sample surface, r is the radial distance relative to the pile axis, and r_p is the radius of the model pile. The tail of the displacement vectors is located at the original position of the soil element (before cycling). The scale used for plotting the displacement vectors varied for each test. Only displacement vectors with magnitudes greater than 0.02 mm and smaller than the maximum displacement d_{max} measured within a zone limited by $6 < z/r_p < 11$ and $1.1 < r/r_p < 4.0$ are displayed in Figure 4.18. As shown in Figure 4.18, the value of d_{max} increases with increasing Δw_{cyclic} (i.e., d_{max} = 0.1 mm for test M0.5-CY0.25-N100-F0.1, and d_{max} =1.0 mm for test M0.5-CY1.5-N100-F0.1).

As can be seen in Figure 4.18(a), for Δw_{cyclic} = 0.25 mm, the displacement vectors are inclined at approximately 45 degrees and point downward. For Δw_{cyclic} = 0.5 mm, shown in Figure 4.18(b), and Δw_{cyclic} = 0.7 mm, shown in Figure 4.18(c), the displacement vectors are nearly horizontal and point towards the pile shaft. Soil elements located in the leftmost positions (at r/r_p=1.15 and $6 < z/r_p < 11$) for Δw_{cyclic} = 1.0 mm, shown in Figure 4.18(d), and Δw_{cyclic}=1.5 mm, shown in Figure 4.18(e), displaced primarily upwards in the vertical direction. Further out radially, the displacement vectors are oriented primarily in the radial direction, towards the pile shaft.

Figure 4.19(a) and Figure 4.19(b) show the average cumulative radial displacement u_{avg} and the average cumulative vertical displacement v_{avg}, respectively, along the pile shaft at r/r_p = 1.2, 1.5, and 4.0 and $6 < z/r_p < 11$ after cyclic loading. Positive values of radial displacement indicate that soil elements move away from the pile shaft, and negative values of radial displacement indicate that they move towards it. Vertical displacements are positive when soil elements move up and negative when they move down. As can be seen in Figure 4.19(a), for Δw_{cyclic} < 1.0 mm, the magnitude of u_{avg} increases with increasing Δw_{cyclic} and decreases with decreasing radial distance from the pile shaft. In Figure 4.19(b), the magnitude of v_{avg} becomes significant ($|v_{avg}| > 0.1$ mm) for Δw_{cyclic} > 1.0 mm. Figure 4.19(a) and (b) indicate that for large cyclic displacements (Δw_{cyclic} > 1.0 mm), the soil displacements close to the pile shaft (at r =1.2r_p) are predominantly vertical.

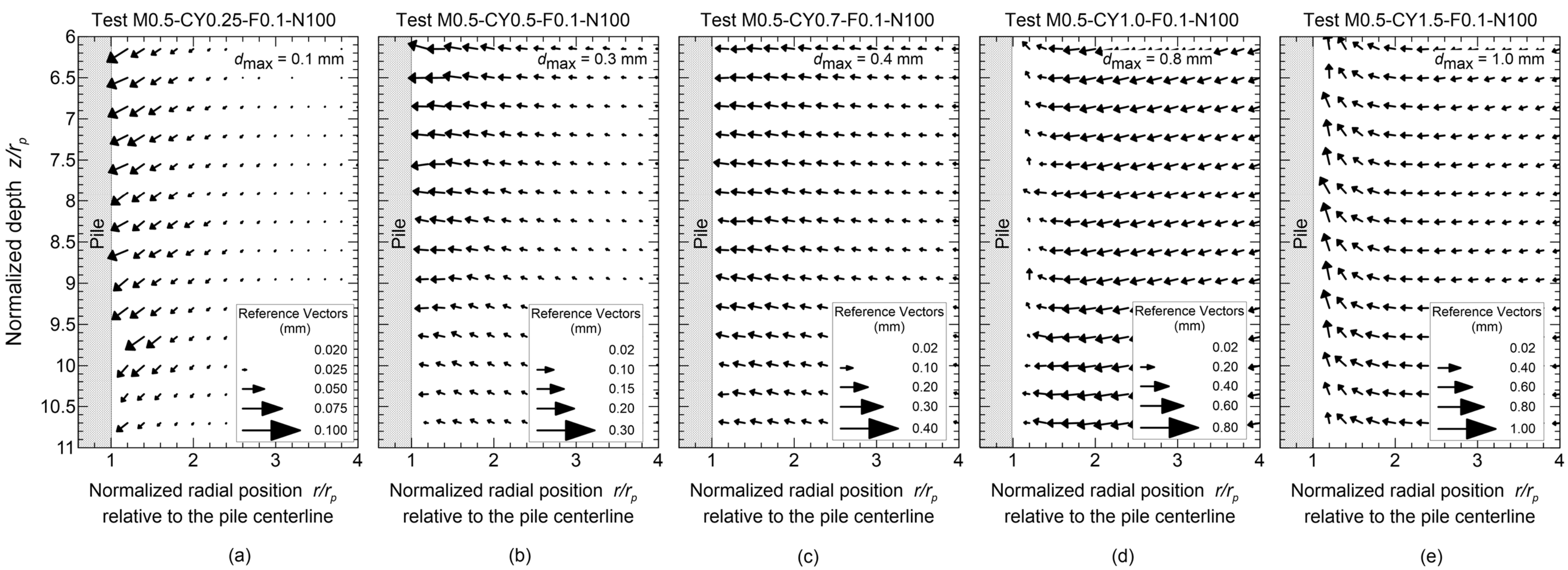

Figure 4.18. Soil displacement vectors after cyclic loading (100 cycles) for tests: (a) M0.5-CY0.25-F0.1-N100, (b) M0.5-CY0.5-F0.1-N100, (c) M0.5-CY0.7-F0.1N100, (d) M0.5-CY1.0-F0.1-N100, and (e) M0.5-CY1.5-F0.1-N100.

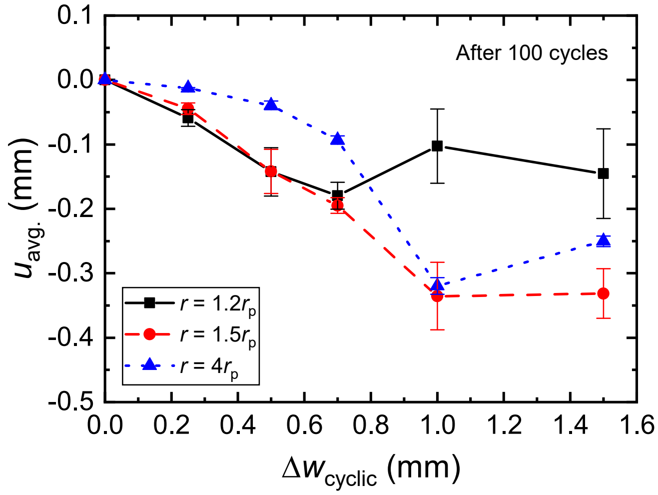

(a)

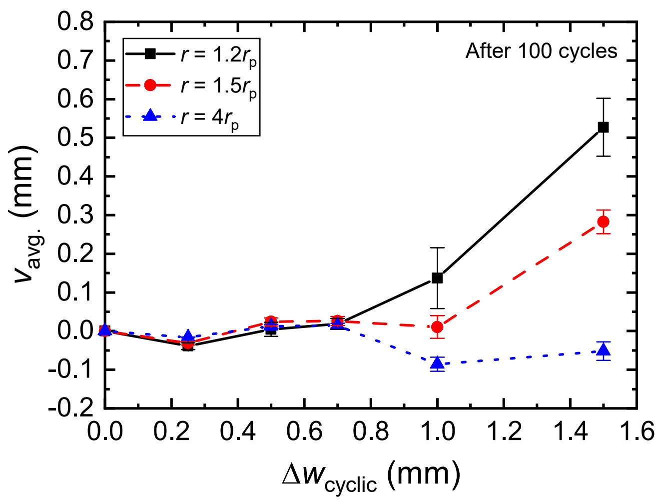

(b)

Figure 4.19. Average cumulative displacements along the pile shaft ($6 < z/r_p < 11$) at given radial positions r from the pile centerline vs. cyclic displacement half amplitude Δw_{cyclic}: (a) average cumulative radial displacement u_{avg} (positive values of radial displacement indicate that soil elements move away from the pile shaft, and negative values indicate that they move towards it) and (b) average cumulative vertical displacement v_{avg} (positive values of vertical displacement indicate that soil elements move up, and negative values indicate that they move down).

Figure 4.20 shows the evolution of the cumulative radial displacement u of soil elements located close to the pile shaft for the cyclic loading stage of tests M0.5-CY0.25-F0.1-N100, M0.5-CY0.5-F0.1-N100, M0.5-CY0.7-F0.1-N100, M0.5-CY1.0-F0.1-N100 and M0.5-CY1.5-F0.1-N100. The selected soil elements are at a radial distance $r = 1.5r_p = 46.2$ mm from the pile centerline (a distance equal to 15.5D_{50} from the pile shaft) and at a vertical distance z =9.5r_p (far away from the pile base and the sample surface). These soil elements are located outside the shear band (the average thickness t_s of the shear band = 3D_{50}) estimated in the compressive load test performed before cycling and outside the crushed particle zone (the average thickness t_{cb} of the crushed particle zone = 4D_{50}) resulting from pile installation. Figure 4.20 shows that the selected soil elements move towards the pile shaft during the cyclic loading stage of the tests. These results are consistent with the sand particle displacement measurements made during cyclic loading (Δw_{cyclic} = 0.5 mm = 0.035B = 0.44D_{50}) in a mini calibration chamber, using X-ray tomography and three-dimensional-digital image correlation, as reported by Doreau-Malioche et al. (2018).

The trends of cumulative radial displacement u vs. number N_c of cycles are also consistent with the $q_{s,max}/q_{s,max0}$ vs. N_c curves shown in Figure 4.17(b). The magnitude of the cumulative radial displacement u increases with increasing cyclic displacement half amplitude Δw_{cyclic}. For Δw_{cyclic} > 0.7 mm, most of the drop in the $q_{s,max}/q_{s,max0}$ and u values occurs in the first cycles (1cycle < N_c < 20 cycles). By the end of the cyclic tests (N_c=100 cycles), the gradients of $q_{s,max}/q_{s,max0}$ vs. N_c lie between 2.3x10^{-3}/cycle (for Δw_{cyclic}= 1.0 mm) and 1.6x10^{-4}/cycle (for Δw_{cyclic} = 1.5) and $|u|$ of the soil elements close to the pile shaft stabilizes at $|u|$ = 0.3 mm. According to DeJong et al. (2006), the cumulative radial displacement no longer changes when the soil at the interface reaches a minimum void ratio. This was confirmed by Doreau-Malioche et al. (2018) based on porosity measurements at a sand-pile interface using x-ray tomography.

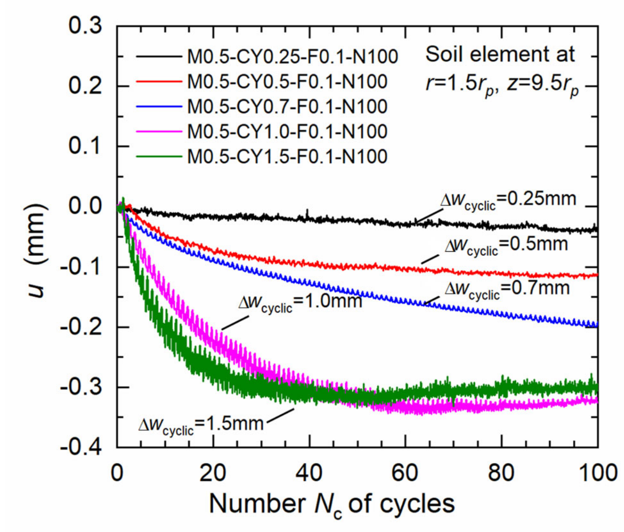

Figure 4.20. Cumulative radial displacement u (positive when soil elements move away from the pile shaft and negative when they move towards it) vs. N_c of soil elements located initially at $r = 1.5r_p$ and $z = 9.5r_p$ during cyclic loading for tests M0.5-CY0.25-F0.1-N100, M0.5-CY0.5-F0.1-N100, M0.5-CY0.7-F0.1-N100, M0.5-CY1.0-F0.1-N100, and M0.5-CY1.5-F0.1-N100.

The oscillations shown in the profiles of u (shown in Figure 4.20) are indicative of the amplitude of the radial displacement induced in the sand during each cycle. As expected, the amplitude of the oscillations is greater for tests with large cyclic displacement half amplitudes (i.e., Δw_{cyclic} =1.0 mm and 1.5 mm) than for small cyclic displacement half amplitudes (i.e., Δw_{cyclic} =0.25 mm, 0.5 mm, and 0.7 mm).

Figure 4.21(a) to Figure 4.21(e) show the cumulative vertical displacement v vs. number N_c of cycles of soil elements located initially at $r = 1.5r_p$ and $z = 9.5r_p$ in the cyclic loading stage of tests M0.5-CY0.25-F0.1-N100, M0.5-CY0.5-F0.1-N100, M0.5-CY0.7-F0.1-N100, M0.5-CY1.0-F0.1-N100 and M0.5-CY1.5-F0.1-N100, respectively. Figure 4.21(a) to Figure 4.21(c) show that the magnitude of cumulate vertical displacement develop during and at the end of cyclic loading stage (after 100 cycles) in tests M0.5-CY0.25-F0.1-N100 (Δw_{cyclic}=0.25 mm), M0.5-CY0.5-F0.1-N100 (Δw_{cyclic}= 0.5 mm) and M0.5-CY0.7-F0.1-N100 (Δw_{cyclic}= 0.7 mm) is negligible ($|v| < 0.05$ mm). On the other hand, for tests M0.5-CY1.0-F0.1-N100 (Δw_{cyclic}=1.0 mm), shown in Figure 4.21(d), and M0.5-CY1.5-F0.1-N100 (Δw_{cyclic}=1.5mm), shown in Figure 4.21(e), the cumulative vertical displacement can reach values as high as 10% and 20% of Δw_{cyclic}, respectively.

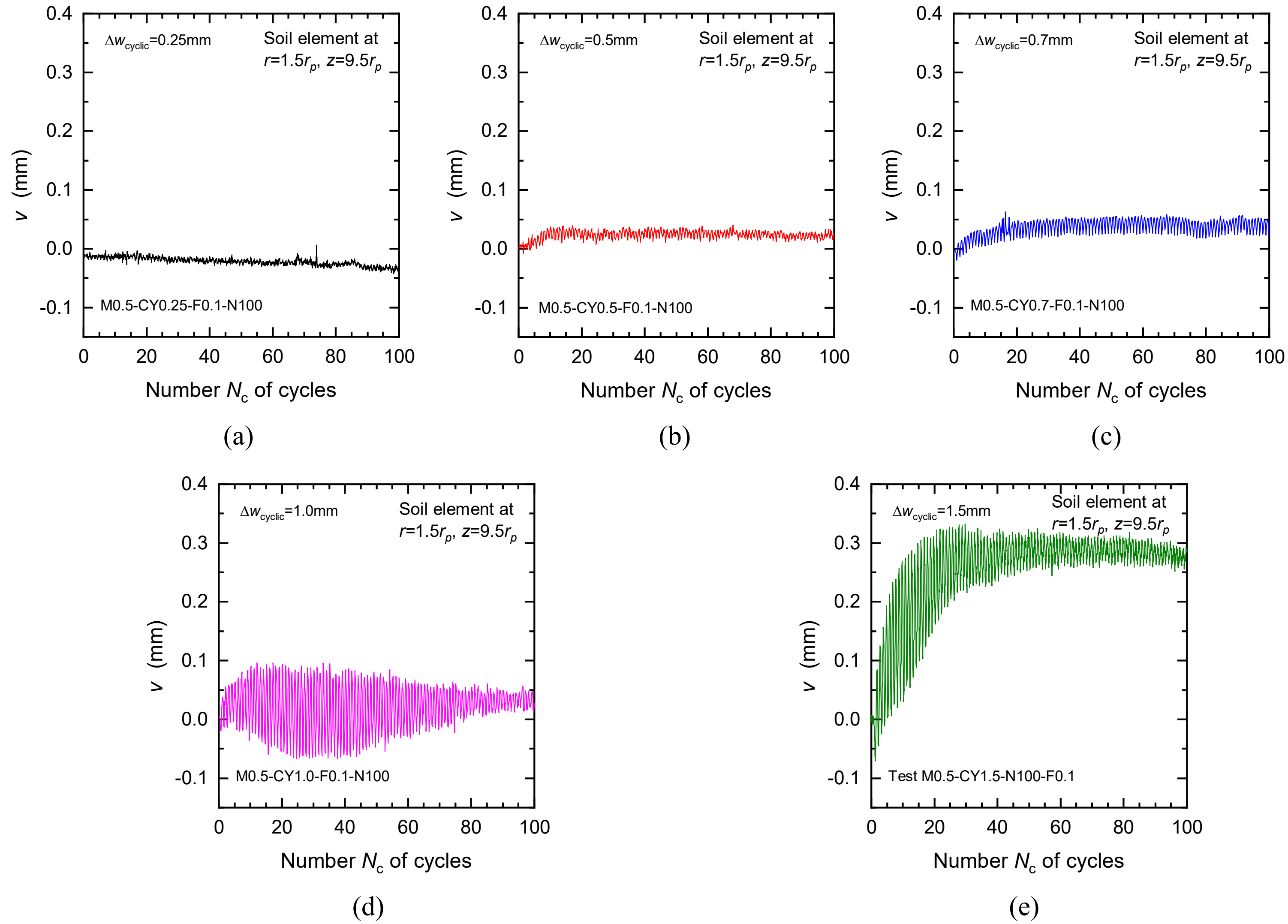

Figure 4.21. Cumulative vertical displacement v (positive when soil elements move up and negative when they move down) vs. N_c of soil elements located initially at $r = 1.5r_p$ and $z = 9.5r_p$ during cyclic loading for tests: (a) M0.5-CY0.25- F0.1- N100, (b) M0.5-CY0.5-F0.1-N100, (c) M0.5-CY0.7 -F0.1-N100, (d) M0.5-CY1.0-F0.1-N100, and (e) M0.5-CY1.5-F0.1-N100.

For the tests M0.5-CY1.0-F0.1-N100 and M0.5-CY1.5-F0.1-N100, the decrease in $q_{s,max}/q_{s,max0}$ with increasing number of cycles (see Figure 4.17) is also accompanied by the development of cumulative radial displacements (see Figure 4.20) and vertical displacements for soil elements near the pile-soil interface (see Figure 4.21(d) and (e)). These observations are consistent with the cyclic simple-shear behavior of sand-steel interfaces under CNS conditions reported by Fakharian (2001) and Fakharian and Evgin (1997).

Strain field in the sand domain

The Green–St Venant strain tensor is obtained using the continuum mechanics formulation implemented in the post-processing tool of the VIC-2D software (Sutton et al., 2009). The solid mechanics sign convention is followed, so that positive cumulative radial strain E_{rr} represents radial stretching of the soil element, whereas negative cumulative radial strain E_{rr} indicates the opposite, radial compression. Figure 4.22 shows the contours of cumulative radial strain E_{rr} after cyclic loading for the tests ended at 100 cycles and performed with cyclic displacement half amplitudes Δw_{cyclic} of 0.25 mm (test M0.5-CY0.25-F0.1-N100), 0.5 mm (test M0.5-CY0.5-F0.1-N100), 1.0 mm (test M0.5-CY1.0-F0.1-N100), and 1.5 mm (test M0.5-CY1.5-F0.1-N100). After 100 cycles, the soil elements near the pile shaft (at $r > 1.2r_p$) exhibit negligible cumulative radial strains ($|E_{rr}| < 0.04$ %) for $\Delta w_{cyclic} = 0.25$mm. For $\Delta w_{cyclic} > 0.25$ mm, as shown in Figure 4.22(b), (c), and (d), the soil elements located close to the pile shaft contract radially (i.e., $E_{rr} < 0$). The zone of soil elements undergoing contraction extends further out radially as Δw_{cyclic} increases. Outside the contractive zone, the soil elements stretch slightly ($|E_{rr}| < 0.4$ %).

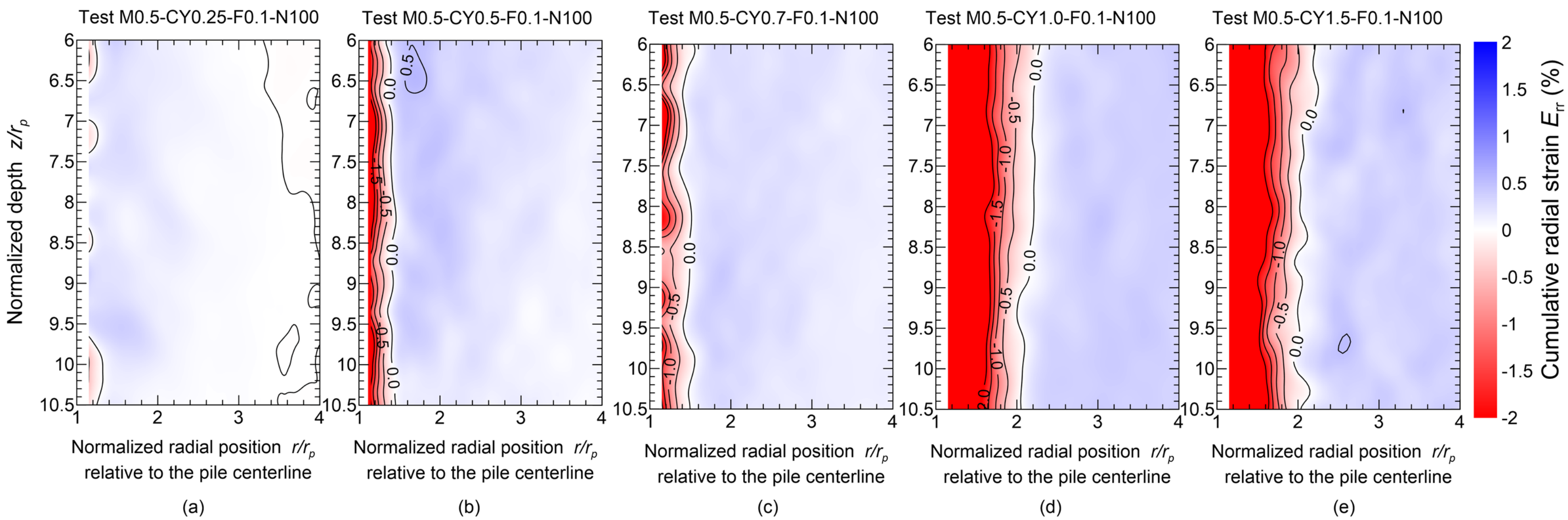

Figure 4.22. Contours of cumulative radial strain E_{rr} (positive for radial stretching and negative for radial compression) at the end of cyclic loading for tests: (a) M0.5-CY0.25-N100-F0.1, (b) M0.5-CY0.5-N100-F0.1, (c) M0.5-CY0.7-N100-F0.1, (d) M1.0-CY0.25-N100-F0.1, and (e) M0.5-CY1.5-N100-F0.1

Figure 4.23 shows the evolution of the cumulative radial strain E_{rr} of soil elements at r = 1.5r_p and z = 9.5r_p during cyclic loading for the same tests shown in Figure 4.22. For tests M0.5-CY0.5-F0.1-N100 (Δw_{cyclic} = 0.5 mm) and M0.5-CY0.7-F0.1-N100 (Δw_{cyclic} = 0.7 mm), the soil elements under consideration are located outside the contractive zone (r < 1.5r_p) and exhibit small dilation (E_{rr} < 0.4 %) at the end of cyclic loading. On the other hand, for tests M0.5-CY1.0-F0.1-N100 (Δw_{cyclic} = 1.0 mm) and M0.5-CY1.5-F0.1-N100 (Δw_{cyclic} = 1.5 mm), after 10 cycles, the soil elements contract radially, with the magnitude of E_{rr} increasing as cycling progress. The cumulative radial strain E_{rr} of the soil elements at the end of cyclic loading is -2.2% for Δw_{cyclic} =1.0 mm and -2.8% for Δw_{cyclic} = 1.5 mm.

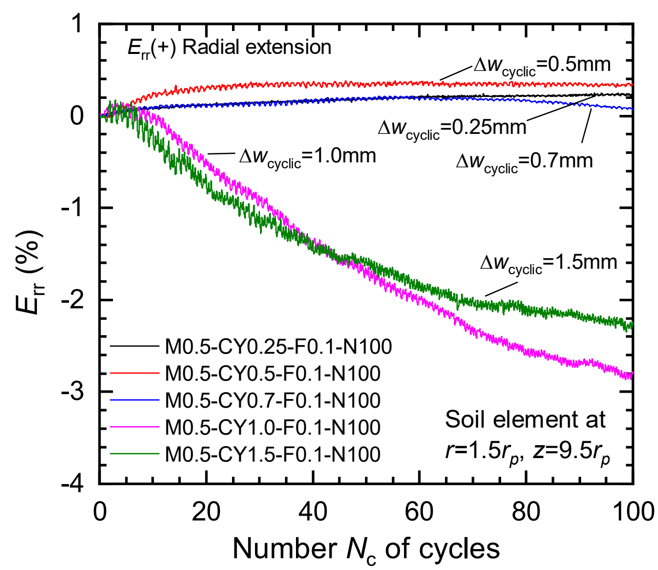

Figure 4.23. Cumulative radial strain E_{rr} vs. N_c of soil elements located initially at r = 1.5r_p and z = 9.5r_p during cyclic loading for tests: M0.5-CY0.25-F0.1-N100, M0.5-CY0.5-F0.1-N100, M0.5-CY0.7-F0.1-N100, M0.5-CY1.0-F0.1-N100, and M0.5-CY1.5-F0.1-N100 .

Figure 4.24 shows the contours of cumulative shear strain E_{rz} at the end of cyclic loading (100 cycles) for the same tests shown in Figure 4.22. Figure 4.24(a) shows negligible cumulative shear strain ($|E_{rz}|$ < 0.01%) near the pile shaft (6 < z/r_p < 11 and 1.1 < r/r_p < 4.0) after 100 displacement cycles with Δw_{cyclic} = 0.25 mm. As shown in Figure 4.24(b) and (c), for Δw_{cyclic} = 0.5 mm and 0.7 mm, the cumulative shear strain E_{rz} does not develop evenly along the length of the pile shaft. Instead, the values of E_{rz} vary from -0.6% to 1.0% at r = 1.2r_p. On the other hand, for

Δw_{cyclic} = 1.0 mm (Figure 4.24 (d)) and 1.5 mm (Figure 4.24 (e)), the cumulative shear strain E_{rz} develops almost evenly along the pile shaft at r/r_p >1.1. At the end of cyclic loading, the average cumulative shear strain E_{rz} at r =1.2r_p is -3.3% for Δw_{cyclic}=1.0 mm and -4.3% for Δw_{cyclic} =1.5 mm. In general, for Δw_{cyclic} > 0.5 mm, the greater the value of Δw_{cyclic}, the larger the magnitude of the cumulative shear strain E_{rz} is. Similarly, as Δw_{cyclic} increases, more soil elements located further out radially exhibit distortion.

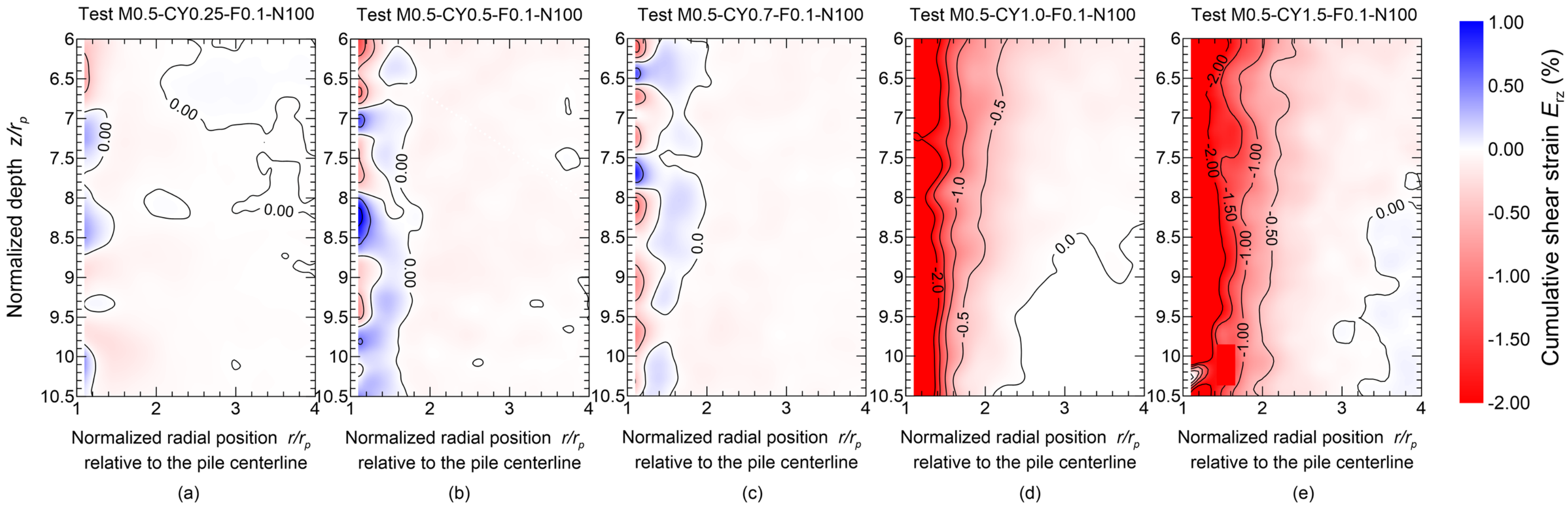

Figure 4.24 Contours of cumulative shear strain E_{rz} at the end of cyclic loading for tests: (a) M0.5-CY0.25-F0.1-N100, (b) M0.5-CY0.5-F0.1-N100, (c) M0.5-CY0.7-F0.1-N100, (d) M0.5-CY1.0-F0.1-N100, and (e) M0.5-CY1.5-F0.1-N100.

Figure 4.25 shows the evolution of shear strain E_{rz} of soil elements at $r = 1.5r_p$ and $z = 9.5r_p$ during cycling for tests M0.5-CY0.25-F0.1-N100, M0.5-CY0.5-F0.1-N100, M0.5-CY0.7-F0.1-N100, M0.5-CY1.0-F0.1-N100, and M0.5-CY1.5-F0.1-N100. For test M0.5-CY0.25-F0.1-N100 (Δw_{cyclic} =0.25 mm), the cumulative shear strain E_{rz} develops during the 100 cycles is negligible ($|E_{rz}|$ < 0.1%). The magnitude $|E_{rz}|$ of the cumulative shear strain increases only slightly as the number of cycles increases for Δw_{cyclic} = 0.5 mm and 0.7 mm (i.e., $|E_{rz}|$ < 0.2 % for N_c =100 cycles). However, for Δw_{cyclic} = 1.0 mm and 1.5 mm, the $|E_{rz}|$ increases with increasing N_c and then it stabilizes at 60 and 30 cycles, respectively. Note that $q_{s,max}$ (see curves for Δw_{cyclic} = 1.0 mm and 1.5 mm in Figure 4.16) reaches minimum values almost at the same time as the magnitude $|E_{rz}|$ of the cumulative shear strain stabilizes (i.e., $|E_{rz}| \approx 1.2\%$ for N_c >60 cycles in test M0.5-CY1.0-F0.1-N100 and $|E_{rz}| \approx 2.2\%$ for N_c >30 cycles in test M0.5-CY1.5-F0.1-N100).

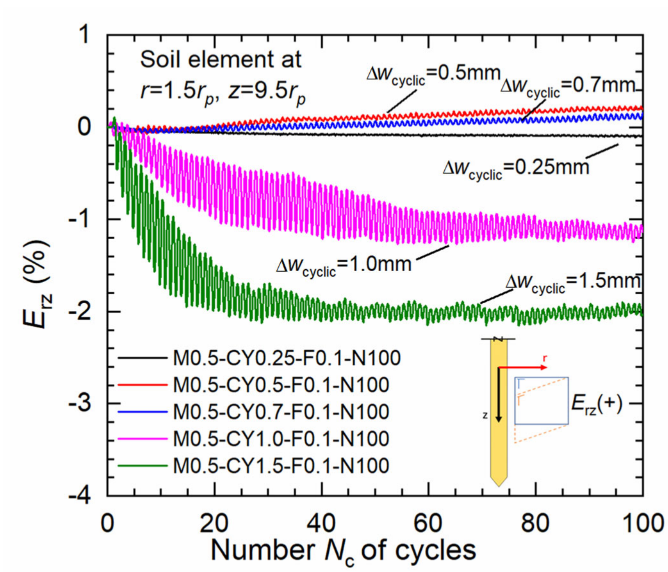

Figure 4.25. Cumulative shear strain E_{rz} vs. N_c of soil elements located initially at $r = 1.5r_p$ and $z = 9.5r_p$ during cyclic loading for tests: M0.5-CY0.25-F0.1-N100, M0.5-CY0.5-F0.1-N100, M0.5-CY0.7-F0.1-N100, M0.5-CY1.0-F0.1-N100, and M0.5-CY1.5-F0.1-N100.

Based on the digital image analysis results, degradation of the limit unit shaft resistance after cyclic loading is caused by significant contraction near the shaft-pile interface as well as development cumulative shear strains near the pile shaft during cyclic loading.

4.4.2.2 Effect of relative density

Unit shaft resistance mobilization

Figure 4.26(a) and Figure 4.26(b) show the maximum unit shaft resistance $q_{s,max}$ normalized by $q_{s,max0}$ and the minimum unit shaft resistance $q_{s,min}$ normalized by $q_{s,min0}$ vs. N_c for tests in dense (test M0.5-CY1.0-F0.1-N100) and medium-dense sand (test M0.5-CY1.0-F0.1-N100$^{(*)}$). The cyclic displacement half amplitude and number of cycles for these tests are the same. From Figure 4.26(a), it can be seen that, for medium-dense sand, the value of $q_{s,max}/q_{s,max0}$ and $q_{s,min}/q_{s,min0}$ drops to a minimum value of 0.20 and 0.50, respectively. For dense sand, $q_{s,max}/q_{s,max0}$ and $q_{s,min}/q_{s,min}$ reach minimum values of 0.30 and 0.50, respectively. The decrease in $q_{s,max}/q_{s,max0}$ and $q_{s,min}/q_{s,min0}$ occurs at a faster rate in medium-dense sand than in dense sand. These results are in agreement with observations from CNS interface cyclic tests by Tabucanon et al. (1995) who showed that the maximum normal and shaft shear stress mobilized in each cycle drops faster in loose sand than in dense sand.

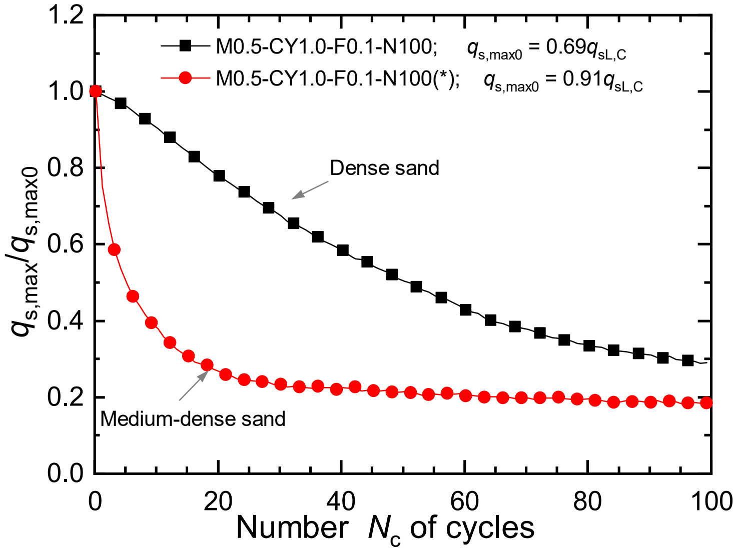

(a)

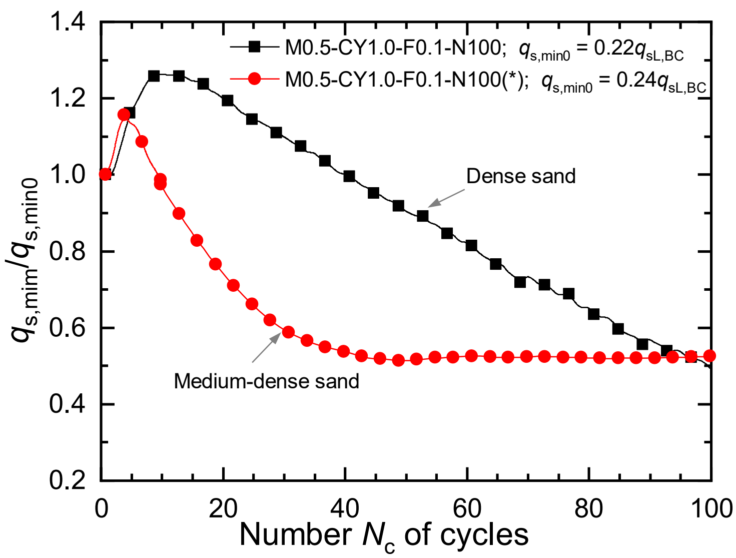

(b)

Figure 4.26. Effect of relative density D_R on the evolution of unit shaft resistance mobilized during cyclic loading: (a) normalized maximum unit shaft resistance $q_{s,max}/q_{sL,BC}$ vs. N_c, and (b) normalized minimum unit shaft resistance $q_{s,min}/q_{sL,BC}$ vs. N_c.

Strain paths for selected soil elements

Figure 4.27(a) and Figure 4.27(b) show the strain paths in terms of radial strain E_{rr} vs. shear strain E_{rz} for a soil element located at $r = 1.5r_p$ and $z = 9.5r_p$ during cyclic loading for tests M0.5-CY1.0-F0.1-N100 and M0.5-CY1.0-F0.1-N100$^{(+)}$, respectively. For the soil element under consideration, the magnitude of the cumulative shear strain E_{rz} after 100 cycles is 3.0 times greater in medium-dense sand (i.e., $|E_{rz}|$= 1.8 %) than in dense sand (i.e., $|E_{rz}|$= 0.6 %). Similar observations can be made for the cumulative radial strain E_{rr}; at the end of cyclic loading, the magnitude of the radial strain E_{rr} is 3.9% in medium-dense sand and 2.9% in dense sand. Figure 4.27(a) shows that the radial strain E_{rr} begins to decrease after only 5 cycles in dense sand. Figure 4.27(b) shows that the radial strain E_{rr} accumulates mainly within the first 20 cycles in medium-dense sand.

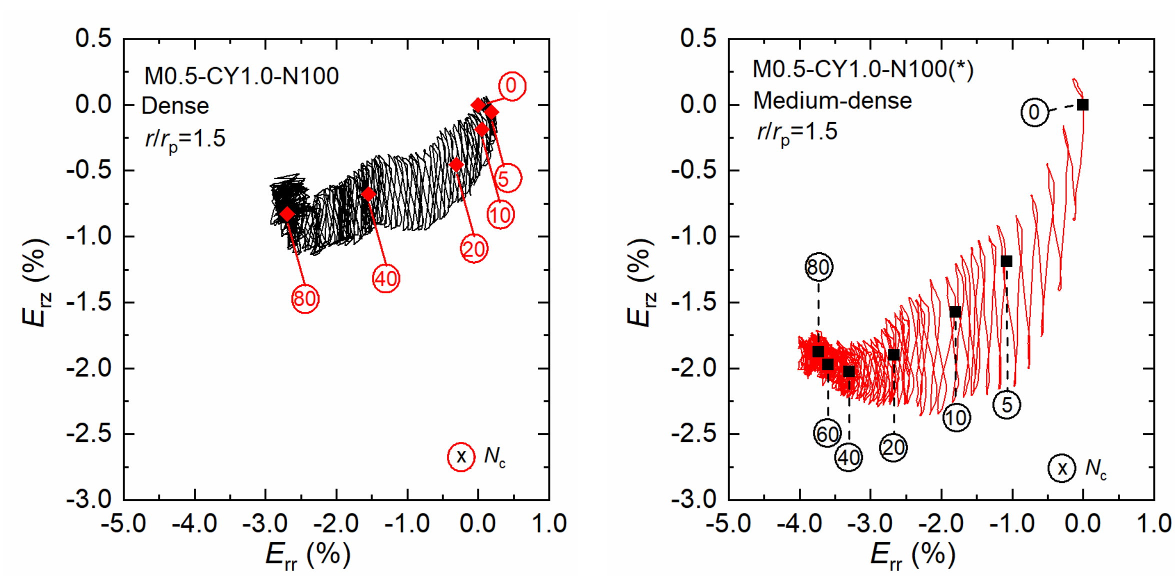

(a) (b)

Figure 4.27. Strain paths of soil elements located at r=1.5r_p and z =9.5r_p during cyclic loading of tests: (a) M0.5-CY1.0-F0.1-N100, and (b) M0.5-CY1.0-F0.1-N100$^{(+)}$.

4.5 Summary and conclusions

This paper presented the results of monotonic and cyclic load tests performed on a model pile jacked into a half-cylindrical calibration chamber filled with silica sand. The tests involved four loading stages: (1) pile installation, (2) compressive load test before cyclic loading, (3) displacement-controlled cyclic loading, and (4) compressive load test after cyclic loading. Digital images of the pile shaft and the surrounding sand were captured during the cyclic load tests and later processed using the DIC technique to generate the displacement and strain fields in the sand domain around the model pile shaft.

Results from the compressive load tests showed that the mean displacement w_{mean} and frequency f of the cyclic loading have a minimal to negligible influence on the post-cyclic unit shaft resistance response.

When the cyclic load tests are performed using 100 cycles with cyclic displacement half amplitudes Δw_{cyclic} smaller than 0.7 mm, the limit unit shaft resistance measured in the compressive load test performed before and after cyclic loading are comparable. On the other hand, for cyclic load tests (100 cycles) performed with cyclic displacement half amplitudes Δw_{cyclic} in the 0.7 mm-to-1.5 mm range, the limit unit shaft shear resistance after cycling decreases (up to 30% for Δw_{cyclic} =1.5 mm).

The effect of the number of cycles on the post-cyclic unit shaft resistance depends on the magnitude of the cyclic displacement amplitude. For cyclic load tests performed with a cyclic displacement half amplitude Δw_{cyclic} smaller than or equal to 0.25 mm, the unit shaft resistance ratio $q_{s,AC}/q_{sL,BC}$ corresponding to a pile head displacement of 4.0 mm (pile head displacement required to mobilize the limit unit shaft resistance before cycling in dense sand) is 1.0 after 100, 1,000 or 2,000 cycles indicating a negligible effect of the number of cycles on the post-cyclic unit shaft resistance. However, for cyclic load tests performed with a cyclic displacement half amplitude greater than 0.25 mm, $q_{s,AC}/q_{sL,BC}$ decreases with increasing the number of cycles. The value of $q_{s,AC}/q_{sL,BC}$ decreases at a higher rate as the cyclic displacement half amplitude increases. For Δw_{cyclic} = 1.0 mm, $q_{s,AC}/q_{sL,BC}$ reduces to 0.48 after 100 cycles and to 0.40 after 200 cycles. Then, $q_{s,AC}/q_{sL,BC}$ tends to stabilize to a minimum value of about 0.35 for a number of cycles greater than 200 cycles.

The mobilization of the unit shaft resistance during monotonic and cyclic loading also depends on the relative density of the sand and the stress state of the soil (studied through the application of surcharge). For 100 cycles, the drop in limit unit shaft resistance after cyclic loading is more significant in medium-dense sand (it decreased to 34% $q_{s,LBC}$) than in dense sand (it decreased to 48 % of $q_{s,LBC}$). Moreover, for dense sand, the degradation of the limit unit shaft resistance is greater under a surcharge of 90 kPa (it decreased to 44% of $q_{s,LBC}$) than under a surcharge of 50 kPa (it decreased to 59 % of $q_{s,LBC}$).

The DIC results showed that for cyclic loading tests performed with a small cyclic displacement half amplitude (e.g., 100 cycles with $\Delta w_{cyclic} < 0.7$ mm), soil elements near the pile shaft exhibit only a small radial contraction (i.e., $|E_{rr}| < 0.2\%$) and a negligible cumulative shear strain (i.e., $|E_{rz}| < 0.2\%$). In contrast, for cyclic loading tests performed with large cyclic displacement half amplitudes (e.g., 100 cycles with $\Delta w_{cyclic} > 0.7$ mm), the magnitude of the cumulative radial and shear strains increases with increasing Δw_{cyclic}. The decrease in the limit unit shaft resistance was linked to the development of large net radial contraction ($E_{rr} < 0$) and cumulative shear strain ($|E_{rz}| > 0.1$ %) of soil elements near the pile shaft during cyclic loading.

5. EFFECT OF CYCLIC LOADING ON THE MOBILIZATION OF UNIT BASE RESISTANCE OF MODEL PILES JACKED IN SAND

This chapter will be submitted to a peer-reviewed journal for publication.

5.1 Abstract

In this paper, we report the results of a series of monotonic compressive and cyclic load tests performed on a closed-ended jacked model pile installed in a half-cylindrical calibration chamber with image analysis capabilities. The monotonic compressive load tests were carried out before and after the performance of a displacement-controlled cyclic load test to determine the impact of cycling on unit base resistance. Digital images of the sand and the model pile were taken during cyclic loading and processed using the digital image correlation (DIC) technique to obtain the cumulative displacement and strain fields in the sand domain. The results show that the ultimate unit base resistance can drop significantly after cycling. The magnitude of the drop in ultimate unit base resistance depends on both the magnitude of the cyclic displacement amplitude and the number of cycles. However, the unit base resistance at plunging increases after large-displacement half amplitude cycling. The DIC-processed data shows that the displacements in the soil domain relative to the cyclic displacement half amplitude increase as the cyclic displacement half amplitude increases. The increase in unit base resistance at plunging after cycling is linked to the addition of sand particles below the conical base, the occurrence of sand particle crushing, and the dilative behavior of the sand outside a bulb of crushed particles formed during cyclic loading.

Keywords: Sand; Model piles; Cyclic loading

5.2 Introduction

Tripod and jacket structures are frame structures with three- or four-legs, each supported on an individual monopile (Gavin et al. 2011). This type of pile foundation is often selected for offshore wind turbines at depths ranging from 30 to 70 m (Achmus 2010; Bhattacharya et al. 2017; Gavin et al. 2011). Due to the low self-weight of these offshore structures, it is likely that the piles will experience complete load reversals (from tension to compression and back) when subjected to wind and wave loading. When the piles of a jacket/tripod structure are short and rigid, the load cycles can have a significant impact on pile base resistance, and consequently on the overall response of the pile.

The boundary-element continuum method [e.g., Lee & Poulos (1993) and Poulos (1989)] and the load-transfer method [e.g., Randolph and Jewell (1989) and Chin and Poulos (1991)] are often used in practice for cyclic axial loading analyses of pile foundations. These methods use simple empirical rules or criteria to simulate pile-soil interaction and predict the effects of cyclic loading on pile response; these effects are degradation of pile capacity and accumulation of permanent displacements. The input parameters in these methods are selected based on engineering judgment, and, in some cases, predictions are validated or calibrated with laboratory- and or field-scale pile load test data (Atkinson Consultants 2000; Chin and Poulos 1992; Poulos 1989b; Seidel and Coronel 2011; Stuyts et al. 2012). However, limited experimental data are available to validate predictions considering the effects of cyclic loading on pile base resistance.

The majority of the reported field pile load tests of displacement piles in sand performed to investigate the effects of cyclic loading on their static capacity (Jardine and Standing 2012, 2000) have focused on the tensile shaft capacity. However, results from multiple compressive static and cyclic load tests on bored piles in sand (Puech 2013) have shown that the total compressive pile capacity can, in some cases, increase after cyclic loading. Puech (2013) suggested that the increase of the total pile capacity is a consequence of a substantial increase in pile base capacity that compensates the loss in shaft capacity; he argued that progressive densification of the sand below the pile base is the cause of this increase.

The effects of cyclic loading on the static base resistance of piles have been investigated through model pile experiments in calibration chambers (Le Kouby et al. 2004) and centrifuges (Blanc et al. 2015; Li et al. 2012). Le Kouby et al. (2004) showed that the static base resistance of jacked and preinstalled model piles decreases after performance of a displacement-controlled cyclic load test with amplitudes varying from 0.1 mm (= $0.005B=0.5D_{50}$) to 2.0 mm (= $0.1B=4D_{50}$). Li et al. (2012) did not observe any influence of the cyclic displacement, which ranged from 0.0005 mm (= $3.94\text{x}10^{-5}B$ $=2.29\text{x}10^{-3}D_{50}$) to 0.0013 mm (= $1.02\text{x}10^{-4}B$ $=5.96\text{x}10^{-3}D_{50}$), on the ultimate base resistance of jacked piles. These results do not address how the magnitude of the cyclic displacement and the number of cycles affect the mobilization of the static unit base resistance.

Image-based deformation techniques in geotechnical modeling have been used to understand and quantify soil deformation in the boundary-value problems of geomechanics. Study of the cone penetration problem (Arshad et al. 2014; Paniagua et al. 2013), pile installation (Boccalini et al. 2015; Chen et al. 2016; White and Bolton 2004), static pile loading (Galvis-Castro et al. 2019a; b; Tehrani et al. 2016; Tovar-Valencia et al. 2018), and cyclic loading (Doreau-Malioche et al. 2019) are some applications of image analysis in this context.

This paper presents the results of a series of monotonic compressive and cyclic displacement-controlled load tests performed on a model pile jacked in silica sand in a half-cylindrical calibration chamber with Digital Image Correlation (DIC) capabilities. We consider the effects of cyclic displacement amplitudes and number of cycles on the unit base resistance of the model pile. We also present strain and displacement fields in the sand domain around the conical base of the model pile and discuss the primary mechanisms controlling the response of the pile base to cyclic loading.

5.3 Materials and methods

5.3.1 Test equipment

Model pile tests were performed in a half-cylindrical calibration chamber at Purdue University, USA (see Figure 5.1). Details of the chamber and the testing equipment are provided in Table 5.1. The front wall of the chamber contains three observation windows that allow capturing of digital images of the model pile and the surrounding soil during model pile load testing. The model pile consists of an instrumented half-circular rod with a conical base. The installation and the monotonic and cyclic loadings of the model pile were performed using a hydraulic actuator mounted on a removable steel frame, as shown in Figure 5.1.

Table 5.1. Equipment components (Adapted from Tovar-Valencia 2019)

Component	Details
Calibration chamber	Half-cylindrical calibration chamber with DIC capabilities
• Diameter *D*	1680 mm
• Height *H*	1200 mm
• Observation windows	300 mm (width) x 250 mm (height)
Model pile	Half-circular brass rod with conical tip (60°-apex angle)
• Pile diameter *B*	38.1 mm
• Pile length *L*	800 mm
• D/B [(a)]	44.1
• B/D_{50} [(b)]	61.4
Surcharge device	Inflatable rubber bladder at the top of the sample
Digital cameras & lenses	1 per observation window
• Camera type	CMOS [(c)] cameras
• Camera resolution	12 Megapixels
• Lenses	60 mm focal length, low distortion
• Image capture rate	Up to 20 pictures per second
Lighting system	Two fluorescent (55W) + 2 LED (42 W) lights

[a] Boundary conditions as described in Ghionna and Jamiolkowski (1991) and Salgado et al. (1998).
[b] Scale effects on base resistance. B/D_{50} should be more than 20 (Gui and Bolton 1998; Salgado 2013).
[c] Complementary Metal-Oxide Semiconductor cameras.

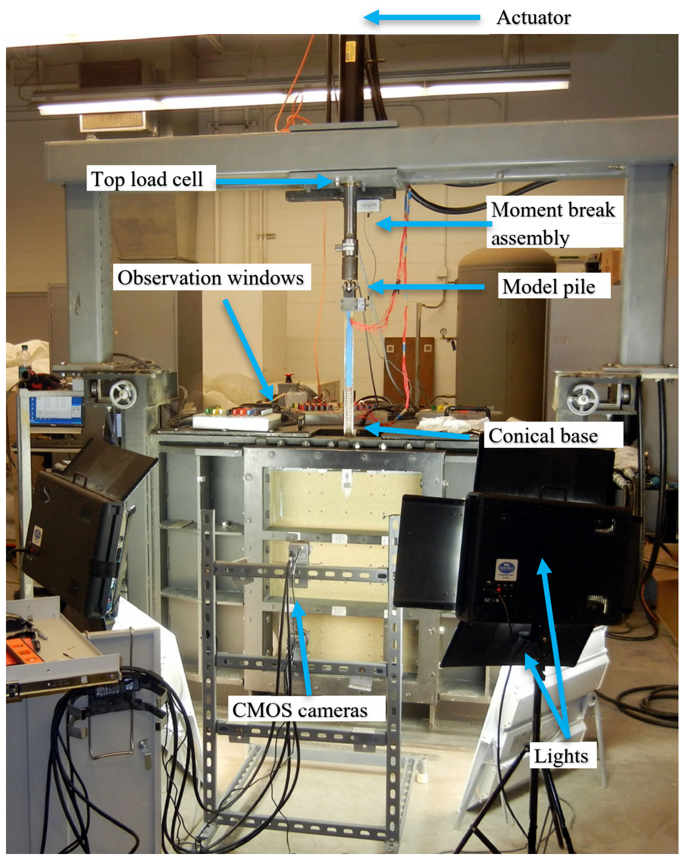

Figure 5.1. Experimental setup at the Bowen Laboratory – Purdue University, USA.

5.3.2 Test sand

Ohio Gold Frac sand, a poorly-graded silica sand (SiO_2=99.7%) with a mean particle size D_{50} of 0.62 mm, was the sand used for sample preparation. The index properties and the values of the roundness and sphericity parameters of Ohio Gold Frac sand are summarized in Table 5.2.

Table 5.2. Index properties of Ohio Gold Frac sand

D_{50} (mm)	C_u	C_c	e_{max}	e_{min}	G_s	R	S	USCS
0.62	1.6	1.0	0.87	0.58	2.65	0.43	0.83	poorly graded

Source: data from Han et al. (2018) and Tovar-Valencia et al. (2018).
R = Roundness (Wadell 1932), *S* = Sphericity (Wadell 1933), USCS = United Soil Classification System.

5.3.3 Image analysis

Digital images were taken during cyclic loading using two complementary metal-oxide-semiconductor (CMOS) cameras (see Figure 5.1) positioned in front of the top and middle observation windows of the chamber. The images captured were analyzed using the two-dimensional Digital Image Correlation (DIC) technique to obtain the displacement and strain fields in the sand domain surrounding the model pile base during cycling loading. The commercial software VIC-2D (Correlated Solutions 2009) was used to perform the DIC analysis of the images taken during testing. The settings used in VIC-2D are summarized in Table 5.3. The fundamentals of the DIC technique are described in Arshad et al. (2014), Tehrani et al. (2016), Tovar-Valencia et al. (2018), and Galvis-Castro et al. (2018).

Table 5.3. Settings in the DIC analysis using VIC-2D (Adapted from Tovar-Valencia et al. 2020)

Parameter	Value / Description
Subset size [(a)]	35 x 35 pixels ($\approx 5D_{50}$ by $5D_{50}$)
Step or grid size [(b)]	8 pixels
Scale of the image	0.095 mm/pixel
Correlation criterion	Normalized squared differences and exhaustive search [(c)]

[a] Size of the set of pixels to be tracked across images.
[b] Size of the square grid used to extract results.
[c] This correlation criterion seeks the minimum difference in grey-level intensity of an image pattern of the subset in the reference and deformed/displaced images (Pan et al. 2009; Sutton et al. 2009; Take 2015).

5.3.4 Test procedure and test program

Twelve model pile tests were carried out in the half-cylindrical calibration chamber. The samples were prepared by air pluviation using a large pluviator positioned at the top of the calibration chamber (Lee et al. 2011). After the sand sample was prepared with the desired density, the loading system and the cameras were carefully positioned (see Figure 5.1) in front of the chamber. Then, a surcharge of 50 kPa was applied at the top of the sample using an inflatable air-rubber bladder. Next, the model pile was installed using jacking strokes 10 mm length at a rate of 1.0 mm/s to a target base depth of 415 mm (= 10.9B). Once the model pile base reached the desired penetration depth, it was unloaded to simulate the end of the installation. Following the installation stage, a compressive load test was performed by pushing the model pile down at a constant rate of 0.1 mm/s for a distance of approximately 12 mm (i.e., 12 mm ≈ 0.3B). Next, the pile head load was removed by detaching the loading system from the head of the model pile. Then, the pile was loaded monotonically to a pile base settlement w_b of $0.01B$, corresponding to a unit base resistance in very dense sand of approximately 28% of the limit unit base resistance $q_{bL,BC}$ before cycling. The model pile was subjected to this working load before the cyclic loading stage started. The limit unit base resistance q_{bL} corresponds to the limiting value of the unit base load at which the soil mass surrounding the pile can no longer generate additional resistance, leading to plunging of the pile (Basu and Salgado 2012). The value of $q_{bL,BC}$ was obtained from the compressive load test performed after the model pile installation. The model pile was then subjected to displacement-controlled cycles. The cycles were performed with uniform sinusoidal displacement half amplitude Δw_{cyclic} ranging from 0.25 mm [$\Delta w_{cyclic} = 0.007B = 0.4D_{50}$] to 3.0 mm [$\Delta w_{cyclic} = 0.079B = 4.8D_{50}$]. The cyclic displacement half amplitude Δw_{cyclic} was applied at the head of the model pile. The number N_c of cycles applied ranged from 100 to 2,000 cycles with a frequency f that varied from 0.1 Hz to 1.0 Hz. The ranges of cycles and frequencies selected for these experiments are typical in cyclic loading events to which offshore structures are subjected to (Andersen et al. 2013). Once the cycling stage was completed, any remaining load on the model pile head was removed by disconnecting the loading system from the head of the model pile. In the final stage of the test, the model pile was loaded in compression under displacement-controlled conditions to a depth of at least 1.0 pile diameter ($1B = 38.1$ mm) at a rate of 0.1 mm/s. Table 5.4 presents the test conditions of all the tests performed. All the tests were performed following the procedure described above. The tests were identified by a testing code that gives the information of the cyclic parameters: cyclic displacement half amplitude Δw_{cyclic}, denoted by CY, and the number N_c of cycles, denoted by N. The number that follows the notation letters represents the value of the variable (in millimeter for Δw_{cyclic} and dimensionless for N_c). All tests were performed in very dense sand samples (relative density D_R ranging from 86.9% to 94.3%).

Table 5.4. Test program

Test code[a,b]	Relative density D_R (%)	Cyclic displacement half amplitude Δw_{cyclic} (mm)	Number of cycles N_c	Frequency f (Hz)
CY3.0-N100	93.0	3.00	100	0.1
CY1.5-N100	88.3	1.50	100	0.1
CY1.0-N100	88.2	1.00	100	0.1
CY1.0-N1000	86.9	1.00	1,000	1.0
CY1.0-N200	88.3	1.00	200	1.0
CY0.7-N100	92.3	0.70	100	0.1
CY0.6-N100	93.6	0.60	100	0.1
CY0.5-N1000	91.4	0.50	1,000	1.0
CY0.5-N100	92.7	0.50	100	0.1
CY0.25-N100	91.3	0.25	100	0.1
CY0.25-N1000	94.3	0.25	1,000	1.0
CY0.25-N2000	92.0	0.25	2,000	1.0

[a] Test code: CY'#'= cyclic displacement half amplitude Δw_{cyclic} followed by its value in mm, N'#' = number of cycles.
[b] The model pile was installed by jacking strokes of 10 mm length. The surcharge was 50 kPa and kept constant during testing.

5.4 Experimental results

5.4.1 Effect of cyclic displacement half amplitude

5.4.1.1 Unit base resistance mobilized during static load tests

Figure 5.2 shows the unit base resistance q_b versus relative settlement w_b/B at the pile base measured for the compressive load tests performed before and after the cyclic loading stage of tests CY0.25-N100, CY1.0-N100, and CY3.0-N100. These tests differ only by the cyclic displacement half amplitude Δw_{cyclic} (= 0.25 mm, 0.5 mm, 1.0 mm, and 1.5 mm) applied in the cyclic loading stage of the tests. Figure 5.2(a) shows that, for Δw_{cyclic} = 0.25 mm [see Figure 5.2(a)], the q_b versus w_b/B curves from the pre-cyclic and the post-cyclic compressive load tests are comparable. For w_{cyclic} = 1.0 mm [see Figure 5.2(b)], at small pile base settlements, the unit base resistance measured in the compressive load test performed after cycling ($q_{b,AC}$) is significantly smaller than that measured in the compressive load test performed before cycling ($q_{b,AC}$) (e.g., at w_b/B = 0.1, $q_{b,AC}$ = $0.58q_{b,BC}$). But, the difference between $q_{b,AC}$ and $q_{b,BC}$ decreases as w_b/B increases. For Δw_{cyclic} = 3.0 mm, as shown in Figure 5.2(c), for $w_b/B < 0.3$, $q_{b,AC} < q_{b,BC}$; at w/B =

0.3, the q_b versus w_b/B curves for the two compressive load tests cross each other; as the relative settlement increases, $q_{b,AC}$ continues increasing while $q_{b,BC}$ keeps constant (limit unit base resistance $q_{bL,BC}$ measured before cycling). At the maximum relative settlement (w_b/B = 1), $q_{b,AC}$ is 40% greater than the limit unit base resistance $q_{bL,BC}$ measured before cycling.

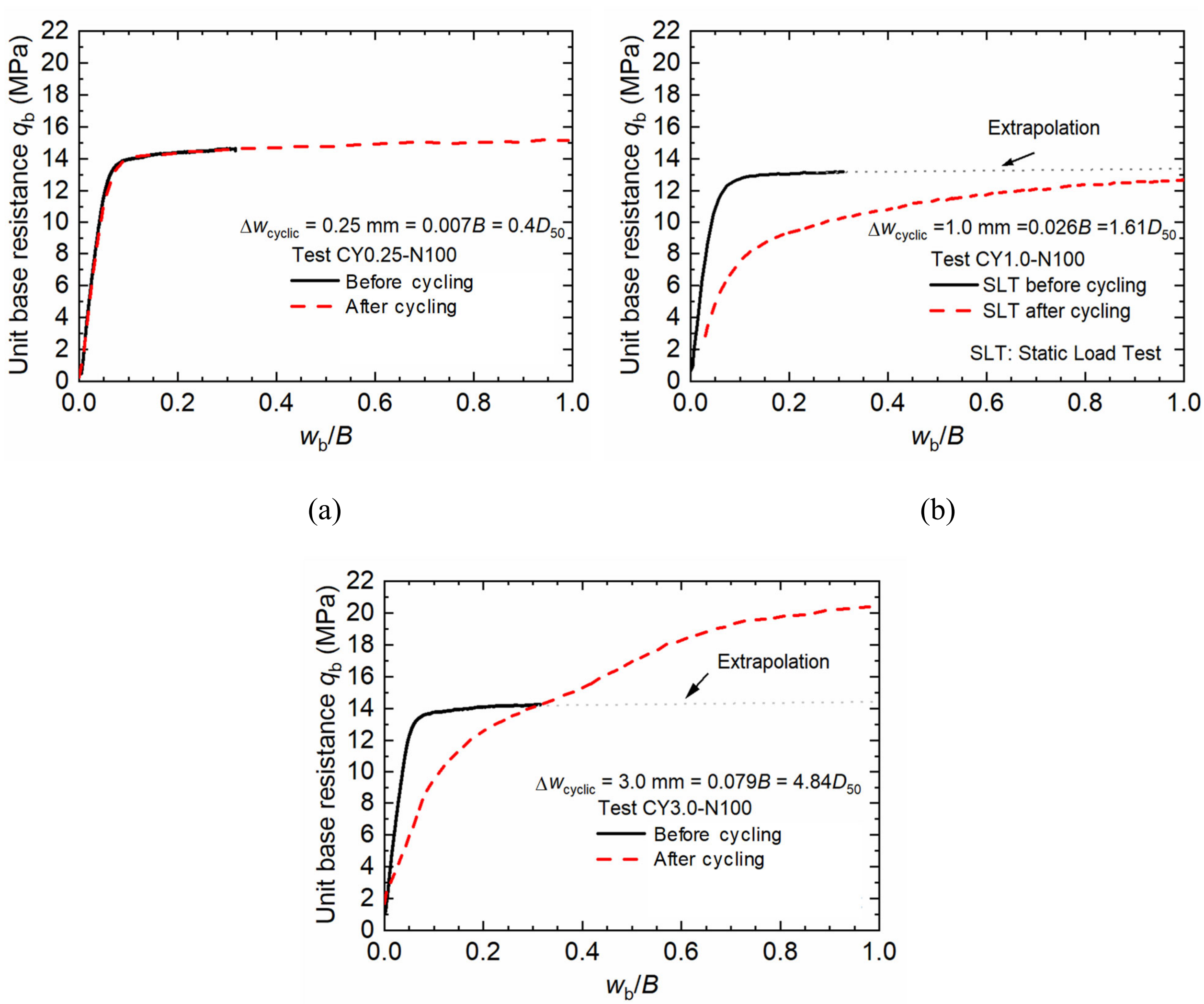

(a) (b)

(c)

Figure 5.2. Effect of cyclic displacement half amplitude Δw_{cyclic} on the unit base resistance q_b: Unit base resistance q_b mobilized in the compressive load tests before and after cycling versus relative settlement w_b/B at the pile base for tests (a) CY0.25-N100, (b) CY1.0-N100, and (c) CY3.0-N100.

The effect of cyclic displacement half amplitude Δw_{cyclic} on the static unit base resistance q_b is examined using the ratio $q_{b,AC}/q_{b,BC}$ of the unit base resistance after cycling to the unit base resistance before cycling, both measured at the same relative base settlement w_b/B of the compressive loadings. Figure 5.3 shows the curves of $q_{b,AC}/q_{b,BC}$ versus Δw_{cyclic} obtained at four different values of relative settlement w_b/B (= 0.1, 0.3, 0.6, and 1) and also at plunging. The values of unit base resistance after cycling at plunging were estimated using Chin's method (Chin 1970). An additional horizontal axis is shown in Figure 5.3: Δw_{cyclic} normalized by D_{50}. It can be seen that the values of $q_{b,AC}/q_{b,BC}$ are equal to 1.0 for cyclic displacements half amplitude Δw_{cyclic} less than 0.5 mm, which corresponds to 0.8 times the mean particle size D_{50} of the test sand. We identify Δw_{cyclic} equal to 0.5 mm as the threshold value below which 100 cycles could be applied without significantly affecting the unit base resistance versus relative pile base settlement response.

For a relative pile base settlement w_b/B equal to $0.1B$ (at the ultimate state), Figure 5.3 shows that the value of $q_{b,AC}/q_{b,BC}$ decreases from 0.90 to 0.48 when Δw_{cyclic} increases from 0.5 mm ($\Delta w_{cyclic}/D_{50} = 0.8$) to 1.5 mm ($\Delta w_{cyclic}/D_{50} = 2.4$). For $\Delta w_{cyclic} > 1.5$ mm, the value of $q_{b,AC}/q_{b,BC}$ tends to increase, at a low rate, with increasing Δw_{cyclic} ($q_{b,AC}/q_{b,BC} = 0.63$ for Δw_{cyclic} 3.0mm). This result indicates that the ultimate unit base resistance is significantly affected by uniform cycles of cyclic displacement half amplitude Δw_{cyclic} in the 0.5 mm to 1.5 mm range.

Figure 5.3 also shows that, for a value of Δw_{cyclic} of 3.0 mm, the ratio $q_{b,AC}/q_{b,BC}$ increases as the relative pile base settlement w_b/B increases. The curve for plunging indicates that the limit unit base resistance after cycling is 1.7 times greater than the value of the limit unit base resistance $q_{bL,BC}$ measured before cycling. This result may suggest that a restrike of the pile could be beneficial for the pile base response.

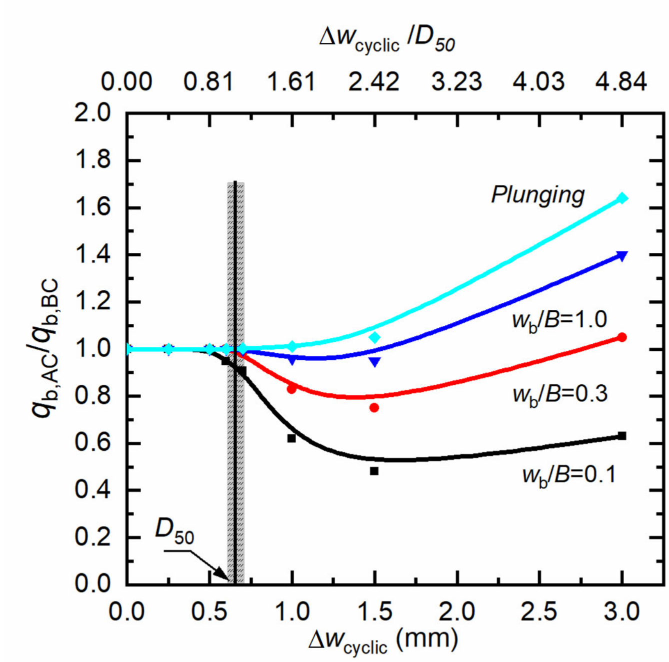

Figure 5.3. Ratio $q_{b,AC}/q_{b,BC}$ of the unit base resistance after cycling to the unit base resistance before cycling versus Δw_{cyclic} and $\Delta w_{cyclic}/D_{50}$ at different values of relative settlement w_b/B at the pile base.

5.4.1.2 Unit base resistance mobilized during cyclic load tests

Figure 5.4(a) to Figure 5.4(d) show the unit base resistance q_b and the pile head displacement w (positive for downward pile head movement and negative for upward pile head movement) mobilized during the cyclic stage of tests CY0.25-N100, CY0.5-N100, CY1.0-N100, and CY3.0-N100 as a function of time t. For each cycle, there is a maximum unit base resistance $q_{b,max}$ (i.e., peaks in q_b versus t), and a minimum unit base resistance $q_{b,min}$ (i.e., valleys in q_b versus t). For a cyclic displacement half amplitude Δw_{cyclic} of 0.25 mm (test CY0.25-100), the maximum $q_{b,max}$ and minimum $q_{b,min}$ unit base resistances remain approximately constant during cycling for t up to 1,000 seconds. For a cyclic displacement half amplitude Δw_{cyclic} of 0.5 mm (test CY0.5-100) and 1.0 mm (test CY1.0-100), q_{max} decreases as cyclic loading progresses. A different response is observed for the test with Δw_{cyclic} of 3.0 mm (test CY3.0-N100); q_{max} decreases during the early stages of cycling ($t < 100$ sec), but then q_{max} increases slightly with time. We also observe that, for $\Delta w_{cyclic} > 0.5$ mm, the pile base is fully unloaded during the pull-out phase of each cycle, for $q_{b,min}$ always reaches a value of zero. This is an indication of a loss in contact between the pile base and the sand.

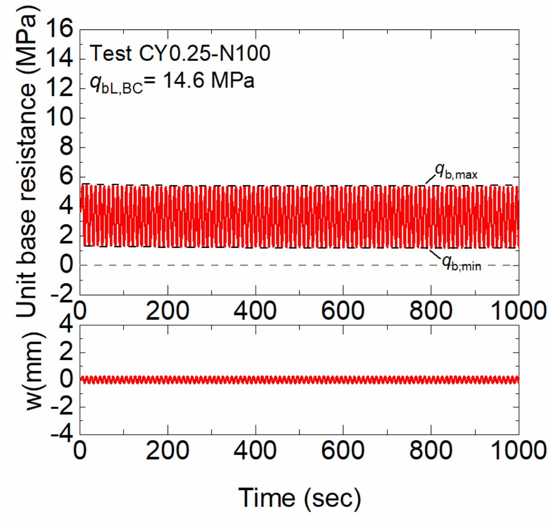

(a)

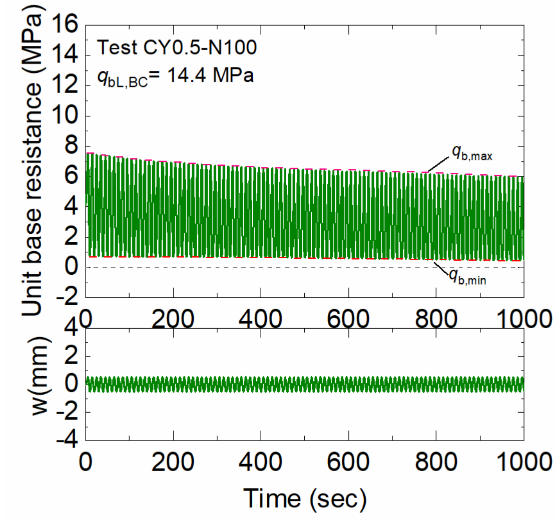

(b)

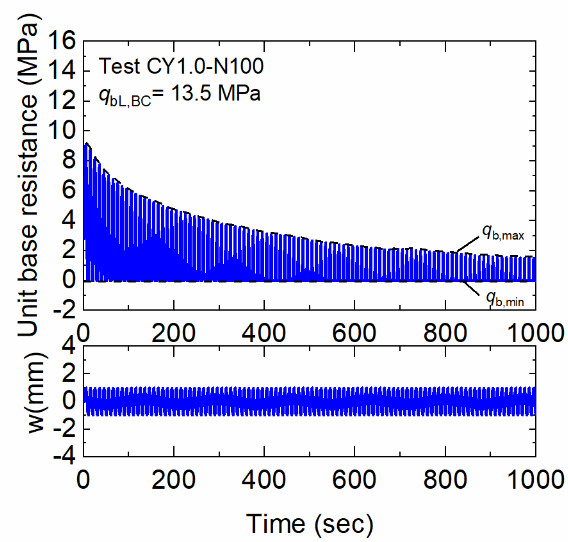

(c)

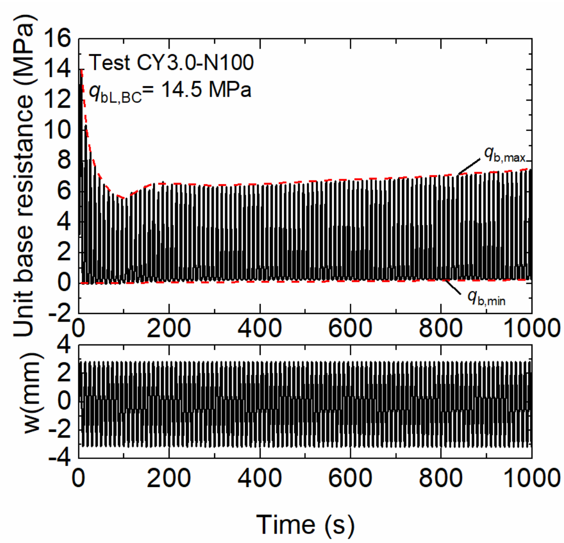

(d)

Figure 5.4. Unit base resistance q_b and pile head displacement w (positive downward and positive upward) versus time for the cyclic loading stage of tests: (a) CY0.25-N100, (b) CY0.5-N100, (c) CY1.0-N100, and (d) CY3.0-N100.

Figure 5.5 compares the maximum unit base resistance $q_{b,max}$ normalized by the maximum unit base resistance $q_{b,max0}$ mobilized in the first cycle of cyclic loading (i.e., normalized unit base resistance $q_{b,max}/q_{b,max0}$) for tests CY0.25-N100 (Δw_{cyclic} = 0.25 mm), CY0.5-N100 (Δw_{cyclic} = 0.5 mm), CY0.6-N100 (Δw_{cyclic} = 0.6 mm), CY1.0-N100 (Δw_{cyclic} = 1.0 mm), CY1.5-N100 (Δw_{cyclic} = 1.5 mm), and CY3.0-N100 (Δw_{cyclic} = 3.0 mm). Figure 5.5 shows that, within the first ten cycles,

$q_{b,max}/q_{b,max0}$ decreases at a higher rate with increasing Δw_{cyclic}. For Δw_{cyclic} = 1.5 mm, $q_{b,max}/q_{b,max0}$ drops 22% within the first 5 cycles (i.e., $q_{b,max}/q_{b,max0}$ = 0.78), while for Δw_{cyclic} = 0.25 mm, $q_{b,max}/q_{b,max0}$ drops only 2% (i.e., $q_{b,max}/q_{b,max0}$ = 0.98). For 0.25 mm < Δw_{cyclic} < 1.0 mm, $q_{b,max}/q_{b,max0}$ keeps decreasing at an approximately constant rate. While for Δw_{cyclic} = 1.0 mm and 1.5 mm, $q_{b,max}/q_{b,max0}$ tends to stabilize near the end of the test at a value of approximately 0.2.

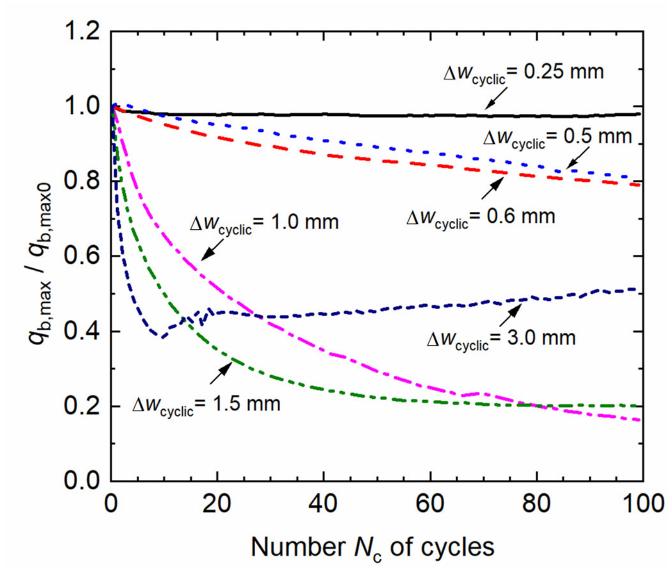

Figure 5.5. Effect of cyclic displacement half amplitude Δw_{cyclic} on the cyclic unit base resistance $q_{b,max}$ mobilized during the cyclic loading stage of tests ended at 100 displacement cycles: maximum unit base resistance $q_{b,max}$ normalized by the maximum unit base resistance $q_{b,max0}$ mobilized in the first cycle of cyclic loading versus number N_c of cycles.

For reference, Table 5.5 provides the values of the limit unit base resistance $q_{bL,BC}$ before cycling, the values of the maximum unit base resistance $q_{b,max0}$ and the minimum unit base resistance $q_{b,min0}$ mobilized in the first cycle, and the values of $q_{b,max}$ and $q_{b,max}$ mobilized in the last cycle (N_c = 100 cycles). As expected, $q_{b,max0}$ increases with increasing cyclic displacement half amplitude Δw_{cyclic}. For test CY3.0-N100 (Δw_{cyclic} = 3.0 mm), $q_{bL,BC}$ is equal to $q_{b,max0}$; thus, the base resistance is fully mobilized in the first cycle. For the test CY0.25-N100 (Δw_{cyclic} = 0.25 mm), $q_{b,max0}$ is approximately equal to $0.37q_{bL,BC}$.

Table 5.5. Limit unit base resistance $q_{bL,BC}$ before cycling, maximum unit base resistance $q_{b,max0}$ and minimum unit base resistance $q_{b,min0}$ mobilized in the first cycle, and maximum unit base resistance $q_{b,max}$ and minimum unit base resistance $q_{b,min}$ mobilized in the last cycle for cyclic tests ended at 100 displacement cycles.

Test code [(a)]	D_R (%)	$q_{bL,BC}$ (MPa)	$q_{b,max0}$ (MPa)	$q_{b,max}$ at cycle 100 (MPa)	$q_{b,min0}$ (MPa)	$q_{b,min}$ at cycle 100 (MPa)
CY3.0-N100	93.0	14.5	14.2	7.4	0.0	0.0
CY1.5-N100	88.3	14.5	12.6	2.5	0.0	0.0
CY1.0-N100	88.2	13.5	9.2	1.5	0.0	0.0
CY0.6-N100	93.6	14.7	7.7	6.2	0.6	0.0
CY0.5-N100	92.7	14.4	7.5	6.2	0.7	0.4
CY0.25-N100	91.3	14.6	5.5	5.4	1.3	1.2

[a] Test code: CY'#'= cyclic displacement half amplitude Δw_{cyclic} followed by its value in mm, N'#' = number of cycles.

5.4.1.3 Particle crushing effects

Figure 5.6 shows the digital images obtained at the end of the cycling stage of tests CY0.5-N100, CY1.0-N100, CY1.5-N100 and CY3.0-N100. For tests CY0.5-N100 [Figure 5.6(a)] and CY1.0-N100 [Figure 5.6(b)], the zone of crushed particles near the pile base seems to be smaller than those for tests CY1.5-N100 [Figure 5.6(c)] and CY3.0-N100 [Figure 5.6(d)]. We estimated the amount of crushing at the end of 100 loading cycles around the conical base by measuring the area where we detected crushed particles (crushed particles are lightly colored). The estimated crushing area A_c was normalized by the projected area A_b of the conical base. The results for the tests in Figure 5.6 show that the area with crushed particles, developed after 100 cycles, increases with increasing cyclic displacement half amplitude. The value of A_c is less than or equal to 30% of the area of the conical base for tests CY0.5-N100 (A_c/A_b = 25.6%) and CY1.0-N100 (A_c/A_b = 30.0%). In contrast, for tests CY1.5-N100 and CY3.0-N100, the area with crushed particles grows to a size of approximately 40.0% and 162% of the area of the conical base, respectively.

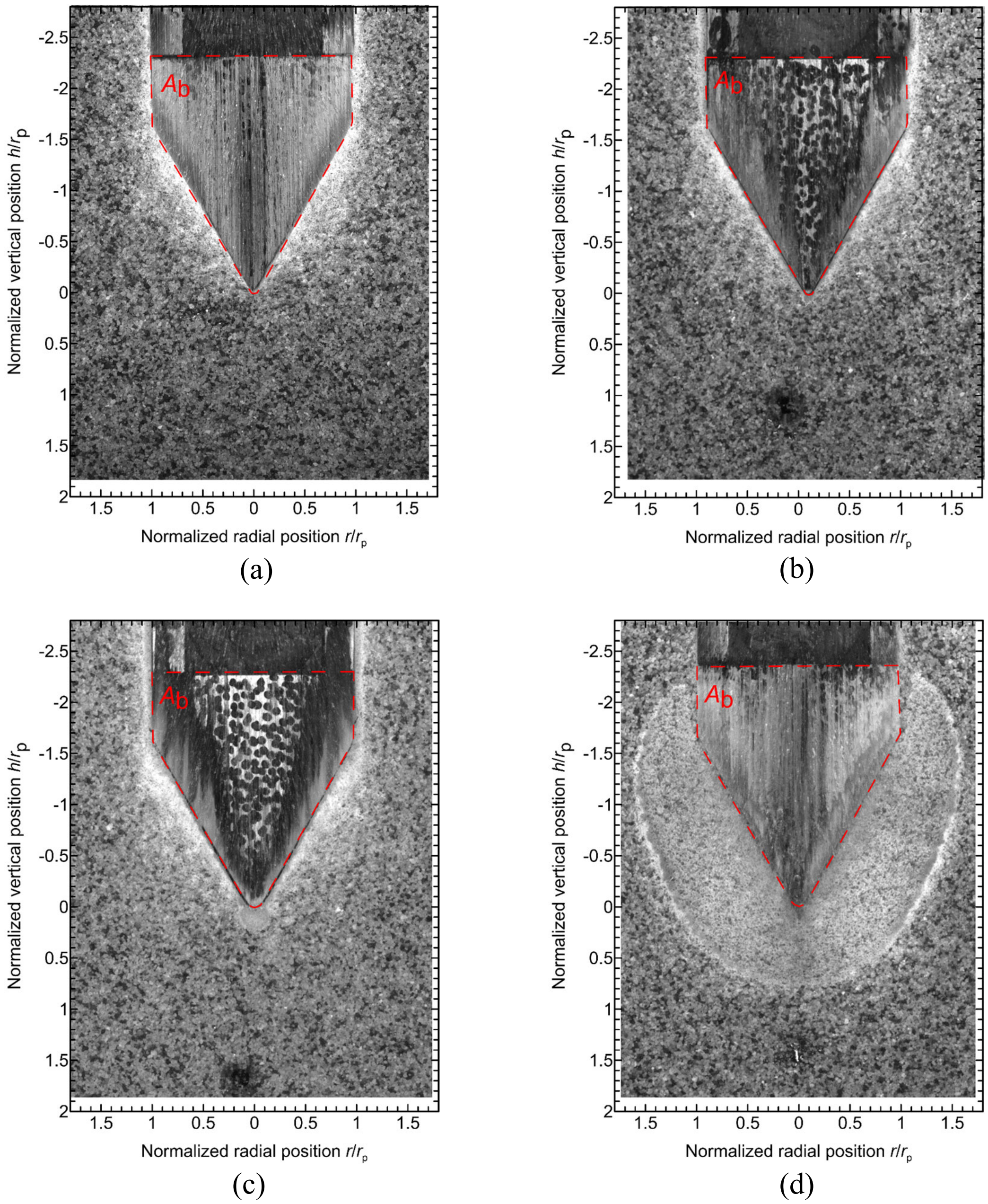

Figure 5.6. Digital images at the end of the cycling stage of tests: (a) CY0.5-N100, (b) CY1.0-N100, (c) CY1.5-N100, and (d) CY3.0-N100.

For tests CY1.0-N100 [Figure 5.6(b)] and CY1.5-N100 [Figure 5.6(c)], we noticed that the area of crushed particles induced by the cyclic loading forms a bulb below the tip of the cone that extends vertically to a distance, measured from the tip, of approximately 0.05B and 0.15B, respectively. For test CY3.0-N100 [Figure 5.6(d)], this distance increases to approximately 0.4B, and the bulb of crushed particles completely surrounds the conical base.

5.4.1.4 Image analysis results

Figure 5.7 and Figure 5.8 show the color map and contours lines of cumulative radial displacement u (positive when soil elements move away from the centerline of the model pile and negative when they move towards it) and cumulative vertical displacement v (positive when soil elements move upward and negative when they move downward) at the end of the cycling stage of tests CY0.25-N100, CY0.5-N100, CY1.0-N100, CY1.5-N100, and CY3.0-N100. The cumulative radial and vertical displacement u and v are both normalized by the value of the cyclic displacement half amplitude Δw_{cyclic} of the corresponding test and plotted at the original undeformed locations of the soil elements. The x-axis of plots shown in Figure 5.7 and Figure 5.8 corresponds to the horizontal distance r from the centerline of the model pile to the soil element, normalized by the model pile radius r_p; the y-axis corresponds to the vertical distance h of the soil element with respect to the pile base ($h = 0$ at the pile base, positive above it, and negative below it), also normalized by the model pile radius r_p.

Figure 5.7 and Figure 5.8 show that, for cyclic displacement half amplitude Δw_{cyclic} of 0.25 mm, the normalized radial and vertical displacements accumulated around the conical base after 100 cycles are negligible (i.e., $|u/\Delta w_{\text{cyclic}}|$ and $|v/\Delta w_{\text{cyclic}}|$ smaller than 0.05). In contrast, for $\Delta w_{\text{cyclic}} \geq 0.5$ mm, the magnitude of $u/\Delta w_{\text{cyclic}}$ and $v/\Delta w_{\text{cyclic}}$ next to the conical base increases as Δw_{cyclic} increases. For $\Delta w_{\text{cyclic}} \geq 0.5$ mm, soil elements underneath the conical base exhibit a positive cumulative radial displacement $u > 0.1\Delta w_{\text{cyclic}}$ and negative cumulative vertical displacement $v < -0.1\Delta w_{\text{cyclic}}$, meaning that soil elements move radially away from the pile axis and downward. At the shoulder of the conical base, soil elements exhibit a negative cumulative radial displacement $u < -0.1\Delta w_{\text{cyclic}}$ and positive cumulative vertical displacement $v > 0.1\Delta w_{\text{cyclic}}$, i.e., soil elements move radially toward the pile axis and upward.

Figure 5.7 and Figure 5.8 also show the region where DIC analysis results are not available. For test CY3.0-N100, this region is significantly larger than for tests CY0.25-N100, CY0.5-N100, CY1.0-N100 and CY1.5-N100, particularly next to the conical shoulder, as shown in Figure 5.7(e) and Figure 5.8(e). Because of the large displacements and rotations of the soil particles located next to the shoulder of the conical base in the cyclic loading stage, the DIC algorithm fails in tracking these soil elements. Considering the DIC data available for test CY3.0-N100, the results in Figure 5(e) show that soil elements with $u/\Delta w_{\text{cyclic}} \geq 0.1$ extend to a radial position r/r_p equal to 4 and a vertical distance h/r_p of -3.0. For the case of cumulative vertical displacements [see Figure

5.8(e)], soil elements located initially between h/r_p of -3.0 and 0 move down more than 20% the value of the cyclic displacement (Δw_{cyclic} = 3.0 mm).

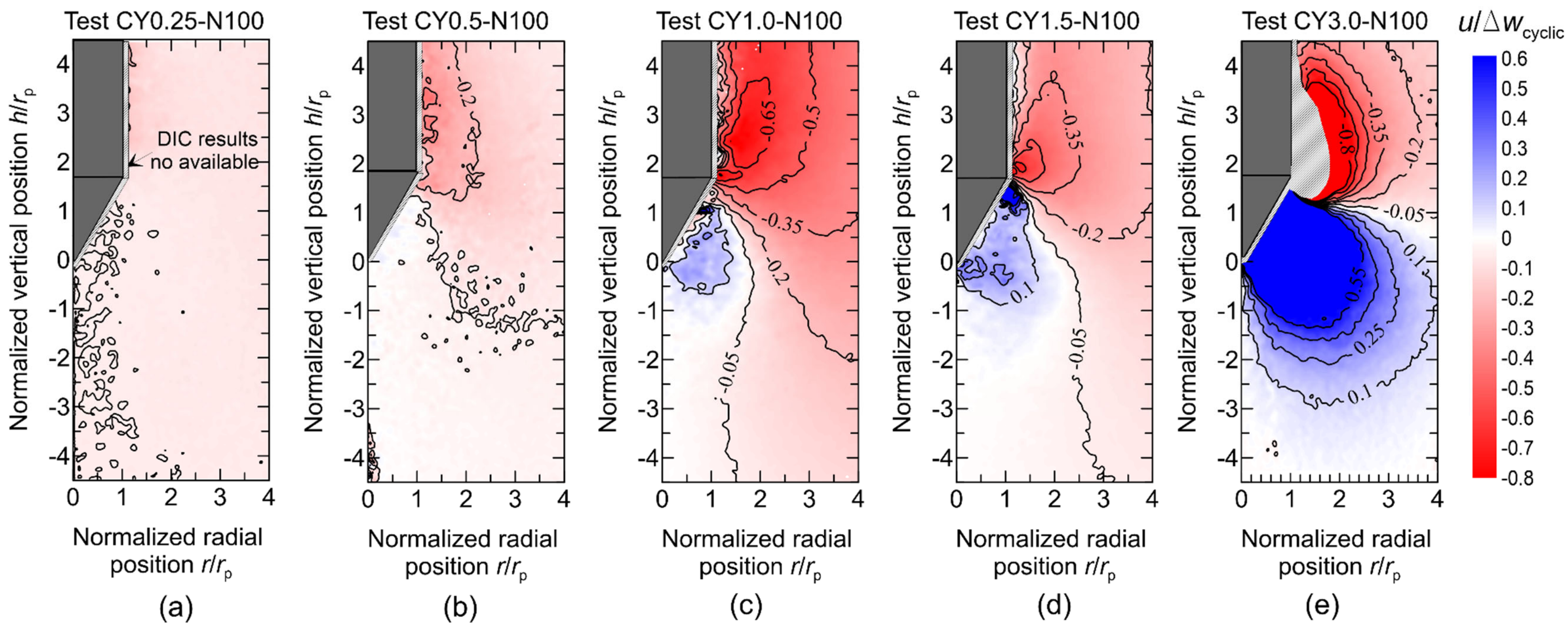

Figure 5.7. Contours of normalized radial displacement $u/\Delta w_{\mathrm{cyclic}}$ (positive when soil moves away from the model pile centerline) near the conical base after 100 cycles with cyclic displacement half amplitude $\Delta w_{\mathrm{cyclic}}$ of (a) 0.25 mm, (b) 0.5 mm, (c) 1.0 mm, (d) 1.5 mm, and (e) 3.0 mm.

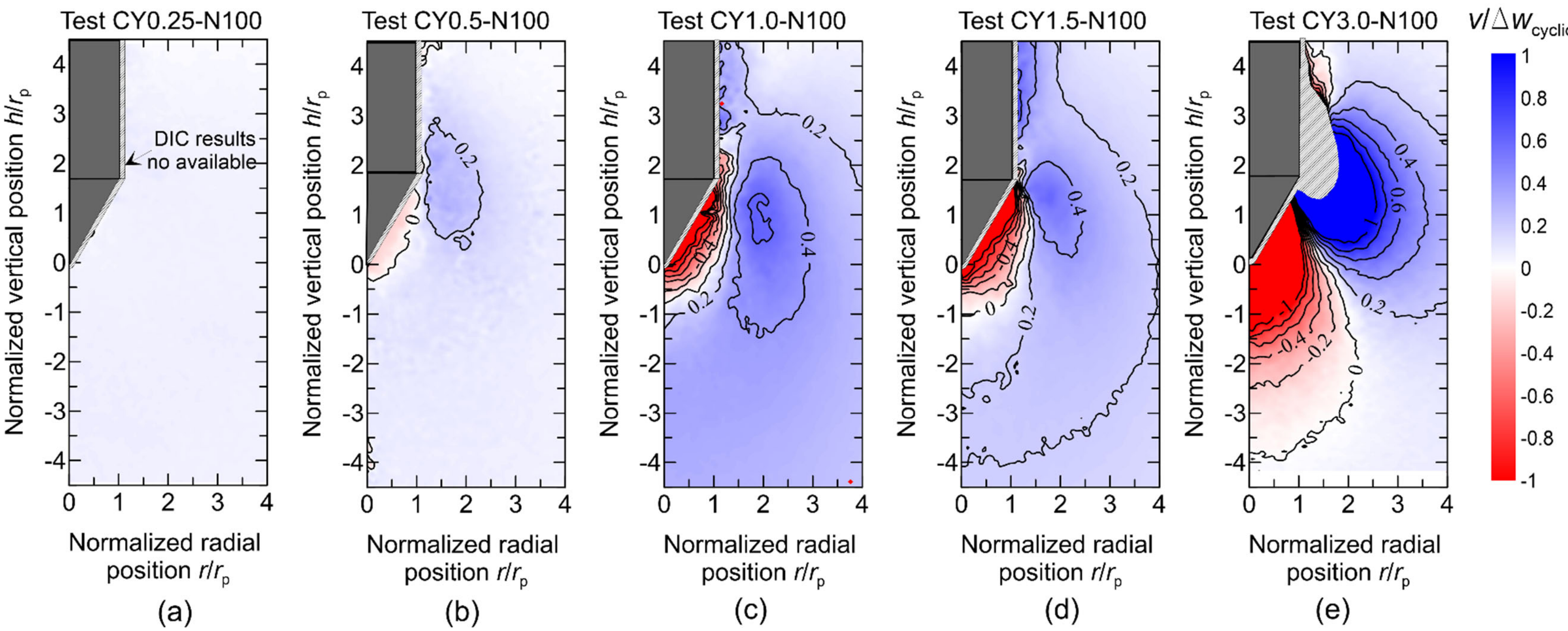

Figure 5.8. Contours of normalized vertical displacement $v/\Delta w_{\text{cyclic}}$ (positive when soil elements move upward) near the conical base after 100 cycles with cyclic displacement half amplitude Δw_{cyclic} of (a) 0.25 mm, (b) 0.5 mm, (c) 1.0 mm, (d) 1.5 mm, and (e) 3.0 mm.

Figure 5.9 shows the heat map and of the cumulative volumetric strain E_{vol} for the same tests shown in Figure 5.8. The solid mechanics sign convention is followed in this figure: positive values of E_{vol} indicate dilation. The volumetric strains are calculated using the expressions presented in Tehrani et al. (2018). Negligible cumulative volumetric strains ($|E_{vol}| < 0.1\%$) were measured after 100 cycles for $\Delta w_{cyclic} = 0.25$ mm. However, for $\Delta w_{cyclic} \geq 0.5$ mm, the magnitude of the volumetric strains and the zone of soil undergoing volumetric deformation increase as Δw_{cyclic} increases. Except for test CY3.0-N100 ($\Delta w_{cyclic} = 3.0$ mm), the soil elements next to the inclined surface of the conical base undergo contraction (negative E_{vol}). Figure 5.9(d) and (e) show that, immediately next to the cone shoulder, a zone of dilation is formed. This dilative zone increases considerably when Δw_{cyclic} is 3.0 mm. An additional area of dilation is observed in test CY3.0-N100 [Figure 5.9(e)] underneath the conical base between $h/r_p = -1$ and $h/r_p = -4$ ($-2B < h < -0.5B$). These results can help explain why $q_{b,AC}$ values for $w_b/B > 0.3B$ are greater than the limit unit base resistance $q_{bL,BC}$ before cycling.

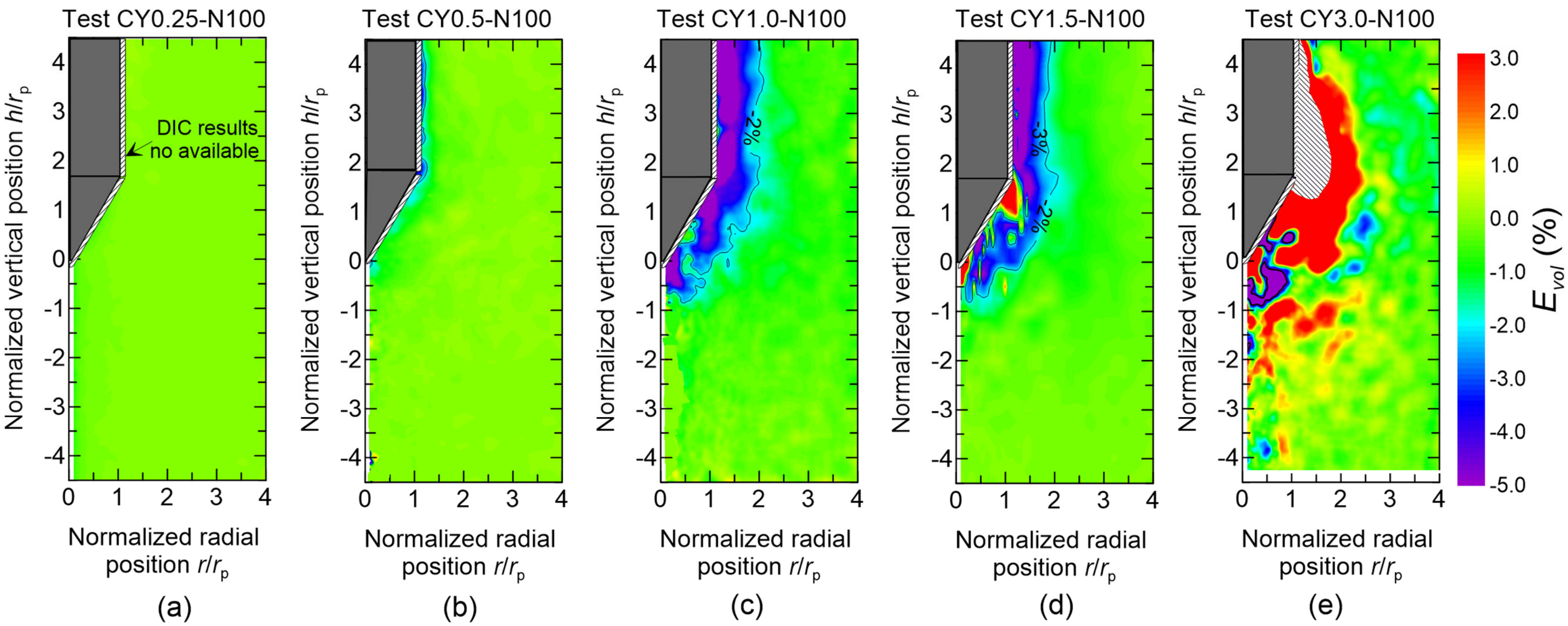

Figure 5.9. Contours of volumetric strain E_{vol} (positive values indicating dilation) near the conical base after 100 cycles with cyclic displacement half amplitude Δw_{cyclic} of (a) 0.25 mm, (b) 0.5 mm, (c) 1.0 mm, (d) 1.5 mm, and (c) 3.0 mm

Figure 5.10 shows the heat map of volumetric strain E_{vol}, plotted at the deformed location of the soil elements, during the cyclic loading stage of test CY3.0-N100. Figure 5.10 (a), (c), (e) and (g) show the contours of E_{vol} at the maximum downward movement of the pile (push-in) in cycle 10, 20, 50, and 100, respectively. Figure 5.10 (b), (d), (f) and (h) show the contours of E_{vol} at the maximum upward movement of the pile (pull-out) in cycle 10, 20, 50, and 100, respectively. As shown in Figure 5.10 (b), (d), (f), and (h), a gap between the sand and the inclined surface of the conical base appears during the upward movement of the model pile. Sand particles flow from a region above the shoulders of the conical base and next to the pile shaft into the gap. This process, which repeats after each cycle, leads to the addition of sand particles into the zone where the gap forms near the conical base. As shown in Figure 5.5, q_{bmax} reaches values always greater than $0.4q_{b,max0}$ = 5.8 MPa, which are values of q_b sufficiently large to produce the crushing of silica sand particles (Tovar-Valencia et al., 2018). Therefore, the sand particles that flow inside this gap end up being crushed in the downward movement of the pile during cycling, as evidenced by the growing bulb of crushed particles formed around the conical base. The digital images shown in Figure 5.10 confirmed that the load at the pile base is fully removed during each pull-out as observed in Figure 5.4(d).

Figure 5.10 also shows that, after 20 cycles, soil elements around the conical base contract (E_{vol} < 0). For N_c > 20 cycles, as cycling progress, some soil elements surrounding the bulb of crushed particles start dilating (e.g., point B in Figure 5.10). Although DIC results inside the bulb of crushed particles are not available, the lower unit base resistance measured in the compressive load test after cycling for w_b/B< 0.3 [see Figure 5.2(c)] suggests that the crushed material in the bulb surrounding the conical base is less dense than that before cycling. As the conical pile base passes the bulb of crushed sand particles, it goes through densified sand with dilative tendency, resulting in higher unit base resistance.

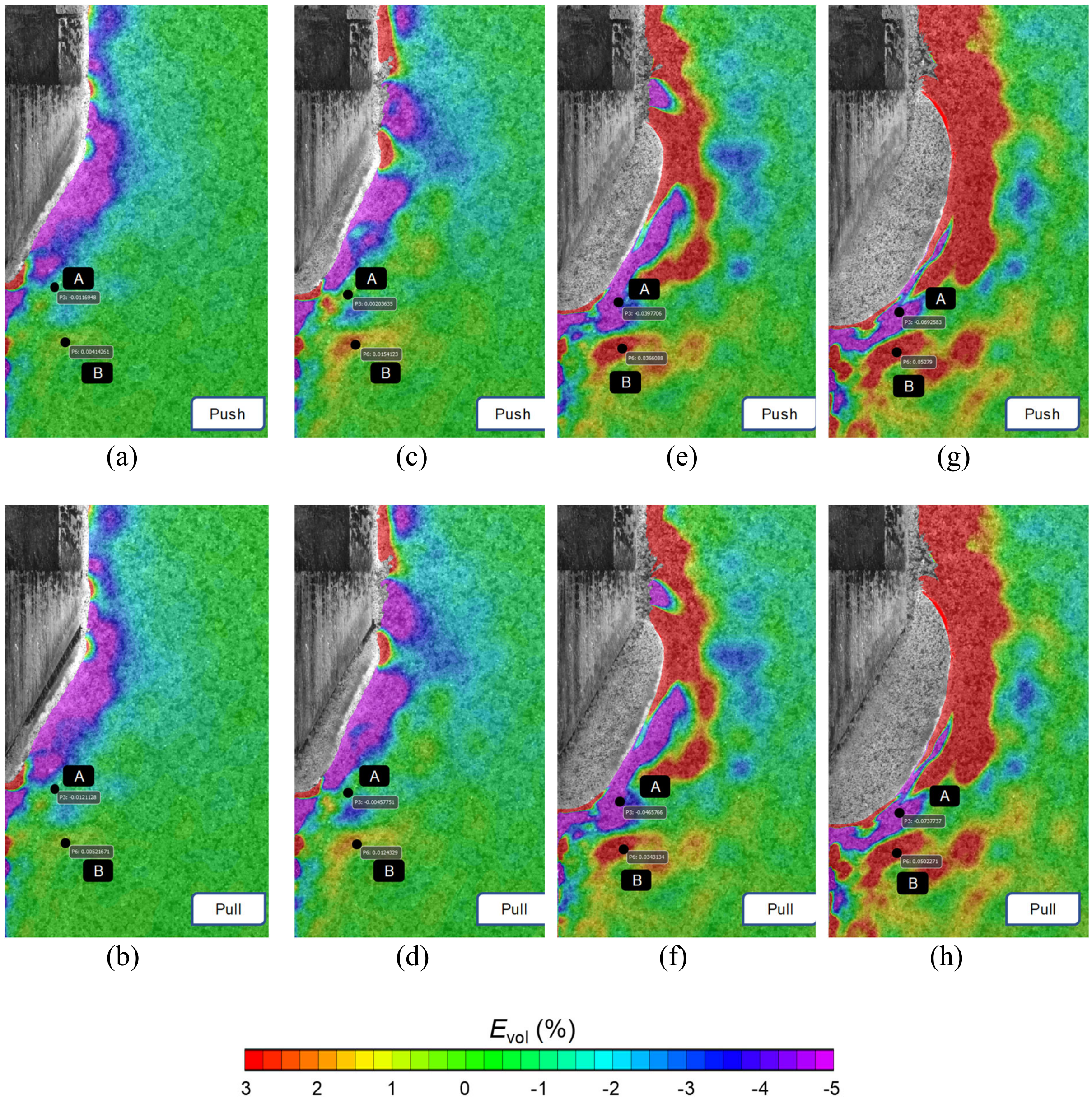

Figure 5.10. Heat map of volumetric strain E_{vol} (positive values indicating dilation) near the conical base at the maximum downward movement of the pile (push-in) in cycles (a) 10, (c) 20, (e) 50, and (g) 100, and at the maximum upward movement of the pile (pull-out) in cycles (b) 10, (d) 20, (f) 50, and (h) 100 for test CY3.0-N100.

5.4.2 Effect of number of cycles

5.4.2.1 Unit base resistance mobilized during static load tests

Figure 5.11 compares the unit base resistance $q_{b,AC}$ mobilized in the compressive load test after cycling normalized by the limit unit base resistance $q_{bL,BC}$ measured before cycling for tests with cyclic loading stage performed with similar cyclic displacement half amplitude Δw_{cyclic}, but with a different number of cycles. Figure 5.11(a) shows that, for $\Delta w_{cyclic} = 0.25$ mm, the $q_{b,AC}/q_{bL,BC}$ versus w_b/B curves for the tests with cyclic loading stage ended at 100 (test CY0.25-N100), 1,000 (test CY0.25-N1000) and 2,000 (test CY0.25-N2000) cycles are comparable, indicating that the number of cycles has a minimal effect on this ratio.

For $\Delta w_{cyclic} = 0.5$ mm [see Figure 5.11(b)], increasing the number of cycles from 100 cycles (test CY0.5-N100) to 1,000 cycles (test CY0.5-N1000) results in lower values of $q_{b,AC}/q_{bL,BC}$ at $w_b/B = 0.1$ ($q_{b,AC}/q_{bL,BC} = 0.93$ and 0.78 for 100 and 1,000 cycles, respectively), but same values of $q_{b,AC}/q_{bL,BC}$ at w_b/B =1 ($q_{b,AC}/q_{bL,BC} = 1.0$ for 100 and 1,000 cycles).

For $\Delta w_{cyclic} = 1.0$ mm, [see Figure 5.11(c)], the values of $q_{b,AC}/q_{bL,BC}$ at $w_b/B = 0.1$ for tests with cyclic loading stages ended at 100, 200, and 1,000 cycles are comparable (i.e., $q_{b,AC}/q_{bL,BC}$ = 0.57, 0.47, 0.56 for 100, 200 and 1,000 cycles, respectively). However, when the number of cycles increases from 200 cycles to 1,000 cycles, $q_{b,AC}/q_{bL,BC}$ increases about 9% for $w/B > 0.12$. These results suggest that, for a given cyclic displacement half amplitude Δw_{cyclic}, there is a threshold number of cycles that produces the lowest ultimate unit base resistance. Table 5.6 provides the ratios of $q_{b,AC}/q_{bL,BC}$ for values of relative pile base settlement w_b/B of 0.1, 0.3, 0.6 and 1.0 for the tests shown in Figure 5.11.

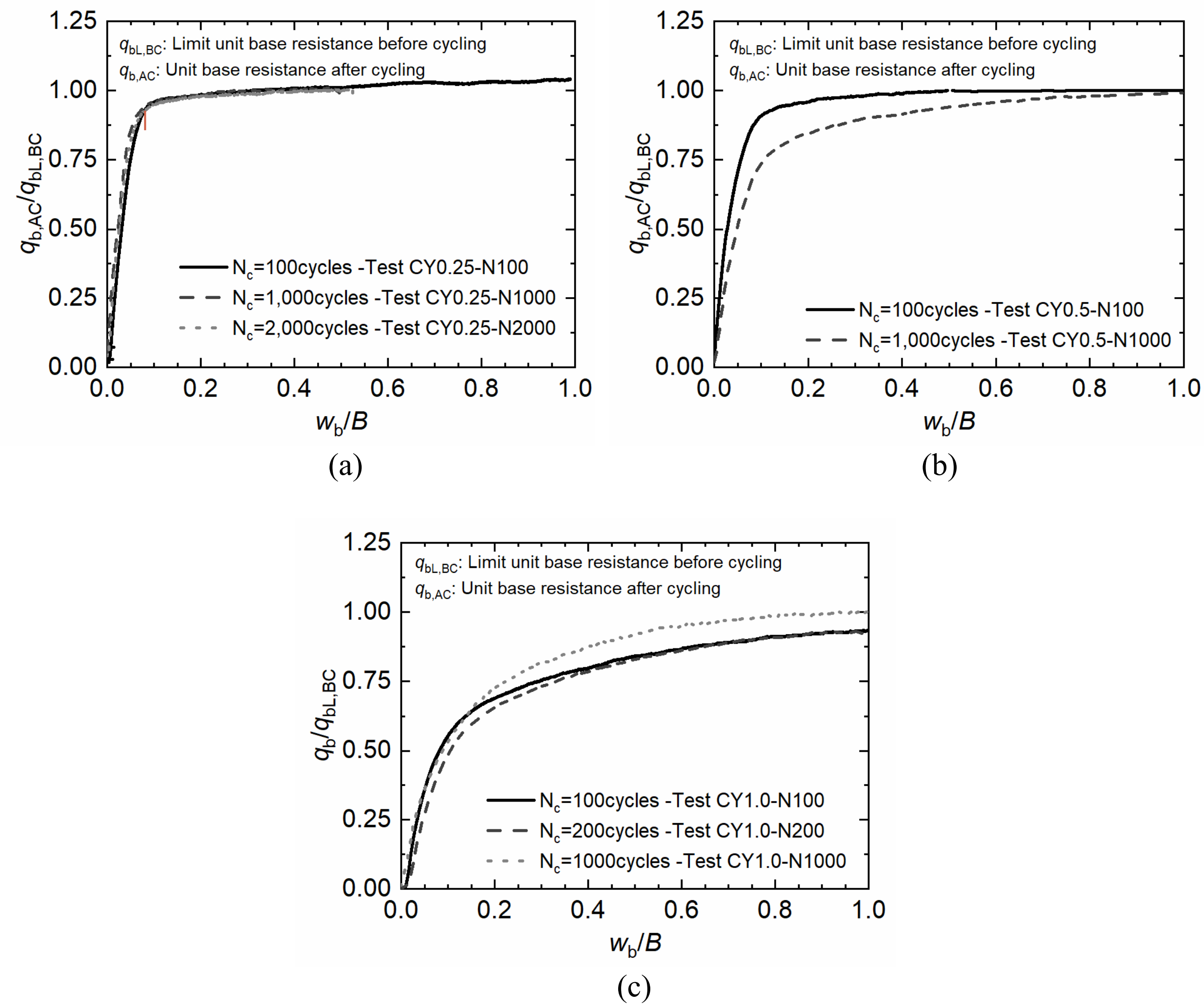

Figure 5.11. Effect of number N_c of cycles on the unit base resistance $q_{b,AC}$ mobilized in the static load test performed after cycling normalized by the limit unit base resistance $q_{bL,BC}$ measured before cycling for tests with cyclic loading stage performed with cyclic displacement half amplitudes Δw_{cyclic} of (a) 0.25 mm, (b) 0.5 mm, and (c) 1.0 mm.

Table 5.6. Values of $q_{b,AC}/q_{bL,BC}$ obtained at four different relative pile base settlements w_b/B for tests with cyclic loading stage performed using a cyclic displacement half amplitude Δw_{cyclic} of 0.25 mm, 0.5 mm, and 1.0 mm.

Test code	Number N_c of cycles	Cyclic displacement half amplitude Δw_{cyclic} (mm) [w_{cyclic}/B] [w_{cyclic}/D_{50}]	$q_{b,AC}/q_{bL,BC}$			
			w/B = 0.1	w/B = 0.3	w/B = 0.6	w/B = 1.0
CY0.25-N100	100	0.25 [0.7%] [0.40]	1.00	1.00	1.00	1.00
CY0.25-N1000	1,000		1.00	1.00	1.00	1.00
CY0.25-N2000	2,000		1.00	1.00	1.00	1.00
CY0.5-N100	100	0.5 [1.3%] [0.81]	0.93	1.00	1.00	1.00
CY0.5-N1000	1,000		0.78	0.95	1.01	1.00
CY1.0-N100	100	1.0 [2.6%] [1.61]	0.57	0.75	0.87	0.95
CY1.0-N200	200		0.47	0.74	0.87	0.94
CY1.0-N1000	1,000		0.56	0.80	0.95	1.00

$q_{bL,BC}$ is the limit unit base resistance measured in the compressive load test performed before cyclic loading.
$q_{b,AC}$ is the unit base resistance measured in the compressive load test performed after cyclic loading.

5.4.2.2 Unit base resistance mobilized during cyclic load tests

Figure 5.12 shows $q_{b,max}/q_{b,max0}$ versus number N_c of cycles for cyclic load tests ended at 1,000 cycles or more (i.e., tests CY0.25-N2000, CY0.5-N1000, and CY1.0-N1000) and $q_{b,max}/q_{b,max0}$ versus N_c for test CY3.0-N100. Figure 5.12 shows that, for test CY0.25-N2000, the value of $q_{b,max}/q_{b,max0}$ remains approximately constant throughout the 2,000 cycles. For test CY0.5-N1000, it is seen that the value of $q_{b,max}/q_{b,max0}$ decreases continuously as the number of cycles increases up to 1,000 cycles. However, for test CY1.0-N1000, the $q_{b,max}/q_{b,max0}$ versus N_c curve has a minimum value at N_c = 133. For N_c >133 cycles, the value of $q_{b,max}/q_{b,max0}$ increases slightly as N_c increases. This result suggests that (i) there is a number of cycles that leads to a minimum value of $q_{b,max}/q_{b,max0}$, and (ii) the minimum value of $q_{b,max}/q_{b,max0}$ is reached with a smaller number of cycles as Δw_{cyclic} increases. For example, for Δw_{cyclic} = 3.0 mm the minimum value of $q_{b,max}/q_{b,max0}$ occurs at N_c = 9 cycles, as shown in Figure 5.5 and Figure 5.12; for Δw_{cyclic} = 1.0 mm, the minimum value of $q_{b,max}/q_{b,max0}$ occurs much later, at N_c = 133.

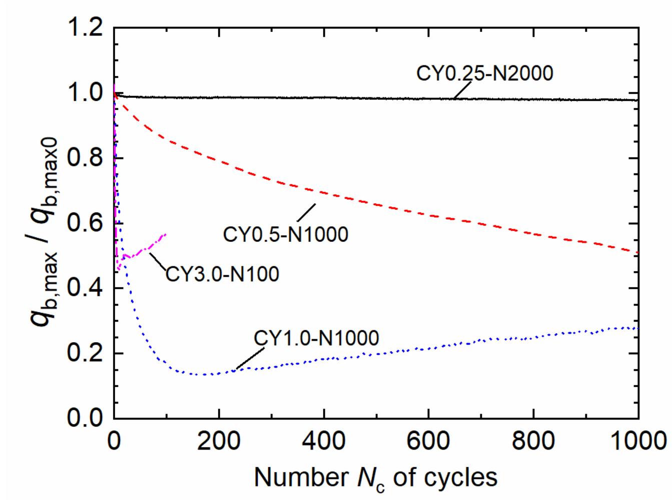

Figure 5.12. Maximum unit base resistance $q_{b,max}$ normalized by the maximum unit base resistance $q_{b,max0}$ measured in the first cycle of cyclic loading stage versus number of cycles for tests CY3.0-N100, CY0.25-N2000, CY0.5-N1000, and CY1.0-N1000.

5.4.2.3 Particle crushing effects

Figure 5.13(a) to Figure 5.13(d) show the digital images at the end of cycle number 100, 200, 400 and 1,000 for the cyclic loading stage of test CY1.0-N1000. For each digital image, the area with crushed particles A_c is estimated and normalized by the projected area A_b of the conical base. The values of A_c/A_b are shown in Figure 5.13 (e) and plotted as a function of the number of cycles. Figure 5.13(e) also shows the evolution of $q_{b,max}/q_{b,max0}$ with cyclic loading.

The plots of A_c/A_b versus N_c and $q_{b,max}/q_{b,max0}$ versus N_c indicate that, during the first 20 cycles, $q_{b,max}/q_{b,max0}$ decreases from 1 to 0.45 at a high rate, while A_c/A_b increases from 10% to 23%. Both curves tend to stabilize at around 100 cycles. From N_c = 133 cycles to 1,000 cycles, $q_{b,max}$ increases slightly, from $0.18q_{b,max0}$ (i.e., $q_{b,max}$ =2.6 MPa) to $0.27q_{b,max0}$ (i.e., $q_{b,max}$ =3.9 MPa) and A_c/A_b grows exponentially, from 35% in cycle 133 to 148% in cycle 1,000.

We observed that the minimum value of $q_{b,max}/q_{b,max0}$ coincides with the onset of local flow of particles from the region above the shoulder of the conical base into the gap left during the pull-out stage of each cycle. Videos generated from the digital images taken during the cyclic loading stage of test CY1.0-N1000 showed that, between cycles 100 and 300, the majority of the particles dropping are crushed particles coming from the crushed particle band next to the pile shaft (formed during pile installation). Only after about 300 cycles, uncrushed and crushed particles from above the shoulder of the pile base are deposited inside the gap. As shown in Figure 5.13(b), some particles reach positions below the tip of the cone and others accumulate below the base shoulder. For $N_c > 300$ cycles, it can be seen that some particles are crushed in the downward movement of the model pile.

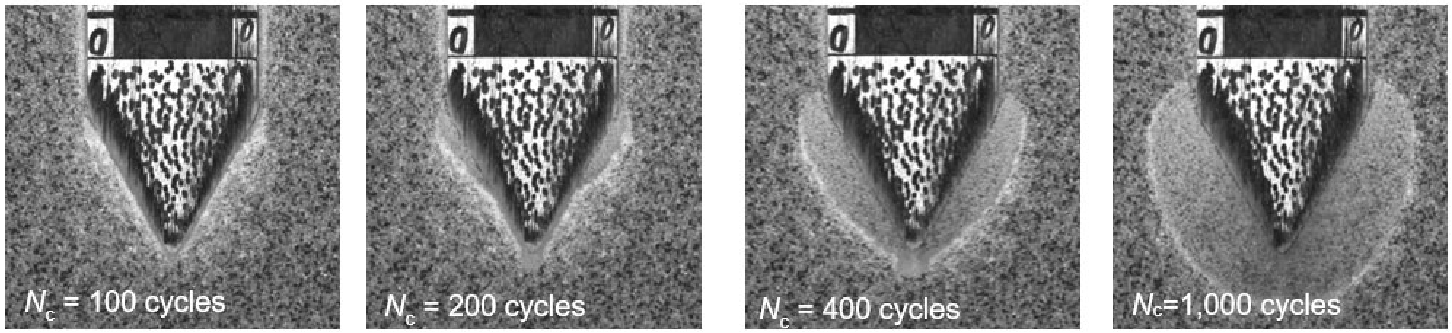

(a) (b) (c) (d)

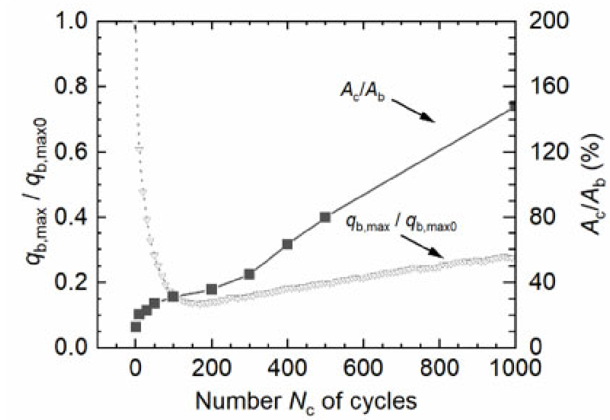

(e)

Figure 5.13. Digital images at the end of cycle number (a) 100, (b) 200, (c) 400, and (d) 1,000; (e) maximum unit base resistance $q_{b,max}$ normalized by the maximum unit base resistance $q_{b,max0}$ in the first cycle of cyclic loading (on the left vertical axis) and normalized area of crushed particles A_c/A_b (on the right vertical axis) versus number N_c of cycles for test CY1.0-N1000.

5.4.2.4 Image analysis results

Figure 5.14 shows the trajectory of soil elements located near the conical base (elements A, B, C, and D) during the cycling stage of test CY1.0-N1000. Table 5.7 shows the position of these soil elements at the beginning of the cycling stage. Element A was chosen to represent soil elements near the shoulder of the conical base. Element C represents soil elements below the conical base and at the pile centerline. Elements B and D represent soil elements located near the inclined face of the conical base, with element B being the closest to it.

Table 5.7. Initial position of soil elements A, B, C, D located around the conical base of the pile for the cycling stage of test CY1.0-N1000

Soil element ID	Normalized radial position r/r_p	Normalized vertical position h/r_p
A	2.5	1.7
B	2.5	0
C	0	-1.6
D	1.0	0.8

Figure 5.14(a) shows that, for N_c <100 cycles, the average trajectory of soil element A forms an angle θ with the horizontal (r/r_p axis) of approximately 135 degrees (measured counter-clockwise from the r/r_p axis on the right side and clockwise on the left side of the pile). For N_c > 100 cycles, the angle θ changes slightly to 120 degrees. We see from Figure 5.14(b) that element B follows approximately the same trajectory (θ =110 degrees) during the first 100 cycles. Then, for N_c > 100 cycles, element B moves following an angle θ equal to approximately 35 degrees with the horizontal. Figure 5.14(c) shows that element C moves slightly upward during the first 100 cycles; then, for N_c > 100 cycles, it moves downward. From Figure 5.14(d), the average trajectory of element D (the element closest to the inclined faces of the conical base) varies from $\theta \approx$ -80 degrees (sub-vertical), for N_c < 100 cycles, to $\theta \approx$ 10 degrees (nearly horizontal), for 300 cycles < N_c < 500 cycles. Element D could not be tracked using DIC after 500 cycles.

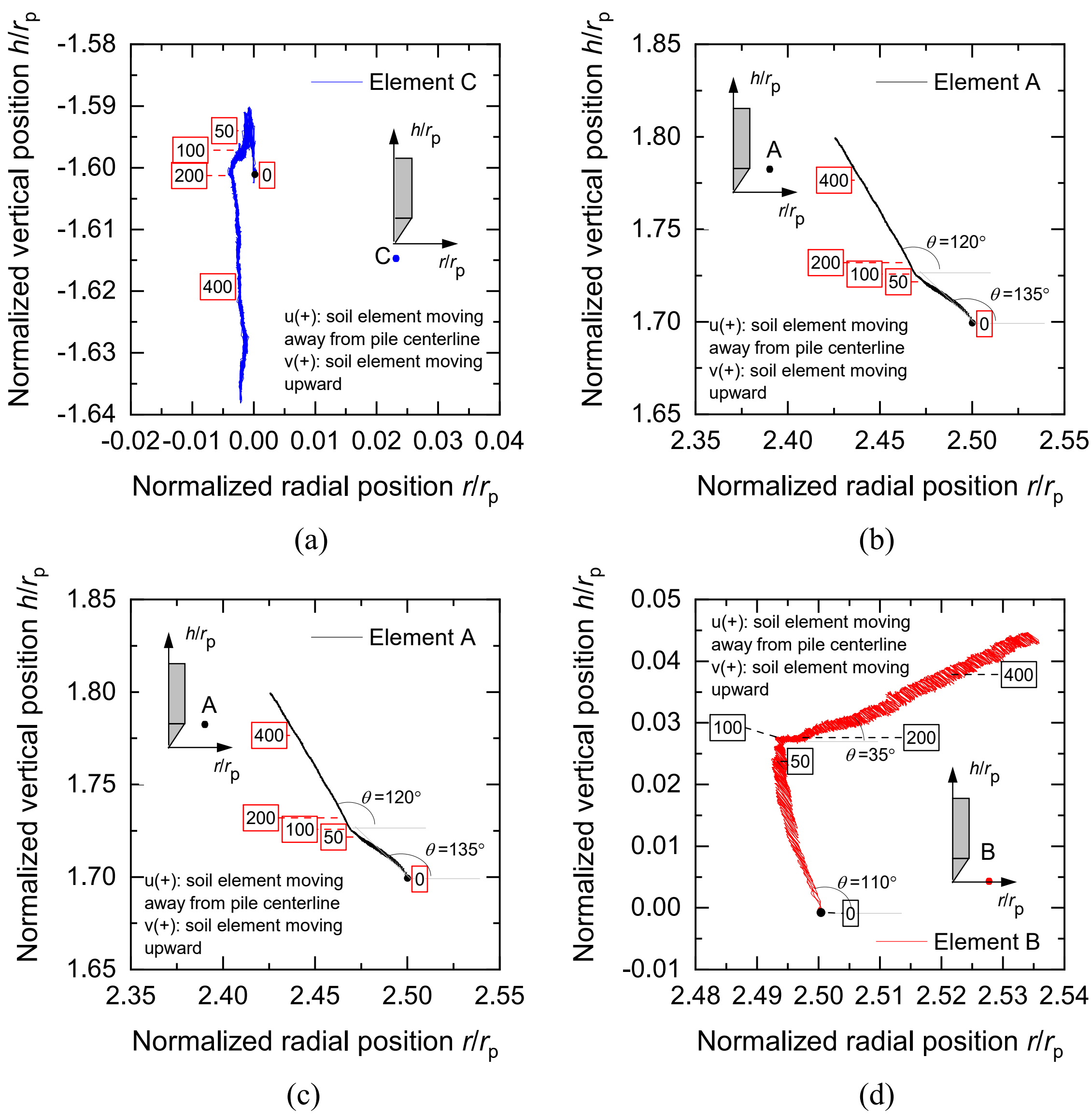

Figure 5.14. Trajectory of soil elements (A, B, C, D) near the conical base of the pile during the cycling stage of test CY1.0-N1000: normalized radial position versus normalized vertical position of (a) soil element A [$r/r_p = 2.5$, $h/r_p = 1.7$], (b) soil element B [$r/r_p = 2.5$, $h/r_p = 0$], (c) soil element C [$r/r_p = 0$, $h/r_p = -1.6$], and (d) soil element D [$r/r_p = 1.0$, $h/r_p = 0.8$]. The selected N_c values are indicated in the red boxes.

Figure 5.15(a) and Figure 5.15(b) show the cumulative radial and vertical displacements of the cycling stage of test CY1.0-N1000 for the same four soil elements (elements A, B, C and D) shown in Figure 5.14. After 100 cycles, when q_{bmax}/q_{bmax0} reaches approximately its minimum value, elements A and B (the two soil elements located at the same initial radial position $r/r_p = 2.5$) have moved radially towards the pile axis and upward (i.e., after 100 cycles, u = -0.64 mm and v = 0.51 mm for element A, and u = -0.14 mm and v = 0.59 mm for element B). Element D (the soil element closest to the pile base) has moved radially outward and downward (i.e., after 100 cycles, u = 0.21 mm and v = -0.83 mm). Element C (the element located right underneath the conical tip, at r/r_p = 0 and h/r_p = -1.6) has experienced mainly vertical displacement in the first 100 cycles of the cyclic loading stage (i.e., after 100 cycles, u = -0.04 mm and v= 0.12 mm). Figure 5.15 shows that, between N_c equal to 100 cycles and 180 cycles, the cumulative radial and vertical displacement of elements A, B and C remain approximately constant. However, for N_c > 200 cycles, there is a reactivation of the radial and vertical movement of elements A and B and the vertical movement of element C; this agrees well with the increase in the area of crushed particles surrounding the conical base and the small increase in $q_{b,max}/q_{b,max0}$, as can be seen in Figure 5.13(e).

Figure 5.15(a) also shows that, for N_c > 200 cycles, the radial displacement u of element A decreases with increasing N_c, indicating that soil element A continues moving radially towards the pile axis, as observed for N_c < 200 cycles. In contrast, the radial displacement u of element B increases with increasing N_c, indicating that the direction of the radial displacement changed after 200 cycles (i.e., element B moves radially away from the pile axis for N_c > 200). The change in the direction of the radial displacement of element B results from the flow of sand particles to the region below the conical base when the pile moves upward during the cycling stage, pushing element B radially away from the conical base. As shown in Figure 5.15(b), element C experiences an increase in downward movement after 200 cycles (i.e., from 200 cycles to 500 cycles, the permanent vertical displacement v changes from 0.02 mm to -0.64 mm); this movement is affected by the increase in the deposition of sand particles below the conical base, which pushed down the particle C.

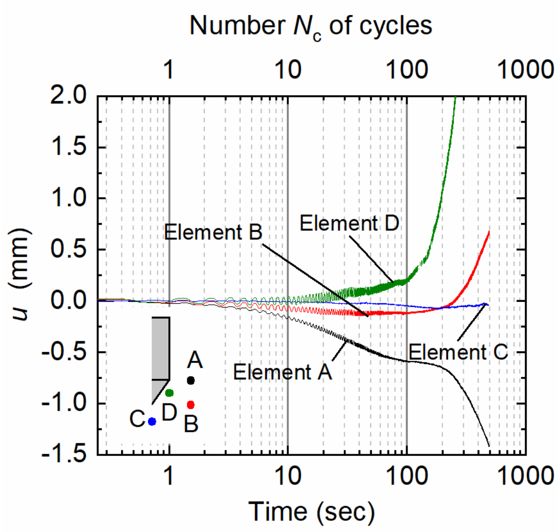

(a)

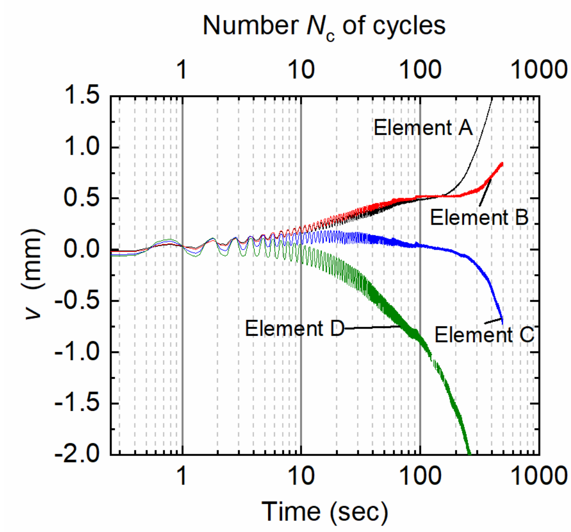

(b)

Figure 5.15. Displacements of soil elements (A, B, C and D) near the conical base during the cycling stage of test CY1.0-N1000 (f = 1.0 Hz): (a) radial displacement u (positive when soil elements move away from the centerline of the model pile and negative when they move towards it) and (b) vertical displacement v (positive when soil elements move upward and negative when they move downward).

Figure 5.15(a) and Figure 5.15(b) show that, of elements A through D, element D has the widest range of displacements around the mean paths of displacement versus the number N_c of cycles in the first 100 cycles. A and B experience the least oscillations.

Figure 5.16 shows the evolution of the cumulative radial strain E_{rr}, vertical strain E_{zz}, shear strain E_{rz}, and volumetric strain E_{vol} during the cycling stage of test CY1.0-N1000 for the same four elements listed in Table 5.7. Figure 5.16(a) and (b) show that the deformation mechanism in element A is the opposite of that in element B. While element A stretches radially and compresses vertically, element B compresses radially and stretches vertically. During the first 180 cycles, the cumulative shear strain [see Figure 5.16(c)] in elements A and B is less than 0.1%; therefore, for $N_c < 180$ cycles, the radial and vertical strains of elements A and B are approximately equal to the principal strains. For $N_c > 180$ cycles, the shear strain of elements A and B become negative and positive, respectively, indicating that soil element A distorts in the opposite direction of element B. In terms of volumetric strains [see Figure 5.16(d)], element A, B and C exhibit volumetric contraction during the first 300 cycles. Then, for $N_c > 300$ cycles, these elements tend to dilate.

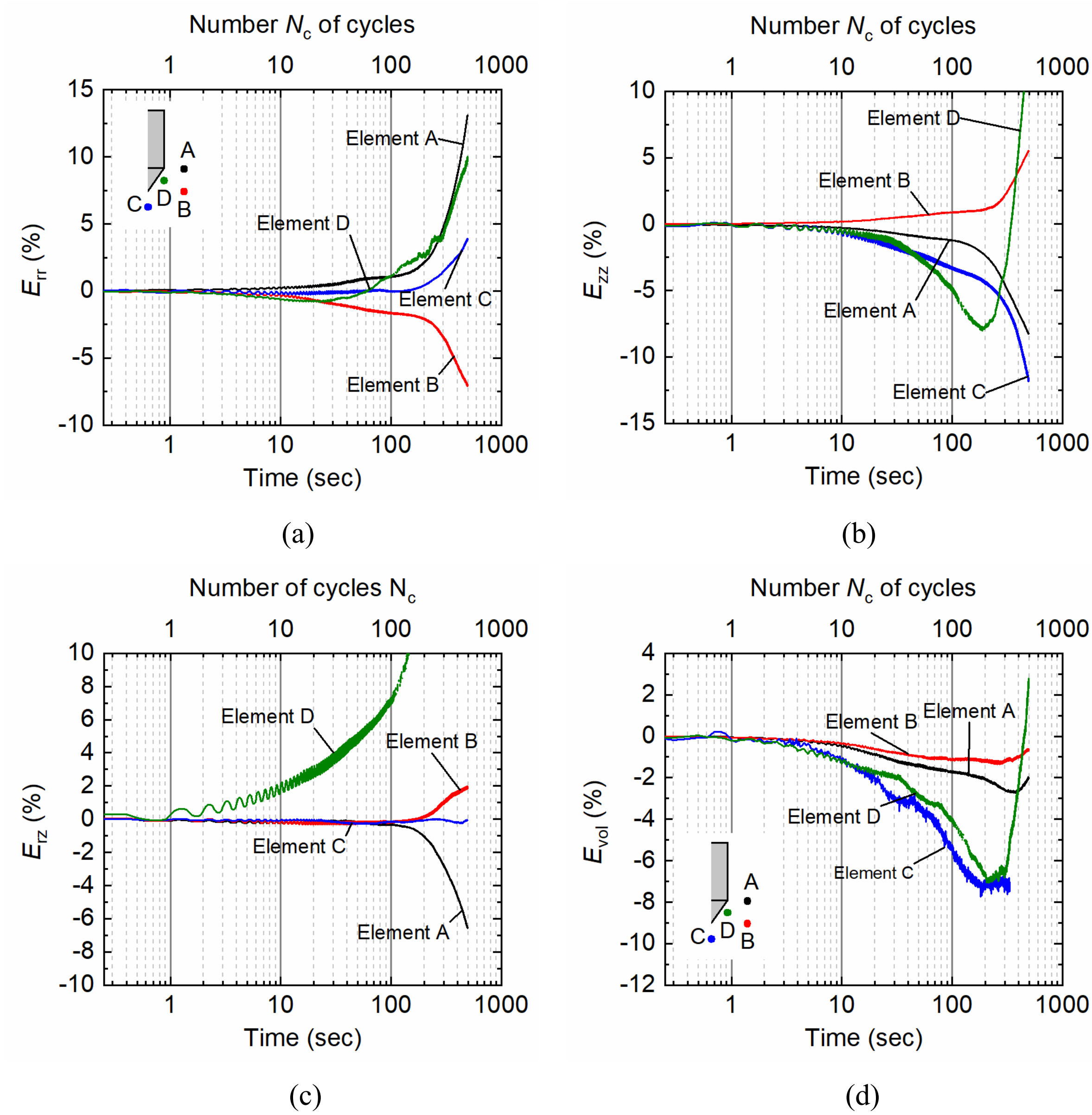

Figure 5.16. Cumulative strains of soil elements (A, B, C, and D) around the conical base during the cycling stage of test CY1.0-N1000 (f = 1.0 Hz): (a) radial strain E_{rr} (positive when soil elements stretch radially); (b) vertical strain E_{zz} (positive when soil elements stretch vertically); (c) shear strain E_{rz}; (d) volumetric strain E_{vol}.

Figure 5.16(a) and (b) also shows that element D contract radially, during the first 70 cycles, and contract vertically, during the first 200 cycles. After that, element D stretches in both directions (radial and vertical). The dilative behavior of soil element D for N_c>200 cycles is confirmed by the values of E_{vol} >0. Figure 5.16(c) indicates that during the first 10 cycles most of the shearing occurs next to the inclined faces of the conical base (near element D), propagating away from it (where elements A, B, and C are located) as cycling progresses.

5.5 Summary and conclusions

In this paper, we reported the results of a series of monotonic and cyclic load tests performed on a closed-ended jacked model pile with a conical base. The model pile load tests were performed in dense silica sand samples prepared in a half-cylindrical calibration chamber that allows image collection. The digital images collected during cyclic loading were processed using the DIC technique to obtain the displacement and strain fields in the sand domain near the conical base.

Cycling performed with a cyclic displacement half amplitude Δw_{cyclic} equal or less than 0.25 mm (= $0.0065B$=$0.4D_{50}$) had a minimal effect on the unit base resistance (the limit and the ultimate unit base resistance changed by less than 6% after cyclic loading) regardless of the number of cycles (100, 1,000, or 2,000 cycles). The results from DIC showed that soil elements near the conical base are minimally disturbed during cyclic loading: the magnitudes of the cumulative displacements relative to the cyclic displacement half amplitude ($|u/\Delta w_{\text{cyclic}}|$ and $|v/\Delta w_{\text{cyclic}}|$) were smaller than 0.05; and the magnitude $|E_{\text{vol}}|$ of the cumulative volumetric strains were less than 0.1% near the conical base. In contrast, after 100 cycles with a cyclic displacement half amplitude Δw_{cyclic} in the 0.5 mm (=$0.8D_{50}$) to 1.5 mm (=$2.4D_{50}$) range, the ultimate unit base resistance (q_{b} at w_{b}/B = 0.1) decreased considerably (by 10% for Δw_{cyclic} = 0.5 mm and by 50% for Δw_{cyclic} = 1.5 mm) with increasing Δw_{cyclic}. The magnitudes of the cumulative displacements relative to the cyclic displacement half amplitude ($|u/\Delta w_{\text{cyclic}}|$ and $|v/\Delta w_{\text{cyclic}}|$) and the cumulative volumetric contraction near the conical base at the end of cyclic loading increased with increasing Δw_{cyclic}.

After 100 cycles of Δw_{cyclic} = 3.0 mm = $4.8D_{50}$, the limit unit base resistance measured after cycling was 1.7 times greater than the reference limit unit base resistance (before cycling). A large number of sand particles from above the shoulders was deposited below the conical base and crushed in the downward movement of the pile during cyclic loading. At the end of 100 cycles, soil elements surrounded the bulb of crushed particles exhibited a net dilation.

The effect of number of cycles on the unit base resistance depend on the magnitude of the cyclic displacement half amplitude. The test results suggested that, for a given Δw_{cyclic}, there is a threshold number of cycles that produce the lowest ultimate unit base resistance. Cyclic loading performed with a number of cycles greater than that threshold value produces an increase of the unit base resistance at plunging.

5.6 Notation

B = diameter of model pile

C_u = coefficient of uniformity

C_c = coefficient of curvature

D_{50} = mean particle size of soil

D_R = relative density

E_{rr} = cumulative Lagrangian radial strain of soil element

E_{zz} = cumulative Lagrangian vertical strain of soil element

E_{rz} = cumulative Lagrangian shear strain of soil element

E_{vol} = cumulative Lagrangian volumetric strain of soil element

e_{max} = maximum void ratio

e_{min} = minimum void ratio

N_c = number of displacement cycles applied in cyclic loading

f = frequency used for displacement-controlled cyclic loading

h = vertical distance of soil element with respect to the pile base

q_b = unit base resistance mobilized during loading

$q_{b,AC}$ = unit base resistance mobilized in compressive loading performed after cycling

$q_{b,BC}$ = unit base resistance mobilized in compressive loading performed before cycling

$q_{bL,BC}$ = limit unit base resistance before cycling

q_{bmax} = maximum unit base resistance mobilized in each cycle during cyclic loading

q_{bmax0} = maximum unit base resistance mobilized at the first cycle of cyclic loading

q_{bmin} = minimum unit base resistance mobilized in each cycle during cyclic loading

q_{bmin0} = maximum unit base resistance mobilized at the first cycle of cyclic loading

r_p = radius of model pile

r = radial distance from soil element to centerline of model pile

u = cumulative radial displacement of soil element

v = cumulative vertical displacement of soil element

Δw_{cyclic} = cyclic displacement half amplitude

w = pile head displacement

w_b = pile base settlement

w_b/B = relative settlement at the pile base

6. SUMMARY AND CONCLUSIONS

This thesis presented studies on the mechanical response of displacement and non-displacement piles installed in sand and tested under monotonic and cyclic loading conditions in a half-cylindrical calibration chamber with digital image correlation (DIC) capability. Using the DIC technique, this study revealed key mechanisms governing the pile response to loading.

To investigate the effect of loading direction and loading sequence on the unit shaft resistance of displacement piles, a series of monotonic load tests were performed using instrumented jacked model piles (with three different values of surface roughness). These tests started with tensile, then followed by compressive loads (TC) or with the reverse sequence, compression followed by tension (CT). The results from the tensile and compressive load tests showed that the unit shaft resistance of jacked piles in sand is always lower under tensile loading than under compressive loading. This resulted in values of the tension-to-compression shaft resistance ratios SRR (measured in tension and compression for the same sample) and SRR_{FTL} (measured from the first-time loadings) of less than one. Furthermore, both SRR and SRR_{FTL} ratios decreased with increasing pile surface roughness (e.g., SRR_{FTL} was 0.67 for the pile with smooth surface roughness and 0.54 for the pile with rough surface roughness). The influence of the loading sequence (TC or CT) was reflected on the greater values of SRR for the model piles loaded first in tension (TC sequence) than in compression (CT). The digital images taken with a microscope as the pile was loaded revealed that the shearing is more localized for compressive than for tensile loading. The DIC analyses indicated that soil elements near the pile shaft tend to move radially towards the pile shaft in tensile loading and radially away from the pile shaft in compressive loading. The soil elements near the pile shaft contract (positive volumetric strains) in tensile loading; while in compressive loading, the soil elements near the pile shaft exhibit negligible volumetric strains. The rotation of principal strains that occur upon reversal of loading direction was found to be the mechanism behind the lower shaft resistance measured in tensile loading.

To investigate the effect of the loading direction on the shaft capacity of virgin and pretested non-displacement piles in sand, a series of TC and CT load tests were performed using model piles pre-installed (wished-in place) in the half-cylindrical calibration chamber. The results from the first-time load tests showed that the magnitudes of peak unit shaft resistance and limit unit shaft resistance in compressive loading are comparable to those in tensile loading for the same relative densities. This result suggested that no reduction factor is needed when computing the tensile unit shaft resistance of non-displacement piles. The displacement and strain fields obtained from the DIC analyses indicated that whether the pile is loaded first in tension or compression, the soil elements dilate radially within a thin band adjacent to the pile shaft and contract radially further out. The similar deformation mechanism occurring in first-time tensile and first-time compressive loadings supports the near-to-one values of the tensile-to-compressive unit shaft resistance ratios. The reversal of loading direction occurring in CT or TC loading sequences substantially reduced the unit shaft resistance of non-displacement piles in sand. The lower limit unit shaft resistance resulting from the load reversal was attributed to a drop in the radial strain (contraction) and a rotation of the principal strain directions exhibited by soil elements near the pile shaft.

A set of monotonic and cyclic load tests were performed in the DIC calibration chamber to study the effect of cyclic loading on the limit unit shaft resistance of displacement piles. The test program was designed to evaluate the influence of factors such as the relative density of the sand, the initial vertical stress, the cyclic displacement amplitude, the number of cycles and the frequency of the displacement cycles. It was found that small-displacement amplitude cycles (cyclic displacement half amplitude smaller than or equal to 0.25 mm) caused a negligible effect on the limit unit shaft resistance, regardless of the number of cycles (100, 1,000, or 2,000 cycles). In contrast, 100 or more displacement cycles with cyclic displacement half amplitude greater than 0.7 mm lead to a degradation of the limit unit shaft resistance. Furthermore, the magnitude of degradation of the limit unit shaft resistance increases with increasing cyclic displacement amplitude but it tends to stabilize for cyclic half displacement amplitudes greater than 2.0 mm. The reduction of the limit unit shaft shear resistance after cyclic loading was also found to be more significant in medium-dense sand samples than in dense sand samples and greater for initial vertical stress of 90 kPa than of 50 kPa. The degradation of the limit unit shaft resistance observed after cyclic loading was linked to the radial contraction and the development of large shear strains of soil elements near the pile shaft during cyclic loading.

A set of monotonic and cyclic load tests were performed in the DIC calibration chamber to study the effect of cyclic loading on the unit base resistance of displacement piles. The changes in the pile base resistance after cycling were evaluated by comparing the mobilized unit base resistance versus pile head settlement curves from the compressive load tests carried out before and after cycling. It was found that the ultimate unit base resistance after cycling reduces when the applied displacement cycles have a cyclic displacement half amplitude greater than 0.5 mm, which is about 0.8 times the mean particle size D_{50} of the tests sand. However, large-displacement amplitude cycling (e.g., cyclic displacement half amplitude of 3.0 mm) was found to be beneficial for the unit base resistance at plunging. The digital image analyses revealed complex mechanisms occurring in the sand domain during cyclic loading. These mechanisms include dilative and contractive behavior of soil elements surrounding the conical pile base, particle crushing and sand deposition below the pile base. Based on the DIC-processed data, the reduction in ultimate unit base resistance was attributed to the cumulative volumetric contraction of the soil next to the inclined faces of the conical base occurring cyclic loading. The increase in unit base resistance at plunging was linked to the addition of sand particles below the conical base, the occurrence of sand particle crushing, and the dilative behavior of soil outside a bulb of crushed particles formed during cyclic loading.

REFERENCES

Achmus, M. (2010). "Design of axially and laterally loaded piles for the support of offshore wind energy converters." *Indian Geotechnical Conference*, 322–327.

Airey, D. W., Al-Douri, R. H., and Poulos, H. G. (1992). "Estimation of pile friction degradation from shearbox tests." *Geotechnical Testing Journal*, 15(4), 388–392.

Al-Douri, R. H. (1992). "Behaviour of single piles and pile groups in calcareous sediments."

Al-Douri, R. H., and Poulos, H. G. (1992). "Static and cyclic direct shear tests on carbonate sands." *Geotechnical testing journal*, 15(2), 138–157.

Al-Douri, R. H., and Poulos, H. G. (1995). "Predicted and observed cyclic performance of piles in calcareous sand." *Journal of Geotechnical Engineering*, 121(1), 1–16.

Altuhafi, F., Sullivan, C. O., Cavarretta, I., O'Sullivan, C., and Cavarretta, I. (2013). "Analysis of an image-based method to quantify the size and shape of sand particles." *Journal of Geotechnical and Geoenviromental Engineering*, 139(8), 1290–1307.

Amira, M., Yokoyama, Y., and Imaizumi, S. (1995). "Friction capacity of axially loaded model pile in sand." *Soils and foundations*, 35(1), 75–82.

Andersen, K. A., Puech, A. A., and Jardine, R. J. (2013). "Cyclic resistant geotechnical design and parameter selection for offshore engineering and other applications." *ISSMGE Technical Committee TC 209 – Offshore Geotechnics*.

Arshad, M. I. (2014). "Experimental study of the displacements caused by cone penetration in sand." Purdue University, West lafayette, IN.

Arshad, M. I., Tehrani, F. S., Prezzi, M., and Salgado, R. (2014). "Experimental study of cone penetration in silica sand using digital image correlation." *Géotechnique*, 64(7), 551–569.

Arthur, J. R. F., Bekenstein, S., Germaine, J. T., and Ladd, C. C. (1981). "Stress path tests with controlled rotation of principal stress directions." *Laboratory Shear Strength of Soil ASTM STP 740*, (R. N. Yong and F. C. Townsend, eds.), America Society for Testing and Materials, West Conshohocken, PA, United States.

Arthur, J. R. F., Dunstan, T., and Chua, K. S. (1977). "Induced anisotropy in a sand." *Géotechnique*, 27(1), 13–30.

Arthur, J. R. F., and Menzies, B. K. (1972). "Inherent anisotropy in a sand." *Geotechnique*, 22(1), 115–128.

ASTM D4253-16. (2016). “Standard test method for maximum index density and unit weight of soils using a vibratory table.” *ASTM International*, ASTM International, West Conshohocken, PA.

ASTM D4254-16. (2016). “Standard test methods for minimum index density and unit weight of soils and calculation of relative density.” *ASTM International*, ASTM International, West Conshohocken, PA.

Atkinson Consultants. (2000). *Cyclic degradation of offshore piles*. London, UK.

Basu, D., and Salgado, R. (2012). “Load and resistance factor design of drilled shafts in sand.” *Journal of Geotechnical and Geoenvironmental Engineering*, 138(12), 1455–1469.

Basu, P., Loukidis, D., Prezzi, M., and Salgado, R. (2011). “Analysis of shaft resistance of jacked piles in sands.” *International Journal for Numerical and Analytical Methods in Geomechanics*, 35(15), 1605–1635.

Basu, P., Prezzi, M., and Basu, D. (2010). “Drilled Displacement Piles – Current Practice and Design.” *DFI Journal - The Journal of the Deep Foundations Institute*, 4(1), 3–20.

Bekki, H., Canou, J., Tali, B., Dupla, J. C., and Bouafia, A. (2013). “Evolution of local friction along a model pile shaft in a calibration chamber for a large number of loading cycles.” *Comptes Rendus - Mecanique*, Elsevier Masson SAS, 341(6), 499–507.

Bekki, H., Canou, J., Tali, B., Dupla, J. C., and Bouafia, A. (2020). “Parametric study of the evolution of shaft friction of a model pile in calibration chamber subjected to cyclic loading at a large number of cycles.” *European Journal of Environmental and Civil Engineering*, Taylor & Francis, 0(0), 1–17.

Belheine, N., Plassiard, J. P., Donzé, F. V., Darve, F., and Seridi, A. (2009). “Numerical simulation of drained triaxial test using 3D discrete element modeling.” *Computers and Geotechnics*, 36(1–2), 320–331.

Benzaria, O., Puech, A., and Kouby, A. Le. (2013). “Cyclic axial load tests on bored piles in dense sands.” *ISSMGE Technical Committee TC 209 – Offshore Geotechnics*, 77–80.

Beringen, F. L., Wind, D., and Van Hooydonk, W. R. (1979). “Results of loading tests on driven piles in sand.” *Recent developments in the design and construction of piles. Proceedings of the Conference Held at the Institution of Electrical Engineers*, A. M. Burt, ed., Institution of Civil Engineers, London, UK, 213–225.

Bhattacharya, S., Nikitas, G., Arany, L., and Nikitas, N. (2017). “Soil–Structure Interactions for Offshore Wind Turbines.” *Engineering & Technology Reference*, 1(1), 1–16.

Blanc, M., Thorel, L., Isorna, R., Dano, C., Kotronis, P., and Philippe, M. (2015). “Centrifuge investigation of the axial cyclic behaviour of a single pile used for the foundation of a jacket type offshore wind turbine.” *Frontiers in Offshore Geotechnics III*, (Figure 1), 978–1.

Boccalini, F., Chen, Z., Omidvar, M., and Iskander, M. (2015). "A study of plane strain pile jacking and driving in granular media." *Geotechnical Special Publication*, 738–747.

Boulon, M., and Foray, P. (1986). "Physical and numerical simulation of lateral shaft friction along offshore piles in sand." *3rd International Conference on Numerical methods in offshore piling*, Nates, France, 127–147.

Brown, D. A., Turner, J. P., and Castelli, R. J. (2010). *Drilled shafts: Construction Procedures and LRFD Design Methods FHWA NHI-10-016. National Highway Institute U.S. Department of Transportation Federal Highway Administration*.

Chen, Y.-J., and Kulhawy, F. H. (2002). "Evaluation of drained axial capacity for drilled shafts." *Deep Foundations 2002 An International Perspective on Theory, Design, Construction, and Performance*, M. W. O'Neill and F. C. Townsend, eds., American Society of Civil Engineers, Reston, VA, United States, 1200–1214.

Chen, Z., Omidvar, M., and Iskander, M. (2016). "Observations of multi-scale granular kinematics around driven piles in plane strain condition." *Geotechnical Testing Journal*, 39(5), 827–841.

Chin, J. T., and Poulos, H. G. (1992). "Cyclic axial pile loading analyses: A comparative study." *Computers and Geotechnics*, 13(3), 137–158.

Chin, J. T., and Poulus, H. G. (1991). "A 'T-Z' approach for cyclic axial loading analysis of single piles." *Computers and Geotechnics*, 12(4), 289–320.

Chow, F. (1997). "Investigations into the behaviour of displacement piles for offshore foundations. PhD Thesis." University of London (Imperial College).

Clausen, C. J. F., Aas, P. M., and Karlsrud, K. (2005). "Bearing capacity of driven piles in sand, the NGI approach." *Frontiers in Offshore Geotechnics, ISFOG 2005 - Proceedings of the 1st International Symposium on Frontiers in Offshore Geotechnics*, 677–681.

Correlated Solutions. (2009). "VIC-2D." Columbia, SC, USA.

DeJong, J. T., Randolph, M. F., and White, D. J. (2003). "Interface load transfer degradation during cyclic loading: a microscale investigation." *Soil and Foundations*, 43(4), 81–93.

DeJong, J. T., White, D. J., and Randolph, M. F. (2006). "Microscale observation and modeling of soil-structure interface behavior using particle image." *Soil and Foundations*, 46(1), 15–28.

Diaz, E. G., and Rodríguez-Roa, F. (2010). "Design load of rigid footings on sand." *Canadian Geotechnical Journal*, 47(8), 872–884.

Doreau-Malioche, J., Combe, G., Viggiani, G., and Toni, J. B. (2018). "Shaft friction changes for cyclically loaded displacement piles: an X-ray investigation." *Géotechnique Letters*, 8(1), 1–7.

Doreau-Malioche, J., Galvis-Castro, A., Tovar-Valencia, R., Viggiani, G., Combe, G., Prezzi, M., and Salgado, R. (2019). "Characterising processes at sand-pile interface using digital image analysis and X-ray CT." *Géotechnique Letters*, 9(4), 254-262.

Einav, I. (2007). "Breakage mechanics-Part I: Theory." *Journal of the Mechanics and Physics of Solids*, 55(6), 1274–1297.

Fakharian, K. (2001). "Friction pile-soil interaction subjected to cyclic axial loads." *Proceedings of the Eleventh (2001) International Offshore and Polar Engineering Conference*, 11.

Fakharian, K., and Evgin, E. (1997). "Cyclic simple-shear behavior of sand-steel interfaces under constant normal stiffness condition." *Journal of Geotechnical and Geoenvironmental Engineering*, 123(12), 1096–1105.

Fioravante, V. (2002). "On the shaft friction modeling of non-displacement piles in sand." *Soils and Foundations*, 42(2), 23–33.

Fioravante, V., Guerra, L., and Jamiolkowski, M. (2010a). "Tensile shaft capacity of bored piles in sand." *Characterization and Behavior of Interfaces: Proceedings of Research Symposium on Characterization and Behavior of Interfaces*, J. D. Frost, ed., IOS Press Amsterdam, The Netherlands., 131–138.

Fioravante, V., Guerra, L., and Jamiolkowski, M. B. (2010b). "On the shaft capacity of non-displacement piles in sand from centrifuge tests." *7th International Conference on Physical Modeling in Geotechnics*, J. Laue and L. Seward, eds., Taylor & Francis Group, London, UK, Zurich, Switzerland, 763–768.

Fleming, K., Weltman, A., Randolph, M., and Keith, E. (2008). *Piling Engineering*. CRC Press.

Fonseca, J. (2011). "The evolution of morphology and fabric of a sand during shearing." *PhD Thesis*, Imperial College London, UK.

Fonseca, J., O'Sullivan, C., Coop, M. R., and Lee, P. D. (2012). "Non-invasive characterization of particle morphology of natural sands." *Soils and Foundations*, Elsevier, 52(4), 712–722.

Foray, P., Balachowski, L., and Rault, G. (1998). "Scale effect in shaft friction due to the localisation of deformations." *Proceedings of the International Conference Centrifuge 98*, T. Kimura, O. Kusakabe, and J. Takemura, eds., A.A. Balkema, Rotterdam, 211–216.

Foray, P. Y., Tsuha, C. H. C., Silva, M., Jardine, R. J., and Yang, Z. X. (2010). "Stress paths measured around a cyclically loaded pile in a Calibration Chamber." *Physical Modelling in Geotechnics - Proceedings of the 7th International Conference on Physical Modelling in Geotechnics 2010, ICPMG 2010*, 933–939.

Galvis-Castro, A. C., Tovar-Valencia, R. D., Prezzi, M., Salgado, R., and Ganju, E. (n.d.). "Effects of cyclic loading on the mobilization of shear stresses of model piles jacked in sand."

Galvis-Castro, A. C., Tovar-Valencia, R. D., Salgado, R., and Prezzi, M. (2019a). “Compressive and tensile shaft resistance of non-displacement piles in sand.” *Journal of Geotechnical and Geoenvironmental Engineering*, 145(9), 0401041.

Galvis-Castro, A. C., Tovar-Valencia, R. D., Salgado, R., and Prezzi, M. (2019b). “Effect of loading direction on the shaft resistance of jacked piles in dense sand.” *Géotechnique*, 69(1), 16–28.

Gao, Z., and Zhao, J. (2017). “A non-coaxial critical-state model for sand accounting for fabric anisotropy and fabric evolution.” *International Journal of Solids and Structures*, 106–107, 200–212.

Garnier, J., Gaudin, C., Springman, S. M., Culligan, P. J., Goodings, D., Konig, D., Kutter, B., Phillips, R., Randolph, M. F., and Thorel, L. (2007). “Catalogue of scaling laws and similitude questions in geotechnical centrifuge modelling.” *International Journal of Physical Modelling in Geotechnics*, 7(3), 01–23.

Gavin, K. G., and O’Kelly, B. C. (2007). “Effect of friction fatigue on pile capacity in dense sand.” *Journal of Geotechnical and Geoenvironmental Engineering*, 133(1), 63–71.

Gavin, K., Igoe, D., and Doherty, P. (2011). “Piles for offshore wind turbines: A state-of-the-art review.” *Proceedings of the Institution of Civil Engineers: Geotechnical Engineering*, 164(4), 245–256.

Ghionna, V. N., and Jamiolkowski, M. (1991). “A critical appraisal of calibration chamber testing of sands.” *Proceedings of 1st Int. Symp. on Calibration Chamber Testing (ISOCCTI)*, A. B. Huang and H. H. Hsu, eds., Elservier, Potsdam, NY, United States, 13–39.

Gui, M. W., and Bolton, M. D. (1998). “Geometry and scale effects in CPT and pile design.” *1st International Conferenc on Site Characterisation, ISC ’98*, P. K. Robertson and P. W. Mayne, eds., Balkema, Rotterdam, Atlanta, GA, USA, 1063–1068.

Guo, N., and Zhao, J. (2013). “The signature of shear-induced anisotropy in granular media.” *Computers and Geotechnics*, 47, 1–15.

Han, F., Ganju, E., Salgado, R., and Prezzi, M. (2018). “Effects of Interface Roughness, Particle Geometry, and Gradation on the Sand-Steel Interface Friction Angle.” *Journal of Geotechnical and Geoenvironmental Engineering Effects*, 144(12), 04018096.

Han, F., Salgado, R., Prezzi, M., and Lim, J. (2017). “Shaft and base resistance of non-displacement piles in sand.” *Computers and Geotechnics*, 83, 184–197.

Hussein, M. H., and Sheahan, J. M. (1993). “Uplift capacity of driven piles from static loading tests.” *3rd International Conference on Case Histories in Geotechnical Engineering*, S. Prakash, ed., University of Missouri-Rolla, MO, USA, 1–11.

IEA. (2019). *Offshore Wind Outlook 2019*.

Ismael, N. F. (2001). “Axial load tests on bored piles and pile groups in cemented sands.” *Journal of Geotechnical and Geoenvironmental Engineering*, 127(9), 766–773.

Jardine, R., Bitang, Z., Foray, P., and Dalton, C. (2009). “Experimental arrangements for investigation of soil stresses developed around a displacement pile.” *Soils and foundations*, 49(5), 661–673.

Jardine, R., Chow, F., Overy, R., and Standing, J. (2005). *ICP design methods for driven piles in sand and clays*. Thomas Telford Ltd.

Jardine, R. J., Lehane, B. M., and Everton, S. J. (1993). “Friction coefficients for piles in sands and silts.” *Offshore site investigation and foundation behaviour and Foundation behaviour*, D. A. Ardus, D. Clare, A. Hill, R. Hobbs, R. J. Jardine, and J. M. Squire, eds., Springer, Dordrecht, Netherlands, 661–677.

Jardine, R. J., and Standing, J. R. (2012). “Field axial cyclic loading experiments on piles driven in sand.” *Soils and Foundations*, Elsevier, 52(4), 723–736.

Jardine, R. J., Standing, J. R., and Chow, F. C. (2006). “Some observations of the effects of time on the capacity of piles driven in sand.” *Géotechnique*, 56(4), 227–244.

Jardine, R. J., Zhu, B. T., Foray, P., and Yang, Z. X. (2013). “Measurement of stresses around closed-ended displacement piles in sand.” *Geotechnique*, 63(1), 1–17.

Jardine, R., Puech, A., and Andersen, K. H. (2012). “Cyclic loading of offshore piles: potential effects and practical design.” *7th International Conference on Offshore Site Investigation and Geotechnics: Integrated Geotechnologies–Present and Future*, SUT, London, UK, 59–97.

Jardine, R., and Standing, J. (2000). *Pile load testing performed for HSE cyclic loading study at Dunkirk. Offshore Technology Report - OTO 2000 008*, Health and Safety Executive, UK.

Karlsrud, K., Nadim, F., and Haugen, T. (1986). “Piles in clay under cyclic axial loading-Field tests and computational modelling.” *3rd International Conference of Numerical Methods in Offshore Piling*, 165–190.

Kolk, H. J., Baaijens, A. E., and Senders, M. (2005). “Design criteria for pipe piles in silica sands.” *Proceedings of the 1st International Symposium on Frontiers in Offshore Geotechnics (IS-FOG 2005)*, S. Gourvenec and M. Cassidy, eds., Taylor & Francis Group, London, UK, Perth, WA, Australia, 711–716.

Konagai, K., Tamura, C., Rangelow, P., and Matsushima, T. (1992). “Laser-Aided Tomography: a Tool for Visualization of Changes in the Fabric of Granular Assemblage.” *Structural Engineering Earthquake Engineering*, 9(3), 193–201.

Le Kouby, A., Canou, J., and Dupla, J. C. (2004). “Behaviour of model piles subjected to cyclic axial loading.” *Cyclic Behaviour of Soils and Liquefaction Phenomena*, 159–166.

Le Kouby, A., Dupla, J. C., Canou, J., and Francis, R. (2013). "Pile response in sand: experimental development and study." *International Journal of Physical Modelling in Geotechnics*, 13(4), 122–137.

Kulhawy, F. (2004). "On the axial behavior of drilled foundations." *GeoSupport 2004: drilled shafts, micropiling, deep mixing, remedial methods, and specialty foundation systems*, J. P. Turner and P. W. Mayne, eds., American Society of Civil Engineers, ASCE, USA, 34–51.

Kulhawy, F. H., and Hirany, A. (1989). "Interpretation of load tests on drilled shafts—Part 2: Axial uplift." *Foundation engineering: current principles and practices*, F. H. Kulhawy, ed., ASCE, New York, NY, United States, 1150-1159.

Lee, C. Y., and Poulos, H. G. (1991). "Tests on model instrumented grouted piles in offshore calcareous Soil." *Journal of Geotechnical Engineering*, 117(11), 1738–1753.

Lee, C. Y., and Poulos, H. G. (1993). "Cyclic analysis of axially loaded piles in calcareous soils." *Canadian Geotechnical Journal*, 30, 82–98.

Lee, J., Prezzi, M., and Salgado, R. (2011). "Experimental investigation of the combined load response of model piles driven in sand." *Geotechnical Testing Journal*, 34(6), 653–667.

Lehane, B. (1992). "Experimental investigations of pile behaviour using instrumented field piles." Imperial College London, UK.

Lehane, B. M., Gaudin, C., and Schneider, J. A. (2005a). "Scale effects on tension capacity for rough piles buried in dense sand." *Géotechnique*, 55(10), 709–719.

Lehane, B. M., Jardine, R. J., Bond, A. J., and Frank, R. (1993). "Mechanisms of shaft friction in sand from instrumented pile tests." *Journal of Geotechnical Engineering*, 119(1), 19–35.

Lehane, B. M., Schneider, J. A., and Xu, X. (2005b). "The UWA-05 method for prediction of axial capacity of driven piles in sand." *Proceedings of the 1st International Symposium on Frontiers in Offshore Geotechnics (IS-FOG 2005)*, M. Cassidy and S. Gourvenec, eds., Taylor & Francis Group, London, UK, Perth, WA, Australia, 683–689.

Li, Y., Yang, Y., Yu, H.-S., and Roberts, G. (2018). "Principal stress rotation under bidirectional simple shear loadings." *KSCE Journal of Civil Engineering*, 22(5), 1651–1660.

Li, Z., Bolton, M. D., and Haigh, S. K. (2012). "Cyclic axial behaviour of piles and pile groups in sand." *Canadian Geotechnical Journal*, 49(9), 1074–1087.

Loukidis, D., and Salgado, R. (2008). "Analysis of the shaft resistance of non-displacement piles in sand." *Géotechnique*, 58(4), 283–296.

Loukidis, D., and Salgado, R. (2009). "Modeling sand response using two-surface plasticity." *Computers and Geotechnics*, Elsevier Ltd, 36(1–2), 166–186.

Lubliner, J. (2008). *Plasticity theory*. Dover Publications, Inc.,Mineola, NY, United States.

Mortara, G., Mangiola, A., and Ghionna, V. N. (2007). "Cyclic shear stress degradation and post-cyclic behaviour from sand–steel interface direct shear tests." *Canadian Geotechnical Journal*, 44(7), 739–752.

El Naggar, M. H., and Wei, J. Q. (2000). "Cyclic response of axially loaded tapered piles." *Geotechnical Testing Journal*, 23(1), 100–115.

De Nicola, A., and Randolph, M. F. (1993). "Tensile and compressive shaft capacity of piles in sand." *Journal of Geotechnical Engineering*, 119(12), 1952–1973.

De Nicola, A., and Randolph, M. F. (1999). "Centrifuge modelling of pipe piles in sand under axial loads." *Géotechnique*, 49(3), 295–318.

O'Neill, M., and Raines, R. (1991). "Load transfer for pipe piles in highly pressured dense sand." *Journal of Geotechnical Engineering*, 117(8), 1208–1226.

O'Neill, M. W. (2001). "Side resistance in piles and drilling shafts." *Journal of Geotechnical and Geoenvironmental Engineering*, 127(1), 3–16.

O'Neill, M. W., and Reese, L. C. (1999). *Drilled shafts: Construction procedures and design methods. Report No. FHWA-IF-99-025*.

Oda, M. (1972a). "The mechanism of fabric changes during compressional deformation of sand." *Soils and foundations*, 12(2), 1–18.

Oda, M. (1972b). "Initial fabrics and their relations to mechanical properties of granular material." *Soils and foundations*, 12(1), 17–36.

Oda, M., and Konishi, J. (1974). "Microscopic deformation mechanism of granular material in simple shear." *Soils and Foundations*, 14(4), 25–38.

Pan, B., Qian, K., Xie, H., and Asundi, A. (2009). "Two-dimensional digital image correlation for in-plane displacement and strain measurement: a review." *Measurement Science and Technology*, IOP Publishing.

Paniagua, P., Andò, E., Silva, M., Emdal, A., Nordal, S., and Viggiani, G. (2013). "Soil deformation around a penetrating cone in silt." *Géotechnique Letters*, Thomas Telford, 3(4), 185–191.

Poules, H. G. (1984). "Cyclic degradation of pile performance in calcareous soils." *Analysis and design of pile foundations:*, ASCE, New York, USA, 99–118.

Poulos, H. G. (1989a). "Cyclic axial loading analysis of piles in sand." *Journal of Geotechnical Engineering*.

Poulos, H. G. (1989b). "Pile behaviour - theory and application." *Geotechnique*, 39(3), 365–415.

Puech, A. (2013). "Advances in axial cyclic pile design : Contribution contribution of the SOLCYP project." *ISSMGE Technical Committee TC 209 – Offshore Geotechnics*, 45–57.

Puech, A., Benzaria, O., Thorel, L., Garnier, J., Foray, P., Silva, M., and Jardine, R. (2013). "Cyclic stability diagrams for piles in sands." *TC 209 Workshop 18th ICSMGE*, A. Puech, ed., Presses des Ponts, Paris, 85–88.

Puech, A., Canou, J., Bernardini, C., Pecker, A., Jardine, R., and Holeyman, A. (2012). "SOLCYP : a four-year JIP on the behaviour of piles under cyclic loading." *7th International Conference on Offshore Site Investigation and Geotechnics: Integrated Geotechnologies–Present and Future*, SUT,London, UK, 263–270.

Puech, A., and Garnier, J. (2017). *Design of piles under cyclic loading: SOLCYP recommendations*. John Wiley & Sons, Inc.

Randolph, M. F. (2003). "Science and empiricism in pile foundation design." *Géotechnique*, 53(10), 847–875.

Randolph, M. F., Dolwin, J., and Beck, R. (1994). "Design of driven piles in sand." *Geotechnique*, 44(3), 427–448.

Randolph, M. F., and Jewell, R. J. (1989). "Load transfer model for pile in calcareous soil." *International Conference on Soil Mechanics and Foundation Engineering, 12th*, Rotterdam, Netherlands., Rio De Janeiro, 479–484.

Rao, K. S. S., and Venkatesh, K. H. (1985). "Uplift behaviour of short piles in uniform sand." *Soils and Foundations*, 25(4), 1–7.

Rimoy, S., Jardine, R., Silva, M., Foray, P., Tsuha, C., and Yang, Z. (2012). "Local and global behaviour of axial cyclic loaded instrumented model displacement piles in sand." *Offshore Site Investigation and Geotechnics 2012: Integrated Technologies - Present and Future, OSIG 2012*, 279–286.

Rimoy, S. P., Jardine, R. J., and Standing, J. R. (2013). "Displacement response to axial cycling of piles driven in sand." *Proceedings of the ICE - Geotechnical Engineering*, 166(2), 131–146.

Salgado, R. (2008). *The Engineering of Foundations*. McGraw Hill.

Salgado, R. (2013). "The mechanics of cone penetration: Contributions from experimental and theoretical studies." *Proceedings of the 4th International Conference on Site Characterization 4, ISC-4*, R. Q. Coutinho and P. W. Mayne, eds., Taylor & Francis, London, UK, 131–153.

Salgado, R., Han, F., and Prezzi, M. (2017). "Axial resistance of non-displacement pile groups in sand." *Rivista Italiana di Geotecnica*, 51(4), 35–46.

Salgado, R., Mitchell, J. K., and Jamiolkowski, M. (1998). “Calibration chamber size effects on penetration resistance in sand.” *Journal of Geotechnical and Geoenvironmental Engineering*, 124(9), 878–888.

Salgado, R., and Prezzi, M. (2007). “Computation of cavity expansion pressure and penetration resistance in sands.” *International Journal of Geomechanics*, 7(4), 251–265.

Seidel, M., and Coronel, M. C. (2011). “A new approach for assessing offshore piles subjected to cyclic axial loading.” *Geotechnik*, 34(4), 276–284.

Senetakis, K., Coop, M. R., and Todisco, M. C. (2013). “The inter-particle coefficient of friction at the contacts of Leighton Buzzard sand quartz minerals.” *Soils and Foundations*, Elsevier, 53(5), 746–755.

Stas, C. V., and Kulhawy, F. H. (1984). *Critical evaluation of design methods for foundations under axial uplift and compression loading. Final Report*. United States.

Stuyts, B., Cathie, D., Falepin, H., and Burgraeve, A. (2012). “Axial pile capacity of wind turbine foundations subject to cyclic loading.” *Proceedings of the 7th International Conference of Offshore Site Investigations and Geotechnics*, 709.

Subhash, G., Nemat-Nasser, S., Mehrabadi, M. M., and Shodj, H. M. (1991). “Experimental investigation of fabric-stress relations in granular materials.” *Mechanics of Materials*, 11(2), 87–106.

Sutton, M., Orteu, J., and Schreier, H. (2009). *Image correlation for shape, motion and deformation measurements: Basic concepts, theory and applications*. Springer, New York, USA.

Tabucanon, J. T., Airey, D. W., and Poulos, H. G. (1995). “Pile skin friction in sand from constant normal stiffness test.” *Geotechnical Testing Journal*, Vol. 18(No. 3), 350–364.

Take, W. A. (2015). “Thirty-Sixth Canadian Geotechnical Colloquium: Advances in visualization of geotechnical processes through digital image correlation.” *Canadian Geotechnical Journal*, 52(9), 1199–1220.

Tehrani, F. S., Arshad, M., Prezzi, M., and Salgado, R. (2017). “Physical modeling of cone penetration in layered sand.” *Journal of Geotechnical and Geoenvironmental Engineering*, 144(1), 04017101.

Tehrani, F. S., Han, F., Salgado, R., Prezzi, M., Tovar, R. D., and Castro, A. G. (2016). “Effect of surface roughness on the shaft resistance of non-displacement piles embedded in sand.” *Géotechnique*, 66(5), 386–400.

Touma, F. T., and Reese, L. C. (1974). “Behavior of bored piles in sand.” *Journal of Geotechnical and Geoenvironmental Engineering*, (7), 749–761.

Tovar-Valencia, R. D. (2019). “Particle-Scale Effects on Pile Response During Installation and Loading.” Purdue University.

Tovar-Valencia, R. D., Galvis-Castro, A. C., Salgado, R., and Prezzi, M. (2018). “Effect of surface roughness on the shaft resistance of displacement model piles in sand.” *Journal of Geotechnical and Geoenviromental Engineering*, 144(3), 04017120.

Tovar-Valencia, R. D., Galvis-Castro, A., Salgado, R., and Prezzi, M. (2020). “Effect of base geometry on the resistance of model piles in sand.” *Journal of Geotechnical and Geoenvironmental Engineering*, (accepted).

Tsuha, C. H. C., Jardine, R. J., Yang, Z., Silva, M., Rimoy, S., Engineering, G., Engineering, E., Engineering, C., and Engineering, G. (2015). “Advanced laboratory investigation of axial cyclic loading in silica sands.” *6th IS-BA 2015 (Sixth International Symposium on Deformation Characteristics of Soils)*, (November).

Uesugi, M., and Kishida, H. (1986a). “Frictional resistance at yield between dry sand and mild steel.” *Soils and Foundations*, 26(4), 139–149.

Uesugi, M., and Kishida, H. (1986b). “Influential factors of friction between steel and dry sands.” *Soils and Foundations*, 26(2), 33–46.

Viggiani, C., Mandolini, A., and Russo, G. (2014). *Piles and Pile Foundations*. CRC Press.

Vipulanandan, C., Wong, D., Ochoa, M., & O’Neill, M. W. (1989). “Modelling of displacement piles in sand using a pressure chamber.” *Foundation Engineering Proceedings Congress*, C. Vipulanandan and F. C. Townsend, eds., American Society of Civil Engineers, 526–54.

Wadell, H. (1932). “Volume , shape , and roundness of rock particles.” *The Journal of Geology*, 40(5), 443–451.

Wadell, H. (1933). “Sphericity and Roundness of Rock Particles.” *The Journal of Geology*, 41(3), 310–331.

Wei, J., and El Naggar, H. (1998). “Experimental study of axial behaviour of tapered piles.” *Canadian Geotechnical Journal*, 35, 641–654.

Westgate, Z. J., and DeJong, J. T. (2006). “Evolution of sand-structure interface response during monotonic shear using particle image velocimetry.” *GeoCongress 2006*, American Society of Civil Engineers, Reston, VA, 1–6.

White, D. J., and Bolton, M. D. (2002). “Observing friction fatigue on a jacked pile.” *Centrifuge and constitutive modelling: Two extremes*, S. M. Springman, ed., Balkema, Rotterdam, Netherlands, 346–354.

White, D. J., and Bolton, M. D. (2004). “Displacement and strain paths during plane-strain model pile installation in sand.” *Géotechnique*, 54(6), 375–397.

White, D. J., Bolton, M. D., and Take, W. A. (2003). "Soil deformation measurement using particle image velocimetry (PIV) and photogrammetry." *Géotechnique*, 53(7), 619–631.

White, D. J., and Lehane, B. M. (2004). "Friction fatigue on displacement piles in sand." *Géotechnique*, 54(10), 645–658.

Wong, R. K. S., and Arthur, J. R. F. (1985). "Induced and inherent anisotropy in sand." *Géotechnique*, 35(4), 471–481.

Woo, S. I., and Salgado, R. (2015). "Bounding surface modeling of sand with consideration of fabric and its evolution during monotonic shearing." *International Journal of Solids and Structures*, 63, 277–288.

Yang, L. T., Li, X., Yu, H. S., and Wanatowski, D. (2016). "A laboratory study of anisotropic geomaterials incorporating recent micromechanical understanding." *Acta Geotechnica*, 11(5), 1111–1129.

Yang, Z. X., Jardine, R. J., Zhu, B. T., Foray, P., and Tsuha, C. H. C. (2010). "Sand grain crushing and interface shearing during displacement pile installation in sand." *Géotechnique*, 60(6), 469–482.

Yang, Z. X., Jardine, R. J., Zhu, B. T., and Rimoy, S. (2014). "Stresses developed around displacement piles penetration in sand." *Journal of Geotechnical and Geoenvironmental Engineering*, 140(3), 04013027.

Yimsiri, S., and Soga, K. (2010). "DEM analysis of soil fabric effects on behaviour of sand." *Géotechnique*, 60(6), 483–495.

Yimsiri, S., and Soga, K. (2011). "Effects of soil fabric on behaviors of granular soils: Microscopic modeling." *Computers and Geotechnics*, 38(7), 861–874.

VITA

Ayda Catalina Galvis Castro was born in Colombia in 1986. She received her Bachelor and Master degree in Civil Engineering from Universidad Nacional de Colombia. In 2013, she started her Ph.D. study with Dr. Rodrigo Salgado and Dr. Monica Prezzi at Purdue University, U.S. Ayda joined Fugro in August of 2019, where she currently serves as a Project Professional. Since joining Fugro, Ayda has provided services on geotechnical studies for LNG projects.

PUBLICATIONS

Ganju, E., Han, F., Castro, A., Prezzi, M., & Salgado, R. “Experimental study of crushing in cone penetration test in silica sand.” *Geo-Congress* (2020) Minneapolis, Minnesota

Galvis-Castro, A.C., Ganju, E., Tovar-Valencia, R.D., Prezzi, M., & Salgado, R. “Effect of installation method on the ratio of tensile to compressive unit shaft resistance of piles in dense sand.” *DFI 44th Annual Conferenc*e (2019) Chicago, Illinois

Galvis-Castro, A. C., Tovar-Valencia, R. D., Salgado, R., Prezzi, M. (2019) “Compressive and tensile shaft resistance of non-displacement piles in sand.” *Journal of Geotechnical and Geoenvironmental Engineering*. 145 (9), 04019041

Doreau-Malioche, J., Galvis-Castro, A. C., Tovar-Valencia, R., Viggiani, G., Combe, G., Prezzi, M., Salgado, R. (2019) “Characterising processes at pile-sand interface using digital image analysis and x-ray CT.” *Géotechnique Letters*, 9 (4), 254-262

Galvis-Castro, A. C., Tovar, R. D., Salgado, R., Prezzi, M (2018) “Effect of loading direction on the shaft resistance of jacked piles in dense sands.” *Géotechnique*, 69 (1), 16-28

Tovar-Valencia, R. D., Galvis-Castro, A. C., Salgado, R., and Prezzi, M. (2019). “Closure to the discussion by Diyaljee on ‘Effect of surface roughness on the shaft resistance of displacement model piles in sand.” *Journal of Geotechnical and Geoenvironmental Engineering*, 144 (12)

Tovar-Valencia, R. D., Galvis-Castro, A., Salgado, R., Prezzi, M. (2018) “Effect of surface roughness on the shaft resistance of displacement model piles in sand.” *Journal of Geotechnical and Geoenviromental Engineering*. 144 (3), 04017120.

Tovar-Valencia, R. D., Galvis-Castro, A. C., Salgado, R., Prezzi, M. (2018) “Short-term setup of jacked piles in a calibration chamber.” *Journal of Geotechnical and Geoenvironmental Engineering*, 144 (12).

Tehrani, F. S., Han, F., Salgado, R., Prezzi, M., Tovar, R. D., and Castro, A. G. (2016) “Effect of surface roughness on the shaft resistance of non-displacement piles embedded in sand.” *Géotechnique*, 66 (5), 386-400

Tovar-Valencia, R. D., Galvis-Castro, A. C., Prezzi, M., & Salgado, R. (2020). “Effect of base geometry on the base resistance of model piles in sand.” *Journal of Geotechnical and Geoenvironmental Engineering* (accepted)

Ganju, E., Janbi, F., Galvis-Castro, A. C., Prezzi, M., & Salgado, R. (2020). “Displacements, strain and shear bands in deep and shallow penetration processes.” *Journal of Geotechnical and Geoenvironmental Engineering* (under review)